

Alma Mater Studiorum – Università di Bologna

DOTTORATO DI RICERCA IN
ASTROFISICA

Ciclo XXX

Settore Concorsuale: 02/C1

Settore Scientifico Disciplinare: FIS/05

MULTI-FREQUENCY POLARIMETRIC STUDY OF A COMPLETE SAMPLE
OF EXTRAGALACTIC RADIO SOURCES: RADIO SOURCE POPULATIONS
AND COSMOLOGICAL PERSPECTIVES

Presentata da: Vincenzo Galluzzi

Coordinatore Dottorato
Ch.mo Prof. Francesco Rosario Ferraro

Supervisore
Dott.ssa Marcella Massardi

Co-Supervisor
Ch.ma Prof.ssa Loretta Gregorini
Ch.mo Prof. Gabriele Giovannini

Esame finale anno 2018

*The present thesis work was carried out
in the framework of the research activities
of the Italian Node of the European ALMA Regional Centre,
hosted by the INAF-Istituto di Radioastronomia (Bologna).
The thesis project was selected among those presented
for the INAF call for PhD project in 2014.
We acknowledge financial support by the Italian Ministero
dell'Istruzione, Università e Ricerca
through the grant Progetti Premiali 2012-iALMA
(CUP C52I13000140001).*

Multi-frequency polarimetric study of a complete sample of extragalactic radio sources: radio source populations and cosmological perspectives

Vincenzo Galluzzi

Abstract

The high-frequency (> 20 GHz), bright flux density (> 200 mJy) radio population is dominated by blazars (BL Lacs and Flat Spectrum Radio Quasars), i.e. compact Doppler-boosted objects observed closely to the line of sight, whose emission at higher and higher frequency mostly arises from self-absorbed, knot-like synchrotron structures in the relativistic jet closer and closer to the active nucleus. Their polarization properties was so far poorly constrained at high frequency, since spectra become steeper and the polarization fraction is typically few percents ($\sim 2.5\%$ at 20 GHz) of the total intensity flux density. Thus, observations require sub-mJy sensitivities and results in literature are easily affected by spectral, detection and variability-related biases. Most of the current estimates rely on extrapolations from low-frequency samples, which are affected by large uncertainties.

Extending the characterization of polarization properties of radio sources to high frequencies provides invaluable information about magnetic fields and plasma in the inner and unresolved regions of relativistic jets. Furthermore, extragalactic radio sources are an important contaminant to the microwave sky in total intensity and in polarization at scales smaller than 30 arcmin, up to 100 GHz: an accurate determination of radio source emission is therefore crucial to extract the Cosmic Microwave Background (CMB) angular power spectrum and, in particular, to study the primordial B-mode polarization that might be extremely weak for low values of the tensor to scalar perturbations ratio ($r = T/S$) associated with the stochastic background of gravitational waves, one of the most ambitious goal of current and future CMB projects. We present the analysis of high sensitivity ($\sigma \sim 0.6$ mJy) multi-frequency and multi-epoch polarimetric observations of a complete sample of 104 compact extragalactic radio sources drawn from the faint (> 200 mJy at 20 GHz in total intensity) Planck-ATCA Co-eval Observations (PACO) catalogue, performed with the Australia Telescope Compact Array (ATCA) at 7 frequencies, between 2.1 and 38 GHz. 89 of our sources have a counterpart in the 72 to 231 MHz GLEAM survey, providing an unparalleled spectral coverage of 2.7 decades of frequency for these sources. We found that polarization spectra of single sources cannot be simply inferred from total intensity ones, as different source components dominate the different emissions,

despite total intensity spectra can be fitted by a double power law in over than 80% of the cases. On average, spectra steepen at frequencies > 30 GHz (both in total intensity and polarization). We distinguish six spectral categories (by using total intensity spectral shape or the number of inferred synchrotron components) finding different behaviours in polarization fractions and polarization position angles among them.

Multi-epoch variability analysis (from 1.5 up to 10 yr time lags) is also presented, taking into account our past polarimetric measurements, in the PACO and AT20G.

Our high sensitivity polarimetry has allowed a 5σ detection of the weak circular polarization for $\sim 38\%$ of the dataset, and a deeper estimate of 20 GHz polarization source counts than has been possible so far.

An ALMA project observed in cycle 3 extends the analysis up to 100 GHz for a (complete) sub-sample of 32 objects. We find synchrotron signal also at these frequencies with no sign of thermal as well as dust emissions: few extended objects are briefly discussed, since they can be used as case studies on which constrain models of magnetic fields and reacceleration mechanisms in the AGN environment. In addition, the observations provide useful informations both for better evaluating the statistical and systematic accuracies of polarization position angles obtained with ALMA and for exploring the possibility of using ALMA measurements of bright and strongly polarized radio sources, in order to help in calibrating the polarization position angle in CMB experiments. In fact, such calibration accuracy is becoming the limiting factor of several CMB polarization measurements. We compute number counts in polarization at ~ 100 GHz by means of one of the most updated models and forecast the contribution of unresolved extragalactic radio sources in terms of the CMB polarization power spectra for forthcoming CMB experiments.

Introduction

Our Universe is hierarchically populated by structures whose typical size can reach $\sim 80 \text{ Mpc h}^{-1}$ scale, i.e. the so-called galaxy filaments. The fundamental building blocks are the galaxies: they can show different shapes, structures and different physical conditions. About 1% of all the galaxies display a special property, i.e. their bolometric luminosities are ~ 3 orders of magnitude higher than “normal” galaxies, with typical values around $10^{40} - 10^{41} \text{ W}$, mainly concentrated in a compact central region, called “Active Galactic Nucleus” (AGN). This huge amount of energy cannot be solely ascribed to star formation activity, gas or dust emissions. The accepted idea is that the central SMBH (with M in the range $10^6 - 10^{10} M_{\odot}$) is the engine of this emission: through the accretion of matter it triggers several mechanisms which result in such powerful emissions in different bands of the electromagnetic spectrum (from radio to gamma rays). Hence, the galaxy which hosts an AGN is dubbed “active galaxy”.

The study of AGNs and their interaction with their host galaxies is among the most active research fields in modern astrophysics: understanding the connection between assumed first principles (e.g. the black hole intrinsic properties in the Kerr metric) and global observables (e.g. radio emissions, optical continuum or line emissions, X-ray and gamma emissions) is crucial to constrain the different morphologies and mechanisms that in AGNs take place and how they evolve with time (i.e. redshift). The study of AGNs could improve our knowledge of how gravity works in extreme regimes and may help in formulating a theory for turbulence, which remains one of the biggest unsolved problems in classical physics. Furthermore, it has been established that AGNs play a relevant role in the early stages of galaxy formation and evolution. The knowledge of AGN population properties, the mechanisms that determine their emission in different bands and their interaction with the environment and the hosting galaxies are crucial to constrain the evolutionary models. In order to achieve such ambitious goals, the scientific community is trying to address open questions about morphology and physical mechanisms.

At present the major framework is represented by the unified model of AGNs, that successfully describes the observed features of different classes of objects as a function of their orientation angles with the line of sight. A small observing angle is responsible for jetted objects classified as blazars, while a quite perpendicular one leads to classical radio galaxies as Fanaroff-Riley (FR) of I and II types. In the first case source appears as point-like in radio map (see the left panel in fig. 1), while in the second case a couple of

jets departing from the central AGN are clearly visible (see Fig. 1, right panel, which reports Cygnus A, a typical FRII).

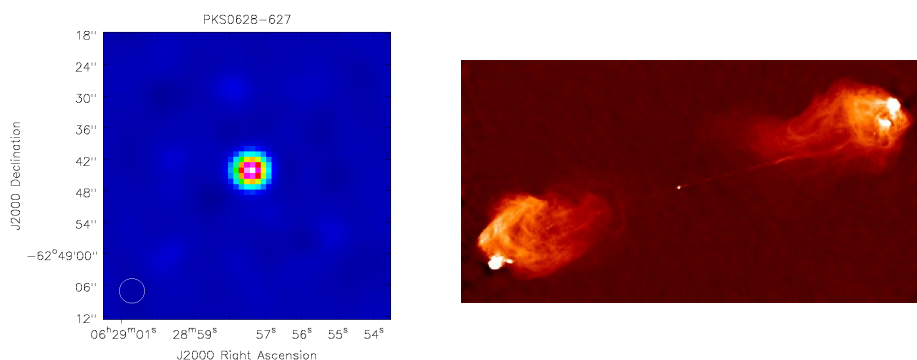


Figure 1: (*left panel*) Flat-Spectrum radio quasar PKS0628-627; (*right panel*) FRII radio galaxy Cygnus A.

Despite the amount of work done trying to get rid of the bestiary of objects arising from several observational criteria, there is still an open debate about how many and what are the prototypical categories to be studied as separate classes of objects, in other words what are the physical observables useful to distinguish them. In order to overcome classification issues, statistical approaches on complete flux density-selected samples can be exploited to investigate physical mechanisms and how they evolve with time. As an example, it is not clear if Flat Spectrum Radio Quasar (FSRQs) and BL Lacertae (BL Lacs) are intrinsically different objects (the first having an higher power) or can be related in some evolutionary scenarios in which the FSRQs evolve into BLLacs. At the same time it seems reasonable that FSRQs are indeed the fraction of FRII seen closer to the line of sight and that BL Lac are the same for FRI.

About 10% of AGNs (hence $\sim 0.1\%$ of all the galaxies) is radio loud, i.e. have a radio emission associated to a jet. There are several open questions related to the emission mechanisms in the radio band: the matter composition of the jet is not exactly known (there are models with an ordinary electron-positron plasma or with a radiating electron-proton plasma); there are indications suggesting a two-component structure in jets; synchrotron signals show an inverse Compton signature but it is still debated whether the role of the electromagnetic field is played only by the lower energy photons emitted and self-absorbed by the lower energy electrons of the emitting region (synchrotron self-Compton, SSC) or there is a contribution from an external field (such as CMB or Extragalactic Background Light, EBL), or even from thermal processes are not negligible and may contribute as well. It is not clear what powers the acceleration and collimation jets and what is the role played by the magnetic field in this process. All these points can be resumed by saying that the energy injection of radio power is not known and that magnetic fields and plasma (together with eventual turbulence and external electromagnetic field) are the main ingredients that provide synchrotron emissions. Since these processes are naturally polarized, observations in the radio band require

a full-polarimetric approach. Another important point concerning with radio observations is the methodology to adopt in coping with these open issues. There are basically two paradigms which are complementary: the Very Long Baseline Interferometry (VLBI) allows to study few objects in great detail, with a typical spatial resolution at the \sim mas scale, while a statistical approach on larger samples is feasible if one uses shallower resolutions (at the \sim arcsec scale).

Even if synchrotron radiation can be up to $\simeq 70 - 80\%$ polarized, the polarization degree of extragalactic sources is rarely observed to be higher than $\sim 10\%$; the median values are $\sim 2.5\%$ at 20 GHz (Massardi et al. 2013). This is the result of several depolarization effects. The measured polarized flux is an average of the emission from sub-structures with different orientations of the magnetic field. Further depolarization may be due to differential Faraday rotation that may be amplified by its frequency dependence within the bandwidth. As a consequence, polarimetric observations generally require high sensitivities and a detailed knowledge of instrumental properties to perform accurate calibration (see Massardi et al. 2016), a delicate procedure at high frequencies where, among other things, the signal is expected to be fainter due to optically-thin synchrotron regime. For these reasons polarimetric surveys of large source samples at $\nu \gtrsim 20$ GHz have become possible only recently thanks to the advent of large bandwidth instruments, with broad band digital correlators, e.g. the new Compact Array Broadband Backend (CABB) system of the Australia Telescope Compact Array (ATCA), or the recent upgrades of the Jansky Very Large Array (JVLA).

Another useful ingredient to investigate the aforementioned unsolved points in AGNs is the multi-frequency approach: taking into account that variability for AGN is related to the principle of causality to the physical size of the emitting region at a given frequency, one should perform high frequency observations sufficiently close in time to get a reliable spectral reconstruction. Doing this, it is possible, at least on a statistical basis and exploiting the whole polarimetric information, to probe regions closer and closer to the base of the jet as the frequency increase. Since the instrument upgrades are quite recent there are so far only few works on complete samples at high frequencies. Typically we can find in literature compilations of multi-frequency data from different epochs, or statistical study which present a bright (~ 1 Jy) flux density selection and/or a spectral selection of flat-spectrum objects. As a results these works are easily affected by variability-related, spectral and detection biases.

The present work, owing to the completeness of the sample, the high sensitivity and the close-in-time multi-frequency characterisation, allows us to minimise all these effects. In this thesis we present a multi-frequency (between 2.1 and 100 GHz) and multi-epoch (time lag spans from 1.5 yr to 10 yr) polarimetric study on a complete sample (up to 104) objects selected from the AT20G survey, i.e. a blind radio survey carried out at 20 GHz with ATCA. The completeness limit in total intensity for our sample is 200 mJy at 20 GHz and this naturally selects Doppler-bosted sources like FSRQs and BLLacs (i.e. blazars). Our polarimetric study is corroborated by total intensity data (for

$\simeq 86\%$ of our sample) from the GLEAM survey (realized with the Murchinson Widefield Array, MWA) between 72 and 231 MHz

Other than being of interest to investigate the source population properties, multi-frequency and multi-epoch polarimetric observations of radio sources are useful cosmological tools for several reasons. Radio sources are the most relevant foreground contaminant of the Cosmic Microwave Background (CMB) polarization maps on scales of up to ~ 30 arcmin in the 70 – 100 GHz frequency range (Massardi et al. 2016), where Galactic foreground emissions are at a minimum. A proper characterisation of the radio source contribution to the power spectrum in polarization is essential for a precise assessment of the lensing B-mode signal (Hanson et al. 2013; Ade et al. 2014). This, in turn, is essential for the detection and the characterisation of the power spectrum of the primordial B-modes associated with the stochastic background of gravitational waves, the most ambitious goal of current and future CMB projects (André et al. 2014). Because of the broad variety of polarized emission spectra, extrapolations from low frequencies (< 20 GHz) are inadequate to model the radio source contribution in CMB polarization maps (Huffenberger et al. 2015).

At the same time, radio sources are the privileged calibrators both of the polarized intensity and of the polarization angle for CMB experiments. The systematic errors due to inaccuracies in the calibration of the polarization angle are becoming the limiting factor for CMB polarization experiments, also taking into account that they produce a leakage of E-modes into B-modes (e.g. Kaufman et al. 2016). Unfortunately, the number of compact, bright, highly polarized and stable enough extragalactic sources, suitable for accurately calibrating CMB polarization maps, is low. One of the aims of our polarization analysis is to identify good candidates for this purpose. In the region occupied by our sample there is Pictor A, a classic double radio galaxy at redshift 0.035. Pictor A was observed as the most relevant target and suitable calibrator for polarization among the sources observed with ATCA by Burke-Spolaor et al. (2009) thanks to its position, its ~ 10 arcmin total extent, and the 20 GHz ~ 0.5 Jy integrated polarized emission, mostly concentrated on the region of the western hotspot, which is highly diffuse so that it is not expected to be variable. We present a preliminary mm-band complete map in total intensity for this object.

The thesis is laid out as follows: in Chapter 1 we introduce and describe the properties of AGNs in general and of blazars in particular; in Chapter 2 we briefly resume the polarimetric technique in radio interferometry in general, hence focusing on particular facilities which provided data for this study. Chapter 3 presents the multi-frequency polarimetric study of the complete sample of 104 sources with some of the results of the low-frequency SKA-oriented simulation T-RECS, which exploits the source population properties we found. Chapter 4 is devoted to the 100 GHz polarimetric follow-up on a complete sub-sample of 32 objects performed with ALMA, and provides the relevant material for cosmological purposes: polarization source counts at 100 GHz and the relative assessment about the level of contamination by compact extragalactic radio sources to the CMB angular power spectrum. The

final chapter recollects conclusions of this thesis.

Throughout this work, we use a Λ CDM cosmology with $h = 0.6777$, $\Omega_m = 0.307$, and $\Omega_\Lambda = 0.693$ (Planck Collaboration et al. 2016). The radio spectral index is defined such that $S(\nu) \propto \nu^\alpha$. Following the IAU convention, all angles are measured counter-clockwise when looking at the source.

Contents

Introduction	iii
List of Figures	xi
List of Tables	xix
1 Active galaxies	1
1.1 Active Galactic Nuclei	1
1.1.1 Radio quiet and radio loud AGNs	5
1.1.2 The unified model of AGNs	7
1.1.3 Historical legacy: steep/flat dichotomy	8
1.2 Polarimetric properties & observations	11
1.3 Perspectives for cosmology	16
1.3.1 Targets for validation of cosmological observatories	18
1.3.2 Targets for Cosmic Polarization Rotation measurements	19
2 Observations and polarimetric data reduction	23
2.1 Selecting a complete sample: from the AT20G to the faint PACO sample	23
2.2 ATCA observations	25
2.3 Polarimetric calibration for a linear feed based array	28
2.3.1 Calibration in MIRIAD	32
2.3.2 September 2014 campaign and implemented calibration	34
2.3.3 March-April 2016 campaign and implemented cali- bration	38
2.3.4 Intra-band depolarization	42
2.4 July 2016 ATCA campaign at 33 and 35 GHz	43
2.5 ALMA observations and calibration	45
2.5.1 Data reduction	46
3 Centimetric band multi-frequency characterization of polarimet- ric and total intensity behaviour of radio sources	51
3.1 Stokes parameters (and related quantities) estimations	51
3.1.1 Error budget	53
3.2 Data analysis	54
3.2.1 Fit procedures	54
3.2.2 Spectral properties of the sample	55

3.3	GLEAM counterparts	64
3.3.1	Linear polarization fraction	73
3.3.2	Polarization angle: cm- and mm-wavelength regime behaviour	77
3.3.3	Circular polarization	80
3.4	Variability	81
3.5	Source counts in polarization	92
3.6	Modelling AGN population in polarization: our contribute to the T-RECS simulation	96
3.6.1	Active Galactic Nuclei model description	96
3.6.2	Number counts	98
3.6.3	Polarization	99
4	ALMA follow-up at 100 GHz	103
4.1	Data analysis	103
4.1.1	Spectral behaviour	104
4.1.2	Polarization fraction	105
4.1.3	Rotation measures at ALMA frequencies	122
4.2	Source Counts	125
4.3	Peculiar objects	125
4.4	Forecasts for forthcoming CMB ground-based experiment	132
4.4.1	PS4C with current and forthcoming CMB ground based experiments	136
4.4.2	PS4C with future space missions	137
4.4.3	An alternative to stacking for characterizing extra- galactic radio sources: the IDA method	138
	Conclusions	144
A	MIRIAD scripts for ATCA data reduction	149
A.1	September 2014 campaign	149
A.1.1	Script for data reduction at 5.5 GHz	149
A.1.2	Script for data reduction at 18 GHz	151
A.2	March–April 2016 campaign	152
A.2.1	Script for data reduction at 2.1 GHz	152
A.2.2	Script for data reduction refinement at 5.5 GHz (merg- ing the I, II slot and the I GT)	154
A.2.3	Script for data reduction at 33 GHz	155
	Bibliography	159

List of Figures

1	(<i>left panel</i>) Flat-Spectrum radio quasar PKS0628-627; (<i>right panel</i>) FR II radio galaxy Cygnus A.	iv
1.1	A cartoon showing the AGN prototypical structure (adapted from Urry & Padovani 1995).	6
1.2	A cartoon of the AGN unified model from Beckmann & Shrader (2012). The different AGN types depending on the angle under which the objects are seen are shown for both radio-loud and radio- quiet objects in the top and in the bottom part of the image, respec- tively.	9
1.3	Median fractional polarizations (error bars report inter-quartile dis- tances) at different frequencies for observations of a complete sam- ple of 53 objects with $S_{20\text{ GHz}} > 200$ mJy (black crosses) and other samples, reported in Tab. 1.1: the AT20G survey (Murphy et al. 2010, blue diamonds), (Klein et al. 2003, red crosses), (Agudo et al. 2014, green triangles), and (Sajina et al. 2011, orange squares).	16
1.4	The CMB B-mode polarization angular power spectrum for differ- ent tensor-to-scalar perturbation ratios (solid black lines), lensing (blue dots), and an estimate of potential residual of Galactic fore- ground (red three dots dashes) compared with the B-mode signal from polarized radio sources at 100 GHz (thin green lines) assum- ing the detection thresholds of 200 mJy (dashes) and 60 mJy (long dashes) in total intensity (Tucci & Toffolatti 2012). Thick green lines show the uncertainty in the radio source contribution coming from a 1% error in the statistical knowledge of their polarization degree. See also the text.	17
2.1	Polar plot showing the distribution of the 5890 sources in the AT20G catalogue	24
2.2	Polar plot showing the distribution of the three PACO samples: cyan filled diamonds are the bright PACO objects ($S_{20\text{ GHz}} > 500$ mJy); pink empty diamonds are for the faint PACO sources ($S_{20\text{ GHz}} >$ 200 mJy, among which the objects we study) and green squares identify the spectrally-selected PACO sample. Black asterisks are ATCA calibrators.	25
2.3	Shadowing diagram for ATCA array configurations H214 (from the ATCA Users' Guide).	27

2.4	Shadowing diagram for ATCA array configurations H75 (from the ATCA Users' Guide).	28
2.5	Diagram showing the data preparation for ATCA RPFITS files (cf. ATCA Users' Guide).	37
2.6	Diagram showing the first step for determining a model for PKS0537-441 at 5.5GHz.	38
2.7	Diagram showing the first step for determining a model for PKS0537-441 at 18GHz.	39
2.8	Calibration scheme used for 18GHz calibration of September 2014 campaign.	40
2.9	Maps in total intensity (<i>colours</i>) and polarization (<i>contours</i>) for AT20GJ0408-7507 at 5.5, 18, 24, 33 and 38 GHz. The two-lobe structure is resolved at the higher frequencies. The eastern lobe appears to be strongly depolarized.	41
2.10	Diagram showing procedure of data reduction for the March and April 2016 campaign valid at each observing frequency and for each slot (cf. Tab. 2.1).	42
2.11	Diagram showing the scheme used to refine leakage solutions, once visibilities from different slots (but at the same frequency) are merged.	43
2.12	Comparison of the fractional polarization measured in the two 1 GHz-wide sub-bands of the 2 GHz-wide bands at 5.5 GHz (<i>top panel</i>) and at 33 GHz (<i>bottom panel</i>). Red asterisks, blue pluses and green diamonds refer to steep-spectrum, flat-spectrum and peaked-spectrum sources, respectively (the spectral classification is described in sec. 3.2.2). The bisector is shown as a dashed line.	44
2.13	Sketch of ALMA full-Stokes calibration (cf. CASA Guide).	49
2.14	Polar plot showing the distribution of the complete PACO sample. The black solid curve surrounds the sample observed in September 2014, the grey one the extension of March and April 2016. The red, blue and green areas are for each SG of ALMA observations.	50
3.1	Spectra in total intensity and polarization, polarization fraction and polarization angle for the 104 objects of the faint PACO sample, observed in the September 2014 and March-April 2016 campaigns. The error bars are not displayed since they are smaller than the symbols. Total intensity: red pluses indicate our observations and the solid magenta lines show the fitting curves. The orange crosses show the median PACO flux densities (July 2009-August 2010) while the brown triangles represent the AT20G observations (best epoch in 2004-2008). (<i>Continued...</i>)	56
3.1	(<i>Continued</i>). Polarization (flux density): black pluses refer our observations. Upper limits are shown as black filled downwards triangles. The solid blue lines indicate the best fit curves. The AT20G observations (best epoch in 2004-2008) are represented by green diamonds. (<i>Continued...</i>)	57

3.1	(Continued). Other quantities available only for the September 2014 and March-April 2016 campaigns: linear polarization fractions : purple asterisks with upper limits shown as downwards pointing purple filled triangles; circular polarization fraction : blue circles and downward triangles for upper limits. Polarization angle (PA) : black diamonds.	58
3.1	Continued.	59
3.1	Continued.	60
3.1	Continued.	61
3.1	Continued.	62
3.2	Radio colour-colour diagrams for (<i>from top to bottom</i>) total intensity and polarized flux density. Symbols identify the spectral type in total intensity: pluses for flat-spectrum, asterisks for steep-spectrum, diamonds for peaked-spectrum. Colours refer to the spectral shape between 2.5 and 18 GHz: red for steep-spectrum, blue for flat-spectrum, green for peaked-spectrum and violet for inverted-spectrum sources.	65
3.3	Spectra in total intensity and polarization taking into account GLEAM observations between 72 and 231 MHz (orange pluses). Our observations in total intensity are the red pluses, while black pluses and downward triangles are for polarization. The fits in total intensity and polarization are given as red and black solid curves, respectively. We report the SUMSS (Sydney University Molonglo Sky Survey, Mauch et al. 2003) flux density at 843 MHz just for comparison, but we do not use it in the fit procedures. For each object, after its name, spectral indices (computed in total intensity) $\alpha_{0.2}^{0.4}$, $\alpha_{2.5}^{5.5}$ and α_{28}^{38} are provided. At the end of the title of each plot there is the spectral classification in terms of estimated synchrotron components (see 3.3.1).	66
3.3	Continued.	67
3.3	Continued.	68
3.3	Continued.	69
3.3	Continued.	70
3.3	Continued.	71
3.3	Continued.	72
3.4	Median polarization fraction behaviour with frequency (at 2.1, 5.5, 9, 18, 24, 33 and 38 GHz) for all the sources (black), for steep sources (red), for peaked (green) and flat ones (blue). The errors on median values are given by $1.253 \text{ rms} / \sqrt{N}$, where rms is the standard deviation around the mean and N is the number of the data (at a given frequency) for a given class of objects (cf. Arkin & Colton 1970).	75

3.5	Median polarization fraction at the observation frequencies (2.1, 5.5, 9, 18, 24, 33 and 38 GHz) for all the sources (black), for 1C sources (red), for 2-3C sources (green) and for sources with more than 3 components (blue, labeled “>3C”). The errors on median values are given by $1.253 \text{ rms} / \sqrt{N}$, where rms is the standard deviation around the mean and N is the number of detected sources (cf. Arkin & Colton 1970).	76
3.6	Faraday map of the Galaxy provided by Oppermann et al. (2015) with the circle surrounding the region in which lines of sight of our 104 sources intercepts the Galactic Faraday screen. RM values reported in the rainbow scale are in rad/m^2	79
3.7	Mean variability indices in total intensity vs. time lag at the observed frequencies (different colours). Variability measurements for the faint PACO sample are also displayed (Massardi et al. 2016).	86
3.8	Mean variability indices in total intensity vs. time lag at the observed frequencies (different colours). Variability measurements for the faint PACO sample are also displayed (Massardi et al. 2016).	86
3.9	Mean variability indices in total intensity vs. flux density at 18 GHz for the 4 – 5 yr time lag.	87
3.10	Mean variability indices in total intensity vs. flux density at 18 GHz for the 6 – 7 yr time lag.	87
3.11	Spectra of the sample with $b < -75^\circ$ in total intensity for 2014 (red symbols) and 2016 (blue symbols) campaigns. Fitting curves are shown in magenta.	88
3.11	<i>Continued.</i>	89
3.11	<i>Continued.</i>	90
3.11	<i>Continued.</i>	91
3.12	Distribution of the polarization fraction at 18 GHz. Errors and upper limits correspond to a 1σ level. The black circles refer to the sample studied in this work, the red pluses to the full AT20G bright sample studied in Massardi et al. (2013). The corresponding fit by a lognormal distribution for each dataset is reported with a solid lines of the same colour.	93
3.13	Differential source counts at 20 GHz in polarization obtained in this work plotted with black circles (black downward triangles are for upper limits). Also shown, for comparison, are the estimates by Massardi et al. (2013) using the polarimetric data from their own survey, somewhat shallower than the present one ($S_{20\text{GHz}} > 500 \text{ mJy}$) combined with the full AT20G catalogue (blue diamonds and blue downward triangles for upper limits). The curves show the predictions of the Tucci & Toffolatti (2012) model: blue curves for the “conservative” case and red curves for the “optimistic” case. The solid lines represent the total number counts; the dotted lines are for steep-spectrum sources (classified at low frequencies); the dashed lines are for flat objects (flat-spectrum radio quasars, i.e. FSRQs and BL Lacs).	95

- 3.14 Comparison between source counts in total intensity at 1.4 (*upper panel*) and 3 GHz (*lower panel*) from the T-RECS generated catalogues on a 25 deg² patch (black pluses are from the sum of all the AGNs and star forming galaxies), red pluses for steep-spectrum AGNs, blue pluses for FSRQ and green pluses for BL Lacs. Solid curves refers to the Bonato 2017 model for all the AGNs (black solid line), the steep-spectrum objects (red solid line), the FSRQs (blue solid line) and the BL Lacs (green solid line). Any other symbol refers to source counts reported in literature, as indicated in the legend. 100
- 3.15 Preliminary comparison between source counts in polarization at 1.4 GHz from the T-RECS generated catalogues (on a 1 deg² patch): indigo squares are from the sum of all the AGNs and SF galaxies and black diamonds represent polarization source counts obtained from the NVSS survey by using a stacking technique. 101
- 4.1 Colour-colour plot showing spectral indices in total intensity and polarization. Different colours refers to different sub-class in total intensity: red for steep, green for peaked and blue for flat-spectrum objects. Rightward triangles are for lower limits for spectral indices in polarization due to non-detections at ATCA frequencies. 106
- 4.2 Spectra in total intensity and polarization, polarization fraction and polarization angle for the 32 objects of the faint PACO sample, observed in August and September 2016 with ALMA. The error bars are not displayed since they are smaller than symbols. **Total intensity:** filled red circles indicate ATCA 2016 and ALMA observations. The filled orange circles show MWA/GLEAM flux densities while the yellow one is for SUMMS. Orange squares are ATCA 2014 observations and blue stars are PACO observations (2009-2010). (*Continued...*) 107
- 4.2 (*Continued*). **Polarization (flux density):** filled black circles refer to ATCA 2016 and ALMA observations. Upper limits are shown as black filled downwards triangles. Black squares represent previous ATCA observations (September 2014). (*Continued...*) 108
- 4.2 (*Continued*). **Linear polarization fractions:** filled purple diamonds with upper limits shown as downwards filled triangles for ALMA and ATCA observations; purple squares with upper limits shown as downward purple triangles for September 2014 ATCA observations. **Polarization angle:** filled indigo diamonds for ATCA 2016 and ALMA observations; indigo squares for previous September 2014 ATCA observations. 109
- 4.2 (*Continued*). 110

4.3	Images for Stokes I, Q and U for the 31 objects unresolved (or barely resolved) observed in September 2016 with ALMA (see the sec. 4.3 for images of the well resolved object AT20GJ040848-750720). When both Stokes are detected (the polarization angle can be determined), I maps also display the polarization vector (intensity being proportional to the linear polarized flux density) thanks to the software KAFE (the Keywords of Astronomical FITS-images Explorer, Burkutean & the Italian ALMA Regional Centre node 2018, submitted to Journal of Astronomical Telescopes, Instruments, and Systems).	111
4.3	<i>(Continued)</i>	112
4.3	<i>Continued</i>	113
4.3	<i>(Continued)</i>	114
4.3	<i>(Continued)</i>	115
4.3	<i>(Continued)</i>	116
4.3	<i>(Continued)</i>	117
4.3	<i>(Continued)</i>	118
4.4	Distribution of the percentage polarization fraction at 97.5 GHz obtained with a bootstrap and re-sampling of the observed distribution of the polarization fractions (green points). The lognormal fit is shown by the blue solid line (the shaded area represents the 1σ uncertainty in the fitting curve). We also plot the distribution obtained by Bonavera et al. (2017) (the orange solid line with the relative 1σ shaded area).	119
4.5	Frequency dependence of the median polarization fraction for sources with different spectral classification. At 2.1, 5.5, 9, 18, 24, 33 and 38 GHz we show the median polarization percentages, with their uncertainties, for the full sample by Galluzzi et al. (2018), comprising a total of 104 sources. To these estimates we have added the median polarization percentage at 97.5 GHz for the complete subsample of 32 objects observed with ALMA. We also subdivide the sources by the number of spectral components: 1 (1C), 2–3 (2–3C) and more ($> 3C$).	120
4.6	Polarization fraction against total flux density at 97.5 GHz for the complete sample of 32 objects observed with ALMA. Red stars, green plus signs and blue diamonds stand for steep-, peaked- and flat-spectrum objects respectively.	122
4.7	Successful RM fits for 19 objects of the complete sample observed with ALMA between 90 and 105 GHz.	124

- 4.8 Euclidean normalized differential number counts at 100 GHz. The dotted, dashed, dot-dashed and blue solid lines represent the number counts for BL Lacs, FSRQs, SSRSs and the total, respectively, as predicted by De Zotti et al. (2005) model in total intensity (upper lines) and in polarization (lower lines). The C2Ex model in total intensity and relative predictions in polarization presented by Tucci & Toffolatti (2012) are shown as grey solid lines (the thick one and the thin one, respectively). The observed total intensity source counts from SPT (diamonds; Mocanu et al. 2013) and from *Planck* (squares; Planck Collaboration et al. 2013) are also plotted. The differential number counts in polarized flux density computed via eq. (3.5.2) are shown by triangles. 126
- 4.9 AT20GJ040848-750720 images. (*Upper-left panel*) ATCA image at 18 GHz (total intensity in rainbow and polarization in red contours); (*upper-right panel*) ALMA image at 97.5 GHz in total intensity (rainbow) with total intensity contours from the ATCA image at 38 GHz. ALMA polarization (rainbow) and total intensity (white contours) with superimposed magnetic field directions (in red) for the eastern lobe (*lower-left panel*) and the western lobe (*lower-right panel*), respectively. 128
- 4.10 Linear polarization emission (colours) and position angles (vectors) in ALMA Band 3 and 7 of PKS0521-365. 128
- 4.11 Mosaic pointing scheme for the ATCA observations at 33 – 35 GHz overlaid to the 18 GHz map of Pictor A obtained in total intensity by Burke-Spolaor et al. (2009). 131
- 4.12 33 GHz total intensity map of PictorA (preliminary results) 131
- 4.13 Forecasts of foreground contamination with PS4C. In all panels, the black dot-dashed lines show the primordial ($r = 0.05$) and lensed CMB B-mode power spectra and the black solid line is the the total CMB B-mode power spectrum. The dotted (dashed) lines are the power spectrum of the polarized Galactic emission (ERS emission) at the different frequencies available for each experiment, the color scale is such that the colors go from purple to yellow as the frequency increases. The power spectra depend are estimated using eq.(4.4.6) in the region outside the UPB77 *Planck* mask (in order to exclude the Galactic plane and ERS above the 3σ detection limit). The different panels corresponds to predictions for different experiments. From top to bottom and from left to right: QUJOTE (11, 13, 17, 19 GHz), CMB-S2 (95 and 150 GHz), CMB-S3 observing with small and large aperture telescopes (30, 40, 95, 150 GHz), LiteBIRD (frequencies between 40 – 166 GHz) and CORE150 (60, 100, 145 GHz). 141

-
- 4.14 Power spectra in polarization of undetected ERS in current and future CMB experiments. Left panel: CMB-S2 (triangles) and CMB-S3 (circles for the small aperture telescope and diamonds for the large aperture telescope). Right panel: LiteBIRD (circles) and CORE150 (squares). The dotted lines are the B-mode power spectra at the acoustic scale ($\ell = 80$) and at the lensing B-modes peak scale ($\ell \approx 1000$). 142
- 4.15 Polarization E/B-mode power spectra of radio sources with the CMB E-mode and B-mode for five values of the tensor to scalar ratio r (0.1, 0.01, 0.003, 0.001, 0.0003); see text for details. Since unresolved point sources contribute, on average, equally to E- and B-mode, their total power spectra have been divided by a factor of 2. 143

List of Tables

1.1	Summary of some of the surveys in polarization available at radio frequencies (update to Table 3 in Tucci <i>et al.</i> 2004).	14
2.1	ATCA observations summary for the three campaigns: September 2014, March-April 2016 and July 2016	26
2.2	ATCA observations calibrators table for the three campaigns: September 2014, March-April 2016 and July 2016	26
2.3	Schematic informations about the ALMA campaign at 3 mm.	46
2.4	List of the calibrators visited during our ALMA observations.	46
3.1	Distribution of sources per spectral type in total intensity and in polarization. The row “NA” refers to the three objects classified in total intensity but missing a spectral fit in polarization. The last row reports the total for a given spectral class in total intensity, while the last column does the same in polarization.	55
3.2	First, second (median), and third quartiles of spectral indices in total intensity and in polarization for different frequency ranges. We give values for the full sample and for the two main spectral classes, as classified in total intensity.	63
3.3	First, second (median) and third quartiles of the polarization fraction at each observed frequency given by the Kaplan-Meier estimator, taking into account the upper limits, for the full sample and for the steep- and peaked-spectrum sources. The last row reports probabilities for the null hypothesis (i.e. the two samples are drawn from the same parent distribution) given by the Kolmogorov-Smirnov test performed on the steep and peaked groups, considering together 5.5 and 9 GHz, the 18 – 38 GHz frequency interval and all the frequencies, respectively.	74
3.4	Median plus I and III quartile values of cm-wavelengths (<i>upper table</i>) and mm-wavelengths (<i>lower table</i>) RMs. In each table the upper set of values refers to the observed RMs while the lower set refers to the RMs at the source for the subset of sources for which redshift measurements are available. The numbers of sources in each group are in parenthesis. Whenever the number of objects is < 10 we provide only the median value. RMs are in rad/m ²	81

3.5	Mean variability indices in total intensity and in polarization (last row). Note that for 18 – 24 GHz we have only ~ 10 observations, hence provided numbers are less significative, especially for the distinction in sub-class and/or in polarization where non-detections might reduce the number of data to few unities.	85
3.6	Distribution of sources per spectral type in total intensity in 2014 and 2016 campaigns. The last row reports the total for a given spectral class for 2014 observations, while the last column does the same for the 2016 campaign.	85
3.7	Distribution of the polarization fractions at 18 GHz for the whole sample of 104 objects.	93
3.8	Euclidean normalized differential source counts at 20 GHz in polarization, obtained in this present work via the convolution of the distribution of the polarization fraction at 18 GHz with the De Zotti et al. (2005) model.	94
3.9	Parameters of the evolutionary model for RL AGNs (Bonato et al. 2017). The luminosity L_* is in W Hz^{-1}	97
4.1	Observed distribution of the percentage polarization fractions at 97.5 GHz for the full sample.	121
4.2	List of the 8 objects with an observed RM in ALMA Band 3 (90 – 105 GHz) non-compatible with 0 at a 1σ level. We also report for each source the corresponding RMs found at lower frequencies (if any), the inferred number of synchrotron components and the redshift, whether available (provided by Galluzzi et al. 2018). All the values are in rad m^{-2}	123
4.3	Median values of the RMs between 90 and 105 GHz. The upper part of the table refers to the observed RMs for the 19 sources with successful fits. The lower part gives the RMs at the source for the subset of sources for which redshift measurements are available. In parenthesis are the numbers of sources in each group. RMs are in rad m^{-2}	125
4.4	Euclidean normalized differential source counts at 100 GHz in polarized flux density given by eq. (3.5.2).	127
4.5	Nominal specifics of CMB experiments described in sec.4.4.	133
4.6	Number of polarized ERS detected above the $P_{3\sigma}$ flux density detection limit in polarization, by current and forthcoming CMB ground based experiments. Counts are estimated both from the (model De Zotti et al. 2005, thereafter D05) and the C2Ex predictions (in brackets).	134
4.7	Number of sources detected above the $\geq S_{\text{lim}}$ and $\geq P_{\text{lim}}$ flux densities limit by the QUIJOTE experiment, assuming the nominal and conservative values for sensitivity. Values are estimated using D05 and C2Ex models (ins brackets).	134
4.8	Number of sources observed above $3\sigma_{\text{det}}$ limit in terms of polarized flux density $P_{3\sigma}$ by the LiteBIRD experiment. Bracketed values are estimated using the C2Ex model.	135

4.9	Comparison of surface densities of polarized ERSs brighter than $P_{4\sigma}$ estimated by De Zotti et al. (2016, DZ16) and by PS4C. Values in brackets refer to C2Ex estimates.	139
-----	--	-----

Chapter 1

Active galaxies

1.1 Active Galactic Nuclei

The concept of Active Galactic Nucleus was at first theoretically proposed by the Russian-Armenian physics Viktor A. Ambarcumjan in 1950. The first quasars (3C 273 and 3C 48) were discovered in the late 1950s, as radio sources in all-sky radio surveys with no corresponding visible object. The radio images appeared point-like (upper limits of the angular dimension were obtained by using small telescopes and the Lovell Telescope in the interferometric mode). During 1960 hundreds of these objects were recorded and published in the Third Cambridge Catalogue (3C) and astronomers systematically scanned the skies for searching their optical counterparts. The first optical association was published in 1963 by Allan Sandage and Thomas A. Matthews for 3C48.

It has been estimated that there are $2 \cdot 10^{12}$ galaxies in the Universe and the rule seems to be the presence of 1 SMBH in each central region. However, in only $\sim 1\%$ of them the black hole is in activity, i.e. the galaxy hosts an AGN. Whenever this happens, galaxy luminosity exceeds by a factor $\sim 10^3$ (reaching $L \sim 10^{40} - 10^{41}$ W) typical values found for normal galaxies, i.e. those galaxies for which the bolometric luminosity can be justified just in terms of stars, gas and dust. Then, we can start describing a prototypical AGN from what is believed to be the central engine of such huge amount of energy, the central SMBH, with mass $\sim 10^6 - 10^{10} M_{\odot}$. According to GR a black holes has “no hair”, i.e. their most general physical state is fully described by only 3 parameters: the mass M , the spin J and the charge Q . Since charge (if there was any at the black hole formation) is expected to be neutralized shortly after the formation only two observables are needed and the Kerr metric solution is determined. The Schwarzschild solution is valid for a static electrically-neutral black hole:

$$ds^2 = \left(1 - \frac{R_S}{r}\right) dr^2 + r^2 (d\theta^2 + \sin^2 \theta d\phi^2) - \left(1 - \frac{R_S}{r}\right) c^2 dt^2, \quad (1.1.1)$$

where the Schwarzschild radius $R_S = 2GM_{BH}/c^2$ refers to the maximal distance from the black hole where the escape velocity becomes $\geq c$, hence no

matter or radiation can escape from the region enclosed. Note that black holes are expected to be the result of gravitational collapse of a collection of stars or gas, hence would have non zero angular momentum. Taking into account the Kerr metric the singularity is no more a point but it becomes a ring, and there appears two physical relevant surfaces on which the metric is singular. The inner surface corresponds to an event horizon (it occurs where the purely radial component g_{rr} of the metric goes to infinity). It, basically, gets closer with respect to the R_S :

$$R_{EH} = R_S - \sqrt{R_S^2 - 4\left(\frac{J}{Mc}\right)^2}, \quad (1.1.2)$$

where J and M are the spin and mass of the black hole, respectively. Another singularity occurs where the purely temporal component g_{tt} of the metric changes sign from positive to negative. The relevant surface (called “ergosurface”) is identified by

$$R_{ES} = R_S + \sqrt{R_S^2 - 4\left(\frac{J}{Mc} \cos^2 \theta\right)^2}, \quad (1.1.3)$$

which represents a sphere flattened at poles (where it touches the event horizon) by the term $\cos \theta$. The space between these two surfaces is called “ergosphere”. Within this volume, particles are forced to co-rotate with the central mass, acquiring momentum. Since they are still outside the event horizon, they can escape the black hole generating jets. In this way it is possible to extract spin energy (and mass) from a rotating black hole as proposed by Roger Penrose in 1969. Note that the mechanisms of accretion onto a black hole and jet launching (supported by observational evidences) are not known but the fact that an energy transfer can be relatively easily addressed in the rotating black hole scenario, represents an insight that supports the latter hypothesis.

Building up the model of AGN from the central engine (see the Fig. 1.1, the closest element is the accretion region, i.e. the region in which the gravitational influence of the SMBH causes the infall of the gas and other eventual matter in the centre. According to leading models there should be an optically thick accretion disk (King 2008) extending from the Innermost Stable Circular Orbit (ISCO), i.e. the innermost stable Keplerian orbit which, in the case of a rotating BH is closer with respect to a non-rotating one: in the maximally rotating case $r_{ISCO} = 1.23R_S$, while in the Schwarzschild case $r_{ISCO} = 6R_S$. It is believed that matter loses angular momentum due to viscosity and turbulent motion getting accreted against the radiative pressure. Then, the correspondent emission is thermal and temperature profile scales radially as $T \propto r^{-3/4}$. This continuum emission is typically observed in AGN spectral energy distributions (SEDs) as a big blue bump, being in the far UV spectrum (or even in the soft X-ray band) and current observations tend again to favour a rotating SMBH scenario. Assessing typical distance scale ranges, we can say that the SMBH event horizon may be located between 0.01 – 10 AU and the accretion disk is comprised in 0.01 – 60 AU. Current research about the accretion disk

involves its shape (thin or thick), angular momentum loss mechanisms and transport, since the total angular momentum is conserved (the disk exists, at least for a given amount of time) and the losses of the innermost gas are compensated by the gain in the more external layers. A model set for accounting this aspect is the Advection-Dominated Accretion Flow (ADAF) in which the cooling time for radiating the heat stored by accretion flow results less than the advection time, so the matter and transport of the momentum naturally arises. The conditions in which this model is formulated are alpha disk at a sub-Eddington accretion rate and a very low gas opacity. Typical accretion rate expected are $\sim 10\%$ of the Eddington rate and this model can account for, e.g., a jet emission. It can be shown that whenever the accretion rate exceeds the Eddington value or the cooling becomes highly inefficient (if the viscosity gets too high) the flow is no more vertically confined and a transition to a geometrically thick disk (a toroid) may occur. This regime is particularly interesting since, again, it can account for a jet emission but the creation of an optically thin hot corona and winds around the disk can be generated as well. In fact, a hot corona in which electrons have a kinetic temperature of $\sim 10^7$ K provides the Comptonizing medium which up-scatters UV photons from the disk and explains power-law soft X-ray emissions found in some AGNs. In thin disk scenario these outflowing features are more difficult to be explained. Accretion disk provides not only continuum emission, but the inner part of this region whose microphysics is directly influenced by intrinsic properties of the SMBH is also room for line emissions, such as the fluorescent Fe K_α line at 6.4 K with median broadening of $\sim 0.3c$ indicating relativistic velocities. The shape of this line is the result of several effects: the dynamical Doppler shift produces two peaks because of the rotation and the relativistic beaming enhances (suppress) the component pointing toward (against) the line of sight; the gravitational redshift introduces also some extra-broadening and contributes at the same time with cosmological redshift to lower the central frequency. It is to say that it is observed directly (power-law component, PLC) or can be received after reflection (reflection-dominated component, RDC) from the electron corona.

Since there is a huge amount of radiation in UV and X bands coming from the central AGN regions, eventual chemical species present in structures around the innermost core can be photoionized. Above the disk, going at $\sim 0.01 - 0.1$ pc from the core, there is a region called “Broad Line Region” (BLR) in which there are moving and turbulent gas clouds with electron densities as high as $10^8 - 10^{11} \text{ cm}^{-3}$. These structures are assumed to be in photoionization equilibrium, i.e. photoionization is balanced by recombination. This means that, observing two or more lines of different ionized species it is possible to estimate the relative number densities and gas temperatures of each of them. Kinetic temperatures about 10^4 K are typical for these clouds and can justify a broadening of lines of the order of 10 km/s, while the observed linewidth are about $\sim 500 - 10^4$ km/s, as a consequence of being well within the gravitational potential well of the SMBH. The bulk motion is expected to be supersonic, but the kinematics is not known: Keplerian orbits, radiatively-driven outflows, infall and various combinations are possible

(Gaskell et al. 2008). A powerful but “expensive” (in terms of observing program) technique is the reverberation mapping, which is useful to probe the BLR scales and infer the black hole mass. If one assumes the UV continuum coming from the accretion disk and observing its variability, a “reverberated” variability in the line emission of the photoionized medium of the BLR is expected to be seen with a delay $\tau = R_{\text{BLR}}/c$. Then, it is possible to show (Peterson & Horne 2004) that

$$M_{\text{BH}} \simeq f R_{\text{BLR}} \frac{\Delta v^2}{G} = \frac{\tau c}{G} f \Delta v^2, \quad (1.1.4)$$

where f is a factor depending on the geometry of the system, Δv is the velocity dispersion and R_{BLR} is the radius of the Broad Line Region. The most prominent lines observed are the hydrogen Balmer series $H\alpha$, $H\beta$ and $H\gamma$ and the hydrogen $Ly\alpha$, but lines of the MgII, CIII and CIV are also common. Beyond the BLR there is an optically thick dusty torus which surrounds the accretion disk and confine the BLR at distances between 1 – 100 pc from the central BH. The presence and geometry of this region is inferred from the obscuration of the optical UV emission from the accretion disk and optical and UV line emissions from the BLR. IR emissions can be partially transmitted by the dust and all these signatures are interpreted in terms of different possible viewing angles with respect to the AGN axis. There seems to be a coexistence of dust at different temperatures, hence observations tend to favour a clumpy structure rather than a smooth one and there are also evidences of a scale height-radius relationship $H/R \sim 1$ in compilations of Seyfert 1 and 2 observations (Schmitt et al. 2001). This can be indicative of the mechanism of formation of such tori: hydrostatic models whereby a toroidal structure formed by molecular clouds is accreted from the host galaxy hardly explains such high ratio, thus hydrodynamical outflows from thick disks (in which winds and vertical motion can be easily supported) offer a more plausible explanation. However, given recent progresses (Simpson 2005), it is possible to better constraint the geometry of torus models considering that the distance of the inner torus wall from the core is expected to be higher if one considers higher luminosity AGNs and that this wall may have a different height with respect to the external one, also depending on the luminosity and it seems to follow a $\propto L^{0.23}$ law. The inner wall position can be related to the sublimation of the dust: the higher the AGN power is, the farther is the region from the core where dust is not sublimated and the torus is effectively present. The height of the inner wall may arise as a trade off between two effects of AGN activity: a higher luminosity tends to erode the inner wall, but at the same time induces an enhanced vertical motion from a thick disk, and the observed law may be the result of such trade-off.

AGNs spectra typically show also narrow lines with FWHM in the range 200 – 900 km/s with most values around 350 – 400 km/s, mainly of OI, OIII. In some cases there appear very highly ionized species (e.g. FeVII, FeX, FeXI and even FeXIV). It is believed these emissions come from clouds with a lower electron density ($\sim 10^4 - 10^6 \text{ cm}^{-3}$) with respect to the BLR ones which allow forbidden lines to be present (otherwise collisionally sup-

pressed). Given the marked asymmetry of lines it is possible to argue a net outflow of the clouds in a dust filled medium or a net infall of structures which are themselves dust filled. This region extends at distances of $10^2 - 10^4$ pc from the AGN core (hence it is easily optically resolved) and is called “Narrow Line Region” (NLR).

1.1.1 Radio quiet and radio loud AGNs

Another important element which can be present or not as an output of the AGN activity is the jet (see Fig. 1.1). This is constituted by a relativistic plasma and has its own magnetic structure, hence the dominant radiative process is the synchrotron emission which, given the energetics of these sources, is typically observed in the radio band but it can reach the optical or even soft-X ray frequencies in some cases. Kellermann et al. (1989) proposed a criterion to distinguish AGNs in radio loud and radio quiet ones: the threshold is provided by the ratio between the 5 GHz flux density and the optical B-band (both evaluated in the source rest frame). Objects with this ratio higher than 10 are classified as radio loud, otherwise they are considered radio quiet. According to this criterion $\sim 90\%$ of AGNs are radio quiet and only $\sim 10\%$ (hence, the 0.1% of all the galaxies) are radio loud, i.e., they have a jet. Given this identification between radio activity and this very distinctive morphological feature, it is now preferred to use terms like “jetted” or “non-jetted” AGN, instead (Padovani 2017).

The exact mechanism of jet formation, the nature of its composition and mechanical configuration are still uncertain. The standard picture involves magnetic fields threading the accretion roughly parallel to the disk axis. These magnetic fields through interacting with ionized material comprise the disk, driving the collimation of the outflow along the AGN rotation axis. Given this symmetry the jet is a bipolar outflow that can extend up to a few hundreds of kpc from the nucleus. The distance where it originates is uncertain as well, maybe the hot corona, but mechanisms which directly involve the ergosphere are also proposed. Jet can appear more or less continuous or with particular bending: typically millarcsec VLBI maps (parsec-scale resolution) reveal superluminal knots, believed to be shocks in the collimated plasma outflow (e.g. Blandford & Königl 1979). Hence, in AGN the ejection of a relativistic plasma “blob” propagating through the outflowing plasma stream could lead to a trail of shocks. Strong polarization and relative enhancement of the magnetic field in the brightest jet features seem to support this scenario (cf. Pushkarev et al. 2008). Lister & Homan (2005) also found consistence with a shock front propagating along the jet axis, although in some cases the polarization angle measurements suggest turbulent magnetic fields. Despite these indications, it is to say that the physics of generating shocks in highly relativistic plasmas is not well known. Many models (e.g. Marscher & Gear 1985; Polko et al. 2010) are based on electrons accelerated at the shock front (instead, e.g., merely local plasma density enhancement) where they radiate losing energy. They also take into account plasma expansion behind the shock, in the transverse direction along the jet: this predicts a stratification

in the energy density, with the highest energy electrons in a narrow region behind the shock front. Despite the relative success of these models in reproducing spectral features in total intensity and polarization and variability, there are several open questions related to jets. In fact, the matter composition of the jet is not exactly known: there are models with electron-positron plasma or with an ordinary electron-proton plasma; there seems to be a two-component structure in jets but the dominant non-thermal (synchrotron) emissions observed might not only come from leptons but also protons may play a significant role; synchrotron signals show an inverse Compton signature and it is not clear whether the up-scattered photons are only those emitted in synchrotron processes (synchrotron self-Compton, SSC), or if there is an appreciable contribution by external photons (e.g. those from the accretion disk, CMB ones or EBL). Indeed even thermal processes might be not negligible and contribute as well. It is not clear what powers the acceleration and collimation of a jet, i.e. if it happens directly at expenses of the rotational energy of the black hole (Blandford & Znajek 1977) or the power is released by the accretion flow (Blandford & Payne 1982); it is not well understood what is the role of magnetic field in the acceleration and collimation of relativistic jets; the topology and strength of magnetic fields, any eventual recollimation, any reacceleration of relativistic particles along the jet are not constrained as well. Since these processes are naturally polarized, it is clear that observations in the radio band particularly require a full-polarimetric approach.

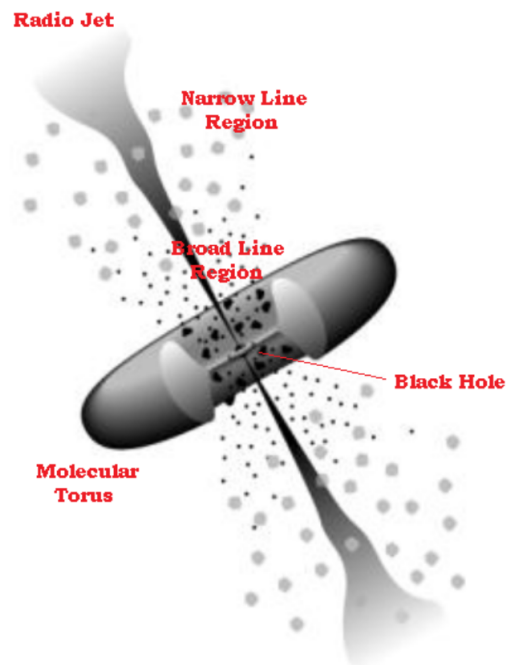


Figure 1.1: A cartoon showing the AGN prototypical structure (adapted from Urry & Padovani 1995).

Other features associated to jets are hot spots and lobes. Leahy (1993) de-

defined a “lobe” as “an extended region of emission which is not a jet, showing billowy or filamentary substructure, whose perimeter is mostly well defined in the sense that the projected magnetic field is parallel to the edge, the intrinsic polarization is $> 40\%$, and the intensity tends to zero as the perimeter is approached”. Bridle et al. (1994) defined a lobe “hot spot” as “the brightest feature in the lobe having a surface brightness greater than four times that of the surrounding emission and a FWHM less than 5% of the largest diameter of the source, while being farther from the AGN than the end of the jet if one is detected”. The presence of hot spots in extended extragalactic radio sources is correlated with an absolute luminosity $P_{1.4\text{GHz}} \sim 10^{25}$ W/Hz as pointed out by Fanaroff & Riley (1974). Thus, they distinguished high power radio galaxies (FR II) in which these limb-brightened structures are present from low power radio galaxies (FR I) where the jet terminates subsonic in the surrounding medium. This distinction seems to be physical, since it can be traced to a greater efficiency of the accretion flow in FR II with respect to FR I (Ghisellini & Celotti 2001).

1.1.2 The unified model of AGNs

In the previous section we briefly described the overall structure (and its variants) of an AGN focusing on intrinsic physical properties associated to different properties, such as the SMBH spin or the accretion flow that can be related to the total power radiated by the AGN and some peculiar structures, e.g. hotspots. It is crucial to identify physical parameters and their ranges to trace different regimes/objects that then can be jointed in an evolutionary path: lack of observational constrains, poorly understood physics (e.g. in case of ultrarelativistic shocks and turbulence), computational problems encountered in simulations make different models quite degenerate. Moreover, geometrical effects like the orientation of the object with respect to the line of sight and/or relativistic aberrations and cosmological effects (the redshift) provide a quite various range of behaviours and appearances which turn out in a bestiary of objects.

Fortunately, these latter aspects are now quite understood and well explained in the frame of the unified model of AGNs (Urry & Padovani 1995): first of all (see Fig. 1.2), there is the distinction between radio loud and radio quiet AGNs, i.e. the presence or not of a jet. Then, another ingredient is the angle formed between the line of sight and the AGN axis: in case of radio quiet objects we can distinguish between Seyfert 1 or 2 objects depending on a low or wide angle formed, respectively. In fact, the presence of a torus with its opacity (absorption) and reprocessing properties (Compton scattering mostly in the IR band) differentiate objects where the line of sight intersects the torus (Seyfert 2) or not (Seyfert 1). In case of radio loud objects the situation is more complex: as mentioned, the power of the jet is an additional parameter and small values ($< 20^\circ$) of the angle between the line of sight and the AGN axis can also induce relativistic effects to be taken into account. As shown in the cartoon, the power criterion applied to jetted AGN divides them into two groups: one formed by FR I and BL Lac (low power) and the other

formed by FR II and FSRQ (high power). Then, at high angles the torus effect that can be responsible for the absorption of the BLR lines (causing only the NLR lines to be seen) produces a further split in the FRI and FR II radio galaxies increasing the angle: BLRG and NLRG for FRI, BLRG QSO (type I) and NLRG QSO (type II) for FR II. At small angles relativistic effects play a major role, the so-called ‘‘Doppler-boosting’’ effect heavily enhances the relativistic jet components pointing toward the observer and suppresses those pointing in the opposite direction. The Doppler boosting factor $\delta = 1/(\gamma(1 \mp \beta \cos \theta))$ (– for the jet and + for counter-jet, θ is the viewing angle of the AGN axis) alters the emitted flux density S^{em} at the frequency of observation ν_{obs} , according to this expression for the observed value $S_{\nu_{\text{obs}}}^{\text{obs}}$:

$$S_{\nu_{\text{obs}}}^{\text{obs}} \stackrel{\text{def}}{=} \frac{h\nu_{\text{obs}} dN_{\text{ph}}}{d\nu_{\text{obs}} dt_{\text{obs}} D^2 d\Omega_{\text{obs}}} = S_{\nu_{\text{obs}}}^{\text{em}} \delta^{3-\alpha}, \quad (1.1.5)$$

where dN_{ph} is the number of photon at the observed frequency, $D^2 d\Omega_{\text{obs}}$ is the element of surface perpendicular to the flux (we can say $d\Sigma$, where D is the distance of the observer from the source) of the detector and α is the spectral index, assuming a power law behaviour in the frequency range $[\nu_{\text{em}}, \nu_{\text{obs}}]$, h is the Planck constant ($h = 6.62607004 \times 10^{-34} \text{ m}^2\text{kg/s}$) and dt_{obs} is the observer’s frame time interval. The global factor $\delta^{3-\alpha}$ is the result of the frequency transformation (the relativistic Doppler shift introduces a δ both at the numerator and the denominator), the time dilation with respect to the proper observer (reduces by a δ) and the relativistic beaming effect (the solid angle $d\Omega_{\text{obs}}$ is reduced by a factor δ^2). At the end, the K–correction introduces a factor $\delta^{-\alpha}$. The ratio R between the observed flux densities of jet (j) and the counter-jet (c-j) at the observed frequency is, then:

$$R \stackrel{\text{def}}{=} \frac{S_j}{S_{c-j}} = \left(\frac{1 + \beta \cos \theta}{1 - \beta \cos \theta} \right)^{(3+\alpha)}, \quad (1.1.6)$$

i.e., for an axis along the line of sight $\theta = 0$ and a $\beta = 0.8$, assuming a $\alpha = -0.7$ (canonical value for optically thin synchrotron emissions), the ratio is $\simeq 157$. Then, it can be easily understood that the counter-jet can be non-detected, while the jet is heavily enhanced.

1.1.3 Historical legacy: steep/flat dichotomy

AGNs are among the most powerful objects in the Universe and, especially the beamed ones, can be easily observed despite the high redshifts. Indeed the first objects that made the jump toward redshifts > 0.5 were quasars, i.e. 3C147 ($z = 0.545$ discovered in 1964-1965) and 3C9 ($z = 2.018$ discovered in 1965). Thus, the novel-borne radio astronomy in the ‘60s knew a steep increase in the number of objects observed, e.g. important catalogue are those compiled by the Cambridge and Bologna groups. Early radio surveys were exploited to probe the geometry of the Universe and remained the main cosmological tool until observations of the Cosmic Microwave Background (CMB) started to produce high precision data in ‘90s with the COBE (COsmic

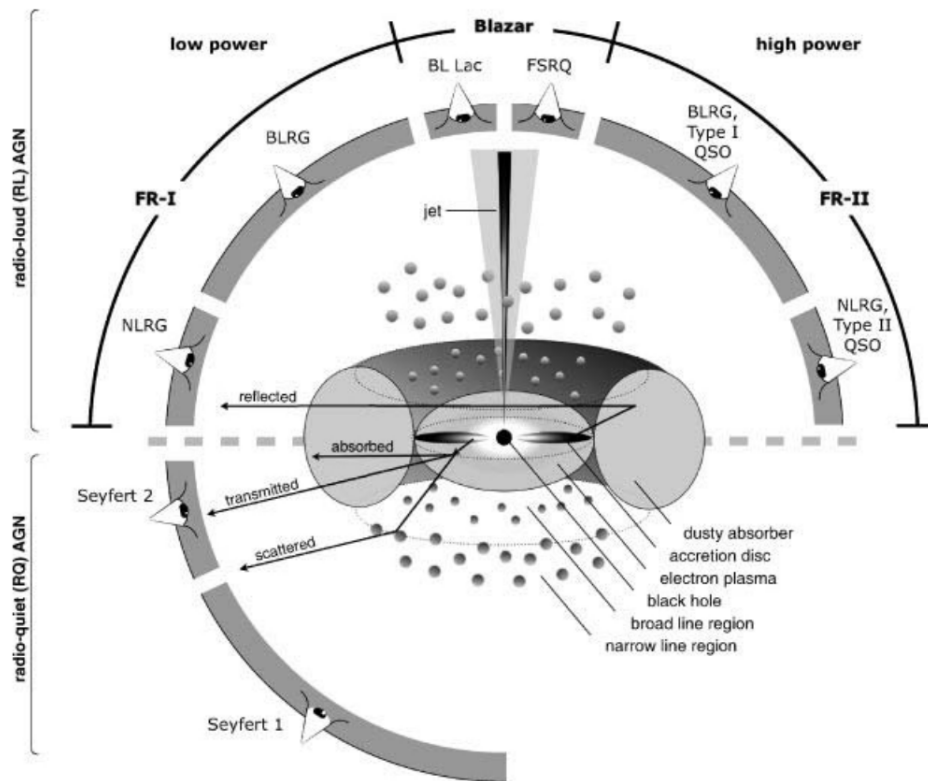


Figure 1.2: A cartoon of the AGN unified model from Beckmann & Shrader (2012). The different AGN types depending on the angle under which the objects are seen are shown for both radio-loud and radio-quiet objects in the top and in the bottom part of the image, respectively.

Background Explorer satellite). Again on the cosmological side, populations of radio sources showed that objects in the Universe evolve either individually or as a population. This concept was not fully accepted until studies about galaxy size and star formation rates found evolution with epoch as well. It is well known that on a limited range, e.g. between meter and cm wavelengths (such as 178 MHz and 5 GHz) where first surveys were available, the spectrum of a radio source emitting synchrotron can be approximated via a single power law model, i.e. $S(\nu) \propto \nu^\alpha$: value of $\alpha \approx -0.7$ is considered canonical for an optically thin synchrotron from a single component in a radio source.

Going down to the mJy level in total intensity there soon appeared a major dichotomy between objects with a flat-spectrum $\alpha \geq -0.5$ and object which can be considered steep-spectrum $\alpha < -0.5$. It is to say that the label for the first category is misleading since not only literally flat objects are included (we can define a proper range between -0.5 and 0.5 in α) but there are also inverted (flux density increases with the frequency) and peaked spectrum objects inside. However, a stronger common feature with respect to the merely condition about the spectral index is the compactness: when observed down to arcsec resolution the flat-spectrum objects are compact or even point-like, while steep-spectrum objects are generally extended.

Genuine flat objects can be interpreted as a superposition of Doppler-

boosted self-absorbed synchrotron components: indeed their compactness is merely due to their close orientation with the line of sight as discussed for the relativistic beaming effect in the previous section and the several argued shocks maybe the signature they can be identified with FSRQ, i.e. the aligned FRII. Other objects classified as flat in an extended meaning are high luminosity ones such as Giga-Hertz Peaked Sources (GPS) and High Frequency Peakers (HFP), which peak at frequency that can be as high as tens of GHz (at the beginning they were classified as inverted, due to limited frequency coverage). As pointed out by Snellen (2008) these are probably mono-component young radio galaxies appearing compact since the magnetoionic material has not had time to travel at distance > 100 pc. There are also populations of high frequency spectral peakers with low luminosity, below a few percent of the Eddington limit: in this case the high frequency of the self-absorption peak may be indicative of a radiatively inefficient accretion (driven by ADAF or by an adiabatic inflow-outflow scenario, ADIOS), argued to be a late phase of AGN evolution. The class of Compact Steep Spectrum objects (CSS, Kapahi 1981; Peacock & Wall 1982; O’Dea 1998) seems an exception of steep sources since they are unresolved or barely resolved at typical interferometric arcsec resolutions. Indeed, their behaviour can be easily interpreted as high power young radio galaxies whose self-absorption peak is below 0.5 GHz. Their median spectral index $\simeq -0.75$ confirms this first guess. Hence, they are more affine to GPS, HFP and another category, formed by Compact Symmetric Objects (CSO), young radio galaxies seen edge on.

Steep spectrum objects are non-Doppler boosted sources whose radio emission is dominated by lobes, optically thin formations which are usually extended up to the Mpc scale, hence can be likely FRI radio galaxies. There are also two classes of ultra-steep ($\alpha < -1.3$) radio sources discovered: one is associated to galaxy clusters, i.e. low power diffuse structures such as radio halos, radio relics and mini-halos, the other is formed by very luminous objects which turn out to be at high redshift.

From this discussion about the basic dichotomy in flat and steep objects, it results that this is a practical way of taking into account radio populations in a simple way, e.g. in providing source counts at a given frequency from observations. However, this approach now results obsolete because the maximum frequency coverage on which it is based now appears quite limited: modern and renewed facilities (such as ATCA, JVLA and ALMA) can observe with sub-mJy sensitivities to much higher frequencies, up to ~ 1 THz and radio sources usually show spectral features of higher complexity. An evolved source has both an extended component (a lobe) that can emerge at low frequencies and one/two compact self-absorbed components or even more (occasionally Doppler-boosted), resulting in an almost flat spectrum up to several tenths of GHz that steepens thereafter due to the aging of emitting particles. Another reason to move to another classification is related to the first limitation we stressed, i.e. the classification is unphysical: e.g. compact steep objects are more similar to objects classified as flatter and the position of the peak (another sub-criterion typically adopted) can be just matter of the redshift at which the object is located (apart from a genuine expansion of

synchrotron components shifting the self-absorption peak towards lower frequencies). Nowadays, starting from the AGN unification scheme which takes into account projection effects and exploiting the multi-frequency (on a wide band) and multi-epochs full Stokes radio observations, it is possible to refine this classification, trying to identify criteria for a more physical approach leading to more homogeneity among objects in the same category. This is an essential ingredient to constrain properties of a given class of objects such as the polarization or the cosmological evolution. In chapter 3 we propose to use synchrotron components inferred by comparing spectra in total intensity with those in polarization to perform these tasks.

1.2 Polarimetric properties & observations

The characterization of the total intensity emission for large samples of radio source population is only a recent achievement, and still open to discussion. Wide-area surveys are necessary to achieve statistics on the bright less numerous samples, while high sensitivity is needed to explore the faintest samples. Only the former were available in the catalogs extracted from full-sky maps from satellite missions like WMAP (with a completeness limit of ≈ 1 Jy at 23 GHz Argüeso et al. 2003; De Zotti et al. 2005; Wright et al. 2009; Gold et al. 2011) and Planck (with a completeness limit of ≈ 500 mJy at 30 GHz, see Planck Collaboration 2015)). New broad-band correlators made high sensitivity available for interferometric observations up to the mm and sub-mm regimes, allowing wide-area deep surveys to be carried out also from the ground at frequencies above ~ 10 GHz. Thus, the Australia Telescope 20 GHz (AT20G) Survey (Murphy et al. 2010; Massardi et al. 2011) covered the full Southern sky with 91% completeness above 100 mJy and 79% completeness above 50 mJy in regions south of declination -15° .

By combining the ground- and satellite-based instrumental capabilities, several authors (Massardi et al. 2008; Sajina et al. 2011; Chen et al. 2013; Massardi et al. 2016) recently provided a broad-band view of the total intensity emission of the bright radio source population: it seems to be dominated by relatively young compact objects. A double power-law model is adequate to describe spectral behaviors for more than 2 decades in frequency: this indicates that a single dominant component is responsible for the (typically optically thin) emission above ~ 30 GHz. Emission is typically variable: objects brighter than 500 mJy (at 20 GHz) on average vary their flux density more than 6% over a 6 months lag, and the rate grows with frequency.

The study of the polarized emission both in frequency and space would help describing the dynamics of the jets. Synchrotron emission of each component is intrinsically highly linearly polarized (up to 70 – 80%, Ginzburg & Syrovatskii 1969) but typically observed integrated polarized fractions for compact extragalactic radio sources are rarely as high as $\sim 10\%$. They are, in fact, the result of vector averaging along the line of sight (depolarization is mostly induced by differential Faraday rotation, cf. Burn 1966), within the observing resolution element (in this case unresolved magnetic sub-structures

cause depolarization), and within the band of the polarized components emission. Hence, polarimetric observations typically still constitute an observational challenge because of the requested high sensitivity, calibration accuracy, and the detailed knowledge of instrumental properties and systematics. Table 1.1 lists some of the available multi-frequency compilations, surveys and complete samples follow-up that include polarimetric information: it does not claim to be an exhaustive picture and aims to trace the basic references in the following discussion.

For the above mentioned reasons, current knowledge of polarimetric properties of radio sources mostly rely on < 10 GHz selected samples including the NVSS survey (Condon et al. 1998) that covered the full sky above -45° , remaining complete down to 2.5 mJy in total intensity and with $\sigma_P \sim 0.2$ mJy in polarized emission.

The polarization of WMAP sources has been investigated by López-Caniego et al. (2009) by using WMAP data: 14 extragalactic objects were significantly detected in polarization. Slightly larger samples were detected in the Planck maps and recorded in the “Planck Catalogue of Compact Sources” (PCCS, 2nd version, Planck Collaboration 2015), listing 122 detections down to a minimum polarized flux density of 117 mJy at 30 GHz but complete only to 0.6 Jy. Ground-based follow-up observations of a complete sample of 203 WMAP sources were carried out with the VLA by Jackson et al. (2010) and Battye et al. (2011): polarized emission was detected for 123, 169 and 167 objects at 8.4, 22 and 43 GHz, respectively.

The Plateau de Bure Interferometer (PdBI) observations by Trippe et al. (2010) of a $S_{90\text{GHz}} > 200$ mJy complete sample of 86 sources found an average fractional polarization level of $\simeq 2 - 7\%$, higher for BLLac ($\simeq 7\%$) than for QSO ($\simeq 5\%$) or Seyfert galaxies ($\simeq 3\%$). The size scales relevant for the polarization emission measurements are found to be comparable to those of interest for total intensity flux density measurements.

The full AT20G catalog (Murphy et al. 2010; Massardi et al. 2011) includes the 20 GHz polarized intensity for 768 sources, 467 of which also have simultaneous polarization detections at 5 and/or 8 GHz, out of a total of 5890 sources. The detection limit is defined as $\max(3\sigma, 0.01S_{20\text{GHz}}, 6\text{ mJy})$. Sadler et al. (2006) presented polarization measurements for a sample of 173 AT20G sources brighter than $S_{20\text{GHz}} = 100$ mJy: 129 ($\simeq 75\%$) were detected at 20 GHz, with a median fractional polarization of 2.3%. Massardi et al. (2008) discussed the polarization properties of the AT20G bright sample ($S_{20\text{GHz}} \geq 500$ mJy), finding 213 polarization detections ($\geq 3\sigma$) at 20 GHz out of a total of 320 sources ($\simeq 67\%$), with a median fractional polarization of 2.5% at 20 GHz (confirmed also by Jackson et al. 2010; Battye et al. 2011). The spectral indices in total intensity and in polarization were found to be similar on average, but there were several objects for which the spectral shape of the polarized emission is substantially different from the spectral shape in total intensity. Several studies of radio source polarization, mostly for samples selected at 1.4 GHz and dominated by steep-spectrum objects, have reported indications that the polarization degree increases with decreasing flux density (Mesa et al. 2002; Tucci et al. 2004a; Taylor et al. 2007; Grant

et al. 2010; Subrahmanyam et al. 2010). Massardi et al. (2013) analyzed high-sensitivity polarization observations (in the 4.8 – 20 GHz frequency range) of a complete AT20G bright ($S_{20\text{GHz}} > 500$ mJy) source sub-sample and found no statistically significant relationship between the polarization fraction and the total intensity flux density, and no clear indication of trends of fractional polarization with frequency, up to 20 GHz. Sajina et al. (2011) obtained polarization measurements with the VLA at 4.86, 8.46, 22.46, and 43.34 GHz of 159 out of the ~ 200 AT20G radio galaxies with $S_{20\text{GHz}} \geq 40$ mJy in an equatorial field of the Atacama Cosmology Telescope survey: polarized flux was detected at $> 95\%$ confidence level for 141, 146, 89, and 59 sources, from low to high frequencies. The measured polarization fractions are typically $< 5\%$, although in some cases they are measured to be up to $\simeq 20\%$. They found indications of increasing polarization fraction with frequency (confirmed also by Agudo et al. (2010) in the 15 – 90 GHz range and by Agudo et al. (2014) in the 86 – 229 GHz range). This trend is stronger for steeper spectrum sources as well as for the lower flux density sources.

Table 1.1: Summary of some of the surveys in polarization available at radio frequencies (update to Table 3 in Tucci *et al.* 2004).

References	Frequency (GHz)	# sources	Notes
Eichendorf & Reinhardt (1979)	[0.4, 15]	510	compilation of multi-frequency data
Tabara & Inoue (1980)	[0.4, 10.7]	1510	compilation of multi-frequency data
Simard-Normandin <i>et al.</i> (1981)	[1.6, 10.5]	555	compilation of multi-frequency data
Perley (1982)	1.5, 4.9	404	compilation of multi-frequency data
Rudnick <i>et al.</i> (1985)	[1.4, 90]	20	compilation of multi-frequency data
Aller <i>et al.</i> (1992)	4.8, 8.0, 14.5	62	90% complete sample with $S_{5\text{GHz}} > 1.3\text{Jy}$
Okudaira <i>et al.</i> (1993)	10	99	flat-spectrum sources with $S_{5\text{GHz}} > 0.8\text{Jy}$
Nartallo <i>et al.</i> (1998)	273	26	compilation of flat-spectrum radio sources
Condon <i>et al.</i> (1998) - NVSS	1.4	$\sim 2 \times 10^6$	100% complete survey down to $S_{1.4\text{GHz}} > 2.5\text{mJy}$
Aller <i>et al.</i> (1999)	4.8, 8.0, 14.5	41	BLLac sources
Fanti <i>et al.</i> (2001)	4.9, 8.5	87	CSS sample with $S_{0.4\text{GHz}} > 0.8\text{Jy}$
Lister <i>et al.</i> (2001)	43	32	90% complete sample with $S_{5\text{GHz}} > 1.3\text{Jy}$
Klein <i>et al.</i> (2003)	1.4, 2.7, 4.8, 10.5	192	compilation of detections of the B3-VLA survey
Ricci <i>et al.</i> (2006)	18.5	250	complete sample with $S_{5\text{GHz}} > 1\text{Jy}$
Jackson <i>et al.</i> (2007)	8.4	~ 16000	JVAS-CLASS surveys
Massardi <i>et al.</i> (2008) AT20G-BSS	4.8, 8.6, 20	320	AT20G bright sample
López-Camiego <i>et al.</i> (2009)	23, 33, 41	22	polarization detections in WMAP maps
Jackson <i>et al.</i> (2010)	8.4, 22, 43	203	WMAP sources follow-up
Murphy <i>et al.</i> (2010) AT20G	4.8, 8.6, 20	5890	93% complete survey with $S_{20\text{GHz}} > 40\text{mJy}$
Trippé <i>et al.</i> (2010)	[80, 267]	86	complete sample with $S_{90\text{GHz}} > 0.2\text{Jy}$
Battye <i>et al.</i> (2011)	8.4, 22, 43	230	WMAP sources follow-up
Sajina <i>et al.</i> (2011)	4.8, 8.4, 22, 43	159	AT20G sources follow-up
Massardi <i>et al.</i> (2013)	4.8, 8.6, 18	193	complete sample with $S_{20\text{GHz}} > 500\text{mJy}$
Agudo <i>et al.</i> (2014)	86, 229	211	complete sample of flat-spectrum sources with $S_{86\text{GHz}} > 1\text{Jy}$
Farnes <i>et al.</i> (2014)	[0.4, 100]	951	Compilation of multi-frequency data
Planck Collaboration (2015)	30, 44, 70	122, 30, 34	polarization detections in Planck LFI maps (PCCS2)
	100, 143, 217, 353	20, 25, 11, 1	polarization detections in Planck HFI maps (PCCS2)
Agudo <i>et al.</i> (2017)	86, 229	36	brightest AGNs in the northern sky

The remarks about the high requirements of a polarimetric campaign and the resulting state-of-the-art in polarimetric observations clearly show that the polarization properties of extragalactic radio sources at high frequencies (> 20 GHz) are still poorly constrained and some provided statistical assessment, e. g. about the polarization fraction are usually biased by several effects, such as lack of completeness, detection, spectral and variability-related issues, which are difficult to take under control. Moreover, briefly presenting distinct radio populations (see previous sections), we stressed that the picture is more complicated with respect to previously thought (see the dichotomy between flat/steep objects): an unbiased multi-frequency and multi-epoch approach to polarimetry is needed to properly characterize these objects.

We now briefly examine observational issues. The completeness is an important requirement to achieve a fair picture of a given population and/or global properties of all the AGNs (or, by extension, all the radio sky) above a given flux density threshold. Another minor problem can happen due to source variability: there is a sea of objects with flux densities below the selection limits at the epoch of selection, then any later follow-up will miss those objects which, in the meantime, entered in the selection and, on the other way, it will observe objects that have left the original selection. As an example, Massardi et al. (2013) estimates a 92% of completeness due to variability on the AT20G bright sample which indeed represents a good level to provide accurate assessment. Detection and spectral biases are related issues in a multi-frequency campaign: when the sensitivity is not tiny enough the risk is to only detect objects with a flatter spectrum and indeed many works in Tab. 1.1, especially those that have a high frequency selection of objects, are likely affected by this problem. A related example pertaining polarimetry is the characterization of the polarization fraction with the frequency: it has been argued that the ordering of magnetic fields should increase in the inner AGN regions, giving a higher polarization degree at higher frequency (Tucci et al. 2004a), while Faraday depolarization should affect more the lower frequency observations, hence an increasing trend of the polarization fraction with the frequency is expected. Since the synchrotron spectrum steepens at higher frequencies (at ≥ 30 GHz is quite strong), the number of non-detections tends to be higher at these frequencies: the net effect is a spurious trend in the polarization fraction that can mimic the predicted astrophysical signal. In Fig. 1.3 we report quartiles for the polarization fraction at different frequencies found by authors whose work is reported in Tab. 1.1: it is not clear if a trend exists and where an increasing trend seems to be present non-detections may play a major role biasing results. Another effect related to variability is that it is expected (and observationally confirmed) that going at high frequency means to go closer to the central AGN, thus the variability time scales are shorter with respect to lower frequencies. Several multi-frequency works reported in the Tab. 1.1 are indeed a compilation of non-coeval multi-frequency observations, hence, especially the spectral reconstruction may be not accurate and objects cannot be properly classified.

In the third chapter we present our polarimetric observations on a complete sample of extra-galactic radio sources selected at 20 GHz from the AT20G

survey with a flux density threshold of 200 mJy. Almost all the sources in this sample are blazars (FSRQ and BLLacs) due to the discussed Doppler favoritism: hence we will characterize this radio population minimizing all the described biases.

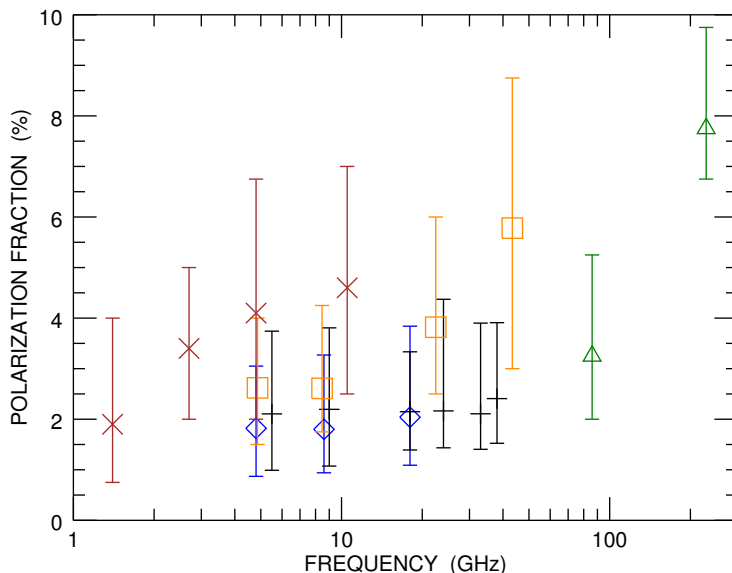


Figure 1.3: Median fractional polarizations (error bars report inter-quartile distances) at different frequencies for observations of a complete sample of 53 objects with $S_{20\text{GHz}} > 200$ mJy (black crosses) and other samples, reported in Tab. 1.1: the AT20G survey (Murphy et al. 2010, blue diamonds), (Klein et al. 2003, red crosses), (Agudo et al. 2014, green triangles), and (Sajina et al. 2011, orange squares).

1.3 Perspectives for cosmology

The angular power spectrum of the cosmic microwave background (CMB) polarized anisotropies can be decomposed into E-modes, mainly generated by scalar perturbations in the primordial universe, and B- modes that could be mainly contributed at large scales (i.e. low multi-poles) by tensor metric perturbations associated to the stochastic background of “primordial” inflationary gravitational waves, according to the relative amplitude of tensor and scalar primordial perturbations. Detecting primordial B-modes is considered the most ambitious goal of current and future CMB projects (Huffenberger et al. 2015, and references therein). As already stressed in the Introduction, extragalactic radio sources are an important, if not dominant, contaminant to the microwave sky (Tucci et al. 2004a) in total intensity and in polarization at scales smaller than 30 arcmin up to ~ 100 GHz. Most of the cosmology-dedicated satellite- or balloon-borne CMB mapping experiments have relatively shallow resolution (\sim arcmin) and sensitivity (of the order of few hun-

dreds of mJy). Only the brightest or most polarized sources could be detected in the maps. Extraction techniques are not capable to extract source contributions below the noise/confusion level. Thus, broad frequency range and multi-epoch observations of low flux density-limited samples are now needed to complement the view of radio source population properties in polarization and provide samples useful for cosmological studies.

Till now, given the lack of polarimetric studies at high frequencies, predictions about foreground contamination from the AGNs have been extrapolated from lower frequencies (< 20 GHz) but this approach turned out to be inadequate to model the radio source contribution in CMB polarization maps (Huffenberger et al. 2015). Future CMB surveys will benefit of sensitive polarization measurements at the CMB observing frequency. In Fig. 1.4 we report the CMB B-mode polarization angular power spectra for different tensor-to-scalar perturbation ratios and examples of the level of suppression of radio source residual contamination to CMB polarization measurements due to a better knowledge of the source polarization degree based on available extrapolations.

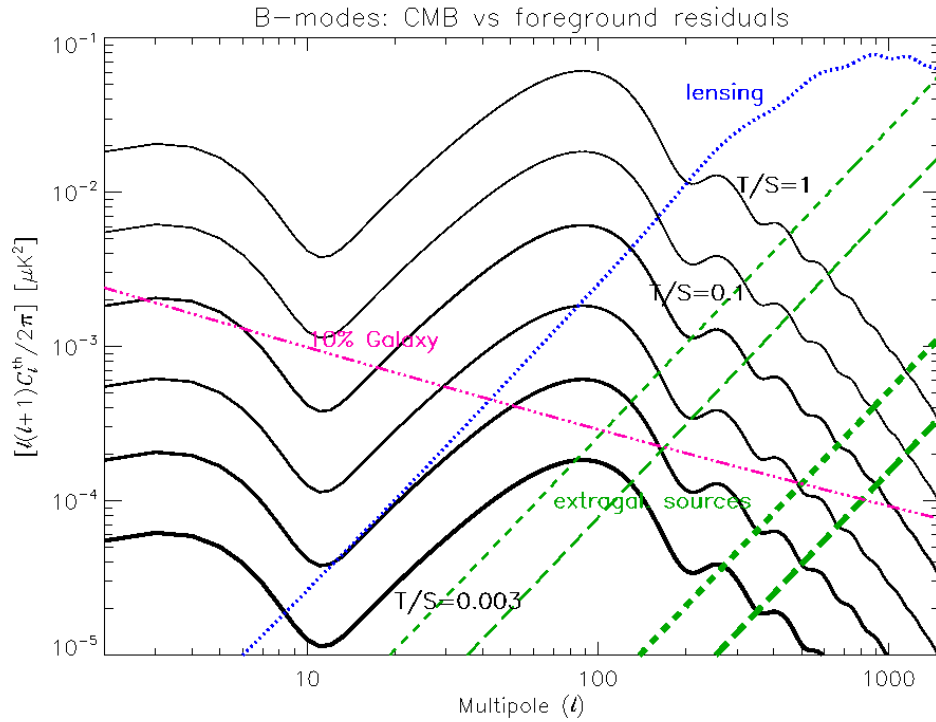


Figure 1.4: The CMB B-mode polarization angular power spectrum for different tensor-to-scalar perturbation ratios (solid black lines), lensing (blue dots), and an estimate of potential residual of Galactic foreground (red three dots dashes) compared with the B-mode signal from polarized radio sources at 100 GHz (thin green lines) assuming the detection thresholds of 200 mJy (dashes) and 60 mJy (long dashes) in total intensity (Tucci & Toffolatti 2012). Thick green lines show the uncertainty in the radio source contribution coming from a 1% error in the statistical knowledge of their polarization degree. See also the text.

1.3.1 Targets for validation of cosmological observatories

The Planck Collaboration (Planck Collaboration 2015) released the second version of the Planck Catalogue of Compact Sources (PCCS) which included also detections of polarimetric sources at the 9 satellite frequency channels between 30 and 857 GHz. In the Planck polarization maps, the polarized sources are embedded in a background which is the combination of instrumental noise and diffuse emission from polarized synchrotron or dust in our Galaxy. The polarization fraction of the compact sources is typically lower than 1 – 2%. Given the low sensitivity, once extended Galactic sources have been removed, only a bunch of extragalactic sources have been reliably detected, at least in the lowest frequency channels.

Few ground based experiments (Procopio et al. 2011; Planck Collaboration et al. 2011; Massardi et al. 2016; Partridge et al. 2016) have been carried out simultaneously to the Planck satellite observations. Other than being important for the statistical characterization of the radio source population at frequencies and epochs of the satellite observations, they have been useful for the validation of the reliability, completeness and photometry of the satellite products, at least in total intensity.

The limited number of polarimetric millimetre surveys, the small number of bright Planck sources with a high significance in polarization, and the fact that the majority of polarized sources are variable (e.g. variability did not allow to directly compare polarized flux densities with the AT20G observations), made it difficult to validate the Planck polarized flux densities with external datasets and to properly calibrate the polarization angles.

A complex combination of effects must be considered to determine the observed source polarization fractions and angles. This includes intra-beam effects and bandwidth depolarization, in addition to intrinsic frequency-dependent changes. Furthermore, the propagation of the radiation through diffuse plasma screens between the source and the observer can cause depolarization and rotation of the polarization angle (“Faraday” depolarization). These effects are difficult to isolate observationally, although we can benefit from the inverse square frequency dependence of the latter effect. The observed polarized signal from a source is the vectorial average of the emissions along the line of sight, within the telescope resolution element and over the observational bandwidth. Faraday depolarization effect are negligible at Planck observing frequencies, but, because of its resolution, beam depolarization imposes a restriction on sources as suitable CMB mission calibrator candidates. The requirements for a good polarized flux density reference target for the fainter end of Planck’s observing frequencies include integrated emission > 1 Jy across the observation bands, polarized intensity at levels > 200 mJy and unresolved emission within the telescope beam. Here below we briefly review suitable objects for these cosmological purposes.

The most polarized object in the AT20G analysis is AT20GJ210933-411020 with 1.9 Jy of total intensity and 10% fractional polarization, flat spectrum, increasing fractional polarization with frequency, and only 14% relative variability over 3 yr time. In the Planck channels the spectra become steep down

to 428 mJy at 100 GHz and only 128 mJy at 217 GHz. AT20GJ063546-751616 has 5.33 Jy of total intensity flux density at 20 GHz, 6.2% polarized, and remains above 1 Jy up to ~ 100 GHz. It is classified as a flat-spectrum radio quasar at redshift $z = 0.653$. It is point-like and modestly variable over few years in ATCA observations. Thanks to its position it is always visible to Southern hemisphere telescopes and stands as the most suitable point-like (at \sim arcsec resolution) polarization calibrator at high frequencies and low declinations.

Tau A was finally used for external validation and calibration for Planck because it is the brightest compact source in polarization in Planck and has been thoroughly studied above 20 GHz (Hafez et al. 2008), despite it is resolved in the higher Planck channels and may not be the best source for validation at these frequencies. Given its position (declination is $+22.01^\circ$) it is not suitable for CMB experiments carried out from the South Pole.

Burke-Spolaor et al. (2009) presented the wide-field imaging and polarimetry at 20 GHz of seven most extended, bright ($S_{\text{total},20\text{GHz}} \geq 0.50$ Jy), high-frequency selected radio sources in the Southern sky with declinations lower than -30° . Among these sources, Pictor A has been identified as a suitable extragalactic polarization calibrator for the Planck Low Frequency Instrument because of its position (in the region of the Ecliptic Pole where the satellite scanned \sim once per minute), the ~ 10 arcmin total extension, and the 20 GHz ~ 0.5 Jy of integrated polarized emission, mostly concentrated on the region of the western hotspot, which is highly diffuse so that it is not expected to be variable (i.e. more suitable as calibrator with respect to compact bright variable objects). The limit for usability as high frequency calibrator rely only in the steep spectrum ($\alpha \sim -0.70$), but the flux density at 100 GHz is still ~ 2.5 Jy in the PCCS. Hence, it is a suitable reference target for calibration and validation efforts for southern hemisphere experiments with \sim arcmin resolution.

1.3.2 Targets for Cosmic Polarization Rotation measurements

Some theoretical models (for a summary see di Serego Alighieri 2015) proposed to explain the matter-antimatter asymmetry introducing terms that can violate the Einstein Equivalence Principle (EEP), the Lorentz invariance or the CPT invariance. These produce, in turn, the rotation of the electric vector position angle (EVPA) along the propagation of the electromagnetic wave: this is the so-called ‘‘Cosmic Polarization Rotation’’ (CPR) and the best upper limits determined are around 1° from CMB experiments and observations of astrophysical objects in optical or radio band. Radio sources have played an important role in the investigation of CPR since its beginning. In fact Carroll et al. (1989) and di Serego Alighieri et al. (2010) stated that measurements of the polarization angle and orientation of cosmological radio sources may be used to search for unusual effects in the propagation of light through the Universe. They indicated extragalactic radio sources as good candidates for CPR measurements because they are polarized targets observable up to high redshift and the jet axis direction should provide an indication of

the expected polarization orientation. This constitutes a reference angle to be compared with the measured one: the difference could be attributed to cosmic birefringence. However, the tests using the polarization of radiogalaxies in the cm-wavelength bands required a correction for the Faraday rotation, it is not based on a strict physical prediction of the polarization orientation at the emission, and holds only statistically on a large sample of sources (see di Serego Alighieri 2015, and reference therein). In fact, AGN electric vectors typically align along the core-jet direction in the inner source regions and are perpendicular to it on the edges (Laing 1996), leading to different behaviors for different class of sources.

Henceforth, also for these analysis, the intrinsic properties of the radio sources and their match with the observing resolution should be taken into account. Burke-Spolaor et al. (2009) studied a sample that include FR II (e.g. PKS0131-36, PKS2356-61), head-tail (PKS1610-60), triples (PKS1333-33) with jet and node structures. In some cases there are evidences of merging events, interactions with the environment (for cluster galaxies) and/or dust features. They found that all the cores have undetected or low polarization fractions mostly because of scattering medium surrounding the region of inner jet formation, or dense plasma, or beam depolarization of unresolved components. They confirmed, in most of the cases, the expected perpendicularity between the radio axis and the electric field orientation. However, several sources showed complex substructures with changes of geometries and, in few cases, the radio axis is aligned with the electric field. These changes could be due to shock fronts in the inner source regions. Hence, only high resolution polarimetric observations might properly disentangle the intrinsic structural misalignment of radial axis and magnetic fields. Such observations are technically difficult as the requested resolution increases (e.g. to reach higher redshift).

Partridge et al. (2016) compared the ground-based observations carried out with the Australia Telescope Compact Array and the Very Large Array with the Planck detections to verify the photometry and to exploit the Planck dipole calibration to provide an absolute reference scale for flux-densities calibration. Among their sample, only 3C273 was detected in polarization in Planck lowest frequency channels that allowed to confirm that the polarization angle of the three instruments agrees within $\pm 2^\circ$. This could be considered the best current estimate of the error that is obtained for the absolute calibration of the polarization angle. And this is the order of magnitude also of the systematics that affects CPR measurements, mostly due to limitation of the calibration quality at millimetric wavelengths.

The main requirements for a good polarization calibrator for CPR studies are: a bright object at high frequencies (reasonably high in the sense that Faraday rotation is negligible), i.e. with total flux density higher than 1 Jy, a polarization fraction at least at few % and a stable (at least on years timescale) polarization angle. The optimum would be a point-like object (in case of CMB facilities, at least at arcmin resolutions) whose all spectropolarimetric properties are stable on (at least) years timescale. This improves the calibration accuracy, particularly demanded in an era of precision cosmology. How-

ever, because of typical variabilities at high frequencies, optimal candidates are extremely rare, especially among the Doppler boosted objects in which any flaring activity is enhanced. We might then relax a little bit requirements, stressing that even a resolved objects whose compact emissions are stable and dominating (by a factor at least 100) over more extended features could serve this purpose as well. It may be easier to find objects in this category: e.g., this seems to be the case of the western hotspot of Pictor A against the diffused lobed emission.

PKS0521-365 (the leakage calibrator for our ALMA observations, see the chap. 4) could be a good candidate being very bright (≈ 4.3 Jy during our observations) and polarized ($\approx 2.2\%$) but indeed is quite variable (even 40% in a year). It is resolved in our 0.5 arcsec resolution observations but its core is much brighter than any other feature. Constraining its polarization angle behaviour will be addressed in future publications by our collaboration (e.g. Liuzzo et al., in prep.). Among the compact objects we observed with the Australia Telescope Compact Array (ATCA) and the Atacama Large Millimeter (and submillimeter) Array (ALMA) we identified some with high flux densities and polarization fractions (especially at frequencies higher than 20 GHz) which are found to be particularly stable once one focuses on the polarization angle at different frequencies and among the different epochs we observe (between 2014 and 2016). The first object we indicate is PKS0637-752, already suggested by Massardi et al. (2013) as a potential leakage calibrator, being at ~ 1 Jy and $\sim 1.6\%$ polarized at 100 GHz. Our ATCA observations (see the chap. 3) show that the polarization angle is quite constant across the 5.5 – 38 GHz frequency range and stable within 8° at 38 GHz (see Fig. 4.2). Other somewhat fainter but more polarized objects we found in our sample at 100 GHz are AT20GJ062005-610732 (120 mJy, 10.5% polarized) and AT20GJ074331-672625 (190 mJy, 5.2% polarized): the first one is constant within 8° both across 18 – 38 GHz frequency range and between the two epochs; the second is less constant between the different frequencies but stable within $\sim 3^\circ$ both at 33 and 38 GHz.

Chapter 2

Observations and polarimetric data reduction

2.1 Selecting a complete sample: from the AT20G to the faint PACO sample

The Australia Telescope survey at 20 GHz (AT20G) is a blind radio survey carried out with the Australia Telescope Compact Array (ATCA) from 2004 to 2008, and covers the whole southern sky. It includes 5890 sources above a 20 GHz flux-density limit of 40 mJy (at 5σ detection). All AT20G sources have total intensity and polarization measured at 20 GHz, and most sources south of declination -15° also have nearly simultaneous (generally, within 15 days) flux-density measurements at 5 and 8 GHz. A total of 1559 sources were detected in polarized intensity at one or more of the three frequencies. The completeness of the AT20G source catalogue is 91% above 100 mJy and 79% above 50 mJy in regions south of declination -15° . North of -15° , some observations of sources between 14 and 20 h in Right Ascension were lost, due to bad weather and could not be repeated, so the catalogue completeness is lower in this region. Each detected source was visually inspected as part of the quality control process, and so the reliability of the final catalogue is essentially 100%. In the following Fig. 2.1 there is a plot in the equal-area Lambert projection showing the distribution of the 5890 sources in the AT20G catalogue. Note that the catalogue also excludes the Galactic plane ($|b| < 1.5^\circ$): data have been acquired but they are not reliable due to Galactic contamination.

The PACO (Planck-ATCA Co-Eval Observations) project (P.I.: M. Mascardi) observed 464 sources drawn from the AT20G catalogues with ATCA. Observations were obtained in 65 epochs between July 2009 and August 2010 (more than 450 hr allocated) in the 4.5 – 40 GHz frequency range (overlapping with the two lowest Planck frequency bands), nearly simultaneous with the Planck satellite (within 10 days), in order to minimize variability issues in the flux density comparisons. Its main goal was to characterize extragalactic radio source total intensity spectra and their variability over a wide frequency range (at least 5–217 GHz, but for some sources up to 857 GHz). This

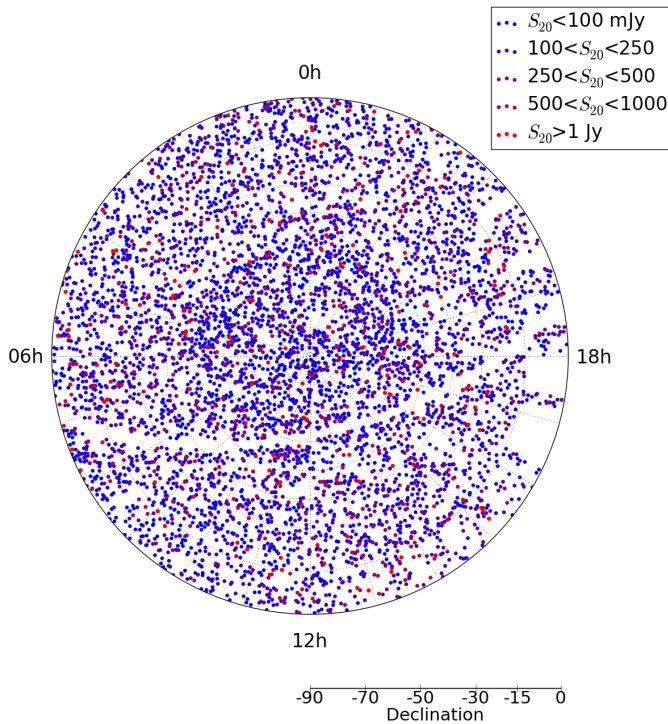


Figure 2.1: Polar plot showing the distribution of the 5890 sources in the AT20G catalogue

project has recently released its final catalogue (Massardi et al. 2016) which includes three, partially overlapping complete sub-samples (see Fig. 2.2): the *bright PACO sample* (Massardi et al. 2011), comprising 189 sources with AT20G flux densities $S_{20\text{GHz}} > 500$ mJy at $\delta < -30^\circ$; the *faint PACO sample* (Bonavera et al. 2011), comprising 159 objects with AT20G flux densities $S_{20\text{GHz}} > 200$ mJy with right ascension $3 < RA < 9$ hr and declination $\delta < -30^\circ$, and the *spectrally-selected PACO sample* (Bonaldi et al. 2013) which consists in 69 sources selected from the whole AT20G catalogue with flux densities $S_{20\text{GHz}} > 200$ mJy and spectra classified in the AT20G catalogue as inverted or upturning over the 5 – 20 GHz frequency range. As an addendum to these sub-samples there are 203 ATCA calibrators (76 of which are also included in the main sub-samples), i.e. sources with $S_{20\text{GHz}} > 200$ mJy showing more than 10% variability at 20 GHz in the epoch 2006-2009.

The spectral analysis and fitting procedures extended in the range 5 – 217 GHz revealed that the vast majority of the spectra are smooth and well fitted by a double power law function, with a steepening occurring for frequencies $\gtrsim 30$ GHz. No clear evidence of rising spectra due to dust emission from the host galaxy, so synchrotron remains the dominant emission mechanism, nor of spectral synchrotron break as possible effect of electron aging is observed at mm wavelength. The latter can be addressed, assuming the continuous injection model to be valid, arguing that the analyzed population is formed mainly by young objects, i.e. with $\tau_{\text{syn}} \lesssim 10^3 - 10^4$ yr.

Extracting polarized emission information for the PACO observations was

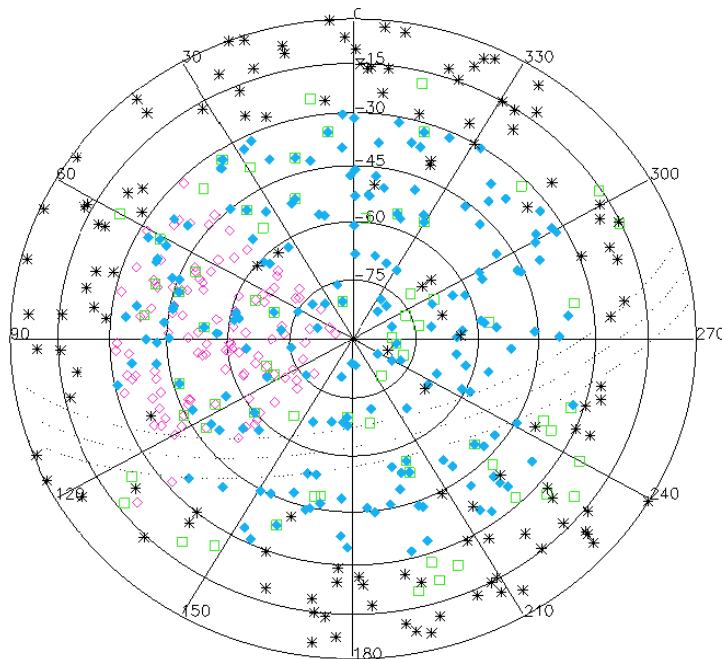


Figure 2.2: Polar plot showing the distribution of the three PACO samples: cyan filled diamonds are the bright PACO objects ($S_{20\text{GHz}} > 500$ mJy); pink empty diamonds are for the faint PACO sources ($S_{20\text{GHz}} > 200$ mJy, among which the objects we study) and green squares identify the spectrally-selected PACO sample. Black asterisks are ATCA calibrators.

unsuccessful because of several calibration issues. Hence, three multi-frequency observing runs were dedicated to polarimetry in September 2014, March–April 2016 and July 2016 (project C2922, PI: Massardi). The sample was chosen among the faint PACO sample ($S_{20\text{GHz}} > 200$ mJy) in the Southern Ecliptic Pole region (having ecliptic latitude $< -65^\circ$), that was the region with the highest sensitivity in Planck satellite observations, hence where we could have a higher chance of finding counterparts at Planck frequencies. The 8 extended sources (i.e. larger than the PACO observations resolution of 1 arcsec) were removed from the sample as the techniques to extract flux densities used in the PACO projects underestimate their flux densities. The final source list consists of a complete sample of 104 compact sources with $S_{20\text{GHz}} > 200$ mJy in the AT20G survey catalogues.

2.2 ATCA observations

In Tab. 2.1 there is a summary of the three ATCA observational campaigns: the epochs (UTC time), the array configurations, the observed frequencies, the integration time per object and the program source observed, roughly indicated by the ecliptic latitude b .

Table 2.1: ATCA observations summary for the three campaigns: September 2014, March-April 2016 and July 2016

Epoch	Array	Freqs.	Time on source	Observed sub-sample
27/09/2014	H214C	18, 24 GHz	2 - 3 × 1.5 min	$b < -75^\circ$
28/09/2014	H214C	33, 38 GHz	2 - 3 × 1.5 min	$b < -75^\circ$
29/09/2014	H214C	5.5, 9 GHz	2 - 3 × 1.5 min	$b < -75^\circ$
29/03/2016	H214D	2.1, 5.5, 9 GHz	1 - 2 min	$b < -75^\circ$
30/03/2016	H214D	2.1, 5.5, 9 GHz	1 min	$-65^\circ < b < -75^\circ + \text{some } b < -75^\circ$
30/03/2016	H214D	18, 24, 33, 38 GHz	1.5 min	some $b < -75^\circ$
31/03/2016	H214D	18, 24, 33, 38 GHz	1.5 min	$-65^\circ < b < -75^\circ + \text{some } b < -75^\circ$
18/04/2016	H214D	2.1 GHz	1 min	some $b < -65^\circ$
20/04/2016	H214D	2.1 GHz	1 min	some $b < -65^\circ$
18/07/2016	H75C	33, 35 GHz	1.5 min	some $b < -75^\circ$

Table 2.2: ATCA observations calibrators table for the three campaigns: September 2014, March-April 2016 and July 2016

Epoch	Freqs.	Bandpass (PKS)	Flux (PKS)	Phase (PKS)	Leakage (PKS)
26/09/2014	18, 24 GHz	0537-441	0537-441	0530-727	0537-441
27/09/2014	33, 38 GHz	0537-441	0537-441	0530-727	0537-441
28/09/2014	5.5, 9 GHz	0537-441	0537-441	0530-727	0530-727
29/03/2016	2.1, 5.5, 9 GHz	0537-441	0530-727	0530-727 (or 0537-441)	0537-441
30/03/2016	2.1, 5.5, 9 GHz	0537-441	0530-727	0530-727 (or 0537-441)	0537-441
30/03/2016	18, 24, 33, 38 GHz	0537-441	0530-727	0530-727 (or 0537-441)	0537-441
31/03/2016	18, 24, 33, 38 GHz	0537-441	0530-727	0530-727 (or 0537-441)	0537-441
18/04/2016	2.1 GHz	1934-638	1934-638	0530-727	1934-638
20/04/2016	2.1 GHz	0537-441	0530-727	0530-727 (or 0537-441)	0537-441
18/07/2016	33, 35 GHz	1921-293	1934-638	0530-727	0530-727

In the first two campaigns (September 2014 and March-April 2016) the array configuration was H214 (in its variances C and D, respectively), while in the July 2016 we observed with H75C. Both are hybrid (antennas are displayed also along N-S direction) compact array. In case of the H214 group the nominal spatial resolution spans from 94 to 5 arcsec at the considered frequency interval (2.1–38 GHz) if we consider only the 5 most packed antennas, while it goes as down as 0.5 – 10 arcsec considering also the longest baselines with the sixth antenna, but with a higher sensitivity. In case of H75 configurations antennas are in the most packed configuration and we observed only at 33 and 35 GHz: the resolution is ≈ 0.6 arcsec with antenna 6 and about 17 – 18 arcsec without it. The particular compactness might be problematic in observing objects far from the transit, since in that case one antenna can be shadowed by another (see the shadowing diagram in Fig. 2.4): in case of our objects (southern of -40° in declination) the antenna 2 sitting in the station N2 may be shadowed by antenna 1 (station W104), 4 (station W106) and 5 (W109), respectively. However, the affected visibilities regard only a bunch of objects (~ 10) observed in July 2016. These, indeed, represent less than 1% of our dataset. However, these data were flagged during preliminary calibration procedures. With H214, instead, the situation is much better, and we easily avoided any shadowing effect (cf. Fig. 2.3 with Fig. 2.4). Using a hybrid configuration results in a more homogeneous uv-plane coverage of the largest spatial scales in a shorter time, hence in a better imaging achievable with respect to a non-hybrid configuration, considered that our sample should contain only point-like objects.

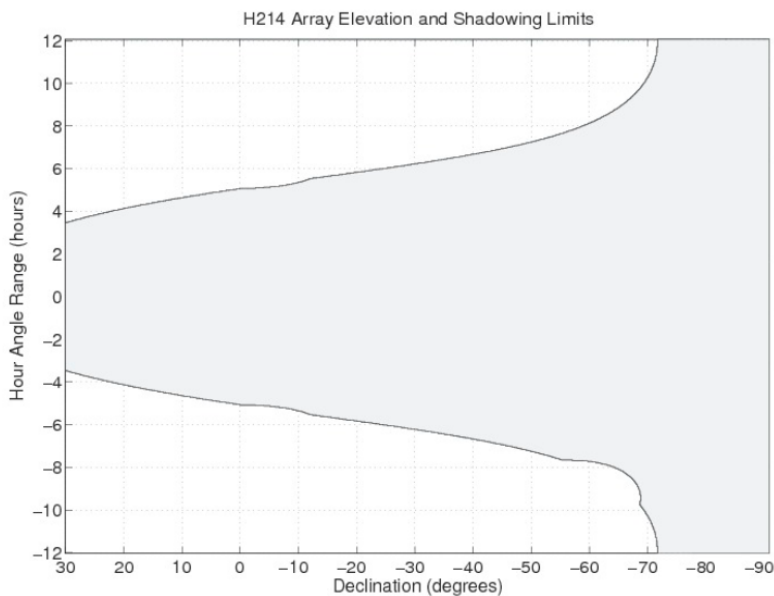


Figure 2.3: Shadowing diagram for ATCA array configurations H214 (from the ATCA Users' Guide).

Considering the flux density threshold selection of 200 mJy at 20 GHz in total intensity and indications of minima for polarization fraction typically reported in literature (Massardi et al. 2013, e.g.) found for a brightest sample,

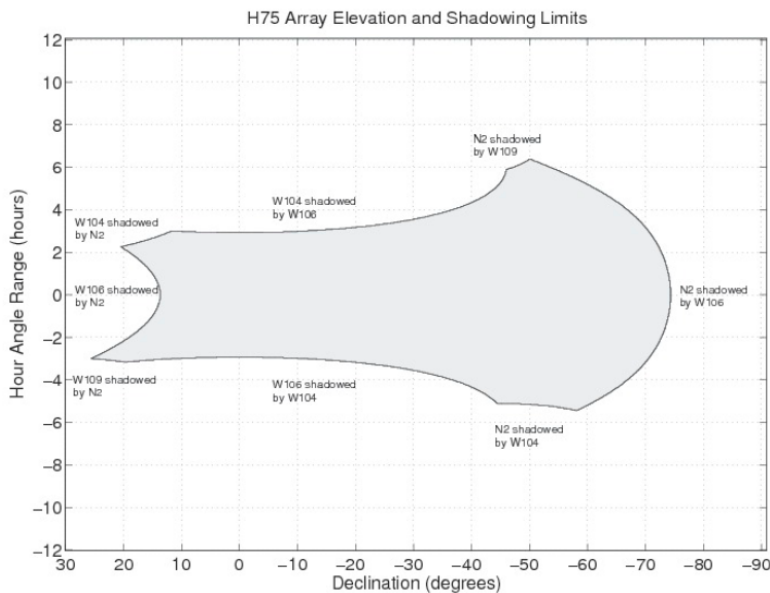


Figure 2.4: Shadowing diagram for ATCA array configurations H75 (from the ATCA Users' Guide).

i.e. $S_{20\text{GHz}} > 500$ mJy, a 1% as minimum), the 3 min on-source observed for each target were expected to be enough to reach a $> 10\sigma$ detection, at least at the selection frequency. However, since spectra generally steepen at higher frequencies and some of the sources are now indeed fallen below the selection threshold, this nominal sensitivity guarantees $> 5\sigma$ detections for all the sources at all the frequencies. In order to achieve better calibration and imaging each source was observed (at least) in 2 cuts at different hour angles (e.g.: 2×1.5 min).

2.3 Polarimetric calibration for a linear feed based array

When we observe an object in the sky with an interferometer, we register the interference pattern produced by the signal of an impinging plane wave received by at each couple of antennas. We can represent the information in terms of complex quantities called visibilities sampled in the uv-plane¹. However, the observed visibilities are corrupted by several effects (the instrumental response, the atmosphere and the parallactic position in the sky of the observed source). The general formalism used to take into account of all of these effects is that of the measurements equation, which is indeed valid for every interferometer, no matter if it is linear feed (like ATCA and ALMA) or circular feed based (like VLA). The equation is indeed a set of matrix equa-

¹The uv plane is the imaginary plane where points are baseline projections as seen by the target of observation. Since the Earth rotates these projections change, thus providing a better coverage of the uv plane, and, according to the Van Cittert-Zernicke theorem, a better sampling of the Fourier transform of the brightness distribution of the targets.

tions (one for each baseline) and can be stated as follows:

$$V^{\text{obs}} = BGDPTV^{\text{true}}, \quad (2.3.1)$$

where V^{obs} are observed visibility 4–vectors² and V^{true} are true visibilities. Matrices B, G, D, P and T are baseline-based operators which represent the bandpass response of the instrument, the electronic gain of the system, the leakage term, the parallax angle variation term and the troposphere contribution, respectively. Note that the data reduction process consists in the algorithm aimed to compute the true visibilities from the observed ones. Since the corruption terms are in principle unknown too, some assumptions are usually made on their form. These assumptions might depend on the particular instrument and calibration software adopted and have an impact on the effective way the system is inverted in order to find the real visibilities. However, since the number of equations is typically higher than the number of unknown in the equations, a step by step iterative process is quite common. An accurate characterization of the corrupting terms in (2.3.1) is generally achieved by observing a number of reference objects, i.e. the calibrators, which are typically bright, compact and that can also exhibit a certain degree of polarization (in case we are interested in a polarimetric campaign). They are generally distinguished with respect to the particular corruption term they solve for. Hence, we have:

- the bandpass calibrator, which mainly serves the purpose of correcting for inhomogeneous amplifiers response along the observational band, i.e. the bandpass shape B;
- the phase calibrator, a known point-like object (for the resolution in use) that should be visited often during observations, since it corrects for atmospheric phase decorrelation effects which are absorbed in the phase of the gain term G. It is important to choose a phase calibrator close to the targets in order to provide an accurate correction (requirements becomes more stringent as frequency increases).
- The flux calibrator, or primary calibrator, provides a reference known flux, i.e. the common amplitude factor which can be factored out from the gain matrix G. The tropospheric term T does not have a dedicated calibrator but it is associated to remote sensing measurements, usually referred as a priori calibration, since they allow to solve for it at the very beginning of the calibration procedure. The measurements are the system temperature T_{sys} , the thermal noise associated to the whole system, i.e. the observing instrument and the environment (which includes also

²An electromagnetic wave can be decomposed in two state of polarization. Two possible basis are the the linear one (X and Y) and the circular one (R and L). Each interferometric antenna is typically equipped with two feeds adopting one of the mentioned basis, hence a visibility, being associated with a couple of antennas is formally an external products with respect to a given basis, i.e. a 4-vector (XX,YY,XY,YX) or (RR,LL,RL,LR).

the target) and the Water Vapour Radiometer (WVR): a 183 GHz absolutely calibrated radio receiver, i.e. “radiometer” measures the mm-wave emission from atmospheric water vapour from which the actual water vapour column along the line of sight of each telescope in the array. Thus, the induced path delays, which can be applied as a phase rotation to the observed visibilities, are applied to each antenna. This latter term is relevant only for instruments observing at such high frequencies (such as ALMA).

Indeed, if one is not interested in polarization, these calibrators are enough to determine the total intensity flux density of the targets. In terms of Stokes’ parameters, those associated to the total intensity, I , is determined when the parallel-hand products (XX and YY in case of linear feeds, RR and LL for circular feeds). Polarization, instead, requires the determination of all the products which translates into the full Stokes’ characterization (I , Q , U and, eventually, V) of a given target. In order to achieve this goal there are two terms for which it is necessary to solve for (cf. eq. (2.3.1)): the parallactic angle change P and the leakage D terms. If we consider an altazimuthal telescope, the sky rotates in the field of view with a parallactic angle ψ depending on time:

$$\psi(t) = \frac{\cos b \sin H(t)}{\sin b \cos \delta - \cos b \sin \delta \cos H(t)}, \quad (2.3.2)$$

where b is the latitude of the observatory, $H(t)$ is the hour angle and δ is the declination of the observed object. Hence, the amount of signal received by two orthogonal linear feeds X and Y (ideally aligned with the alt-azimuth coordinate system) is expressed by the rotation matrix P^{lin} in terms of Ψ :

$$P^{\text{lin}} = \begin{pmatrix} \cos \Psi & \sin \Psi \\ -\sin \Psi & \cos \Psi \end{pmatrix} \quad (2.3.3)$$

When the object is observed at the meridian $H = 0$, Ψ is 0° as well and the eq. 2.3.3 reduces to a diagonal form. P^{lin} has been written for a single antenna and the result can be easily generalized to obtain P in the eq. (2.3.1) by an external product between P^{lin} and its transposed and conjugate $P^{\text{lin}*}$. However, it is important to note that real feeds usually display a mechanical feed position angle offset from the altitude-azimuth alignments, hence each entry in the matrix eq. (2.3.3) indeed contains an offset with respect to Ψ , hence P^{lin} does not reduce to a diagonal when Ψ is 0° . It is possible to show that the parallactic angle variation plus the offset in the mechanical feed position angle introduces a time-varying phase difference 2Ψ (now Ψ contains the offset) between X and Y feeds in each antenna, which translates in a zero-point error in the measured polarization angle. Typically there are two implemented ways to cope with this issue: one is to mount on a feed of the reference antenna a noise diode which injects a known signal. Hence, there is an on-line monitoring of the XY -phase difference, since the phase delay is measured from the Y feed. This is the strategy adopted, for example, by ATCA and data are corrected by this effect when they are loaded into the MIRIAD software. In absence

of dedicated ancillary systems an alternative can be to observe a well known polarized calibrator (for which both Q and U Stokes' or, equivalently, the linear polarization and the polarization angle are well determined). Then, even a single observation on the calibrator would suffice to determine the offset term in Ψ . However, such objects are very rare (especially in the southern sky), so it is more common to observe a polarized objects for which the polarization parameters are not known. The price to pay in order to solve the system in this case where the true polarized signal of the object is not known is observing it at different parallactic angles. Common practice suggests that at least three scans with a global parallactic angle coverage of ~ 3 hr generally allows to achieve good results, removing degeneracies in the system unknowns. However, polarization observations are particularly demanding since there is at least another effect to take into account to obtain an accurate polarimetric measurement of a given target: the leakage term D in the equ. 2.3.1. Again, we can describe it in matrix terms on a single antenna by introducing the D^{ant} matrix that can be easily generalized to the visibility products (or in terms of Stokes's parameters as well):

$$D^{\text{ant}} = \begin{pmatrix} 1 & d_Y(\nu) \\ d_X(\nu) & 1 \end{pmatrix}, \quad (2.3.4)$$

where $d_X(\nu)$ and $d_Y(\nu)$ are the (frequency-dependent only) off-diagonal terms which tell us what fraction of polarization in a given direction leaks on the other one. The origins of this effects can be found in the mechanical imperfect orthogonality between the two feeds, but the main reason can be found in the reflections (e.g. standing waves generation) which might establish during the electronic propagation of collected signals that flips one polarization direction into the other, or even in impurities in polarizers or asymmetries in the optical system. For an interferometer made of antennas with similar design the sum of all the leakage terms for all the antennas can be safely assumed to be 0. This is indeed the case of ATCA and ALMA. In case of ALMA data this sanity check is performed during the second phase of Quality Assurance (QA2) prior to deliver calibrated data to the PI. For ATCA data, instead, we perform this check directly on leakage terms on log files written by the data reduction pipeline we implemented (see the next subsection): not only their sums are close to zero but also each term is reasonably small. As a further test, we compared leakage terms for different calibrators (PKS0537-441, PKS0530-727 and PKS0637-752³) finding compatible solutions.

There are indeed other non-idealities which are important at this first-order of accuracy in polarimetric calibration, e.g. non-ellipticities in the orthogonal feeds that in principle causes diagonal terms in eq. (2.3.4) not to be exactly 1. However, all the diagonal effects can be easily reabsorbed in B and G term, since they do not couple different polarization states. In principle, if ones has already solved for the parallactic angle-related term P , a single observation of an unpolarized calibrator can be in principle used to determine leakage

³This calibrator was found to be barely resolved at the higher ATCA frequencies, hence we decided to avoid its usage at all.

corrections. The main limitation here comes from the confidence level at which the calibrator can be assumed to be non-polarized (e.g. for the object PKS1934-638 at frequencies higher than 10 GHz this assumption might be no longer valid). A well characterized (in polarized flux density and polarization angle or, equivalently, in Stokes' Q and U) calibrator can be used as well, but, again, the main limit is related to the accuracy we know the calibrator, given that variability effects are expected to be higher in polarization and a calibrator monitoring program should be finer than those in total intensity only. Again, a more practical solution is to observe a polarized object with an unknown degree of polarization at different parallactic angles to both reconstruct the leakage solutions and determine the polarization parameters of the calibrator, and avoid degeneracies in the set of equations.

From the above discussion about the two relevant terms for polarization it emerges that a polarized calibrator (in principle with an unknown polarization degree) observed at different parallactic angles (at least three scans with a coverage of at least 3 hr) is a good solution to solve for both parallactic angle and leakage terms. This is the strategy we adopted in both ATCA and ALMA campaigns, as presented in the following sections.

2.3.1 Calibration in MIRIAD

In this subsection we briefly present the MIRIAD tasks used to calibrate the polarimetric ATCA data. This to allow the reader to understand the calibration schemes reported for the different ATCA observational campaigns. We also briefly summarize the preliminary steps in order to prepare raw data for calibration procedures.

One of the MIRIAD qualities is to support scripting in order to automatize calibration procedure as much as possible: such feature has been exploited to develop a reduction pipeline. However, ATCA data are in RPFITS format, while MIRIAD process visibilities stored in the FITS format. Thus, before to effectively start data reduction, all data must be prepared (see Fig. 2.5). We need to illustrate only the preparation procedure for paired frequencies in each session, since it applies at the same way for all paired frequencies at different sessions. Hence, we have performed the MIRIAD task ATLOD (which converts an RPFITS into a directory containing FITS files), specifying in input the two files of interest. However, since we have preferred (and it is strongly recommended) to treat a single frequency at time, we have specified a number by using the keyword IFSEL: 1 for selecting the lower frequency, 2 the higher one. ATLOD task also can discard autocorrelations (keyword "nocorr"), eliminate spurious effect due to the correlator ("birdie") and flagging channels known to be affected by RFI (keyword "rfflag"), apply atmospheric opacity corrections (keyword "opcorr") and on-line XY phase offset measurements from the nose diode mounted on each ATCA antenna (keyword "xycorr"). All these keywords have been used in handling our data.

Once created the directory containing FITS files, one can proceed to break the multi-source, multi-frequency dataset into a collection of single-source, single-frequency datasets. In fact, MIRIAD is poor at handling the calibra-

tion of datasets containing multiple sources and multiple frequency bands. The task to do this is UVSPLIT. It generates the names of the output datasets itself, forming these from the source name and the central frequency (in MHz) of the data. Furthermore, since we want to produce a well constrained spectral behaviour for each object and we have enough signal to noise ratio also in smaller fractional bandwidths, we split the 2 GHz band into smaller bandwidth chunks. This can be done using the "maxwidth" parameter in the UVSPLIT task and proceed to the data reduction in an independent way for each chunk. The maxwidth parameter should be set to the largest bandwidth allowed in a single dataset, in GHz. In our case, we have retained to split the 2 GHz Compact Array Broadband Backend (CABB) continuum bands into 512 MHz chunks. However, since polarization fluxes of the considered sources can be as low as ~ 1 mJy, the splitting of each frequency in four 512 MHz chunks decreases the nominal sensitivity of 0.2 mJy of a factor ~ 2 , thus preventing a 5σ detection for the minimum polarized flux expected (especially if we also take into account the channel flagging, which lowers the sensitivity even more). Thus, in handling polarized flux data we adopted a 1 GHz split sub-bands.

The next general step is the flagging of the data, mainly focusing on calibrators. In fact, what turns out to be flagged in calibrators is routinely flagged in the source programme, since if something has gone wrong in the calibrator observations it is likely gone wrong in the source observations too. However, flagging a calibrator alone basically translate in reducing the number of constraint to make calibration solution to converge, hence, data referred to a particular observation of the calibrator which has been heavily flagged might be not usable as well. In the case of our programme we have stressed we didn't have any relevant problem with shadowing but, mostly at 2.1 GHz and partly at 5.5 and 9.0 GHz (more at 9.0 than 5.5 GHz) flagging RFI spikes and correlator induced signals were particularly needed. Thus, after removing the most evident spurious features in our data, we adopt an automatic flagging recipe to remove the others, as suggested by the ATCA Users's Guide. This approach is based on the flagger framework "AOFlagger", presented by Offringa et al. (2012) and it is applied once the visibilities are bandpass corrected: in the case of point-like objects the visibilities are constant, hence by selecting a threshold in the units of the rms with respect to the median value, it is possible to identify most of data which are likely affected by RFI and/or electronic artifacts. The MIRIAD task which implements this method is PGFLAG and the iterative way called in our calibration recipes has been determined by Craig Anderson (ATNF) through trials and errors, focusing in particular on 16 cm data, but it is now recommended at any band.

MFCAL solves for antenna gains and bandpass function. However, it does assume an unpolarized calibrator and that the polarization leakage terms are zero. If you have measured only the XX and YY correlations, you have to make these assumptions. However, as in this case, we have measured all four polarization products, then you can correct for these assumptions by running GPCAL after MFCAL (see the scheme). GPCAL is a MIRIAD task that determines calibration corrections (both antenna gains and instrumental po-

larization characteristics) for an array with dual feeds, from an observation of a point source. The source can be polarized, with unknown polarization characteristics. GPCAL is the main workhorse of the MIRIAD calibration system, although it is only particularly useful if you have measured all four polarization products (XX, YY, XY and YX). It offers many options to turn on and off various solvers. Most of these will be irrelevant to normal use - particularly when calibrating a source, such as PKS1934-638, which is known to be unpolarized. However, it does not determine a bandpass function. GPCAL will normally apply any bandpass function it finds with the dataset before it performs real work, and that's why we precede it with an MFCAL.

As the name suggests, GPCOPY is a MIRIAD task which copies or merges calibration corrections (antenna gains, polarization leakages, frequency table, bandpass item) from one dataset to another.

Tasks GPBOOT and MFBOOT are both mainly related to ensure for the phase calibrator the right flux scaling. However, there are some differences between them (for further info see MIRIAD Users' Guide). In our case the flux calibrator is not a planet, then GPBOOT alone is enough to guarantee correct flux scaling. The ideal is to select observations of the phase and flux calibrators that were taken at the same time and elevation, because atmospheric opacity affects the amplitude gain calibration. Since our observations held in very good and stable weather conditions, good results can be obtained selecting the time range where the phase calibration (observed many times during the source programme) elevation is the closest to the elevation at which the flux calibrator was observed. In this context MFBOOT corrects both the bandpass slope of the phase calibrator, and the flux scaling. For a known flux calibrator (as in the case of our observations, when we have PKS1934-638) MFBOOT constructs a model of what the flux should be on each baseline and for all frequencies across the band. Then, it determines by how much the gains must be scaled to make the observed flux at the centre of the band match the model value. Hence, it scales all the datasets it has been given by that factor. It also calculates the slope of the model between two points either side of the band centre, and then corrects the bandpass table to make the observed spectrum match that slope.

2.3.2 September 2014 campaign and implemented calibration

The original faint PACO sub-sample (53 objects) observed in September 2014 Galluzzi et al. (2017) covers a region in the ecliptic coordinate with $b < -75^\circ$, as it is possible to see from Fig. 2.14 with a black solid line surrounding the subsample in exam. Observations amounted to three slots (each of 5 h), one-a-day between Saturday the 27th and Monday the 29th: we indeed exploited some extra-time (about 4h) available before our observing slots to perform setup procedures, thus anticipating the programme (to repeat some observations at a different hour angles). As regards spectral bands, three sets

of 2X2 GHz between 5.5 – 38 GHz were considered, i.e. 5.5 and 9 GHz, 18 and 24 GHz, 33 and 38 GHz (instead of 39.0 GHz, like in PACO, due to setup procedure problems). Observations were set up to obtain higher sensitivity (~ 0.2 mJy/beam) and a more accurate leakage calibration than achieved during the previous PACO observing runs. As said it has been possible to reach the latter target by integrating 3 min per source at any frequency, separating each source on at least 2 cuts at different hour angles (e.g. 2×1.5 min)⁴ in order to also produce images of observed objects.

The observations lasted approximately 19 h (≈ 6 h per band, including overheads and calibration), during which weather conditions were very good. Essentially, during the first slot (Saturday the 26th UTC) setup procedures, calibrations and target programme observations were conducted at 18 and 24 GHz. The same is true for the frequencies 33.0 and 38.0 GHz, referring to the second slot (Sunday the 27th). The lowest frequencies (5.5 and 9.0 GHz) were observed during the last slot (Monday the 28th) since priority was given to exploit the very good weather conditions for the higher frequency observations. Since in the last day there was no possibility for observing the primary calibrator (i.e. the flux calibrator) PKS1934-638, a stable bright unpolarized⁵ point-like source (at ATCA resolutions) which with Uranus (typically adopted for frequencies > 30 GHz) is the most used in the southern hemisphere for flux calibration, since its model (the spectrum) is quite accurate and it has been quite recently upgraded⁶. Thus, in order to properly calibrate fluxes for the last observational slot, we exploited the extra time available at the beginning of the first two slots to observe the bandpass calibrator PKS0537-441 at 5.5 and 9 GHz with the primary calibrator PKS1934-638 in order to bootstrap the right absolute flux density scale during the observing program. Such an operation would have been resulted more delicate for higher frequencies, because the model of PKS1934-638 is more accurate at lower frequencies (in our case 5.5 and 9.0 GHz) and since the variability is higher at higher frequencies. In fact we check the stability of the flux densities of PKS0537-441 in the first two slots in order to safely use the determined flux density in the third one.

The standard procedure of raw data calibration reported in the ATCA Users' Guide can be synthesized in the following two steps scheme (optimized to minimize calibration errors and to provide the best correction for the bandpass slope. In fact, the first step serves the purpose of determining a model for the bandpass calibrator, by using both the IFs for a given band, while the second is the effective data reduction pipeline. In the September 2014 we were able to adopt this approach at all the observed frequencies: a minor difference is related to the fact that 5.5 – 9 GHz, we do not have the first step allocated in the same slot of target observations, but the day before and with a limited amount of time. We start presenting this first step for obtaining

⁴Since the availability of more observing time and being sources scheduled in order of increasing RA, a third cut has been executed for some sources at some frequencies.

⁵PKS1934-638 is the only object known till now to be also unpolarized, other than being a stable, bright and point-like source.

⁶A fact that must be taken into account when comparing multi-epoch observations even with the same observational setup.

the model of the bandpass calibrator PKS0537-441 (the scheme is reported in Fig. 2.6). Since the observations are within ≈ 25 min, there is no possibility of obtaining reliable leakage solutions (which requires at least 3 h of parallactic angle coverage) from the leakage calibrator, hence the first guesses about Q , U (and V) are made directly from PKS1934-638 which is expected to be unpolarized especially at lower frequencies. Once the same procedure is applied to the other IF, the calibrated I Stokes visibilities are fitted with a power law (order 1) via the task UVFMEAS with the following parameters:

```
$uvfmeas stokes=i order=1 options= plotvec,log, mfflux
```

Whenever there is at least 3 h of parallactic angle coverage, this first step present the keyword “qusolve” (for determining the first order leakage terms) among the options of gpcal launched on the leakage (and phase) calibrator. Here in Fig. 2.7 there is the slightly different flowchart used for the 18–24 GHz and 33–38 GHz modelling of the bandpass calibrator PKS0537-441. Once one has the three values $S(\nu_0)$ (flux density at a reference frequency ν_0), the reference frequency ν_0 itself and the bandpass slope α of the single power law, the actual data reduction pipeline can start with an MFCAL on the bandpass calibrator specifying these three values via the keyword “flux”, as reported in the second step of the script (implemented for 18 GHz, see Appendix A) and the flowchart reported in Fig. 2.8. Another difference between the 5.5–9 GHz with respect to the higher frequencies is that we use PKS0530-727 as leakage calibrator instead of PKS0537-441 (cf. Tab. 2.2) because the latter achieve a parallactic angle coverage of only 2 h.

Validation of flux density extraction: visibility Vs imaging

To check our assumption of target compactness at all the frequencies and the flux density extraction, we created maps for each Stokes parameter by means of the standard MIRIAD procedure. We adopted the natural weighting, the standard for point sources, to ensure the lowest noise level. We used multi-frequency synthesis imaging and a standard Högbom algorithm. The detection threshold was set at 5σ in both I and P . The $\sigma_{I_{\text{map}}}$ was derived from the I image region with no emission.

We use the task UVFLUX for flux density measurements (except for a few cases described below). This task is designed for point-like sources and works directly on visibilities, minimizing artifacts and phase-instabilities which may affect more image-based measurements. Since our sample excludes extended sources (at least up to 20 GHz), we expect that flux densities provided by UVFLUX and by IMSTAT (the MIRIAD task for flux density estimation from imaging) show differences no greater than $\approx 10\%$ in total intensity (due to residual phase instabilities in the images). Moreover, we assumed a source pointing accurate enough to keep objects in the phase center of the uv -plane. The latter hypothesis is supported by the fact that the PACO catalogue is drawn from the AT20G one, for which all positions are known with an accuracy $\lesssim 1$ arcsec (Murphy et al. 2010).

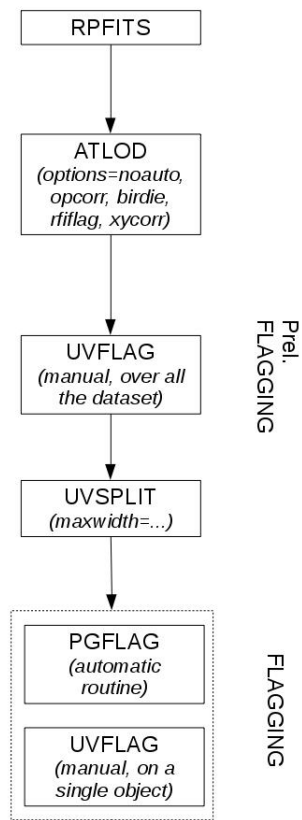


Figure 2.5: Diagram showing the data preparation for ATCA RPFITS files (cf. ATCA Users' Guide).

Afterwards, we compared the IMSTAT image peak (in mJy/beam) and the UVFLUX flux density estimation (for all the objects for which the uv-coverage allows imaging, i.e. $\approx 90\%$ of the cases) to reveal, in both I and P, whether an extended or displaced (from the phase centre) component is present. The median discrepancies, $\Delta I/I$ and $\Delta P/P$, are $\approx 2.7\%$ and $\approx 4.3\%$, respectively. In total intensity the relative discrepancy is $> 10\%$ for $\approx 4\%$ of the images. These large discrepancies are registered for frequencies > 24 GHz; they reach maximum values between 20% and 25% for 2 objects (AT20GJ080633-711217 and AT20GJ080649-610131, respectively) at 38 GHz. In all the cases the image peak values are higher than the UVFLUX estimation. A visual inspection of the images confirms that the sources are barely resolved.

In polarization the fractional discrepancy is $> 15\%$ in $\approx 11\%$ of the available images and $> 20\%$ in $\approx 8\%$ of the cases. In particular, there is one object, AT20GJ040848-750720, for which the excess of flux density (with respect to UVFLUX) measured in correspondence of the peak in the image reaches $\approx 361\%$ at 33 GHz and $\approx 352\%$ at 38 GHz. We show images for this source

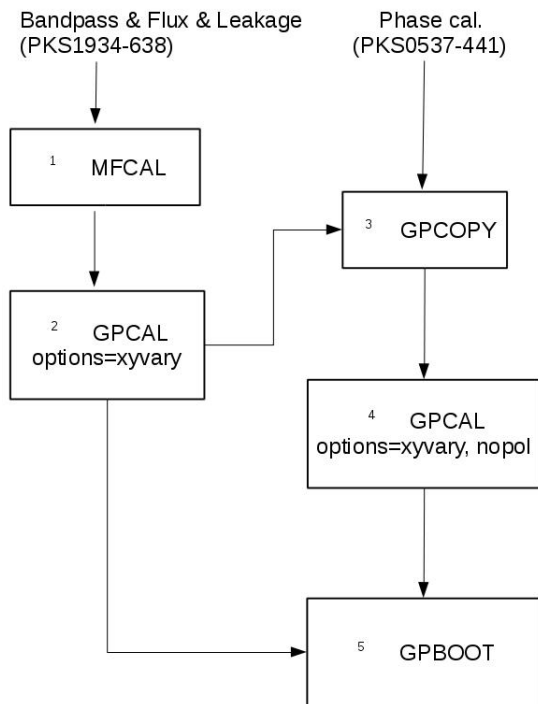


Figure 2.6: Diagram showing the first step for determining a model for PKS0537-441 at 5.5GHz.

(see Fig. 2.9) at all the 5 frequencies at which they could be obtained in total intensity. Polarized emissions are instead displayed by contour levels. It can be seen that the object is marginally resolved at the lower frequencies. At the higher frequencies a second component appears and the polarized emission mainly comes from it. According to Morganti et al. (1999) AT20GJ0408-7507 is a bright FR II radio galaxy at $z \simeq 0.7$, dominated by two bright lobes. Both lobes have high depolarization, slightly higher in the eastern one.

Given the good matching between flux densities from imaging and from visibilities for point-like objects (both in total intensity and in polarization), we decided to integrate over a suitable region on I images to recover the total intensity flux densities in case of slightly resolved objects. In case of the flux discrepancies in polarization, since images reveal an emerging point-like component displaced from the phase center, we estimated the flux density by considering the peak of the P image.

The complete catalogue (flux densities and fitting parameters, polarization fractions and angles) for the observations discussed in the paper Galluzzi et al. (2017) is available online, as supplementary material.

2.3.3 March-April 2016 campaign and implemented calibration

New observations of 104 compact sources were allocated between March the 30th and April the 20th 2016 (UTC time). They complement and extend the

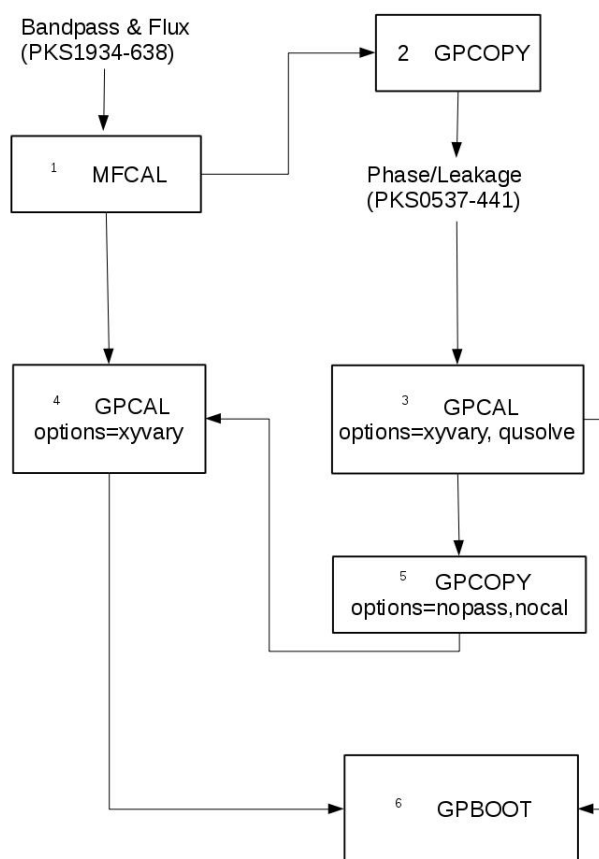


Figure 2.7: Diagram showing the first step for determining a model for PKS0537-441 at 18GHz.

old campaign held in September 2014. We extended the original sample by including those sources between -65° and -75° in ecliptic latitude, exploiting the same spectral and spatial configuration of ATCA (H214): at 5.5 and 9 GHz we also reobserved the whole old sample, while at 18–24 and 33–38 GHz we only managed to repeat observations for 20% of it. Moreover, we observed the whole enlarged sample (consisting of 104 objects) at 2.1 GHz. Again, we obtained three slots in three contiguous days to have the higher frequencies simultaneously observed. These new observations lasted ≈ 34 h (including overheads and calibration). In order to achieve the same sensitivity level of previous observations (i.e., ≈ 0.6 mJy/beam) we integrated 1 min at 2.1, 5.5 and 9 GHz and 1.5 min at the higher frequencies. Since the 2.1 GHz band is usually the more affected by radio-frequency interferences (RFI), the effective sensitivity reached in polarization is a bit higher than requested, i.e. 1 mJy/beam. Weather conditions were good also during this campaign. We again consider only data from the 5 closest antennas in the particular configuration of the array (H214), discarding the baselines with the sixth and furthest antenna, as the longest baselines are more noisy. The data preparation is the standard one described in the previous sub-sec. 2.3.2, while this time the bandpass calibrator PKS0537-441 was not observable when PKS1934-638 was high on the horizon, i.e. during extra-time slots we requested to

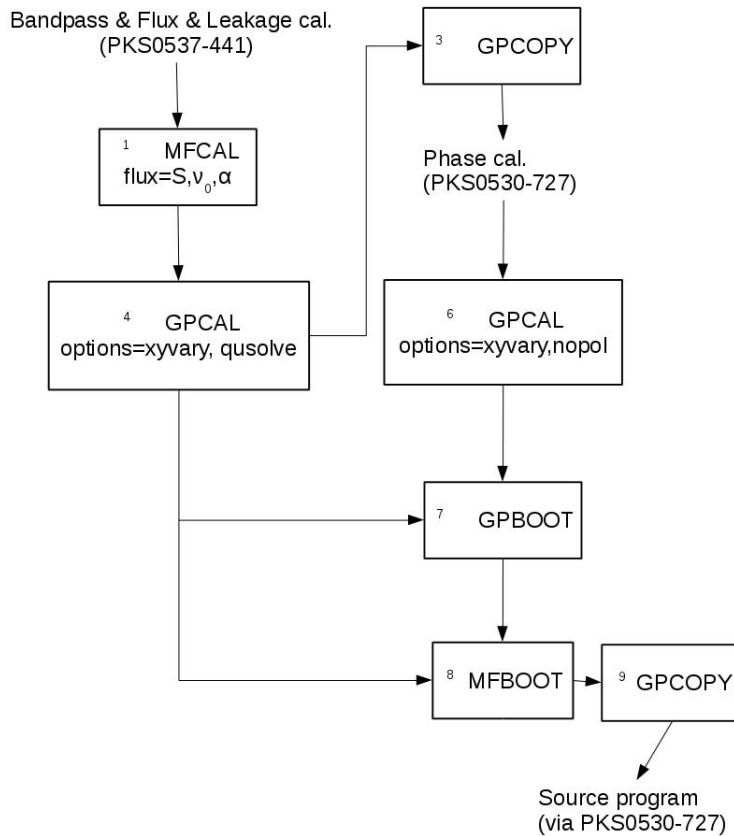


Figure 2.8: Calibration scheme used for 18GHz calibration of September 2014 campaign.

provide flux density absolute calibration. Thus, we use PKS0530-727 (observable with PKS1934-638) to perform this task: this time we determine in the extra-time at each frequency all the Stokes parameters by exploiting PKS1934-638, then in the relative slot we use this first guess in the keyword “flux” for each occurrence of GPCAL on the object, usually adopted as phase calibrator for most part of the sample. Whenever possible (all the March-April 2016 epochs except for the observational slot of April the 18th), we use PKS0537-441 as leakage calibrator: in some cases (typically among the objects with $-75^\circ < b < -65^\circ$) this objects is closer with respect to PKS0530-727, hence it is used as phase calibrator as well. We report the schema (see Fig. 2.10) and the script (see Appendix A for the calibration at 2.1 GHz). However, during the two extra time slots used for providing a flux density reference (one between the two observing block at 2.1, 5.5–9 GHz and the other just before the observations at 18–24 and 33–38 GHz), we observed in both a bounce of program source objects and collect about ≈ 2 hr of parallactic angle coverage for PKS0530-727. In order to increase the signal to noise ratio, also refining the leakage calibration solutions, we perform a second step in the calibration, starting from the calibrated visibilities in each single observing slot at a given frequency. As it is possible to see from the diagram in Fig. 2.11 (and the script reported in the Appendix A), the first step is to merge all the data

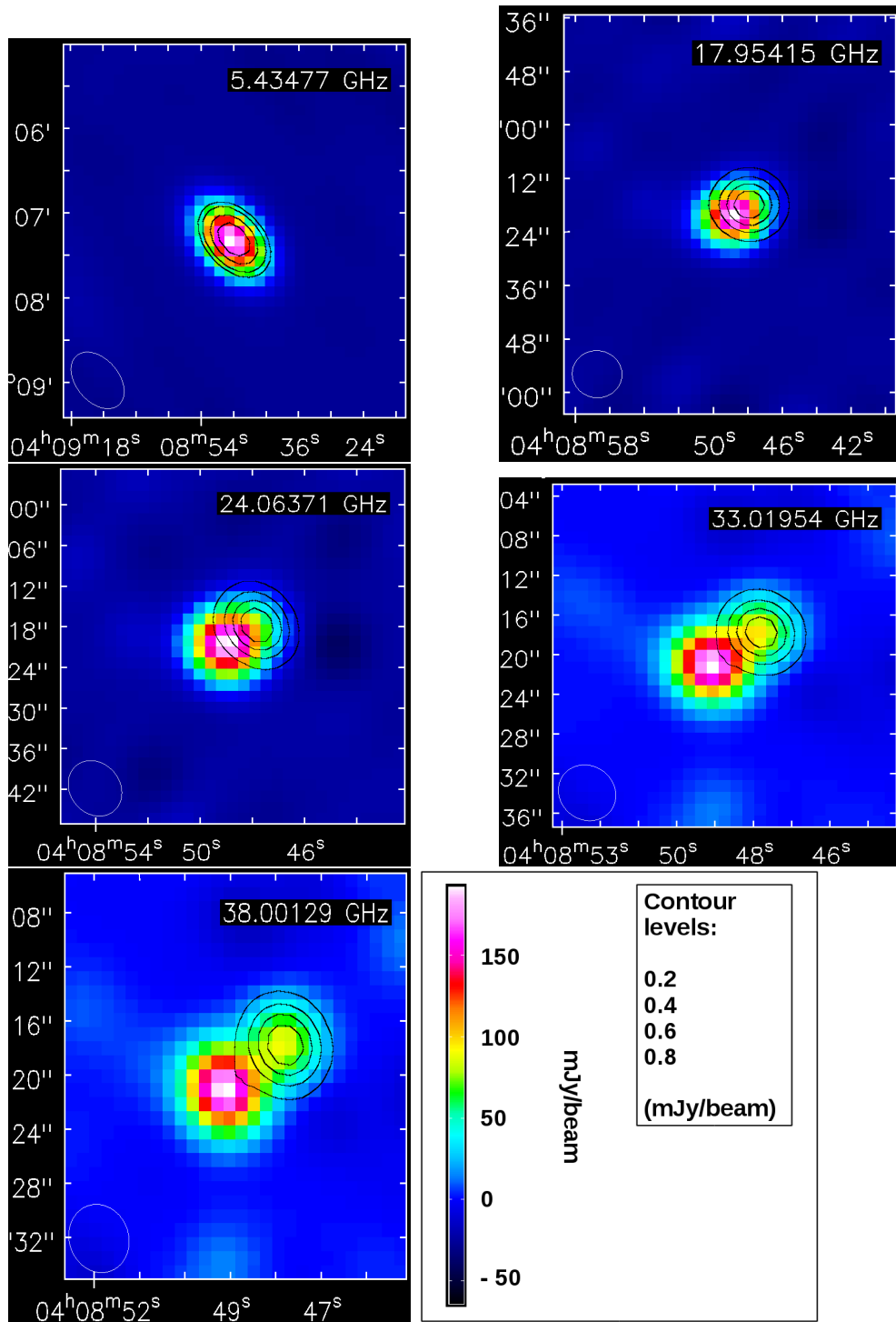


Figure 2.9: Maps in total intensity (*colours*) and polarization (*contours*) for AT20GJ0408-7507 at 5.5, 18, 24, 33 and 38 GHz. The two-lobe structure is resolved at the higher frequencies. The eastern lobe appears to be strongly depolarized.

coming from different slots which refer to a given object at a given frequency by using the MIRIAD task UVCAT. This concatenates visibilities after having applied the calibration tables on each chunk. Then, we run GPCAL on PKS0530-727 to produce new gain tables (complete of the leakage terms). As a further step, before applying solutions to targets, we rescaled again the flux densities with respect to PKS1934-638, as the GPCAL step might alter the previous flux density normalization. At the end, we apply the solutions from the phase and leakage calibrator PKS0530-727 to the scientific objects, eventually using PKS0537-441 (recalibrated with the upgraded leakage tables and renormalized to the absolute flux scale as well) when it results closer to a given source with respect to the first choice calibrator.

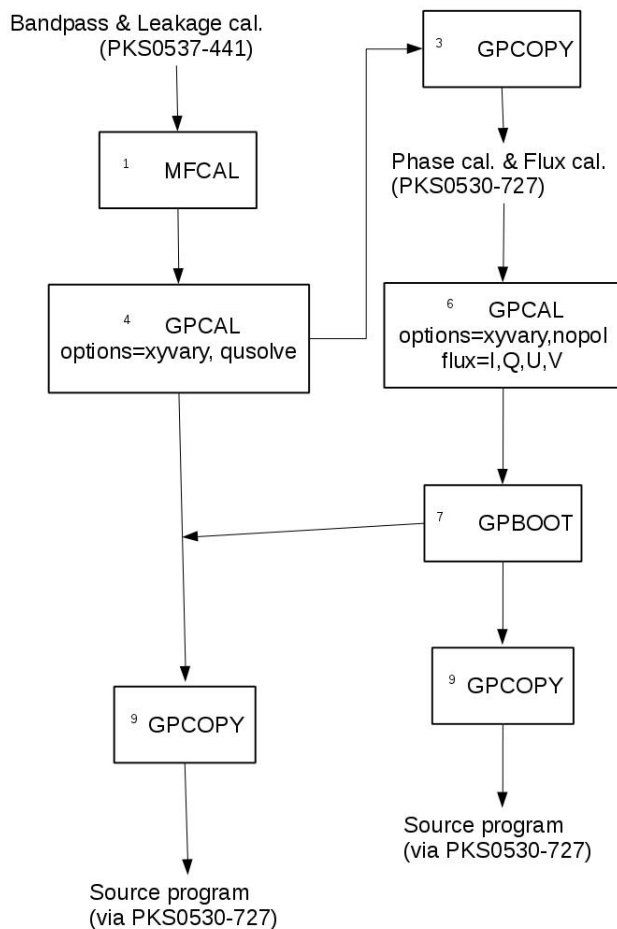


Figure 2.10: Diagram showing procedure of data reduction for the March and April 2016 campaign valid at each observing frequency and for each slot (cf. Tab. 2.1).

2.3.4 Intra-band depolarization

We have retained to split the 2 GHz CABB continuum bands into 1 GHz chunks in polarization: splitting data into smaller chunks permits to have more points to try to fit SEDs; it helps in putting into evidence problems like intra-band depolarization, which can be important to lower polarized fluxes,

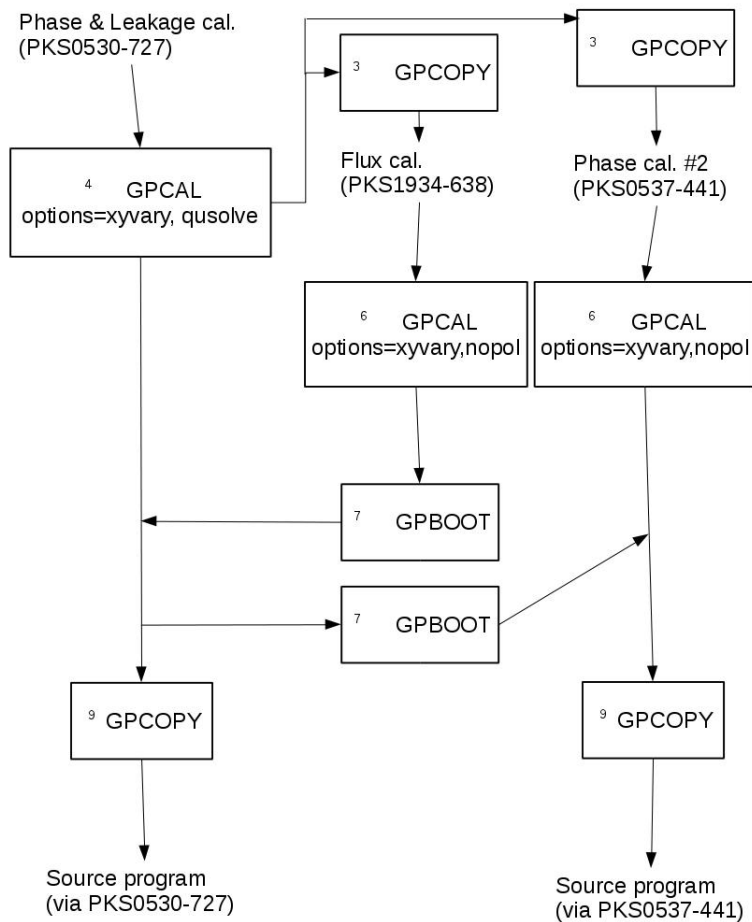


Figure 2.11: Diagram showing the scheme used to refine leakage solutions, once visibilities from different slots (but at the same frequency) are merged.

especially at lower frequency. However, since polarization fluxes of the considered sources can be as low as ~ 1 mJy, the splitting of each frequency in two chunks decreases the nominal sensitivity of 0.2 mJy of a factor $\sim \sqrt{2}$, thus it may prevent a 5σ detection for the minimum polarized flux expected (especially if we also take into account the channel flagging, which lowers the sensitivity even more). In our case we reach a good compromise both with detection rate and intra-band depolarization control. We plotted calibrated visibilities both for non-split and splitted data, and calculated (with relative comparison) polarization angles for each chunk of a given spectral window. As a confirmation, polarization fraction comparison between the two sub-bands at 5.5 GHz and 33 GHz are shown in Fig. 2.12.

2.4 July 2016 ATCA campaign at 33 and 35 GHz

During the March and April 2016 campaign we only manage to reobserve about 20% of the complete sample with $b < -75^\circ$ at 18–24 and 33–38 GHz.

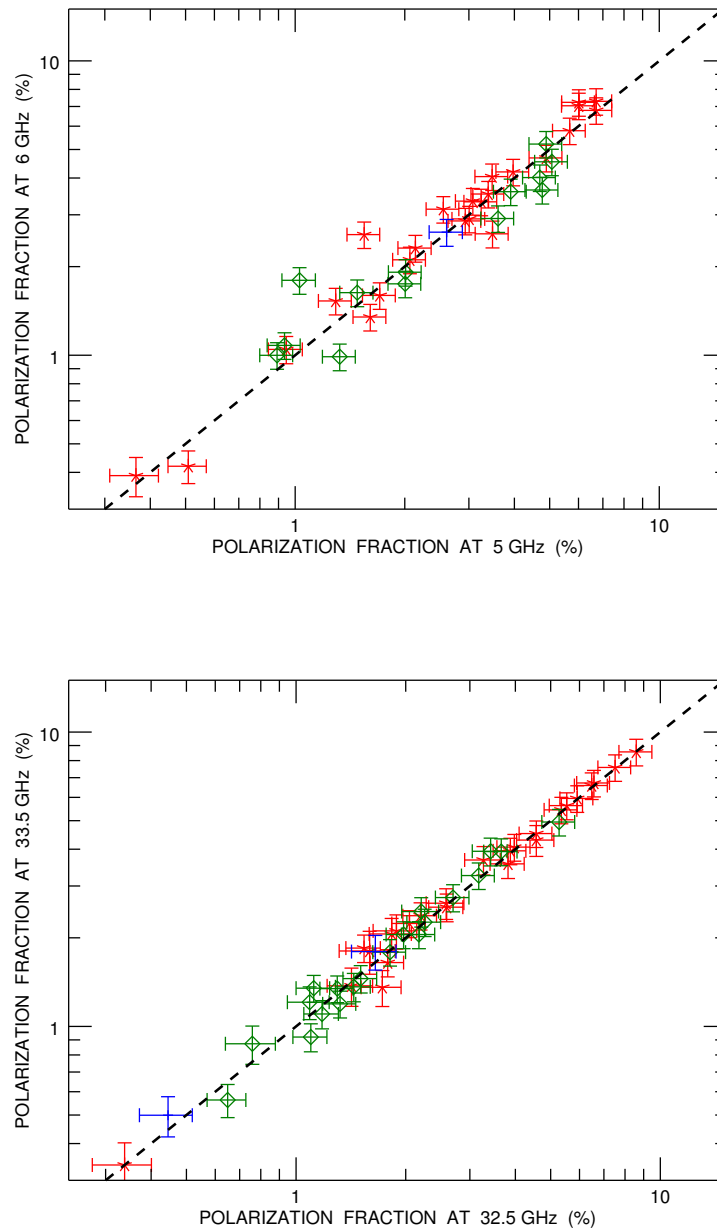


Figure 2.12: Comparison of the fractional polarization measured in the two 1 GHz-wide sub-bands of the 2 GHz-wide bands at 5.5 GHz (*top panel*) and at 33 GHz (*bottom panel*). Red asterisks, blue pluses and green diamonds refer to steep-spectrum, flat-spectrum and peaked-spectrum sources, respectively (the spectral classification is described in sec. 3.2.2). The bisector is shown as a dashed line.

Exploiting the occasion of another polarimetric project (C3085, PI: Massardi) observing in the same region at 33 – 35 GHz, we observed 35 objects of that sub-sample (between 3 h 40 min and 6 h 58 min). These observations are the closest in time with the ALMA campaign of September 2016, when a complete sample of 32 objects was observed. Since the latter were selected in the region $b < -75^\circ$, there are 20 objects with almost co-eval flux density measurements at 7 mm (33 – 35 GHz) and 3 mm (97.5 GHz). Among the other 12 sources left in the ALMA campaign, 10 were observed at 33 – 38 GHz during the March and April 2016 campaign. For this dataset we manage to use the updated recipe of the ATCA Users' Guide implementing the bandpass calibration on the object PKS1291-293, which is as bright as ≈ 3 Jy at these frequencies. Hence the data reduction scheme is the same we presented for September 2014 data.

2.5 ALMA observations and calibration

The observations were carried out by the end of September 2016 with ALMA (Cycle 3, ProjID: 2015.1.01522.S, PI:Galluzzi), at 4×2 GHz-wide spectral bands centered at 90.5, 92.5, 102.5 and 104.5 GHz, respectively, using a compact array configuration (baseline range 118 – 1318 m, corresponding to 4.8 – 0.3 arcsec at 97.5 GHz).

The complete sample is made of 32 objects drawn from the faint PACO sample in three circular regions with 10deg diameter that cover the $\sim 60\%$ of all the objects at $b < -75^\circ$. The area selection has been performed in order to have the largest statistically significant sample of sources already observed with ATCA in the smallest possible number of Science Goals (SG, see Fig. 2.14, showing the different complete samples studied in the present and previous papers for the PACO project), optimizing the use of ALMA time. In fact, each ALMA SG in Cycle 3 should include only objects within 10° from each other, so that they could share the same calibration. The calibration of each polarimetric SG requires at least 3 h in which target observations are interleaved with polarization calibrator ones for a complete characterization of the XY-phase offset as function of the parallactic angle.

We requested a sensitivity of $\sim 30 \mu\text{Jy}$, by fitting with a double power-law spectra between 5.5 and 38 GHz and extrapolating the ATCA spectra in total intensity and polarization up to 100 GHz for each source. A first execution was not enough to reach the requested sensitivity for our 3 SGs so that each scheduling block was executed twice with a resulting better uv coverage, thanks to the 39⁷ ALMA antennas available in Cycle 3 and to the 8GHz continuum bandwidth for each polarization. This allowed us a 3σ detection rate of 97% (just one non-detection). In Tab. 2.3 we summarize information about the three different epochs of observation for our project (each one corresponding to one SG).

The sources had been observed to be point-like up to 38 GHz and any

⁷For the data of our projects we have on average: 34, 38 and 37 unflagged antennas.

Table 2.3: Schematic informations about the ALMA campaign at 3 mm.

Epoch	SG	Array conf.	min.-max. scale (")	time on source (min)	th. sens. (μ Jy)
24/08/2016	1	C40-6	0.4 – 4.8	5.04	40
22/09/2016	3	C40-6	0.2 – 4.8	11.69	20
27/09/2016	2	C40-6	0.2 – 4.8	11.69	20

ALMA (standard) configuration was, in principle, suitable to achieve expected spatial resolution. During our observation it was $\simeq 0.3$ arcsec, about a factor $\simeq 10$ higher than ATCA observations at 38 GHz. While planning the observations it was conceived that a few sources might be resolved by the ALMA beam size. This possibility was considered in our flux density estimation approach and in some of the analysis described in the following sections.

2.5.1 Data reduction

ALMA data were reduced via the CASA software and delivered to the PI. All the 4 spectral windows frequency were treated together, as indicated by the CASA Users' Guide⁸. However, an expert PI might decide to recalibrate data, e.g. adopting a self-calibration approach to improve the signal-to-noise (S/N) ratio, hence reducing the rms in the calibrated image. In Tab. 2.4 we report the list of the calibrators visited during the ALMA campaign. The ALMA data reduction composes of two steps: a first one which corrects only the parallel hands products, i.e. XX and YY and the second one (needed in case of polarimetry) addressed to the cross product XY and YX and to the refinement of XX and YY gains. An intermediate step which prepare data outcoming from the first step for the second one is the task CONCAT, which first orders the visibilities of the same object but in different scan, then concatenate them. This is the CASA equivalent of MIRIAD UVCAT, but the latter simply concatenate data without ordering them.

Table 2.4: List of the calibrators visited during our ALMA observations.

Epoch	SG	Bandpass	Flux	Phase	Leakage
24/08/2016	1	J0635-7516	J0519-4546	J0715-6829	J0538-4405
22/09/2016	3	J0635-7516	J0519-4546	J0440-6952	J0522-3627
27/09/2016	2	J0635-7516	J0519-4546	J0715-6829	J0538-4405

In the scheme reported in Fig. 2.13 we sketch the step-by-step procedure for handling polarimetric ALMA data with CASA, stressing the two main phases. Once raw data are loaded, the distinct execution blocks are taken separately: in our case each execution block simply corresponds to a repetition of the *schedula* for a given SG. The first editing on the visibility is the *a priori* flagging, performed by using the task FLAGDATA: as an example,

⁸https://casaguides.nrao.edu/index.php/Main_Page

some scans in the data are used by the online system for pointing and side-band ratio calibration, hence are no longer needed and can be flagged easily by selecting visibilities with this “intent”. Autocorrelations can be flagged as well. In this respect it is to say that ALMA, as it looks at the mm and sub-mm window of the electromagnetic spectrum, needs a particular approach in calibrating for atmospheric effects (e.g. tropospheric water vapour induces phase delays) and the flagging of data can be much more easily influenced by bad atmospheric conditions and/or atmospheric lines than RFI, the latter typically affecting lower frequencies (e.g. the 16 cm band in ATCA data). Another aspect which might be more problematic in compact configurations, especially in arrays with a high number of antennas, is the shadowing: we have discussed it in the section dedicated to the ATCA observations since in few cases objects were not high enough on the horizon to avoid this problem. However, also in case of ALMA observations, the combination of minimum baseline about 200 m, the dish diameter of 12 m only (compared to the 22 m of ATCA) and the optimum scheduling minimizes this shortcoming.

After this preliminary flagging, there is the a priori calibration step, i.e. the T_{sys} (system temperature) and WVR (water vapour radiometer) calibration: the T_{sys} calibration provides a first-order correction for the atmospheric opacity as a function of time and frequency, hence associates weighting for each visibility which is maintained through imaging; the WVR corrections are provided by a remote sensing system (a 183 GHz absolutely calibrated radio receiver, i.e. “radiometer”) that measures the mm-wave emission from atmospheric water vapour from which the actual water vapour column along the line of sight of each telescope in the array. Thus the induced path delay, which can be applied as a phase rotation to the observed visibilities are applied to each antenna. An important feature of CASA is that calibration tables are only computed by the corresponding task, but they are not applied until with another task explicitly does so. At this stage a further data inspection for flagging is common practice not only for eliminating bad data that might hamper the calibration process, but also to eliminate data no longer needed, such as those collected for preliminary atmospheric calibration.

The next step is to proceed with the “real” calibration, in the sense it demands observations of dedicated sources. The procedure for handling total intensity data consists in the standard series of procedures reported by the CASA Guide⁹ to determine bandpass solutions (after a preliminary phase correction to reduce loss of signal due to phase decorrelation), gains and (once a model is loaded for the flux calibrator) flux rescaling. Instead, the second calibration block also involving the cross products XY and YX is still under refinement (e.g., to ensure leakage corrections accurate to the 2th order for future Stokes’ V studies). The steps we briefly present now have only been released few years ago in the CASA Guide and refinements is still ongoing. The schematic sequence is:

1. gain calibration of the polarization calibrator;

⁹https://casaguides.nrao.edu/index.php/Main_Page

2. rough estimate of the source polarization;
3. cross-hand delay phase calibration;
4. revise cross-hand phase and QU-sign ambiguities;
5. revise gain calibration using the source polarization model;
6. instrumental polarization (D-term) calibration;
7. correct the X/Y gain ratio.

The first GAINCAL (the CASA task devoted to gain calculations) call in this list served the purpose of determining gain solutions on the polarization calibrators by assuming a starting model with $I = 1$ and all the other Stokes' parameters set to zero. Then, a first guess of ratios Q/I and U/I parameters is obtained from these gains (step 2). Another GAINCAL is needed (step 3), but in the "KCROSS" mode, i.e. to determine the frequency-dependent XY phase difference for the reference antenna. However, the KCROSS solution accounts for any linear phase slope in the phase bandpass only and there is typically a residual non-linear phase bandpass shape in the XY-phase. Correcting for this is necessary to extract correct Stokes parameters. Again a GAINCAL (this time ran in the mode "XYf+QU") allows to do this (step 4): the remaining Q and U sign ambiguity can be solved by taking into account preliminary Stokes's parameters estimation (at step 2). At this stage we have a model for the polarization calibrator, hence gains can be revised also correcting for the parallactic angle effect (step 5). The instrumental polarization (leakage terms) can now be determined by using the task POLCAL (step 6). In all the steps performed till now for polarization calibration we have assumed that X/Y gain amplitude ratio for each antenna is exactly 1, but actually deviations up to 10% are considered normal, while mismatches $> 15\%$ are signs that the affected antennas are likely to be flagged. Thus, a final run of GAINCAL (step 7) in the amplitude mode only is used to fix this issue. The very final step is to apply all the determined calibration tables on the target we want to study.

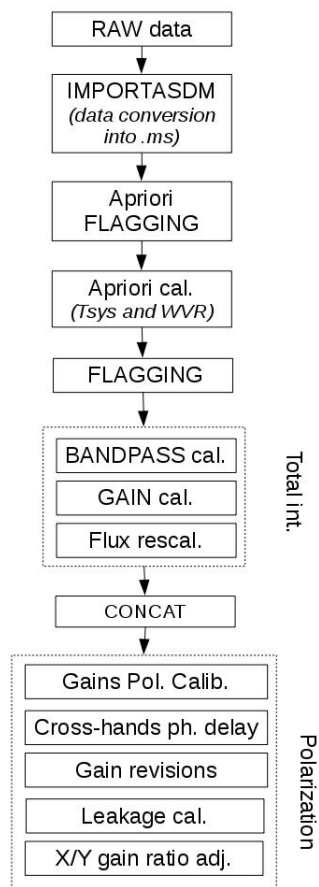


Figure 2.13: Sketch of ALMA full-Stokes calibration (cf. CASA Guide).

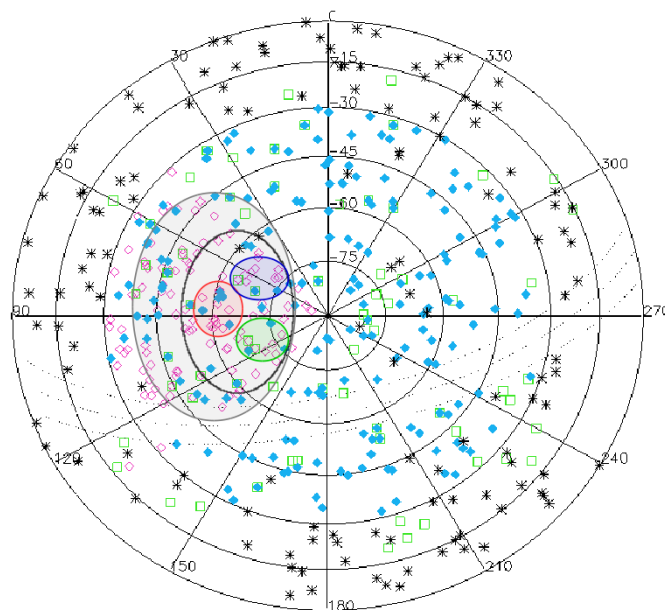


Figure 2.14: Polar plot showing the distribution of the complete PACO sample. The black solid curve surrounds the sample observed in September 2014, the grey one the extension of March and April 2016. The red, blue and green areas are for each SG of ALMA observations.

Chapter 3

Centimetric band multi-frequency characterization of polarimetric and total intensity behaviour of radio sources

We present here the analysis of high sensitivity ($\sigma_P \simeq 0.6$ mJy) polarimetric observations in seven bands, from 2.1 to 38 GHz, of this complete sample of 104 compact extragalactic radio sources. Because of Doppler boosting we expect the sample to be dominated by blazars, i.e. FSRQs and BL Lacs and the observed compactness of these objects can be considered as a first confirmation. However, in order to better quantify the blazar population we cross-matched our catalogue with the last available Fermi catalogue for AGNs (the third version, named “3LAC”). We found that 34 ($\simeq 32\%$ of the sample) objects present a detected gamma emission: 17 are classified as FSRQ, only 5 are the BL Lacs and Pictor A core is labeled as radio galaxy. The remaining 11 objects are not identified (labeled as “bcu_II” in the catalogue) since the absence of any spectral feature (e.g. spectral lines in optical band) prevent any conclusion about their location into the blazar family.

By looking at the lower frequencies, 89 of our sources have a counterpart in the 72 to 231 MHz GLEAM survey (Hurley-Walker et al. 2017), hence we provide an unprecedented spectral coverage of 2.7 decades of frequency for these sources. These results have been published in Galluzzi et al. (2017) and Galluzzi et al. (2018).

3.1 Stokes parameters (and related quantities) estimations

As discussed in chapter 2, data were reduced via the MIRIAD software (Sault et al. 1995). Each frequency band was treated separately, as indicated in the ATCA Users’ Guide¹. In order to better characterize the source spectra,

¹www.narrabri.atnf.csiro.au/observing/users_guide.

we decided to split each 2 GHz-wide frequency band in sub-bands, except for the 2.1 GHz one that was kept un-split because of the heavy RFI contamination. Each sub-band was calibrated separately. For total intensity, we split each band into 512 MHz-wide sub-bands. For polarized flux densities we split bands in only 2 sub-bands to limit the $\Delta\nu^{-1/2}$ degradation in sensitivity. Flux densities were estimated via the MIRIAD task UVFLUX. Our sources are known to exhibit linear polarization (up to $\sim 10\%$; Massardi et al. 2008, 2013), defined by the Q and U Stokes parameters. Observations of the circular polarization of extragalactic radio sources demonstrated that it is generally below 0.1 – 0.2%, at least one order of magnitude lower than the linear polarization (Rayner et al. 2000). Hence, the rms σ_V of the retrieved Stokes V parameter is frequently used as a noise estimator.

We achieved a 5σ detection of circular polarization, V , in $\sim 38\%$ of the dataset, i.e. $\sim 89\%$ of the objects are detected in Stokes V in at least at one frequency. Further discussion about the circular polarization is in subsect. 3.3.3. For only $\sim 15\%$ of detections, the circular to linear polarization ratio is $\geq 20\%$; the mean circular polarization is substantially smaller than our calibration error of the polarized flux density, which is $\simeq 10\%$ (Galluzzi et al. 2017). Since the contribution of Stokes V is so small, the polarized emission, P , can be estimated neglecting the V contribution and adopting σ_V as the rms noise for the Stokes parameters Q and U :

$$P = \sqrt{Q^2 + U^2 - \sigma_V^2}. \quad (3.1.1)$$

The σ_V^2 term removes the noise bias on P (e.g. Wardle & Kronberg 1974).² We find that ignoring the σ_V term in eq. (3.1.1) results in a mean error of 0.01%.

The polarization angle ϕ and fraction m (usually in terms of a percentage) are:

$$\phi = \frac{1}{2} \arctan\left(\frac{U}{Q}\right), \quad (3.1.2)$$

$$m = 100 \cdot P/I, \quad (3.1.3)$$

where the Stokes I is the total intensity flux density. The errors in total intensity, linear polarization flux density and position angle were computed as in (Galluzzi et al. 2017, , details are reported in the next sub-section), i.e. adopting calibration errors of 2.5% for I and of a conservative 10.0% for the polarization fraction, P , for data between 5.5 and 38 GHz. At 2.1 GHz, due to the mentioned RFI issues, we use a 5% in I and a 12.5% in P as calibration errors. Under the assumption of equal calibration errors for Q and U , Galluzzi et al. (2017) reported a $\simeq 3^\circ$ calibration error in the polarization position angle (3.75° at 2.1 GHz). For circular polarization we again assumed a 10% (12.5% at 2.1 GHz) calibration error (i.e. a factor $\simeq \sqrt{2}$ larger than the calibration errors associated to Q and U). We note however that, due to the weakness of

²The error associated to the bias correction is negligible and will be ignored in the following.

the signal and the corresponding lack of good calibrators, the calibration error for V is very difficult to estimate.

In order to check the assumption about the equally-spread calibration error between Stokes' Q and U , we compare the distributions for σ_Q , σ_U and σ_V over the whole ATCA dataset. Here we provide details about average values about σ_Q , σ_U and σ_V :

$$\begin{aligned}\sigma_Q &= (0.00125 \pm 0.00014) \text{ Jy} \\ \sigma_U &= (0.00134 \pm 0.00023) \text{ Jy} \\ \sigma_V &= (0.00062 \pm 0.00023) \text{ Jy}\end{aligned}$$

3.1.1 Error budget

Assuming Gaussian noise, the error scales as $1/\sqrt{N}$, N being the number of correlations at a given ν . A suitable estimate of the total intensity error is the sum in quadrature of σ_V with a systematic term, mainly accounting for the calibration uncertainty. Based on the past experience with PACO observations and on a comparison between flux densities obtained from different calibrators, the calibration error amounts to $\sim 2.5\%$ of the I flux density, giving for σ_I , the global error on I :

$$\sigma_I^2 = \sigma_V^2 + (0.025 I)^2. \quad (3.1.4)$$

The error, σ_P , on the polarized flux density, P , can be derived from the eq. (3.1.1). A conservative $\sim 10\%$ error in the polarization calibration is adopted in this case. Then, we have:

$$\sigma_P^2 = \frac{Q^2 \sigma_Q^2 + U^2 \sigma_U^2}{Q^2 + U^2} + (0.1 P)^2, \quad (3.1.5)$$

$\sigma_{Q,U}$ being the rms errors on the Stokes parameters Q and U , respectively. This estimate of the calibration error is consistent with the differences between flux densities obtained using two different calibrators for reducing our data.

From error propagation, the global error on the polarization fraction is:

$$\sigma_m^2 = \left(\frac{\sigma_I}{I}\right)^2 + \left(\frac{\sigma_P}{P}\right)^2, \quad (3.1.6)$$

and that on ϕ is:

$$\sigma_\phi^2 = \frac{Q^2 \sigma_U^2 + U^2 \sigma_Q^2}{4(Q^2 + U^2)^2} + \sigma_{\phi \text{CAL}}^2, \quad (3.1.7)$$

where, again, the calibration error on the polarization angle, $\sigma_{\phi \text{CAL}}$, is added in quadrature. Under the hypothesis that the calibration error equally affects the Q and U parameters ($\sigma_{Q \text{CAL}} \simeq \sigma_{U \text{CAL}} = \sigma_{\text{CAL}}$), $\sigma_{P \text{CAL}} \simeq 0.1P$ gives $\sigma_{\text{CAL}} = 0.1P/\sqrt{2}$. Finally:

$$\sigma_{\phi \text{CAL}}^2 \simeq \frac{1}{4(Q^2 + U^2)} 2\sigma_{\text{CAL}}^2 \simeq (0.05 \text{ rad})^2, \quad (3.1.8)$$

implying $\sigma_{\phi \text{CAL}} \simeq 3^\circ$. This estimation turns out to be consistent with differences in the polarization angle obtained by using different calibrators.

3.2 Data analysis

We adopt a 5σ level for detections in polarization. The median error is $\simeq 0.6$ mJy. We reach a detection rate of $\simeq 90\%$ for all the sources at all frequencies from 5.5 to 38 GHz. The number of detections is nearly uniform across the observed frequencies (99 sources detected at 5.5 GHz and 94 at 38 GHz). Following Galluzzi et al. (2017, their Figure 1) we checked the level of intra-band depolarization in this frequency range, by subdividing each 2 GHz-wide band into 1 GHz-wide sub-bands. No systematic differences were found with respect to the previous assessment. At 2 GHz, due to the impact of RFI, we cannot proceed with this check, and the detection rate decreases to $\simeq 86\%$. Three of our 107 observations include the extended source Pictor A. These observations were discarded from the following analysis that therefore deals with 104 compact (according to AT20G at 20 GHz) objects.

3.2.1 Fit procedures

To properly fit source spectra in total intensity, we start considering a double power law represented by the expression

$$S(\nu) = \frac{S_0}{\left(\frac{\nu}{\nu_0}\right)^{-a} + \left(\frac{\nu}{\nu_0}\right)^{-b}}, \quad (3.2.1)$$

or by a concave version of it (needed in two cases)

$$S(\nu) = S_0 \left(1 - \frac{1}{\left(\frac{\nu}{\nu_0}\right)^{-a} + \left(\frac{\nu}{\nu_0}\right)^{-b}} \right), \quad (3.2.2)$$

where S_0 , ν_0 , a and b are free parameters. This function properly fits the total intensity data in $\simeq 96\%$ of the cases, confirming what found in previous works (e.g. Massardi et al. 2016). In two cases (sources AT20GJ0546-6415 and AT20GJ0719-6218) the double power law provided a poor fit and we resorted to a triple power law model which requires 3 additional parameters, i.e. S_1 , ν_1 and c :

$$S(\nu) = \frac{S_0}{\left(\frac{\nu}{\nu_0}\right)^{-a} + \left(\frac{\nu}{\nu_0}\right)^{-b}} + \frac{S_1}{\left(\frac{\nu}{\nu_1}\right)^{-b} + \left(\frac{\nu}{\nu_1}\right)^{-c}}. \quad (3.2.3)$$

For fitting procedures in polarization, we adopted the same model in eqs. (3.2.1)–(3.2.3). We required detections at no less than 5 frequencies (over a maximum of 12) in case of a double power law and at no less than 8 frequencies for a triple power law. If a point source was not detected in one (or both) of the split frequency ranges of a band, we used the corresponding non-split detection, when available. Given the small fraction (less than 10%) of non-detections we did not consider the upper limits in doing the spectral fits. About 85% of all the spectra (both in total intensity and in polarization) could be successfully fitted in this way. In only three cases (AT20GJ041239-833521,

Table 3.1: Distribution of sources per spectral type in total intensity and in polarization. The row “NA” refers to the three objects classified in total intensity but missing a spectral fit in polarization. The last row reports the total for a given spectral class in total intensity, while the last column does the same in polarization.

Tot. Int. →	(In)	(Pe)	(F)	(S)	(U)	
Pol. Int. ↓						
(In)	0	3	0	1	0	4
(Pe)	0	24	4	20	0	48
(F)	0	5	4	4	0	13
(S)	0	5	8	7	0	20
(U)	0	8	5	3	0	16
(NA)	0	1	1	1	0	3
	0	46	22	36	0	

AT20GJ054641-641522, AT20GJ062524-602030), we do not have detections in polarization at enough frequencies to get a proper fit.

Similarly to what was found for the earlier sample, most (68%) of our source spectra in polarization could be fitted with a double power-law downturning at high frequencies. An upturning double power-law was required in 15 cases, and a triple power-law in 20 cases. The median values of the reduced χ^2 are 1.12 and 1.89 for Stokes I and P , respectively. The spectra for all the sources are presented in Figure 3.1. The fitting curves and, when available, the previous PACO best epoch (2009 – 2010) observations in total intensity, and the AT20G best epoch (2004-2008) observations in total intensity and in polarization are also presented. In the lower part of each panel we show the polarization fractions (both linear and circular, when detected), followed by the polarization position angles at the different frequencies.

3.2.2 Spectral properties of the sample

The spectral index $\alpha_{\nu_1}^{\nu_2}$ between the frequencies ν_1 and ν_2 is defined as:

$$\alpha_{\nu_1}^{\nu_2} = \frac{\log(S(\nu_2)/S(\nu_1))}{\log(\nu_2/\nu_1)}, \quad (3.2.4)$$

where $S(\nu_1)$ and $S(\nu_2)$ are the flux densities associated to the two frequencies. With respect to the previous work (Galluzzi et al. 2017) we simply add the 2.5 GHz to the reference frequencies 5.5, 10, 18, 28 and 38 GHz in order to preserve the equal spacing in logarithmic scale. Then, we proceed as usual for the spectral classification, taking into account $\alpha_{2.5}^{5.5}$ and α_{28}^{38} and distinguishing in flat- (F), steep- (S), peaked- (Pe), inverted- (In) and upturning-spectrum (U) object. The choice of these frequency intervals follows from the fact that the majority of spectral peaks occur around 10 – 20 GHz.

We defined as flat-spectrum (F) sources those with $-0.5 < \alpha_{2.5}^{5.5} < 0.5$ and $-0.5 < \alpha_{28}^{38} < 0.5$. Sources outside these spectral index ranges were sub-divided as:

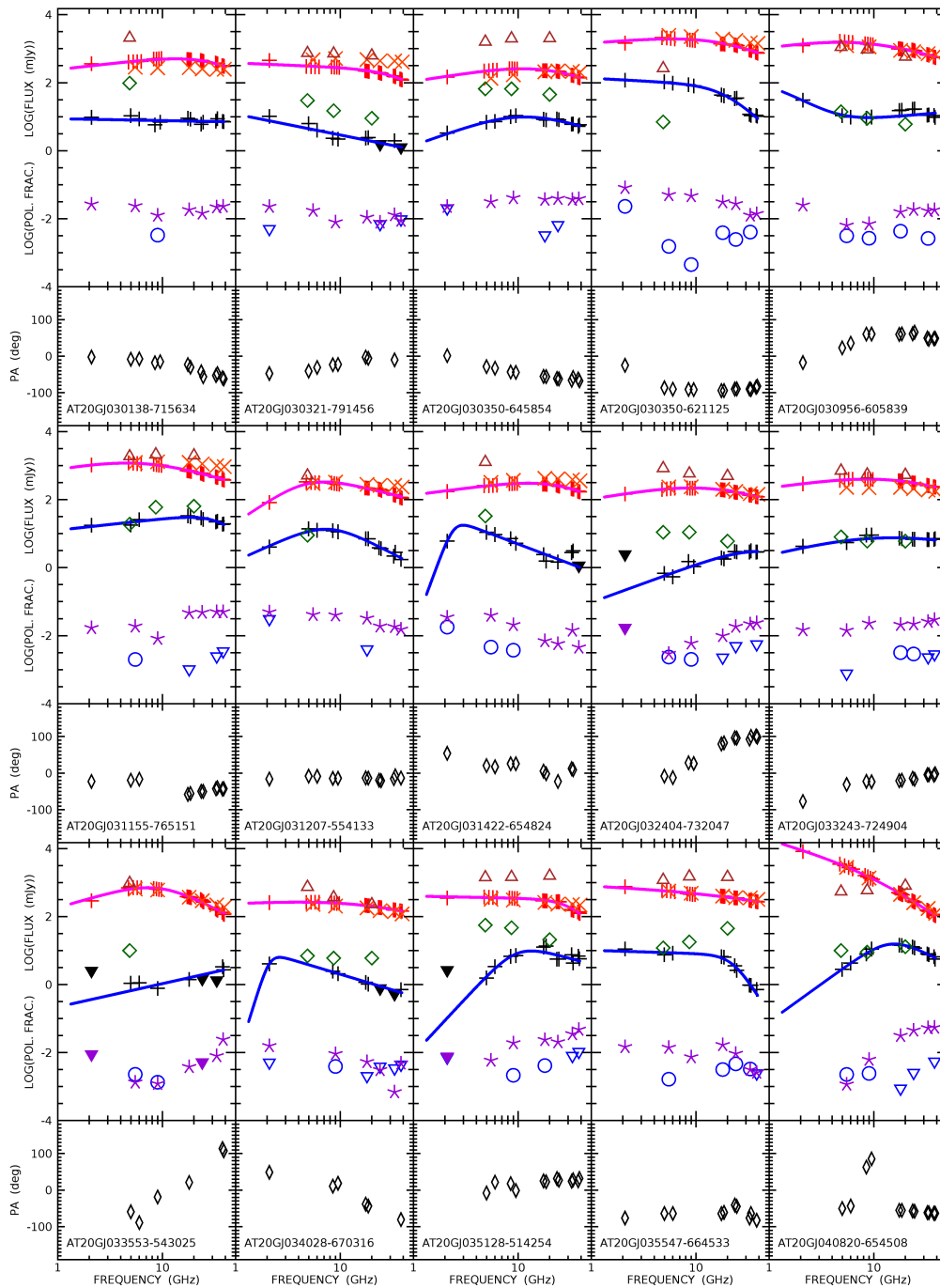


Figure 3.1: Spectra in total intensity and polarization, polarization fraction and polarization angle for the 104 objects of the faint PACO sample, observed in the September 2014 and March-April 2016 campaigns. The error bars are not displayed since they are smaller than the symbols. **Total intensity:** red pluses indicate our observations and the solid magenta lines show the fitting curves. The orange crosses show the median PACO flux densities (July 2009-August 2010) while the brown triangles represent the AT20G observations (best epoch in 2004-2008). (*Continued...*)

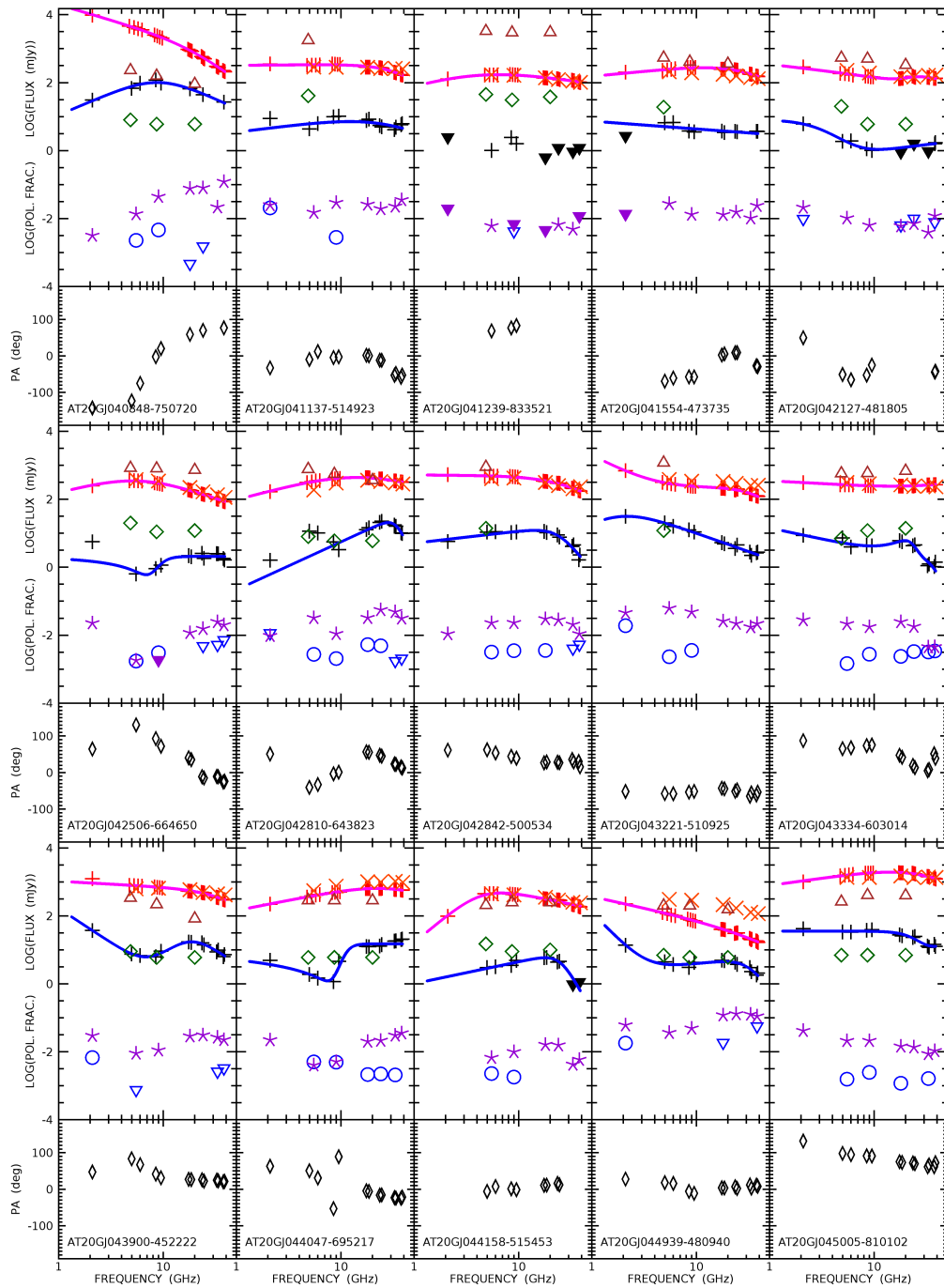


Figure 3.1: (*Continued*). **Polarization (flux density)**: black pluses refer our observations. Upper limits are shown as black filled downwards triangles. The solid blue lines indicate the best fit curves. The AT20G observations (best epoch in 2004-2008) are represented by green diamonds. (*Continued...*)

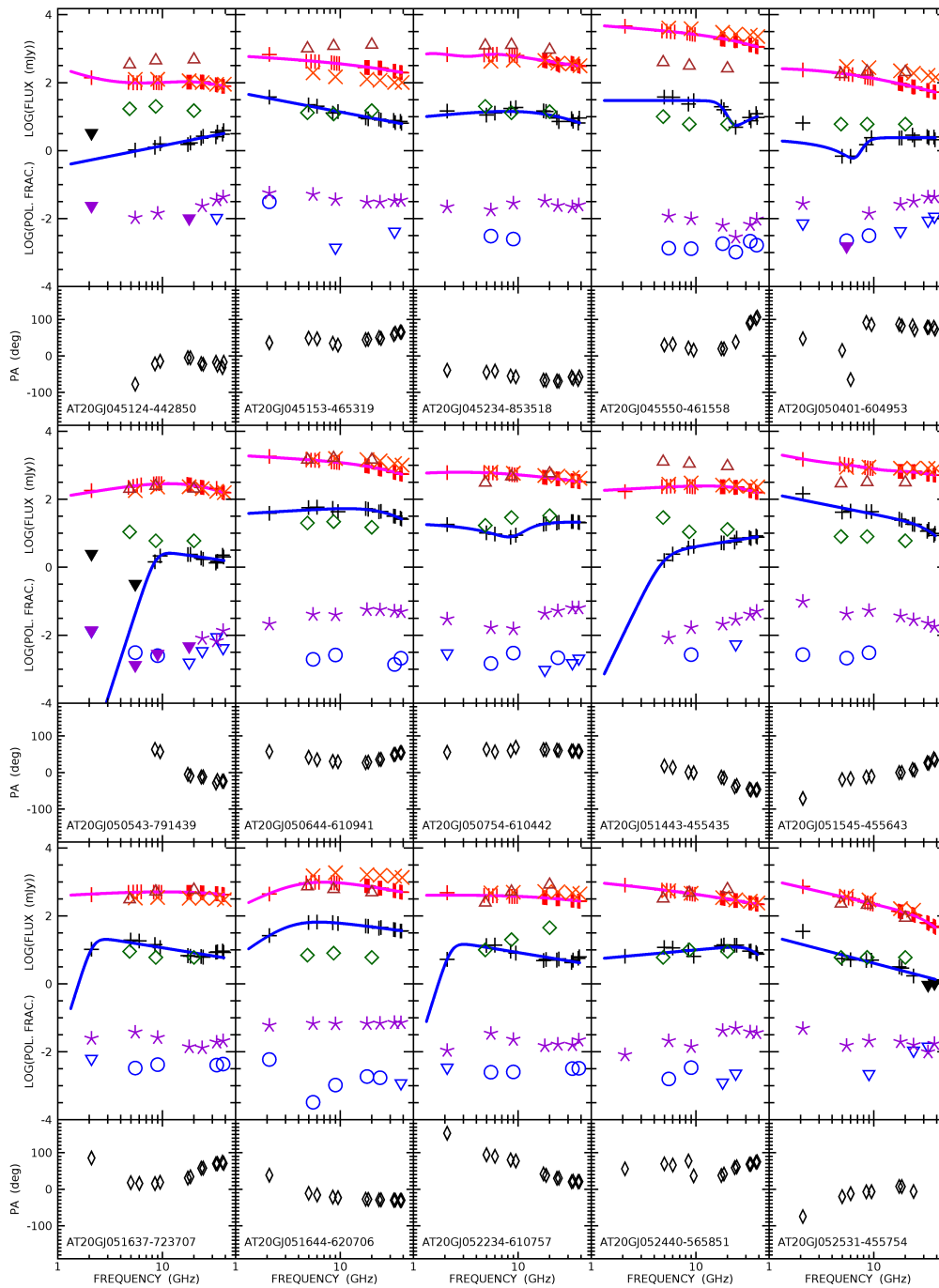
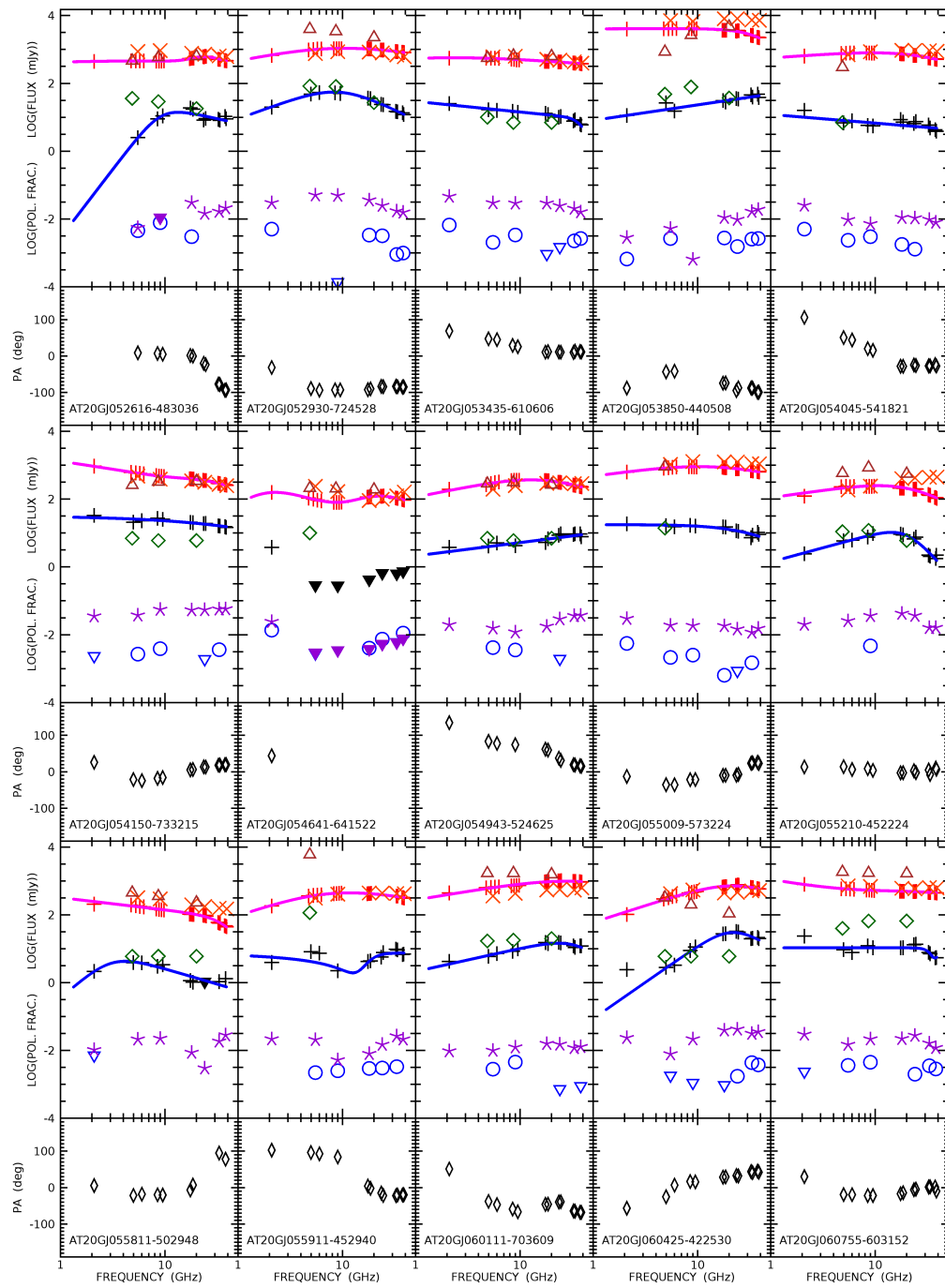


Figure 3.1: (*Continued*). Other quantities available only for the September 2014 and March-April 2016 campaigns: **linear polarization fractions**: purple asterisks with upper limits shown as downwards pointing purple filled triangles; **circular polarization fraction**: blue circles and downward triangles for upper limits. **Polarization angle (PA)**: black diamonds.

Figure 3.1: *Continued.*

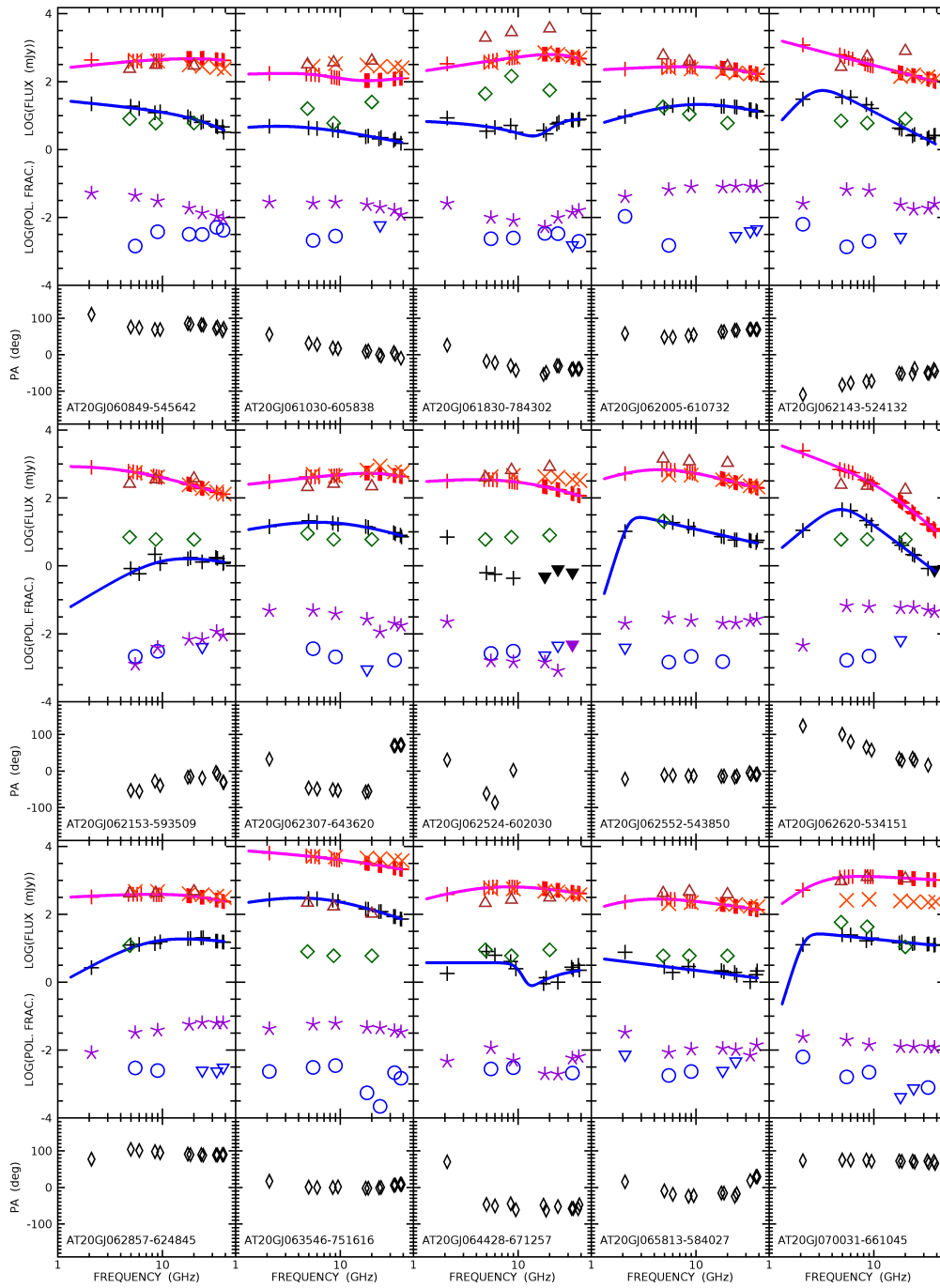
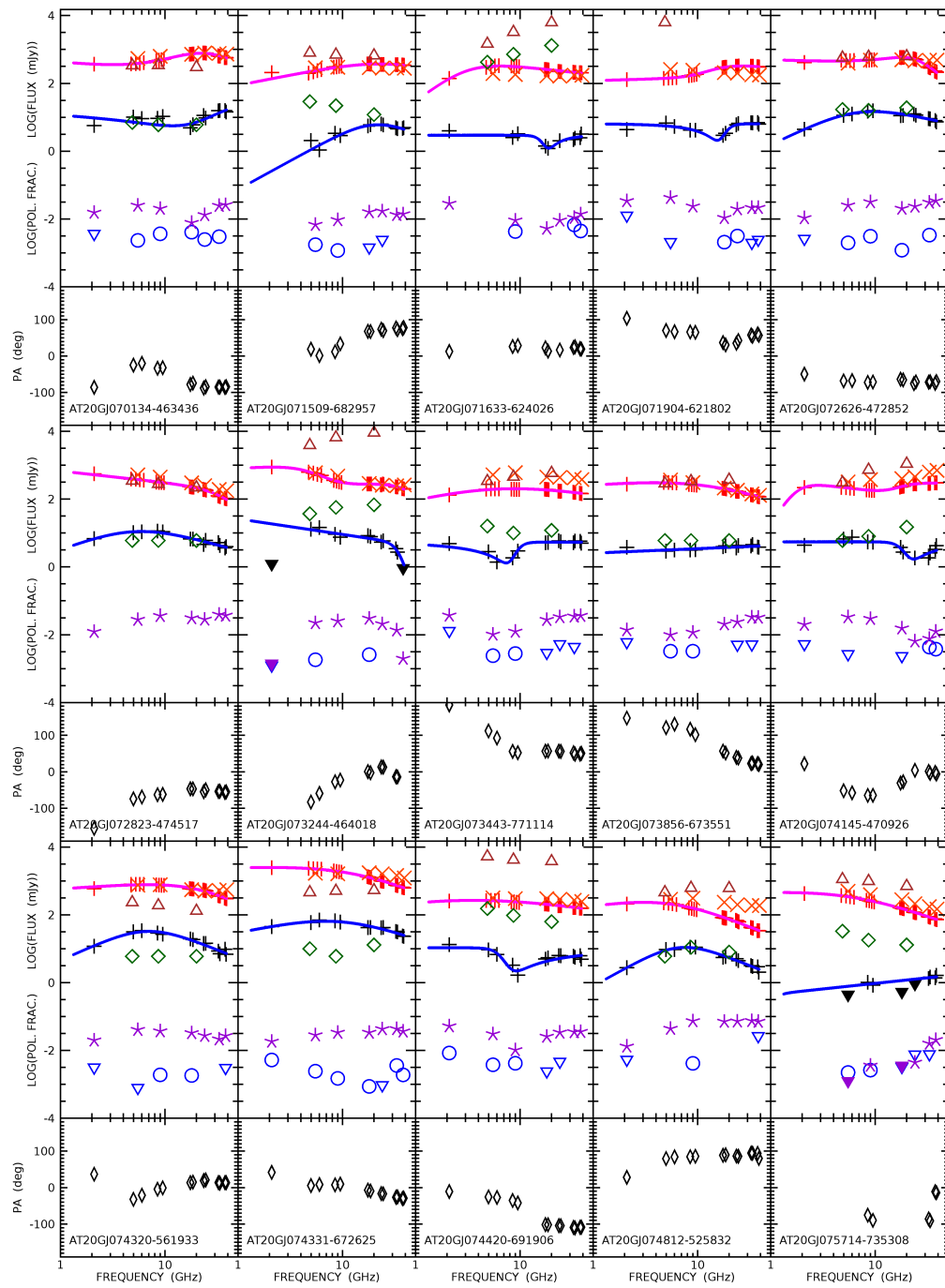


Figure 3.1: *Continued.*

Figure 3.1: *Continued.*

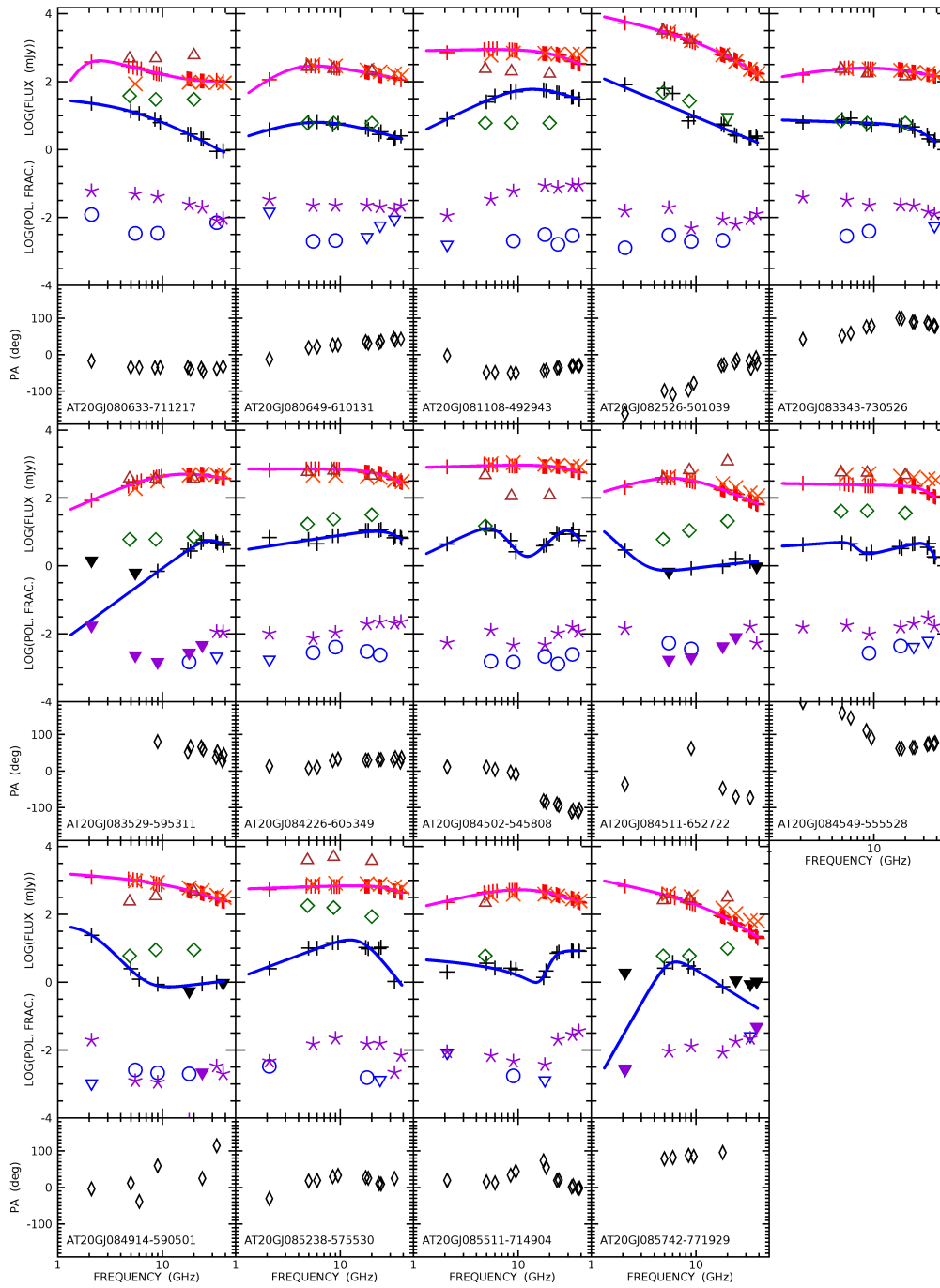


Figure 3.1: *Continued.*

Table 3.2: First, second (median), and third quartiles of spectral indices in total intensity and in polarization for different frequency ranges. We give values for the full sample and for the two main spectral classes, as classified in total intensity.

Tot. Int.	2.5 – 5.5			5.5 – 10			10 – 18 GHz		
Quart.	Q1	Q2	Q3	Q1	Q2	Q3	Q1	Q2	Q3
All	-0.29	-0.02	0.31	-0.35	-0.11	0.09	-0.46	-0.24	-0.08
Steep	-0.64	-0.33	-0.13	-0.67	-0.37	-0.22	-0.80	-0.46	-0.30
Peaked	0.10	0.32	0.54	-0.04	0.06	0.27	-0.30	-0.14	0.01
Flat	-0.16	-0.01	0.27	-0.25	-0.12	0.06	-0.26	-0.14	-0.05

Tot. Int.	18 – 28			28 – 38 GHz		
Quart.	Q1	Q2	Q3	Q1	Q2	Q3
All	-0.75	-0.46	-0.27	-1.00	-0.75	-0.44
Steep	-0.91	-0.76	-0.56	-1.56	-1.02	-0.81
Peaked	-0.56	-0.42	-0.28	-0.85	-0.74	-0.56
Flat	-0.33	-0.26	0.09	-0.42	-0.34	-0.20

Pol. Int.	2.5 – 5.5			5.5 – 10			10 – 18 GHz		
Quart.	Q1	Q2	Q3	Q1	Q2	Q3	Q1	Q2	Q3
All	-0.28	0.15	0.85	-0.43	-0.06	0.38	-0.61	-0.15	0.34
Steep	-0.46	0.33	0.61	-0.59	-0.06	0.33	-0.74	-0.24	0.29
Peaked	-0.06	0.49	1.04	-0.19	-0.01	0.71	-0.35	-0.06	0.36
Flat	-0.57	-0.21	-0.06	-0.54	-0.29	-0.06	-0.59	-0.33	0.54

Pol. Int.	18 – 28			28 – 38 GHz		
Quart.	Q1	Q2	Q3	Q1	Q2	Q3
All	-0.98	-0.53	0.02	-1.44	-0.80	-0.03
Steep	-1.00	-0.76	-0.10	-1.47	-0.92	-0.37
Peaked	-0.80	-0.32	0.31	-1.21	-0.73	-0.23
Flat	-1.01	-0.54	0.14	-1.61	-0.68	0.04

- steep-spectrum (S), if $\alpha_{2.5}^{5.5} < 0$ and $\alpha_{28}^{38} < 0$;
- inverted-spectrum (In), if $\alpha_{2.5}^{5.5} > 0$ and $\alpha_{28}^{38} > 0$;
- peaked-spectrum (Pe), if $\alpha_{2.5}^{5.5} > 0$ and $\alpha_{28}^{38} < 0$;
- upturning-spectrum (U), if $\alpha_{2.5}^{5.5} < 0$ and $\alpha_{28}^{38} > 0$.

We populate the Tab. 3.1 with the outcome of the classification performed in total intensity and polarization, while we report the quartiles of distributions of spectral indices in Tab. 3.2. Less than 40% of sources have the same spectral behaviour in total intensity and in polarization, and high- and low-frequency spectral indices are essentially uncorrelated, as shown in Fig. 3.2. The most populated entries of Tab. 3.1 are sources peaking both in total intensity and polarization and sources which are steep-spectrum in total intensity but have a spectral peak in polarization. This change in spectral shape toward

a peaked- or even an upturning-spectrum in polarization might be the sign of Faraday depolarization which typically lowers the polarization signal at lower frequencies.

Galluzzi et al. (2017) pointed out that past high frequency flux density measurements may suffer from the low accuracy of the model for the primary calibrator. In fact, they found that the mean high-frequency spectral index of “PACO faint” sources in total intensity reported by Bonavera et al. (2011) was flatter by $\delta\alpha \sim 0.3$. In this work we used the new model for the primary calibrator (PKS 1934-638) now encoded into MIRIAD. Since the model was not implemented yet, Galluzzi et al. (2017), instead, applied a-posteriori corrections.

The differences with the results by Galluzzi et al. (2017) are relatively small. We confirm that the high-frequency spectral indices in total intensity and in polarization steepen at high frequencies and are essentially uncorrelated, although the mean values ($\alpha_{28}^{38} \simeq -0.75$ and $\alpha_{p28}^{38} \simeq -0.80$, respectively) are less steep and closer to each other than found by Galluzzi et al. (2017). The distribution of sources among the different spectral types is also very similar; the biggest difference is in the fraction of objects classified as flat-spectrum in total intensity that increases from $\simeq 4\%$ to $\simeq 21\%$.

3.3 GLEAM counterparts

To extend the spectral coverage we have exploited the information provided by the GLEAM (GaLactic and Extragalactic All-sky Murchison Wide-field Array) survey at 20 frequencies between 72 and 231 MHz (Hurley-Walker et al. 2017). The spatial resolution is $\simeq 2$ arcmin at 200 MHz, similar to the ~ 90 arcsec resolution of our 2.1 GHz observations. We have 89 matching sources ($\simeq 86\%$ of our sample) in the GLEAM survey. For these sources we have the unparalleled coverage of 2.7 decades in frequency. Since the GLEAM survey covers all the sky south of $+30^\circ$ in declination with a mean sensitivity of ~ 10 mJy, and our sample is located between -86° and -42° , we can associate an upper limit of 50 mJy (at 5σ) to those sources without a GLEAM counterpart.

The fitting curves (triple power-laws), although not always successful, generally show a good consistency between the ATCA and GLEAM measurements (cf. Fig. 3.1). But while in the range 5.5 GHz – 38 GHz the spectra are consistent with a single emitting region (Galluzzi et al. 2017), the GLEAM flux densities are clearly above the extrapolations from higher frequencies in $\sim 40\%$ of the cases, strongly suggesting the presence of at least another, generally steeper, component. The joint analysis with polarization data suggests even more complex structures (cf. Farnes et al. 2014, see sub-sec. 3.3.1).

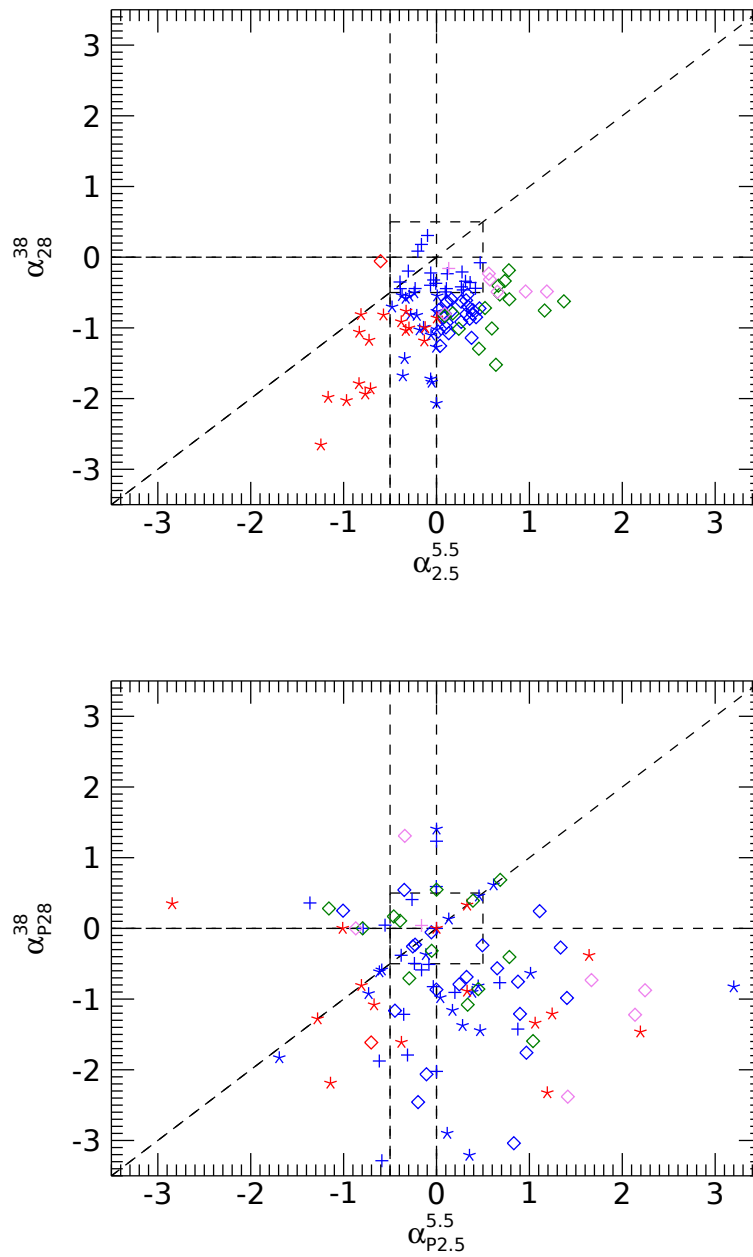


Figure 3.2: Radio colour-colour diagrams for (*from top to bottom*) total intensity and polarized flux density. Symbols identify the spectral type in total intensity: pluses for flat-spectrum, asterisks for steep-spectrum, diamonds for peaked-spectrum. Colours refer to the spectral shape between 2.5 and 18 GHz: red for steep-spectrum, blue for flat-spectrum, green for peaked-spectrum and violet for inverted-spectrum sources.

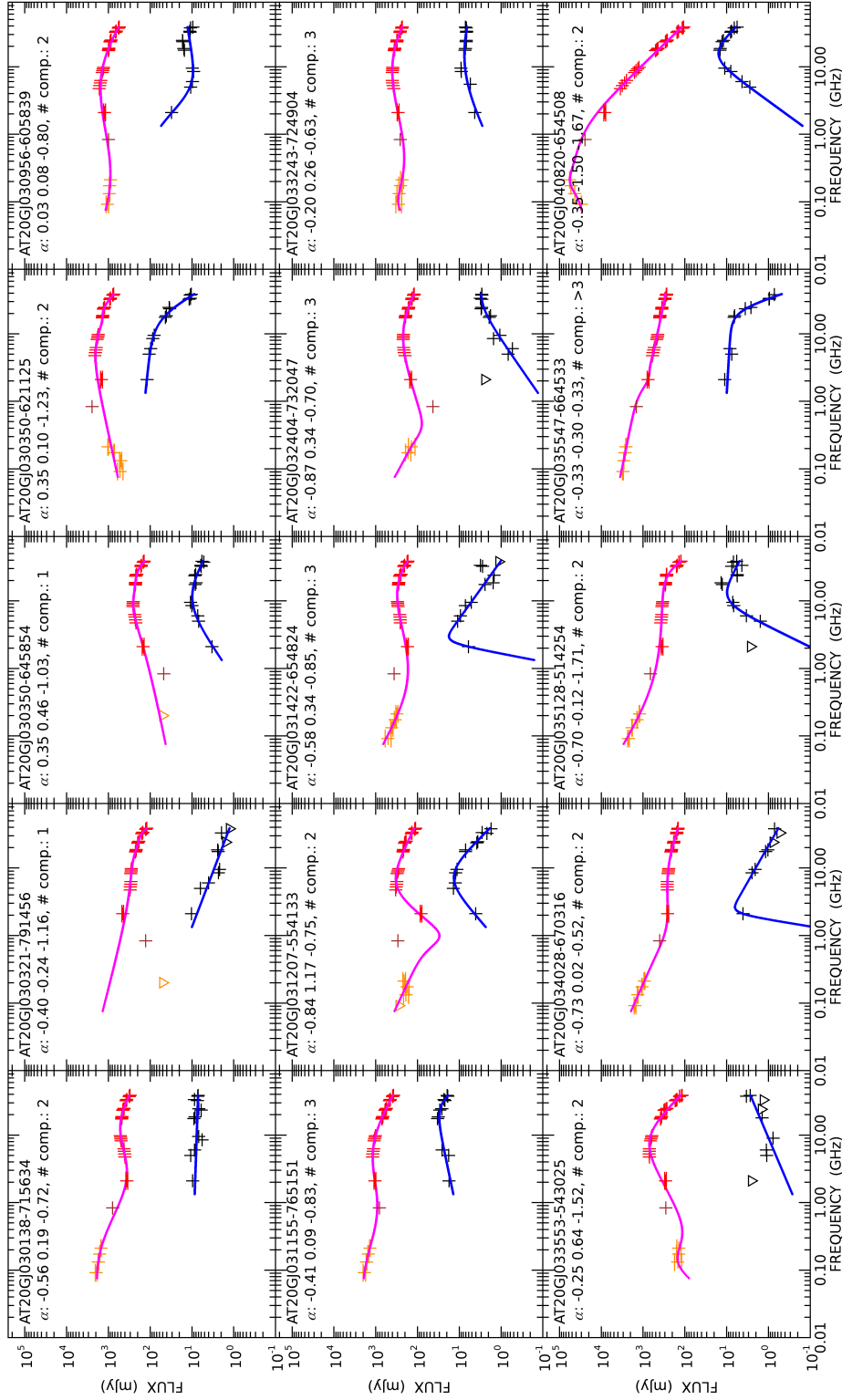


Figure 3.3: Spectra in total intensity and polarization taking into account GLEAM observations between 72 and 231 MHz (orange pluses). Our observations in total intensity are the red pluses, while black pluses and downward triangles are for polarization. The fits in total intensity and polarization are given as red and black solid curves, respectively. We report the SUMSS (Sydney University Molonglo Sky Survey, Mauch et al. 2003) flux density at 843 MHz just for comparison, but we do not use it in the fit procedures. For each object, after its name, spectral indices (computed in total intensity) $\alpha_{0.2}^{0.4}$, $\alpha_{2.5}^{5.5}$ and α_{28}^{38} are provided. At the end of the title of each plot there is the spectral classification in terms of estimated synchrotron components (see 3.3.1).

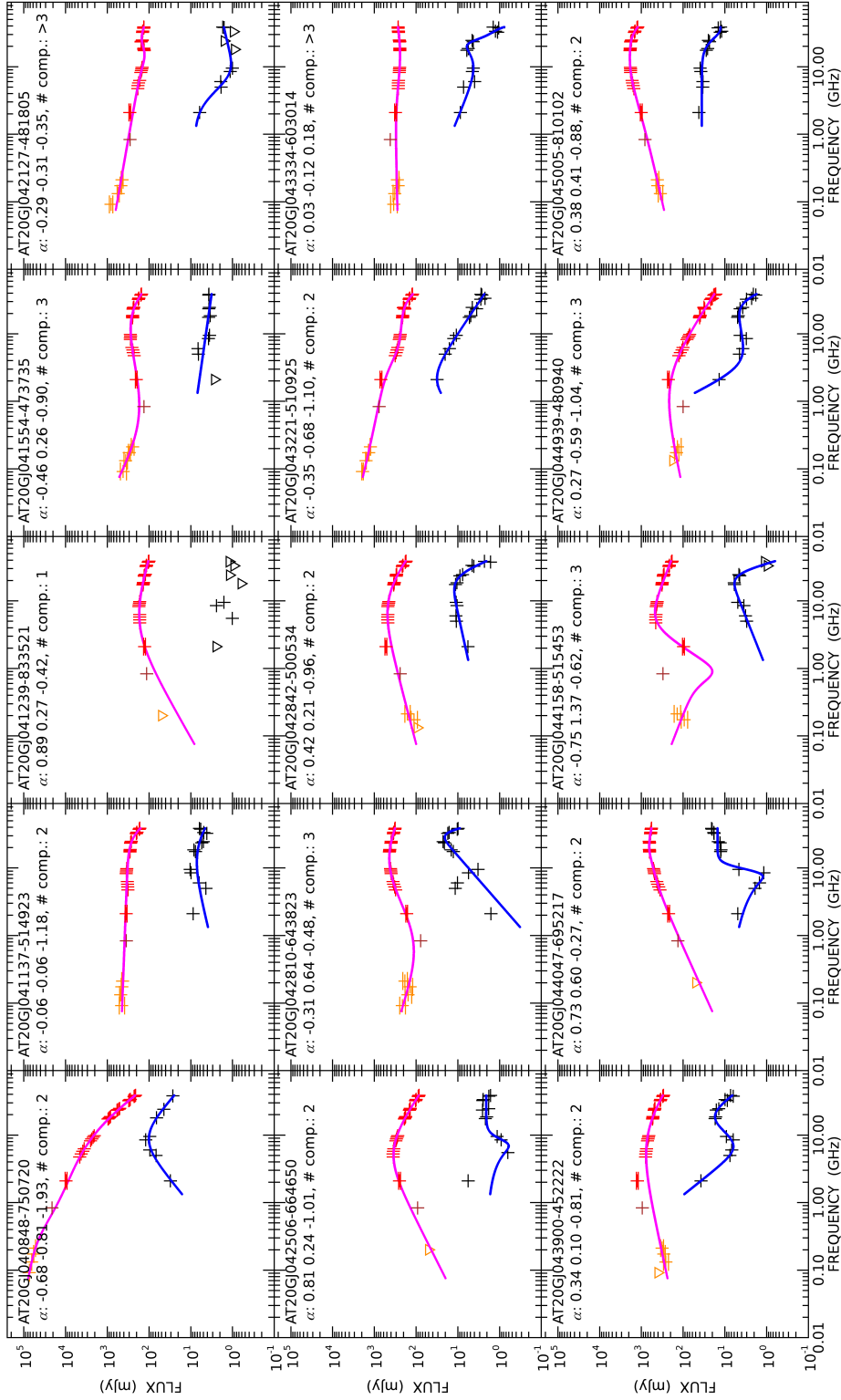


Figure 3.3: Continued.

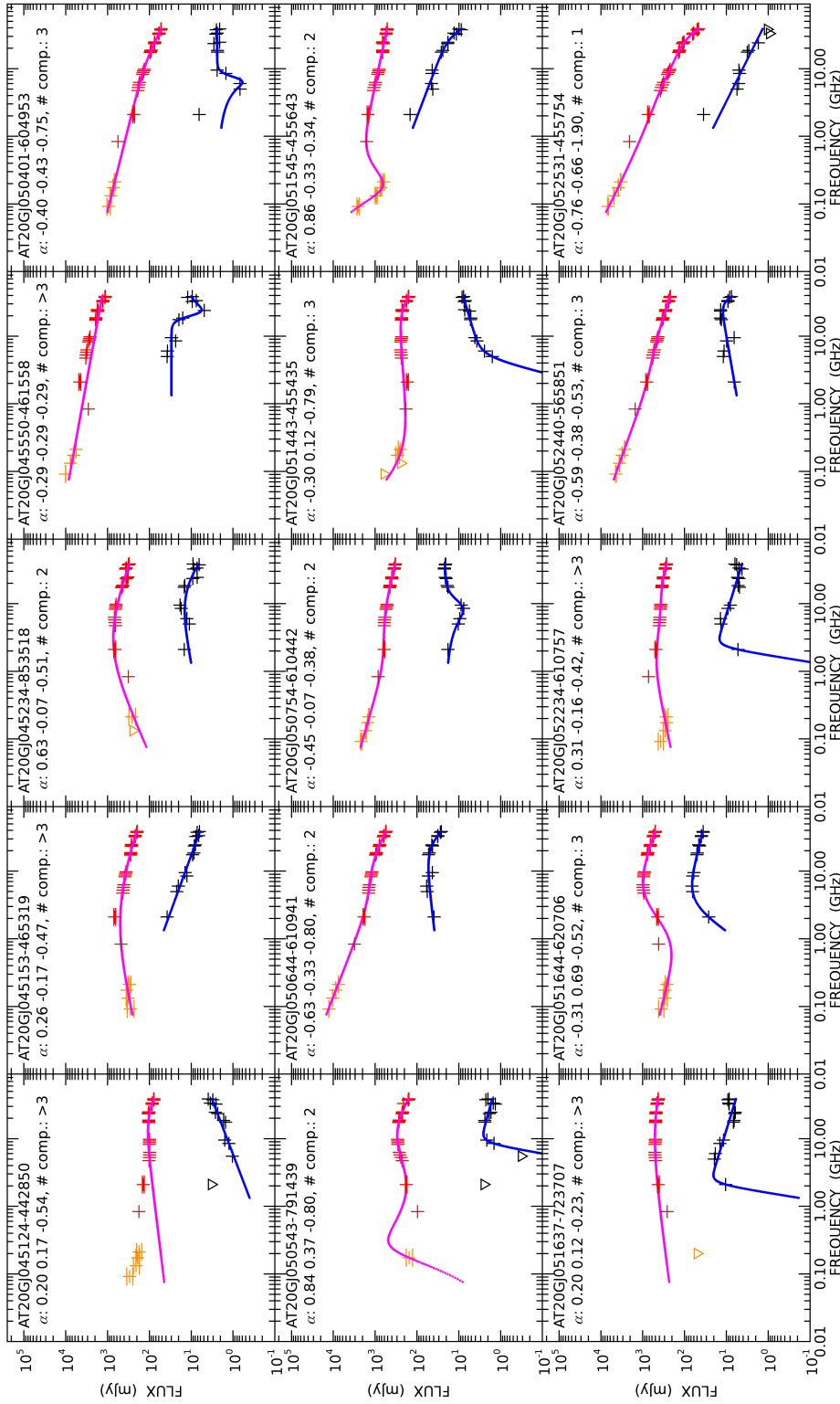


Figure 3.3: Continued.

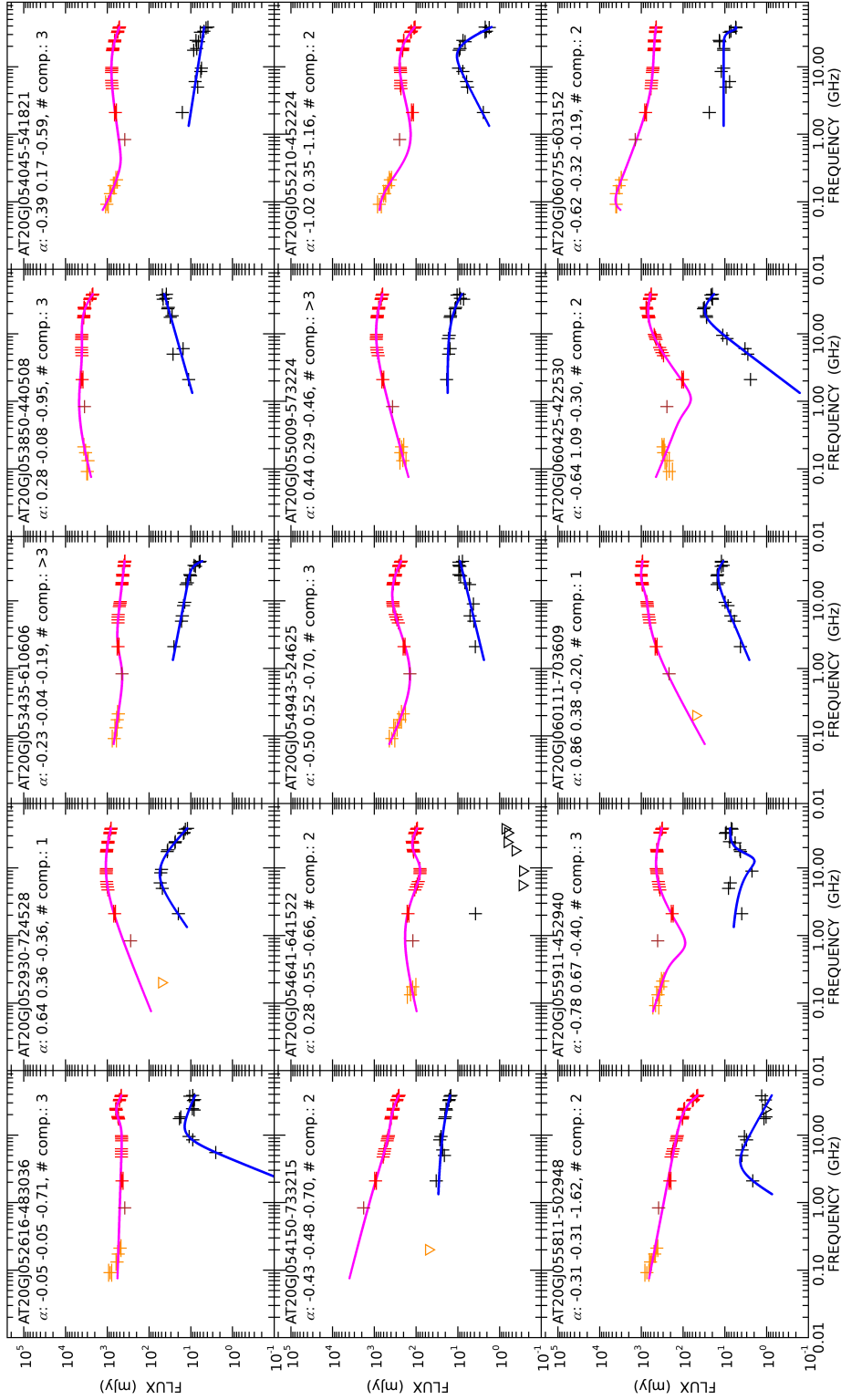


Figure 3.3: Continued.

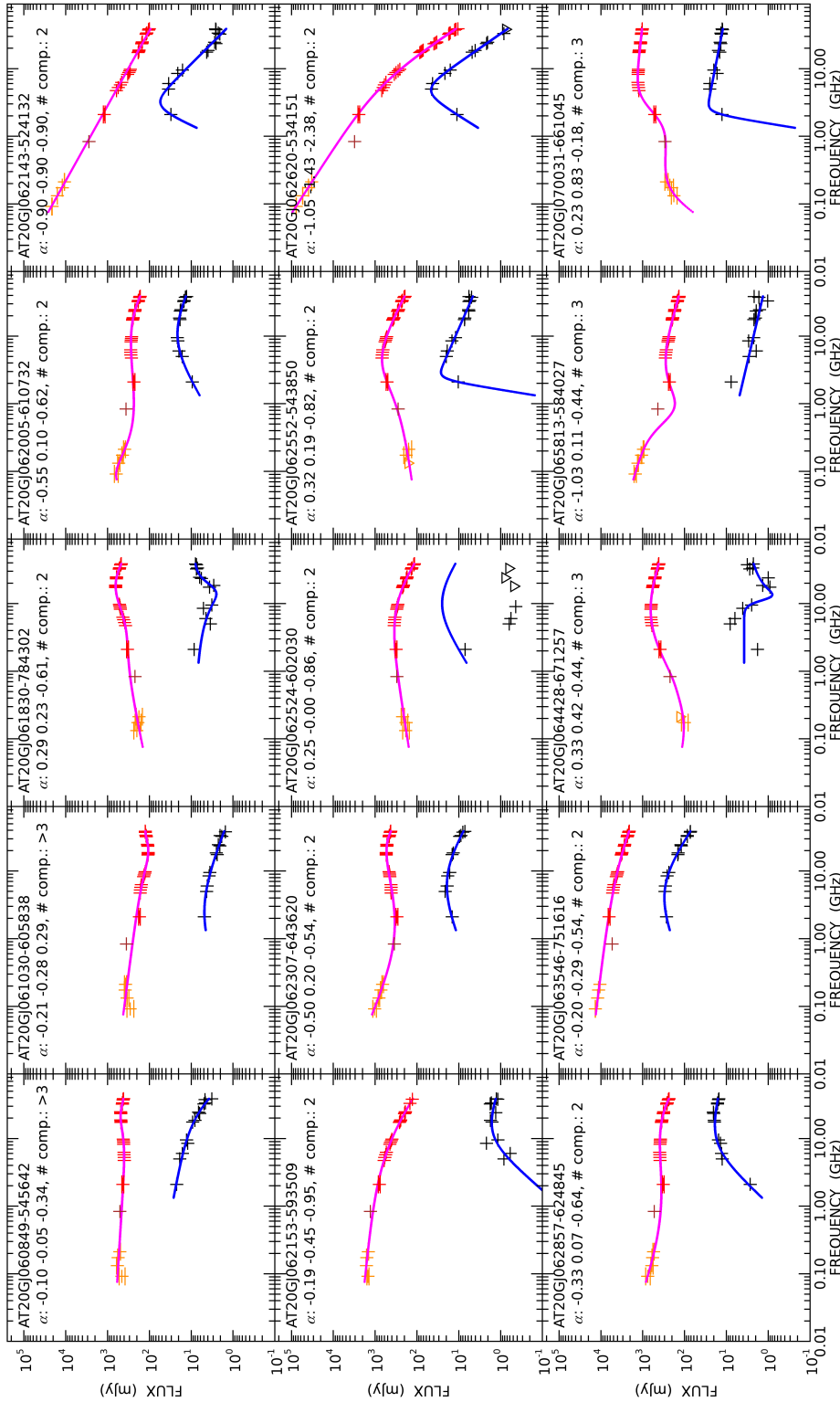


Figure 3.3: Continued.

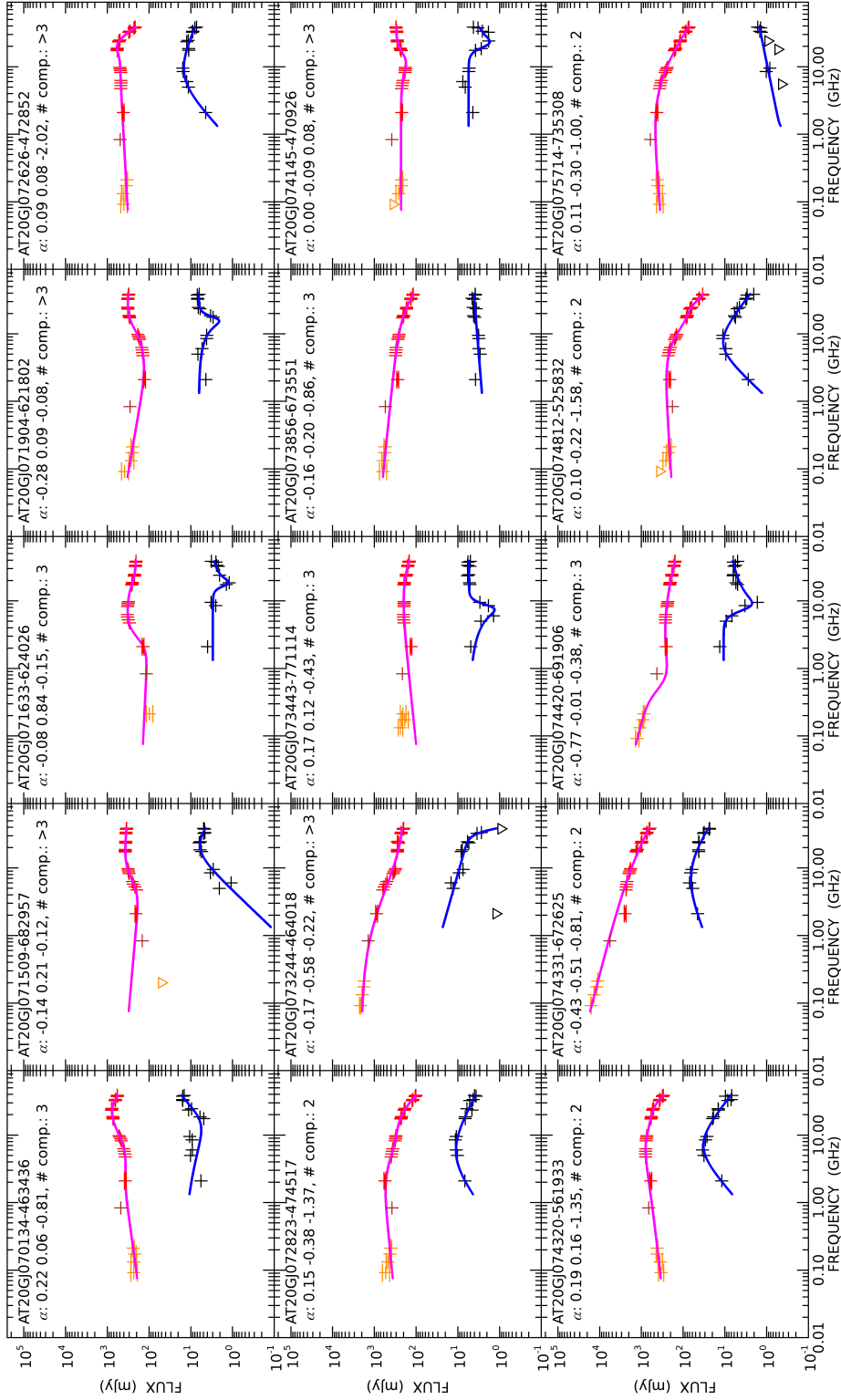


Figure 3.3: Continued.

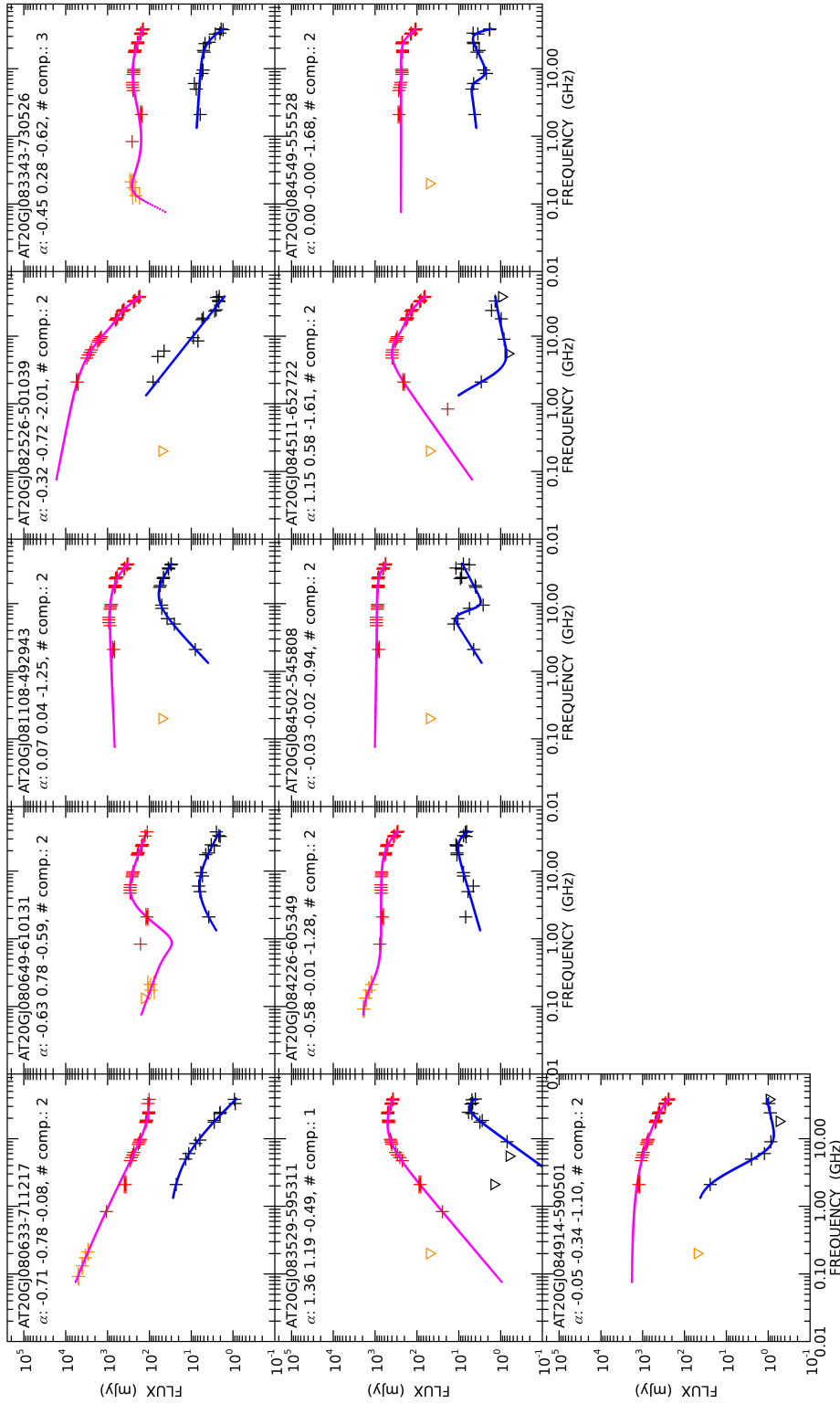


Figure 3.3: Continued.

3.3.1 Linear polarization fraction

Galluzzi et al. (2017) did not find any systematic variation of the mean polarization fraction with either flux density or frequency, down to ≈ 5 GHz, in agreement with the results by Massardi et al. (2013). A similar conclusion was reached by Battye et al. (2011), who however had measurements only down to 8.4 GHz. On the other hand, claims of a systematic decrease of the polarization fraction with decreasing frequency were made by Agudo et al. (2010, 2014) and Sajina et al. (2011), suggesting that Faraday depolarization may work up to ≈ 10 GHz or that the magnetic field is more ordered at high frequencies (Tucci et al. 2004a). However the conclusions by Agudo et al. (2010, 2014) and Sajina et al. (2011) may be biased towards greater polarization fractions by not having taken into account non-detections (Tucci & Toffolatti 2012).

As for Galluzzi et al. (2017), our high detection rate (over 90%) safeguards against any selection bias. Although the polarization fraction declines for several sources drops at the lowest frequency (cf. Fig. 3.1), there is no statistical evidence of a decrease of the mean value for the whole sample or for its sub-samples (cf. Tab. 3.3 and Fig. 3.4). However, as discussed below, such apparent uniformity may hide a more complex situation. The steep-spectrum objects (36) indeed show a slight trend, but comparing to the distributions of polarization fraction at 2.1 and 38 GHz, the rejection of the null hypothesis reaches the $\approx 2\sigma$ level. The sample of flat-spectrum objects (22 objects in total) seems to reveal an opposite trend, but also in this case the significance is less than 3σ .

The spectra of the polarization fraction are less smooth than the total intensity spectra. Only about 15% of the sources have an approximately constant polarization fraction over the full frequency range. Five sources with smooth total intensity spectra above 2 GHz have double peaked fractional polarization, suggesting at least two emission components, seeing different screens. The polarization fraction of $\sim 15\%$ of the sources has an upturn at 2 GHz, where the emission components seen in the GLEAM data may yield a substantial contribution. The polarized flux from these components can drown out the decrease of the polarization fraction of the higher frequency component, due to Faraday depolarization. The most straightforward interpretation of these results is that the extension (and, correspondingly, the age) of emission components increases with decreasing frequency.

On the whole, a joint inspection of total intensity (including GLEAM measurements between 72 MHz and 231 MHz) and polarization spectra indicates the presence of at least 2 (sometimes 3) emission components for about 93% of the sources. This is expected for GPS/CSS sources due to their double lobe structure (Tingay & de Kool 2003; Callingham et al. 2015). For about half of these, the clearest indication comes from polarization data. Hence, we reclassify our sample by distinguishing cases in which there is no sign of an additional synchrotron component (we label it “1C”) from situations in which there are hints of 2–3 synchrotron components (“2-3C”) or more complicated cases which seems to reveal more than 3 components in the spectrum. The

Table 3.3: First, second (median) and third quartiles of the polarization fraction at each observed frequency given by the Kaplan-Meier estimator, taking into account the upper limits, for the full sample and for the steep- and peaked-spectrum sources. The last row reports probabilities for the null hypothesis (i.e. the two samples are drawn from the same parent distribution) given by the Kolmogorov-Smirnov test performed on the steep and peaked groups, considering together 5.5 and 9 GHz, the 18 – 38 GHz frequency interval and all the frequencies, respectively.

Class.	frequencies (GHz)											
	2.1			5.5			9			18		
	Q1	Q2	Q3	Q1	Q2	Q3	Q1	Q2	Q3	Q1	Q2	Q3
All	1.09	2.16	2.98	0.84	1.88	3.25	0.79	1.65	3.02	0.99	2.01	3.07
Steep	0.95	1.54	2.54	0.81	1.74	3.23	0.95	1.64	3.69	0.87	2.33	3.13
Peaked	1.14	2.22	2.75	0.67	1.71	3.16	0.64	1.54	2.78	0.85	1.75	3.05
Flat	1.73	2.79	3.36	1.09	1.88	3.38	1.19	2.00	2.81	1.35	1.82	2.67
Prob.	(5.5 – 9 GHz)			0.825			(18 – 38 GHz)			8.176 · 10 ⁻⁴		

Class.	frequencies (GHz)								
	24			33			38		
	Q1	Q2	Q3	Q1	Q2	Q3	Q1	Q2	Q3
All	1.06	1.95	2.87	1.17	1.85	3.29	1.20	2.09	3.54
Steep	0.66	2.19	4.28	1.31	2.37	3.84	1.17	2.62	4.00
Peaked	1.26	1.84	2.72	1.25	1.75	2.81	1.31	2.11	3.42
Flat	0.98	1.64	2.45	0.66	1.60	2.08	1.06	1.40	2.11
Prob.	(All freqs.)			0.011					

latter are quite flat sources in total intensity from 70 MHz up to ~ 30 GHz, where a steepening typically occurs. Among these 17 objects ($\approx 16\%$) 10 are classified in the flat (F) spectral category, i.e. objects with a flat spectrum in total intensity between 2.1 and 38 GHz.

According to Fig. 3.5 we do not have evidences of trends of the linear polarization fraction with the frequency for the full sample and for “1C” sources. “2-3C” sources have a minimum of the polarization fraction at ≈ 9 GHz, consistent with different emission components at lower and higher frequencies. For the >3C objects, whose spectra show indications of several overlapping synchrotron components, there is a hint of a *decrease* with increasing frequency (rather than of the increase expected by some authors, see e.g. Tucci & Toffolatti 2012) of the polarization fraction: the mean values decline from $\approx 2.1 - 2.4\%$ at ≤ 5.5 GHz to 1.2% at 38 GHz. We anticipate here that in subsec. 3.3.2, we find these sources to have very large rotation measures (RMs) at mm wavelengths. This could indicate that their high frequency components are characterized by a really dense and/or a magnetized medium that strongly rotates the polarization angle (cf. Pasetto et al. 2016).

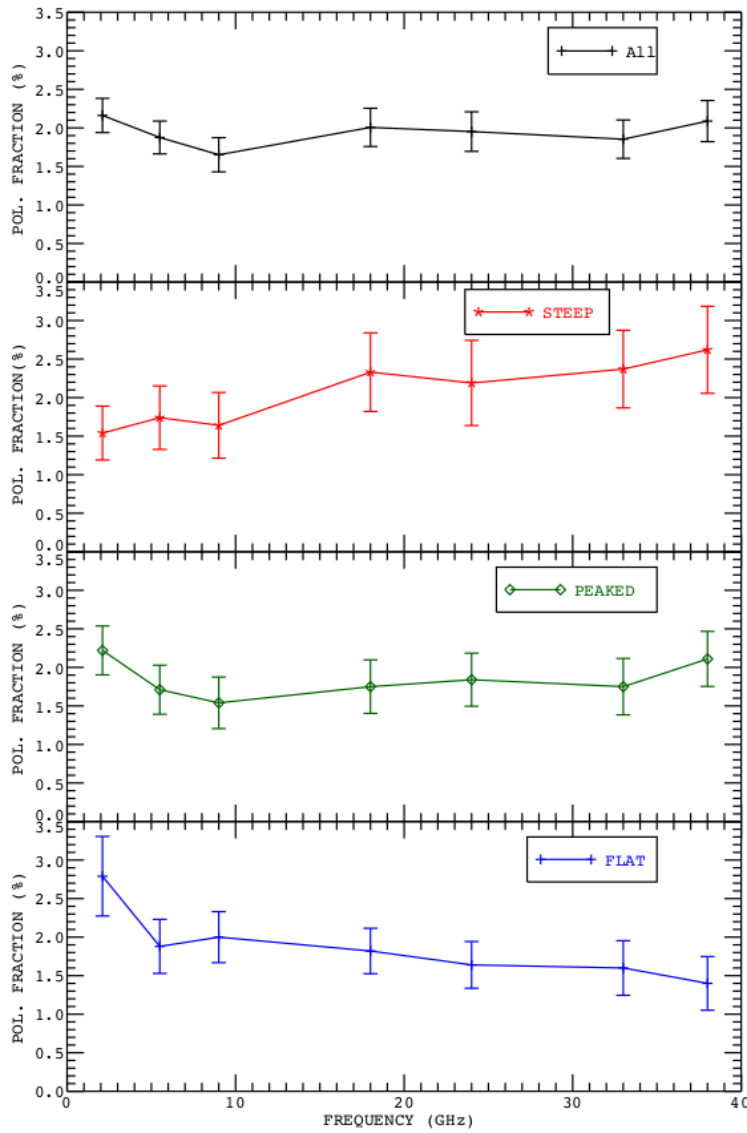


Figure 3.4: Median polarization fraction behaviour with frequency (at 2.1, 5.5, 9, 18, 24, 33 and 38 GHz) for all the sources (black), for steep sources (red), for peaked (green) and flat ones (blue). The errors on median values are given by $1.253 \text{ rms} / \sqrt{N}$, where rms is the standard deviation around the mean and N is the number of the data (at a given frequency) for a given class of objects (cf. Arkin & Colton 1970).

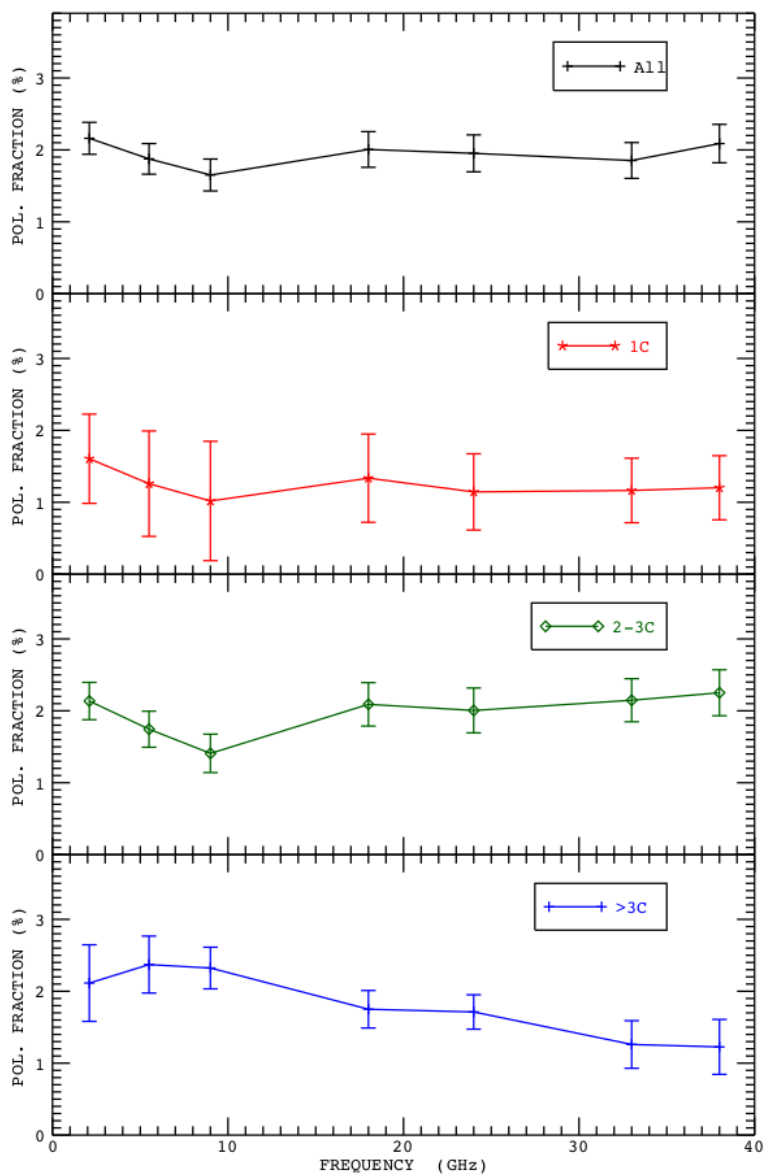


Figure 3.5: Median polarization fraction at the observation frequencies (2.1, 5.5, 9, 18, 24, 33 and 38 GHz) for all the sources (black), for 1C sources (red), for 2-3C sources (green) and for sources with more than 3 components (blue, labeled “>3C”). The errors on median values are given by $1.253 \text{ rms} / \sqrt{N}$, where rms is the standard deviation around the mean and N is the number of detected sources (cf. Arkin & Colton 1970).

3.3.2 Polarization angle: cm- and mm-wavelength regime behaviour

The polarization angle was calibrated setting the parameter “xycorr” in the MIRIAD task ATLOD which applies phase corrections provided by a noise diode mounted on one antenna feed. Partridge et al. (2016) found that the polarization angles measured by ATCA in this way agree with those measured by *Planck* based on the CMB dipole measurements to within $\pm 2^\circ$.

Galluzzi et al. (2017) found evidence of non-zero Faraday rotation for only 2 objects (over a total of 53), since for the overwhelming majority of the sources the dependence of the rotation measure (RM) with λ^2 has a complex behaviour. Only 9 objects of our larger sample can be described by a linear RM– λ^2 relation over the our full frequency range (2.1–38 GHz). For these sources RM estimates are between -72 and 57 rad/m², with 4 cases compatible with a low ($\sim \pm 10$ rad/m²) or a null rotation.

Exploiting our larger frequency range, we can identify two regimes for the RM vs λ^2 relation, one at cm-wavelengths and the other at mm-wavelengths. We have investigated this more complex scenario by fitting the polarization angle as a function of the λ^2 separately for the two regimes (from 2.1 to 9 GHz and from 18 to 38 GHz). We required at least three measured polarization angles in each regime to perform the fit via the IDL “linfit” procedure. A fit was regarded as acceptable when the reduced $\chi^2 < 2$ (probability > 0.1). We obtained $\sim 40\%$ and $\sim 57\%$ successful fits for the low and high frequency regimes, respectively. The corresponding median values of the reduced χ^2 are 0.37 and 0.69, respectively.

The medians and quartiles at cm- and mm-wavelengths are reported in Tab. 3.4 both for all objects for which acceptable fits were obtained and for the “1C”, “2-3C” and $>3C$ types, defined in sub-sec. 3.3.1). We warn the reader that the error associated to the estimated RMs can be large especially at the higher frequencies because of its dependence on $1/\lambda^2$. Typical uncertainties are of about 9% and 32% at low and high frequencies, respectively; thus while at the lower frequencies only 2 ($\sim 5\%$) of the estimated RMs are compatible with a null rotation at the 1σ significance level, this fraction raises to 15% at the higher frequencies.

The median *observed* (i.e. uncorrected for the effect of redshift) values of the RM in the low frequency regime are ~ 40 rad/m² irrespective of the spectral type. At high frequencies they are larger for the whole sample (by a factor ~ 15 , i.e. ~ 600 rad/m²) and for “1C” or “2-3C” objects, and much larger for the $>3C$ objects (~ 1100 rad/m²). Large values of RMs for multi-component sources were previously reported by Pasetto et al. (2016) who suggested that the youngest, highest frequency components can be characterized by a really dense and/or a magnetized medium that strongly rotates the polarization angle.

So far we dealt with *observed* RMs, RM_{obs} . The RM at the source, RM_{AGN} , are related to RM_{obs} by Johnston-Hollitt & Ekers (2004):

$$RM_{\text{obs}} = \frac{RM_{\text{AGN}}}{(1+z)^2} + RM_{\text{Gal}} + RM_{\text{ion}}, \quad (3.3.1)$$

where RM_{Gal} and RM_{ion} are the contributions of our own Galaxy and of Earth's ionosphere, respectively. The Galactic contribution can typically vary from -300 to 300 rad/m^2 , depending on the line of sight. Our sample is located in a region around the Southern Ecliptic Pole and we adopt the Galactic Faraday rotation map provided by Oppermann et al. (2015) (see Fig. 3.6) to get the appropriate correction for each object of our sample.

N. Oppermann et al.: The Galactic Faraday sky

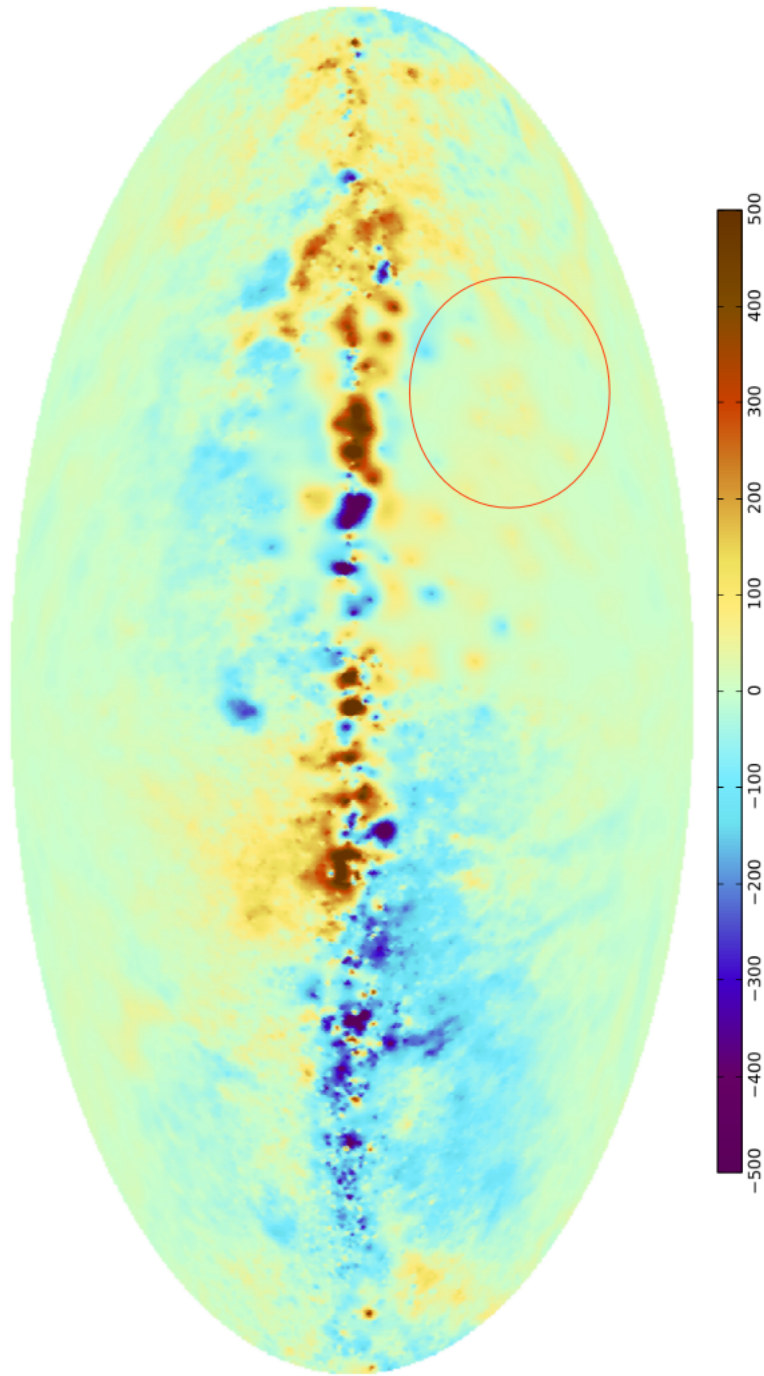


Figure 3.6: Faraday map of the Galaxy provided by Oppermann et al. (2015) with the circle surrounding the region in which lines of sight of our 104 sources intercepts the Galactic Faraday screen. RM values reported in the rainbow scale are in rad/m^2 .

The ionospheric contributions is found to be typically $\lesssim 5 \text{ rad/m}^2$ (Johnston-Hollitt & Ekers 2004), hence it can be safely neglected.

We have found redshifts in the AT20G catalogue (Mahony et al. 2011), an complemented them searching in the NED (NASA/IPAC Extragalactic Database) database. For sources with redshift (44) we have computed also RM_{AGN} (see Tab. 3.4). The median low-frequency value is around 90 rad/m^2 . At high frequencies there seems to be a strong increase of the median RM_{AGN} from “1C” to “2-3C” to “>3C” objects (median RM_{AGN} of $\simeq 700$, $\simeq 2400$ and $\simeq 4000 \text{ rad/m}^2$, but the small numbers of “1C” and “>3C” objects prevents any firm conclusion. It is, however, remarkable that the large RMs of “>3C” objects echo the decrease of their median polarization fraction at mm wavelengths (sub-sect. 3.3.1).

3.3.3 Circular polarization

The circularly polarized emission is weak, typically $\lesssim 0.1\%$ (Rayner et al. 2000), but potentially very interesting because its measurements may permit to gain information on various properties of jets, such as the magnetic field strength and its topology, the net magnetic flux carried by jets (and hence generated in the central engine), the energy spectrum of radiating particles, and the jet composition, i.e. whether jets are mainly composed of electron-positron pairs or electron-proton plasma (Ruszkowski & Begelman 2002).

The most obvious candidate for explaining circular polarization of compact radio sources is intrinsic emission, but the expected level under realistic conditions appears to be too low to explain the observed polarization (Wardle & Homan 2003). Pacholczyk (1973) pointed out that magnetic fields computed from the circular polarization, assuming that it is intrinsic, are usually so high to cause a turnover in the intensity spectrum through synchrotron self-absorption at a considerably higher frequency than is actually observed. The most promising mechanism is Faraday conversion, a birefringence effect that converts linear into circular polarization (Ruszkowski & Begelman 2002; Wardle & Homan 2003). At only two frequencies (5.5 and 9 GHz) more than 50% of the sources were detected in circular polarization so that median values of the circular polarization fractions, m_V , could be determined. We find $m_{V \text{ median}} = (0.23 \pm 0.01)\%$ and $(0.27 \pm 0.02)\%$, respectively. For comparison, the median m_V for the Rayner et al. (2000) sample, selected at 4.85 GHz, estimated from the data in their Table 3, is $\simeq (0.05 \pm 0.02)\%$. Our larger median values may be due to the fact that, because of the higher selection frequency, the overwhelming majority of objects in our sample are blazars; Rayner et al. (2000) have found that these objects have larger circular polarization fractions than radio galaxies that constitute a significant fraction ($\simeq 25\%$) of their sample.

Table 3.4: Median plus I and III quartile values of cm-wavelengths (*upper table*) and mm-wavelengths (*lower table*) RMs. In each table the upper set of values refers to the observed RMs while the lower set refers to the RMs at the source for the subset of sources for which redshift measurements are available. The numbers of sources in each group are in parenthesis. Whenever the number of objects is < 10 we provide only the median value. RMs are in rad/m^2 .

All sample (42)			1C (3)			2-3C (31)			>3C (8)		
I	med	III	I	med	III	I	med	III	I	med	III
18	37	58	-	60	-	15	34	53	-	37	-
All sample (23)			1C (2)			2-3C (18)			>3C (3)		
I	med	III	I	med	III	I	med	III	I	med	III
40	94	244	-	335	-	46	84	220	-	122	-
All sample (59)			1C (4)			2-3C (50)			>3C (5)		
I	med	III	I	med	III	I	med	III	I	med	III
225	635	1397	-	342	-	283	637	1397	-	1141	-
All sample (27)			1C (2)			2-3C (22)			>3C (3)		
I	med	III	I	med	III	I	med	III	I	med	III
679	2300	5252	-	742	-	716	2351	5191	-	4022	-

3.4 Variability

Taking into account the PACO and the AT20G measurements, the observations of September 2014 and the March-April (and July 2016) campaigns we have at least four epochs of observations in total intensity and three epochs in polarization (no polarization data was observed in the PACO epochs). The AT20G data were taken between 2004 and 2008, the PACO data between July 2009 and August 2010. The typical global time span of our dataset is up to 9 – 10 years. Hence, we can arrange a set of comparisons between different epochs to investigate the variability for our sample. Since we re-observed the objects with $b < -75^\circ$ in the 2016 campaign (all of them at 5.5 and 9 GHz, $\sim 20\%$ at 18–24 GHz and $\sim 94\%$ at 33–38 or 33–35 GHz) we have information about the 1.5 yr variability timescale in total intensity and polarization up to 38 GHz. By comparing the September 2014 data and the 2016 data (for the objects with $-75^\circ < b < -65^\circ$) with the PACO ones, we have informations about variability (at least in total intensity) on 4 – 5 yr and 6 – 7 yr timescales, respectively. Furthermore, if we consider both the 2014 and 2016 campaigns with respect to the AT20G survey, we provide variability assessments both in total intensity and polarization up to 20 GHz over a time lag of 9 – 10 yr.

Before discussing results, we should describe the comparisons we made. Since our July observations were at 33 – 35 GHz instead of 33 – 38 GHz, we rescaled the 35 GHz to 38 GHz where possible, i.e. in total intensity, according to the estimated fitting curves. In combining the PACO measurements with the our datasets, we neglected the small differences in the central frequencies (39 instead of 38 GHz) of the highest frequency channels. For each but three sources in the $b < -75^\circ$ sub-sample there is at least one PACO epoch for which all the six frequencies were observed. The same is true for 4 ob-

jects in the $-75^\circ < b < -65^\circ$ sub-sample. In several cases all the frequencies were observed two or three times. In many more cases we have repeated observations for only a subset of frequencies. We have considered only PACO observations of at least 4 frequencies, all carried out within several months. Multiple PACO observations of a sources at a given frequency were averaged. Indeed, similarly to what done here with total intensity flux densities, the PACO catalogue reports for each 2 GHz frequency band 4 flux densities, one for each 512 MHz sub-band. Before performing any temporal average, we consider the median value over the 4 chunks to provide a value for each frequency. Then, the error associated to the averaged PACO flux densities σ_{PACO} is given by:

$$\sigma_{\text{PACO}} = \sqrt{\sigma_{\text{max}}^2 + \sigma_{\langle S \rangle_{\text{PACO}}}^2}, \quad (3.4.1)$$

were σ_{max} is the maximum error over the four 512 MHz sub-bands and $\sigma_{\langle S \rangle_{\text{PACO}}}$ the error associated to the average of the PACO fluxes over the selected epochs, $\langle S \rangle_{\text{PACO}}$.

The AT20G data were collected at 4.86, 8.64 and 20 GHz with the old ATCA correlator set with 2×128 MHz contiguous bands for each frequency. We can straightforwardly compare these observations with ours at 5.5, 9 and 18 GHz, neglecting the small differences in the central frequencies.

Following Sadler et al. (2006), the variability index (V.I.) of a population is defined as:

$$\text{V.I.} = \frac{100}{\langle S \rangle} \sqrt{\frac{\sum_{i=1}^n (S_i - \langle S \rangle)^2 - \sum_{i=1}^n \sigma_i^2}{n}}, \quad (3.4.2)$$

$\langle S \rangle$ being the average of the n flux density measurements at a given frequency, S_i , having error σ_i . In our case we compute the variability index between two epochs, hence $n = 2$.

Since the variability on timescales from a few months to 2 – 4 years were discussed in previous works of our group (e.g. Massardi et al. 2016), we integrate here the analysis with typically longer timescales (up to 9 – 10 yr) and polarization. In Tab. 3.5 we report the mean V.I.'s in total intensity at each frequency for the time lags 1.5, 4 – 5, 6 – 7 and 9 – 10 yr, respectively. Then, the same scheme replies in polarization for 1.5 and 9 – 10 yr only. Variability indices were computed also by distinguishing between steep-, peaked- and flat-spectrum objects. The errors provided in the table are the rms of the V.I.'s rescaled by the \sqrt{N} , where N is the number of objects in the considered class.

Figure 3.7 reports for each frequency (different colours) the variability index against the time lag. Our time lag coverage is complemented by variability measurements provided by Massardi et al. (2016) for the faint PACO sample: on average, there seems to be an increase of the variability index with the time lag at all the frequencies. Moreover, for those time lags for which there are also measurements at the highest frequencies, namely 33 and 38 GHz, the variability indices are typically higher than those associated to

lower frequencies. We noticed in particular for comparison between all faint PACO data with AT20G ones but also for our sample with AT20G (cf. 3 and 9.5 yr, respectively) somewhat higher than expected V.I.s. These odd features may be, at least partially, explained because the AT20G data (which among other things refer to pre-CABB era) are calibrated with an older model of the flux density calibrator 1934-638 (and/or with Uranus), while both our data (natively during the calibration procedures) and the PACO ones (by correcting higher frequencies flux densities) consider the last model for this primary calibrator.

Figure 3.8 reports the V.I. against the frequency for each time lag. There seems to be indication of a trend with increasing frequency mainly for observations at frequencies higher than 18 GHz, since up to 9 – 10 yr results for lower frequencies bands are quite similar within errorbars.

We now focus on the different spectral classes. For steep objects we find an increasing variability with the frequency, consistent with earlier results (Impey & Neugebauer 1988; Ciaramella et al. 2004; Bonavera et al. 2011). This is confirmed for all the considered time lag. The bigger jump we find is between 24 GHz and 33 GHz for the 1.5 yr time lag, a result compatible with the aging of a flaring component (remarkably faster on shorter time-lags at higher frequencies). For peaked objects we have, again, an increasing trend but generally with slightly lower values with respect to steep objects: we argue here that this can be the footprint of a minor component of genuine GPS/HFP objects for which variability is expected to be lower. Flat-spectrum objects show a similar trend with frequency (again with a lower variability with respect to steep objects). On longer time lags (about 6 – 7 yr) there seems to be a considerable jump passing from 18 – 24 GHz to 33 – 38 GHz. Both these elements might echo the fact that these radio emissions are driven by a superposition of synchrotron components experiencing recurrent flaring activity triggered by a newly emitted magnetoionic component along the jet which represents the major flaring components, generally traced by frequencies higher than 30 GHz (which corresponds to a region close to the base of the jet). This “major” event is less frequent than the typical flaring activity due to the interacting recollimating regions along the jet (synchrotron knots), which alone would result in a lower level of variability, due to the fact that the major disturbance travels reactivating the previous emitted regions in different epochs.

In Figs. 3.9 and 3.10 we report the variability diagrams (in total intensity for 4 – 5 yr and 6 – 7 yr time lags, respectively) at 18 GHz with respect to the flux density by distinguishing the three spectral types: in case of 4 – 5 yr we can notice that flat spectrum objects seem typically less variable with respect to the rest of the sample, but this fact seems not to be confirmed for the longer time lag: the small sample statistics can easily affect the result.

Due to the lack of PACO polarization data we could estimate the V.I. only for the 1.5 and 9 – 10 yr time lags (last line of Tab. 3.5). The V.I. turned out to be systematically larger than in total intensity (by a factor $\sim 1.5 - 2$), with a not clear frequency dependence if we consider the 9 – 10 year, but with a mild increasing trend displayed by 1.5 yr time lag data for all the sample. We

stress that data at 18 – 24 GHz on this time lag might particularly suffer from low statistics, but mainly focusing onto 5.5 – 9 GHz compared to 33 – 38 GHz, we see a clear trend for steep objects only: for both peaked and flat objects we find quite constant high values at different frequencies, i.e. $\approx 22 - 25\%$, while for steep-spectrum objects there is an increasing trend in frequency with typical values higher by a factor ~ 2 with respect to the total intensity counterparts. These findings seem to be compatible with the structure we argue for the objects in the sample: steep-spectrum radio sources should have a lower number of knot-like structures (in the simplest scenario just one, optically thin), hence the polarization behaviour on average should echo the increasing variability with the frequency (adiabatic expansion and flaring activities). The larger values compared to the total intensity might be due to turbulent dissipation which tends to disrupt the shock-induced magnetic order. In the case of peaked- or flat-spectrum objects the number of components is expected to be higher: some of them are more depolarized than others and what we see in polarization is a smaller subset peaking at different frequencies: the final outcome can result in a similar variability pattern at all the frequencies.

In order to further gain insights about the structure of objects in our sample, we can have a look how spectra eventually changes on short time scales due to adiabatic expansion and/or flaring activity. Then, we can isolate genuine candidates for CSS/CSO and GPS/HFP, namely those objects which are compact because they are genuinely young (or, at least, frustrated). Since the 2016 campaign re-observed the $b < -75^\circ$ sample only partially at 18–24 GHz and non-detections may also hamper the spectral reconstruction in polarization, we limit our discussion to the total intensity only. Some plots are presented here and clearly show the evidence for new flaring activity (or new emitting components) and/or adiabatic expansion of previously emitted (or past flaring components): in some cases the variability shown is very high (up to $\sim 120\%$). Following the same approach of the sec. 3.2.2 we build up a table for the spectral classifications in total intensity for 2014 and 2016 epochs.

As we can see 12% objects seem to keep their steep behaviour (they probably simply expand without additional activity). Among these, the less variable objects are good candidate for CSS/CSO radio sources. Conversely, there is also a smaller number of objects (3) for which there seems to be an ongoing flaring activity. Among Flat-spectrum objects only less than 25% preserve their behaviour, typically unveiling a residual optically thin synchrotron (S objects in 2016) or (self absorbed, Pe) component. Peaked-spectrum objects in 2014 change their behaviour in more than 50% of the cases: they might simply show an adiabatic evolution towards lower peaking/steep states or might be genuinely young objects. Interestingly there is also 10 objects which show a flattening in the spectrum, in some cases associated to a very high variability. In these cases a flaring component or, for extreme variability, even a newly super-luminal component closer to the base of the jet might explain what we see in the 2.1 – 38 GHz frequency range. Here below we report the plot for the total intensity spectra of the old sample as measured in September 2014 (blue points) and in the March–April (and July) campaign (red points). The fit for the latter is also displayed in magenta (see Fig. 3.11).

Table 3.5: Mean variability indices in total intensity and in polarization (last row). Note that for 18 – 24 GHz we have only ~ 10 observations, hence provided numbers are less significant, especially for the distinction in sub-class and/or in polarization where non-detections might reduce the number of data to few unities.

Selection	Time (yr)	5.5	9	18	24	33	38
All	1.5	5.5 ± 0.7	6.7 ± 0.8	10 ± 1	14 ± 2	14 ± 2	15 ± 2
	4 – 5	14 ± 2	14 ± 2	15 ± 2	16 ± 2	19 ± 2	18 ± 2
	6 – 7	14 ± 1	15 ± 2	16 ± 2	16 ± 2	21 ± 2	24 ± 3
	9 – 10	39 ± 2	40 ± 3	39 ± 3			
Steep	1.5	3.4 ± 0.5	4 ± 1	5 ± 1	8 ± 1	13 ± 5	13 ± 5
	4 – 5	17 ± 3	19 ± 3	19 ± 3	22 ± 4	26 ± 4	23 ± 4
	6 – 7	12 ± 2	12 ± 2	15 ± 3	14 ± 3	20 ± 4	25 ± 4
	9 – 10	41 ± 4	49 ± 5	44 ± 5			
Peaked	1.5	7 ± 1	8 ± 1	13 ± 2	17 ± 2	14 ± 3	15 ± 3
	4 – 5	12 ± 3	12 ± 3	14 ± 3	14 ± 3	18 ± 3	18 ± 3
	6 – 7	14 ± 3	14 ± 3	15 ± 3	15 ± 3	21 ± 4	21 ± 4
	9 – 10	36 ± 4	32 ± 4	38 ± 4			
Flat	1.5	5 ± 1	6 ± 1	8 ± 2	11 ± 3	14 ± 3	17 ± 4
	4 – 5	14 ± 5	12 ± 4	10 ± 3	12 ± 4	13 ± 3	12 ± 3
	6 – 7	16 ± 3	20 ± 4	20 ± 4	19 ± 5	24 ± 6	28 ± 7
	9 – 10	41 ± 5	39 ± 5	34 ± 5			
All (pol.)	1.5	16 ± 3	22 ± 2	23 ± 4	16 ± 4	24 ± 3	28 ± 3
	9 – 10	52 ± 4	49 ± 5	42 ± 4			
Steep (pol.)	1.5	6 ± 6	11 ± 3	29 ± 4	11 ± 5	25 ± 3	27 ± 8
	9 – 10	51 ± 7	52 ± 12	47 ± 7			
Peaked (pol.)	1.5	20 ± 4	25 ± 3	20 ± 6	11 ± 2	22 ± 5	26 ± 4
	9 – 10	53 ± 6	56 ± 7	36 ± 6			
Flat (pol.)	1.5	16 ± 4	25 ± 5	25 ± 9	23 ± 8	26 ± 7	30 ± 7
	9 – 10	48 ± 9	34 ± 9	38 ± 8			

Table 3.6: Distribution of sources per spectral type in total intensity in 2014 and 2016 campaigns. The last row reports the total for a given spectral class for 2014 observations, while the last column does the same for the 2016 campaign.

I '16→	(In)	(Pe)	(F)	(S)	(U)	
I '14↓						
(In)	0	0	0	0	0	0
(Pe)	0	8	10	3	0	21
(F)	0	7	7	3	0	17
(S)	0	1	2	12	0	15
(U)	0	0	0	0	0	
	0	16	19	18	0	

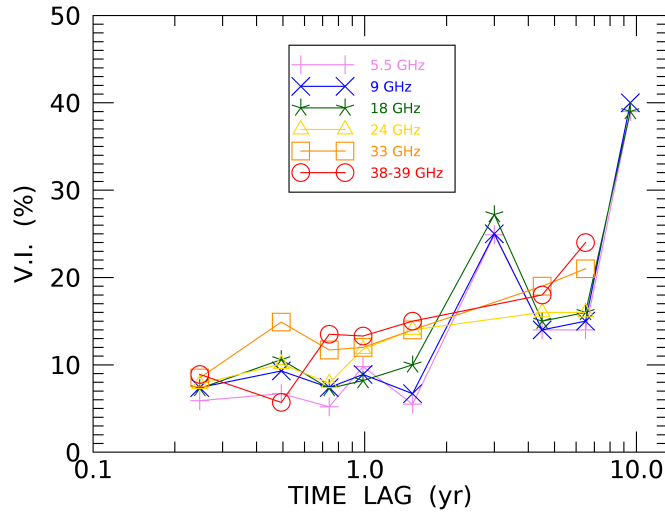


Figure 3.7: Mean variability indices in total intensity *vs.* time lag at the observed frequencies (different colours). Variability measurements for the faint PACO sample are also displayed (Massardi et al. 2016).

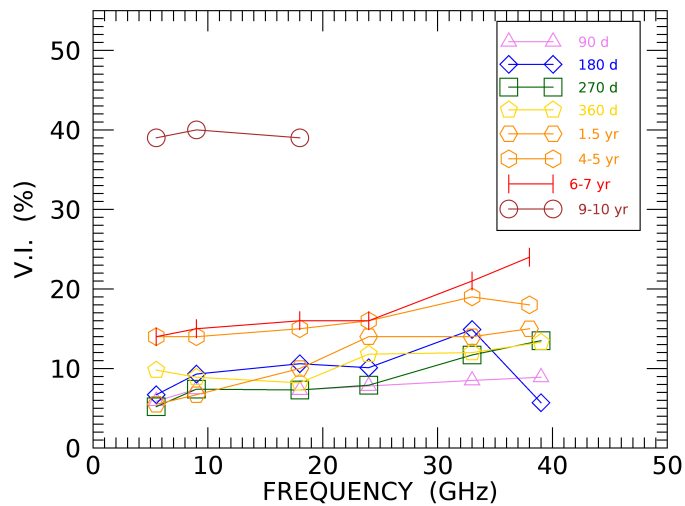


Figure 3.8: Mean variability indices in total intensity *vs.* time lag at the observed frequencies (different colours). Variability measurements for the faint PACO sample are also displayed (Massardi et al. 2016).

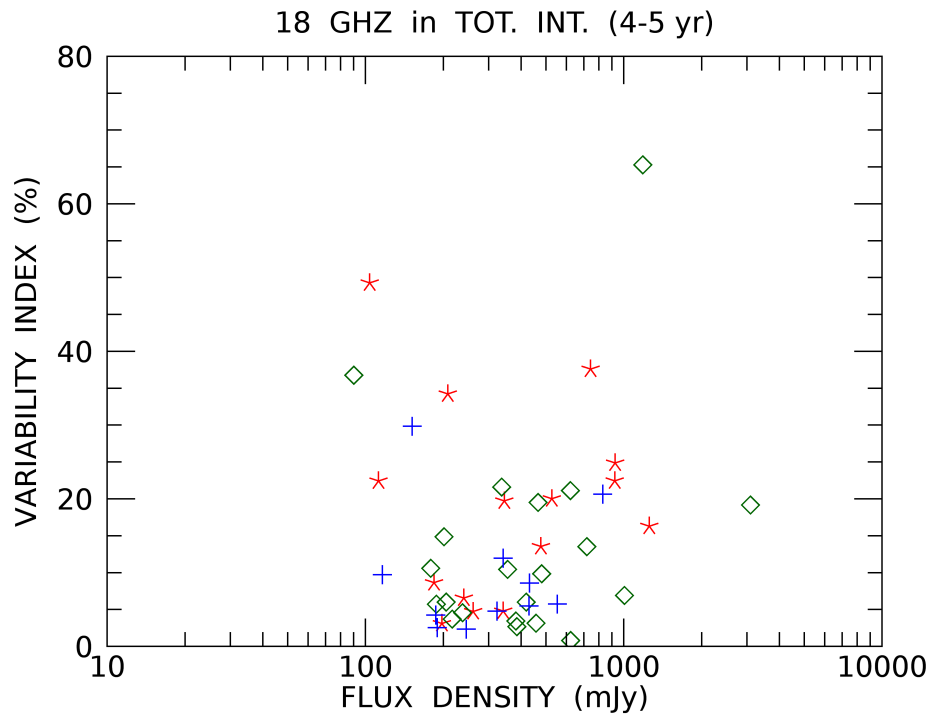


Figure 3.9: Mean variability indices in total intensity vs. flux density at 18 GHz for the 4 – 5 yr time lag.

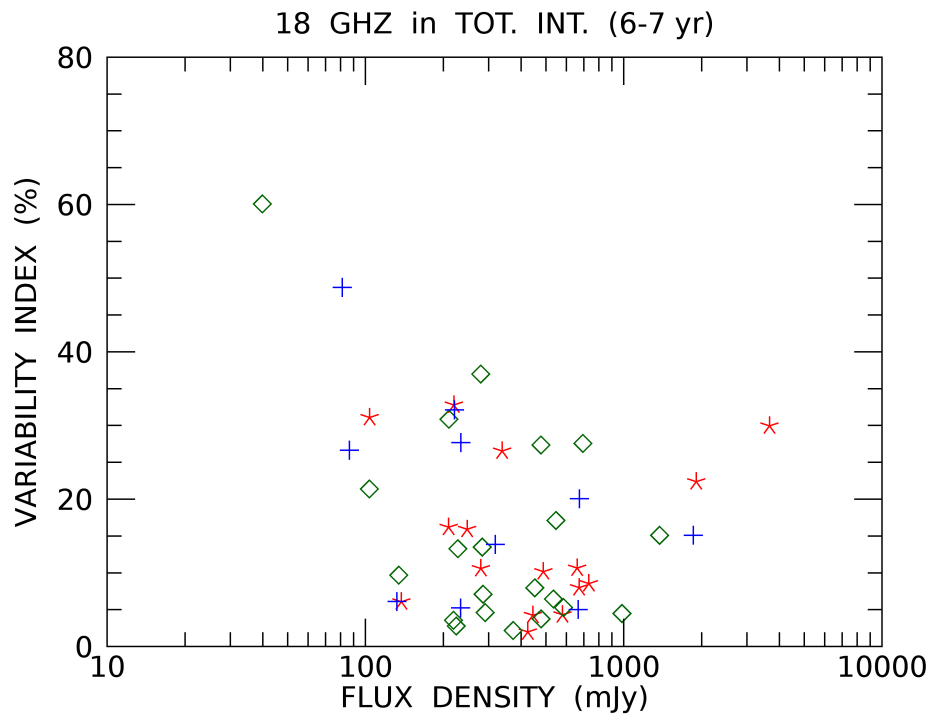


Figure 3.10: Mean variability indices in total intensity vs. flux density at 18 GHz for the 6 – 7 yr time lag.

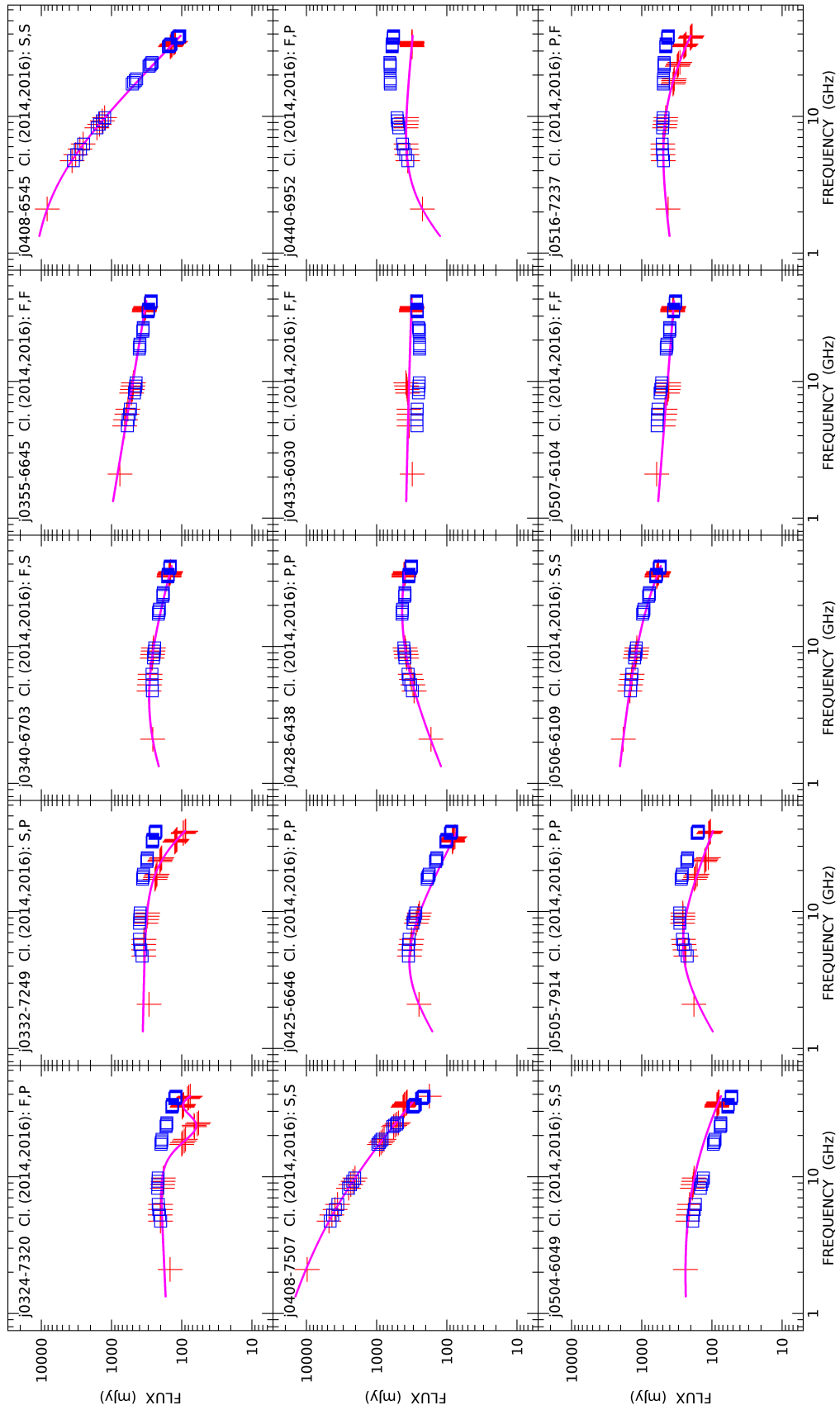


Figure 3.1.1: Spectra of the sample with $b < -75^\circ$ in total intensity for 2014 (red symbols) and 2016 (blue symbols) campaigns. Fitting curves are shown in magenta.

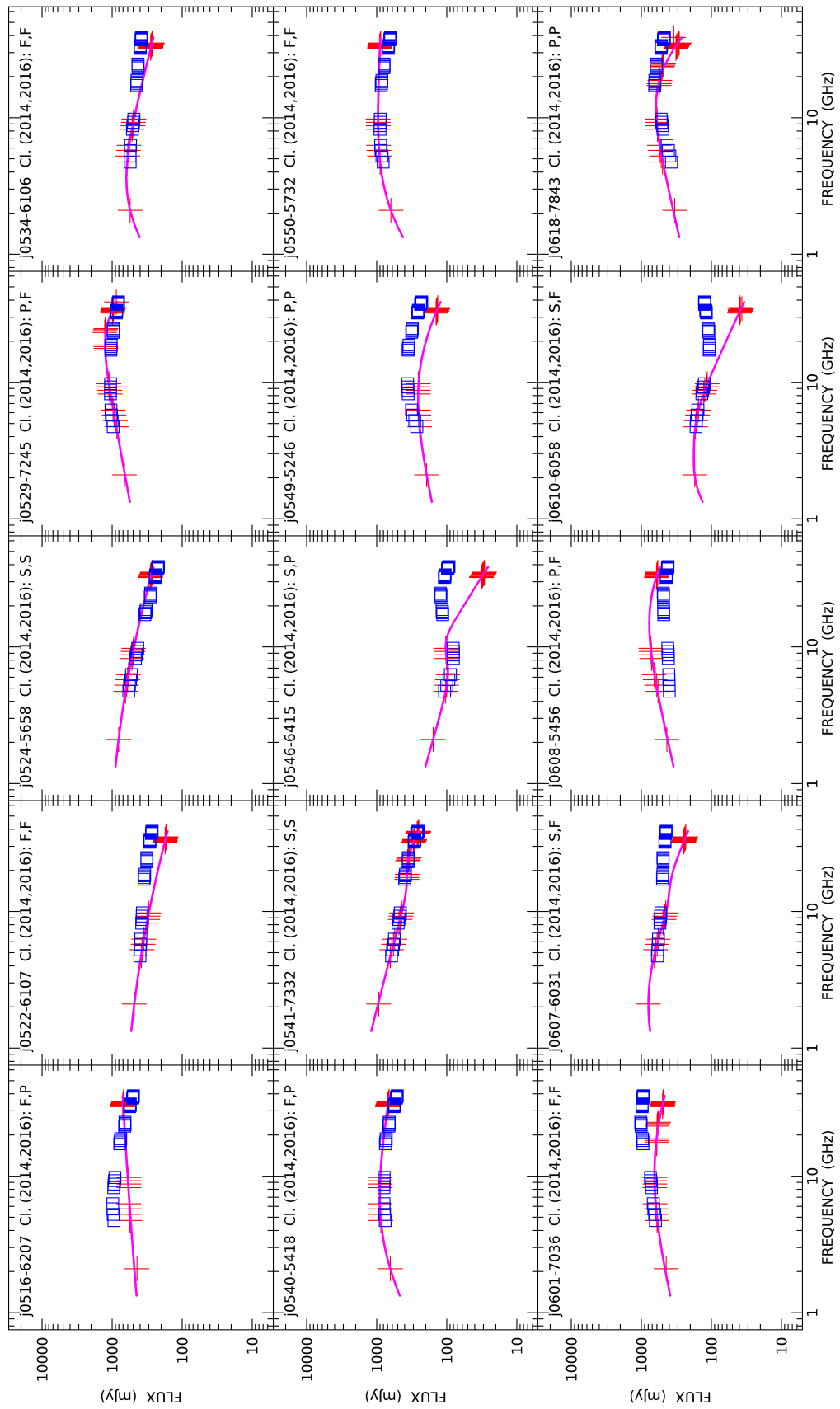


Figure 3.11: Continued.

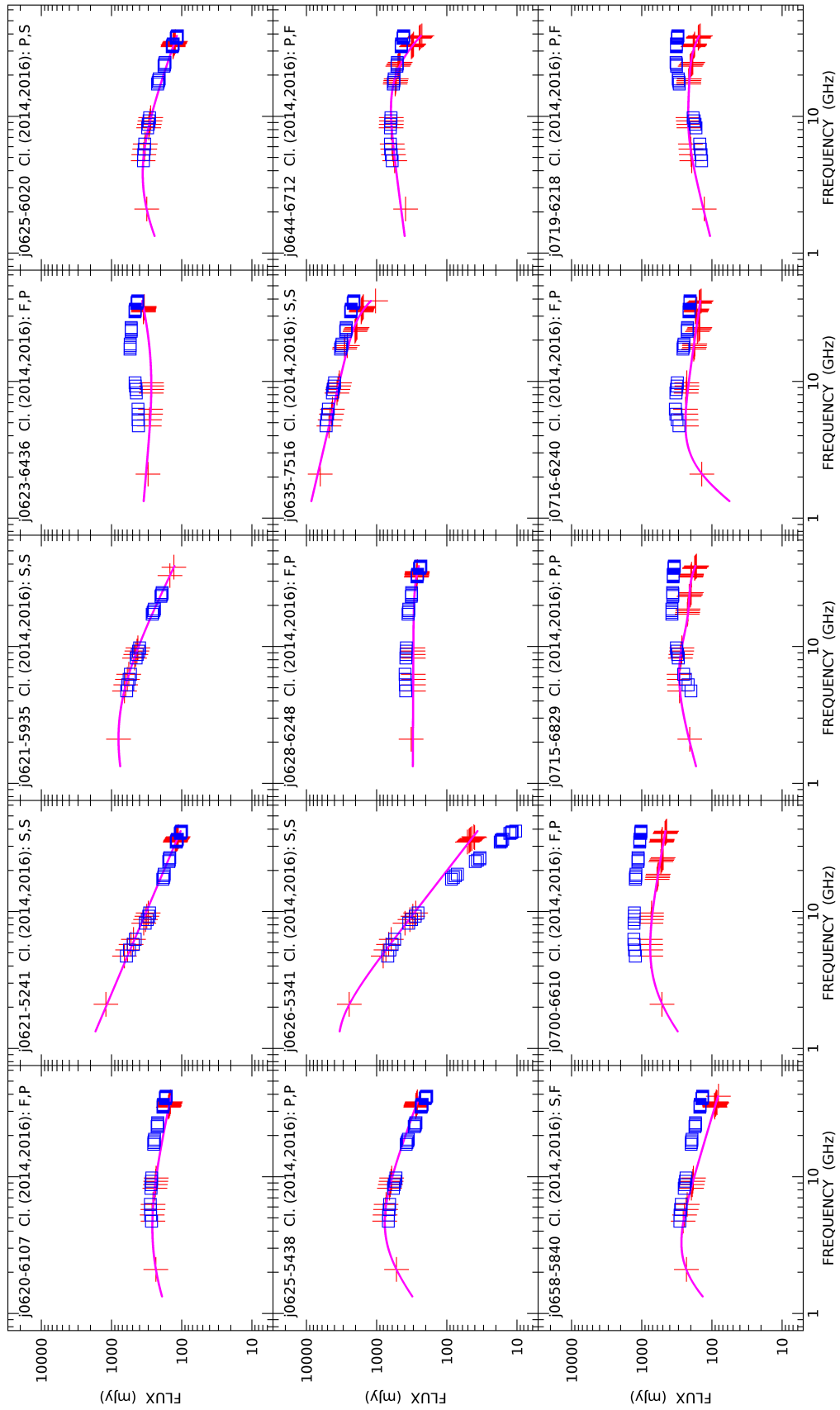


Figure 3.11: *Continued.*

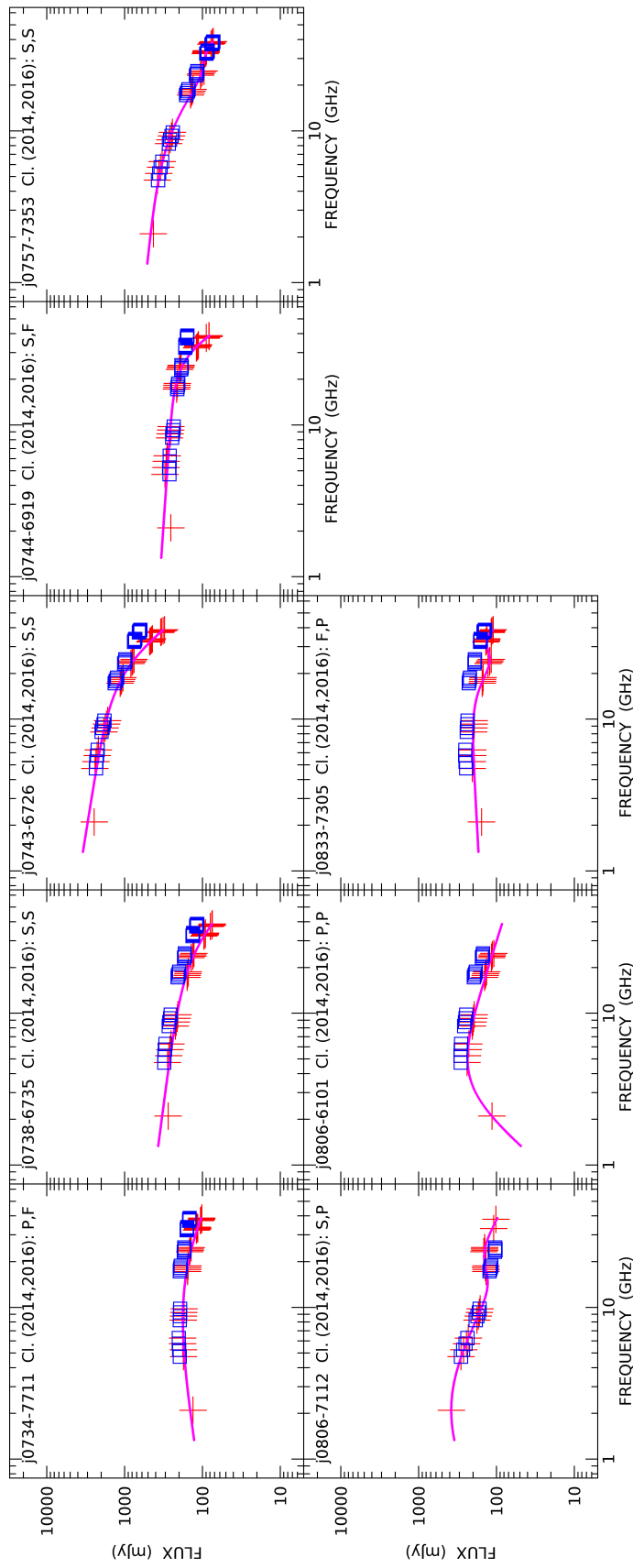


Figure 3.11: Continued.

3.5 Source counts in polarization

Figure 3.13 shows the source counts in polarization at 20 GHz obtained through the convolution of the total intensity differential source counts reported by the model De Zotti et al. (2005) with our distribution of polarization fractions at 18 GHz. In the Tab. 3.7 and in the Figure 3.12 we report the observed distribution (black circles): in each bin uncertainties are derived assuming a Poisson statistics, following the indications of Gehrels (1986). The solid line is the fit assuming a lognormal distribution

$$f(\Pi) = \text{const} \cdot \frac{1}{\sqrt{2\pi}\sigma\Pi} \exp^{-\frac{1}{2}\ln^2(\Pi/\Pi_m)/\sigma^2}, \quad (3.5.1)$$

where $\text{const} = 0.96$, $\sigma = 0.76$ and $\Pi_m = 2.00\%$, i.e. the median value of the distribution. The reduced χ^2 value is 0.21. In Tab. 3.8 and in figure 3.13 (black circles) we plot the differential source counts in polarization, following the recipe reported by Tucci & Toffolatti (2012): since there is no evidence of a correlation between the total intensity flux density and the polarization fraction, the number counts $n(P) \equiv dN/dP$ can be determined by

$$n(P) = \int_{S_0=P}^{\infty} \mathcal{P}\left(m = \frac{P}{S}\right) n(S) \frac{dS}{S}, \quad (3.5.2)$$

where $n(S)$ is the assumed source counts in total intensity, \mathcal{P} is the probability density distribution for the polarization fraction m , i.e. $\Pi/100$. Note that in each bin in P the integration over S is truncated at $S_0 = P$, which corresponds to the maximum degree of the polarization fraction (i.e. $m = 1.0$). We compare our results with source counts provided by Massardi et al. (2013, blue diamonds) via a MCMC simulation of the whole AT20G catalogue (Massardi et al. 2011), as well as with the Tucci & Toffolatti model (2012, red and blue lines, which refer to the lower and upper level expected, respectively). Since our sample is mainly composed by blazars (BL Lacs and FSRQs), which typically are labelled as “flat” and represent the dominant population at 20 GHz (dashed lines), we expect and find a good agreement with the limits on the total source counts provided by the model. Hence, given the assumptions by Tucci & Toffolatti (2012) on the median polarization fraction of steep-spectrum radio sources (presented in their Tab. 4), that are higher than our current findings (see our Fig. 3.4, for a comparison), their overestimation of source number counts in polarization below 10 mJy can be (at least partially) explained. Note that eq. (3.5.2) assumes independence of the polarization fraction from the total flux density. However this assumption can be broken as another population, namely steep-spectrum sources, with different polarization properties, becomes increasingly important with decreasing flux density.

Table 3.7: Distribution of the polarization fractions at 18 GHz for the whole sample of 104 objects.

Π (per cent)	Probability	lower uncert.	upper uncert.
0.600	0.2404	0.0453	0.0453
1.800	0.2644	0.0446	0.0446
3.000	0.1843	0.0381	0.0470
4.200	0.0721	0.0222	0.0317
5.400	0.0321	0.0153	0.0253
6.600	0.0160	0.0104	0.0211
7.800	0.0160	0.0104	0.0211
9.000	<0.01843		
10.200	<0.00801		
11.400	0.0080	0.0066	0.0184

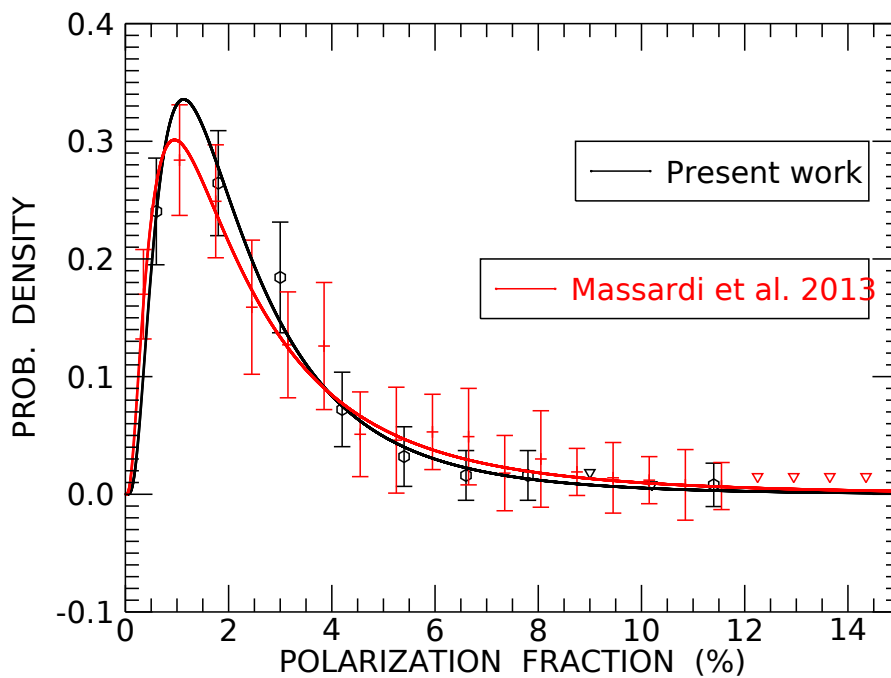


Figure 3.12: Distribution of the polarization fraction at 18 GHz. Errors and upper limits correspond to a 1σ level. The black circles refer to the sample studied in this work, the red pluses to the full AT20G bright sample studied in Massardi et al. (2013). The corresponding fit by a lognormal distribution for each dataset is reported with a solid lines of the same colour.

Table 3.8: Euclidean normalized differential source counts at 20 GHz in polarization, obtained in this present work via the convolution of the distribution of the polarization fraction at 18 GHz with the De Zotti et al. (2005) model.

$\log [P(\text{Jy})]$	$S^{5/2}n(S)$ ($\text{Jy}^{3/2}\text{sr}^{-1}$)	lower uncert.	upper uncert.
-2.897	0.0667	0.0007	0.0007
-2.692	0.0760	0.0011	0.0011
-2.486	0.0869	0.0017	0.0017
-2.281	0.1011	0.0025	0.0025
-2.075	0.1198	0.0039	0.0039
-1.870	0.1426	0.0061	0.0061
-1.664	0.1662	0.0094	0.0094
-1.459	0.1856	0.0142	0.0142
-1.253	0.1978	0.0209	0.0209
-1.048	0.1987	0.0299	0.0299
-0.842	0.1886	0.0417	0.0519
-0.637	0.1734	0.0549	0.0766
-0.431	0.1580	0.0726	0.1199
-0.226	0.1447	0.0996	0.2034
-0.020	0.1337	0.1297	0.3606
0.185	<0.31886		
0.391	< 0.64841		
0.596	<1.31855		

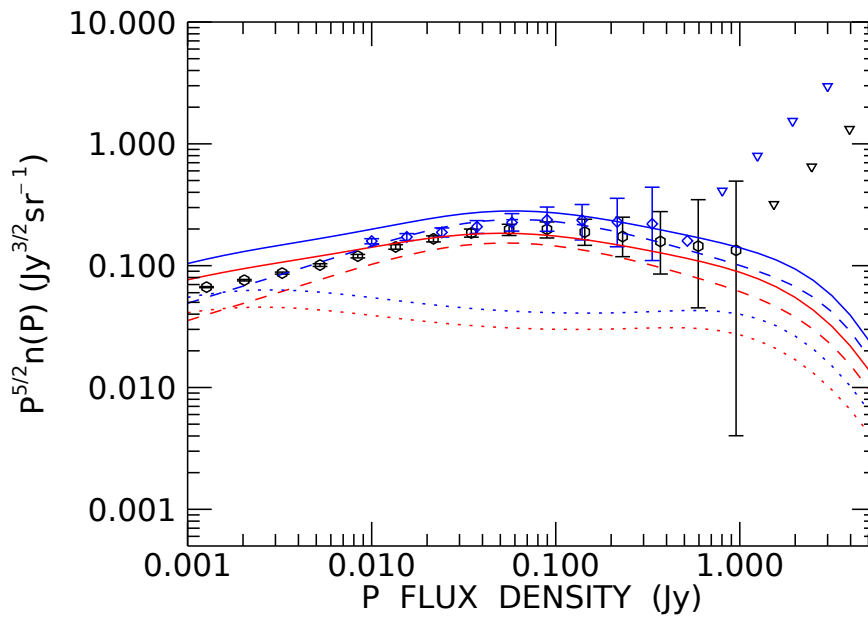


Figure 3.13: Differential source counts at 20 GHz in polarization obtained in this work plotted with black circles (black downward triangles are for upper limits). Also shown, for comparison, are the estimates by Massardi et al. (2013) using the polarimetric data from their own survey, somewhat shallower than the present one ($S_{20\text{ GHz}} > 500\text{ mJy}$) combined with the full AT20G catalogue (blue diamonds and blue downward triangles for upper limits). The curves show the predictions of the Tucci & Toffolatti (2012) model: blue curves for the “conservative” case and red curves for the “optimistic” case. The solid lines represent the total number counts; the dotted lines are for steep-spectrum sources (classified at low frequencies); the dashed lines are for flat objects (flat-spectrum radio quasars, i.e. FSRQs and BL Lacs).

3.6 Modelling AGN population in polarization: our contribute to the T-RECS simulation

The Tiered Radio Extragalactic Continuum Simulation (T-RECS, PI: Anna Bonaldi, Bonaldi et al. 2018, in prep.) is a P-Millennium based simulation (Baugh et al., in prep.) which would propose to the scientific community a powerful tool with an unprecedented quantity of physical informations, ideal to support the SKA science cases. The P-Millennium simulation is a dark matter (DM)-only simulation with *Planck* cosmology: $H_0 = 67.77 \text{ km s}^{-1} \text{ Mpc}^{-1}$, $\Omega_\Lambda = 0.693$, $\Omega_m = 0.307$, $\sigma_8 = 0.8288$ (Planck Collaboration et al. 2014). The box size is 800 Mpc^3 and the particle resolution $1.061 \times 10^8 h^{-1} M_\odot$ (which gives 5040^3 DM particles). Initial conditions are generated at a redshift of $z = 127$ and 272 snapshots are created down to $z = 0$. To generate merger trees, a friend-of-friend algorithm is run to identify haloes and subhaloes. Finally, subhaloes are tracked between output times and consistently assigned memberships as described in Jiang et al. (2014). From the merger tree outputs of this simulation we create lightcones of bound dark matter halos, onto which we assign galaxies based according the state-of-the-art of luminosity functions both for AGNs and Star Forming Galaxies (SFGs).

We generate a lightcone up to $z = 8$, which is sampled by 201 snapshots. The 800 Mpc^3 size of the simulation box allows us to have a full field of view of $5 \times 5 \text{ deg}^2$ out to this redshift. The main outcomes of the simulation are two catalogues in such patch of simulated sky, one for AGNs and the other for SFGs, containing among other quantities (e.g. coordinates, redshifts, type classification, physical size and viewing angle) flux densities and intrinsic luminosities (in total intensity and polarization) at several frequencies between 150 MHz and up to $\sim 20 \text{ GHz}$. In principle the simulation can be run several times in order to provide synthetic catalogues on several $5 \times 5 \text{ deg}^2$ patches.

3.6.1 Active Galactic Nuclei model description

To describe the cosmological evolution of the luminosity function (LF) of radio-loud (RL) Active Galactic Nuclei (AGNs) we adopted the Massardi et al. (2010) model, as updated by Bonato et al. (2017). The model successfully fitted a large amount of data on LFs of steep- and flat-spectrum sources, multi-frequency source counts and redshift distributions. It comprises three source populations with different evolutionary properties: steep-spectrum sources (SS-AGNs), flat-spectrum radio quasars (FSRQs) and BL Lacs. For sources of each population a simple power-law spectrum is adopted: $S \propto \nu^\alpha$, with $\alpha_{\text{FSRQ}} = \alpha_{\text{BLLac}} = -0.1$, and $\alpha_{\text{steep}} = -0.8$.

The epoch-dependent comoving LFs (in units of $\text{Mpc}^{-3} (\text{d log } L)^{-1}$) are modeled as double power-laws:

$$\Phi(L(z), z) = \frac{n_0}{(L(0)/L_\star(0))^a + (L(0)/L_\star(0))^b} \frac{d \log L(0)}{d \log L(z)}. \quad (3.6.1)$$

The evolution with redshift of the characteristic luminosity L_\star of each popu-

Table 3.9: Parameters of the evolutionary model for RL AGNs (Bonato et al. 2017). The luminosity L_* is in W Hz^{-1} .

Parameter	FSRQ	BLLac	SS-AGN
a	0.743	0.786	0.487
b	3.293	1.750	2.410
$\log n_0$	-11.262	-7.683	-5.866
$\log L_*(0)$	27.285	26.223	25.472
k_{evo}	-0.976	0.582	1.244
$z_{\text{top},0}$	1.749	1.054	1.063
δz_{top}	0.001	–	0.772
m_{ev}	-0.207	1	0.278

lation is described by the analytic formula

$$L_*(z) = L_*(0) \text{dex} \left[k_{\text{evo}} z \left(2z_{\text{top}} - z^{m_{\text{ev}}} z_{\text{top}}^{(1-m_{\text{ev}})} / (1+m_{\text{ev}}) \right) \right], \quad (3.6.2)$$

that entails a high- z decline of the comoving LF. The redshift, z_{top} , at which $L_*(z)/L_*(0)$ reaches its maximum is luminosity-dependent

$$z_{\text{top}} = z_{\text{top},0} + \frac{\delta z_{\text{top}}}{1 + L_*(0)/L}. \quad (3.6.3)$$

This expression allows for the evidences that the high- z decline of the space density is more pronounced and starts at lower redshifts for less powerful sources, in a way qualitatively similar to the *downsizing* observed for galaxies and for optically and X-ray selected quasars (see, e.g., de Zotti et al. 2010).

The best fit values of the parameters obtained by Bonato et al. (2017) are given in Tab. 3.9. The luminosity dependence of the peak redshift required by the data is substantial for the steep-spectrum population. In the case of FSRQs the evolution of the low luminosity portion of the LF is poorly constrained by the data; as a result, there is only a weak evidence of a luminosity dependence of z_{top} ($\delta z_{\text{top}} \ll 1$). As for BL Lacs, the data are not enough to constrain the parameters governing the luminosity dependence of the evolution. Thus, for this population, following Massardi et al. (2010), Bonato et al. (2017) have set $m_{\text{ev}} = 1$ and $\delta z_{\text{top}} = 0$.

We note that, in the framework of this luminosity-dependent luminosity evolution model, the steep slope of the bright end of the LFs ($L \gg L_*$), particularly of FSRQs and SS-AGNs, implies strong evolution. In the case of SS-AGNs we are in the luminosity range of FR II radio sources (Fanaroff & Riley 1974), nearly all of which have 1.4 GHz luminosity above $10^{25} \text{ W Hz}^{-1}$. These sources are believed to be typically powered by radiatively efficient accretion of cold gas from a geometrically thin, optically thick accretion disc. This accretion produces high-excitation emission lines; hence these objects are referred to as high-excitation radio galaxies (HERGs) (e.g. McAlpine 2013).

On the contrary, the relatively flat shape of the faint end of the LFs, particularly in the case of SS-AGNs, implies a weak evolution of sources with

$L \ll L_*$, consistent with the results by McAlpine (2013) and Best et al. (2014). These sources have luminosities in the range of FR I radio sources (Fanaroff & Riley 1974). They are currently interpreted as being powered by radiatively inefficient accretion flows at low Eddington ratios (Heckman & Best 2014). The bulk of their energetic output is in kinetic form, in two-sided collimated outflows (jets); they are therefore referred to as “jet-mode” AGNs. The strong emission lines normally found in powerful AGNs are generally absent; they are thus referred to as low-excitation radio galaxies (LERGs).

3.6.2 Number counts

The model described in the previous sub-section has been exploited to simulate the number counts of AGNs at 1.4 GHz. In practice we adopted the following procedure. Consider a small flux density interval $\Delta S_j = S_{\max,j} - S_{\min,j}$ and let $\Phi(L|z)$ be the luminosity function per dex (i.e. per unit $d \log(L)$) at the redshift z . The contribution to the counts from the small redshift interval Δz_i is, approximately:

$$\Delta N(S)_{i,j} = \Omega \Phi(L|z_i) \left(\frac{dV(z)}{dz} \right)_{z=z_i} \Delta \log(L_{i,j}) \Delta z_i, \quad (3.6.4)$$

where Ω is the solid angle of the simulation, z_i is the center of the redshift bin, $dV(z)/dz$ is the volume element per unit solid angle and $\Delta \log(L_{i,j}) = \log[L(S_{\max,j}, z_{\max,i})] - \log[L(S_{\min,j}, z_{\min,i})]$. Obviously the maximum and minimum values refer to the boundaries of the corresponding bins. The total counts within ΔS_j and Ω are then

$$N(S)\Delta S_j = \sum_i \Delta N(S)_{i,j}. \quad (3.6.5)$$

The $N(S)\Delta S_j$ sources were then randomly distributed within the $\Delta \log(L)$ and associated to the halos in the volume corresponding to $\Omega\Delta z_i$ area. The accuracy of this approximation was tested comparing the derived $N(S)\Delta S_j$ with the model counts and found it to be good for $\delta \log z \simeq 0.006$ and $\delta \log S = 0.11$.

To make the simulations more realistic we decided to go beyond the simple approximation of a single spectral index for all sources of each population. The approach we have chosen also allows us to take into account systematic variations with frequency of the spectral index distributions, clearly demonstrated by multi-frequency observations (e.g. Bonavera et al. 2011; Bonaldi et al. 2013; Massardi et al. 2011, 2016). The effective spectral index between the frequencies ν_1 and ν_2 of sources of a given population with flux density S_1 , within dS_1 , at ν_1 ,

$$\alpha_{\text{eff}}(\nu_1, \nu_2) = \log(S_2/S_1) / \log(\nu_2/\nu_1), \quad (3.6.6)$$

was computed finding the flux density S_2 at ν_2 such as $N_1(S_1)dS_1 = N_2(S_2)dS_2$. Thus $\alpha_{\text{eff}}(\nu_1, \nu_2)$ is the single spectral index relating the counts at ν_1 to those at

ν_2 . The differential source counts $N(S)$ at the two frequencies were obtained from models fitting the data: the updated Massardi et al. (2010) model (Bonato et al. 2017) up to 5 GHz and the De Zotti et al. (2005) model at higher frequencies.

We adopted a Gaussian spectral index distribution with mean $\alpha(\nu_1, \nu_2)$ and dispersion σ ; the mean spectral index is related to $\alpha_{\text{eff}}(\nu_1, \nu_2)$ by (Kellermann 1964; Condon 1984; Danese & de Zotti 1984):

$$\alpha_{\text{eff}}(\nu_1, \nu_2) = \alpha(\nu_1, \nu_2) - \sigma^2(1 - \beta) \ln(\nu_2/\nu_1), \quad (3.6.7)$$

where β is the slope of the differential number counts at S_1 , computed from the models. For each population, α_{eff} is the fixed spectral index used in the models. The dispersion was set at $\sigma = 0.25$ for all populations, consistent with the results by Ricci et al. (2006) after allowing for the contribution of measurement errors to the observed dispersion. Then, $\alpha(\nu_1, \nu_2)$ was obtained from eq. (3.6.7). As shown by this equation, the mean spectral index varies with flux density because of the variation of the slope, β , of the counts. If $\nu_1 < \nu_2$ the effective spectral index, α_{eff} , is larger than the mean value α , as a consequence of the fact that higher frequency surveys favour sources with “harder” spectra.

The simulations cover the frequency range from 150 MHz to 20 GHz. We have taken 1.4 GHz as our reference frequency and reached 20 GHz in two steps. First we have computed the mean spectral indices of between 1.4 and 4.8 GHz in steps of $\delta \log(S) = 0.08$; the variations of β over this flux density interval are negligibly small. The maximum variation of the mean $\alpha(1.4, 4.8)$ over the full flux density range of our simulations is $\delta\alpha \simeq 0.08$. We have then repeated the procedure between 4.8 and 20 GHz; in this case $\delta\alpha \simeq 0.09$.

To each simulated source drawn from the redshift-dependent 1.4 GHz (rest-frame) LF of its population, we have attributed a spectral index extracted at random from the Gaussian distribution with mean $\alpha(1.4, 4.8)$ and dispersion σ up to 4.8 GHz, and a second spectral index extracted from the 4.8–20 GHz distribution up to 20 GHz. After having checked that the 1.4–4.8 GHz distribution yields number counts in good agreement with observations, we have used it also to assign monochromatic luminosities down to 150 MHz.

In Fig. 3.14 the counts from the simulation are compared with those given by the model and with the data. Note that the simulated area ($5 \times 5 \text{ deg}^2$) is too small to adequately sample sources brighter than a few hundred mJy at 1.4 GHz.

3.6.3 Polarization

We also include polarization information for each simulated source. For steep-spectrum sources the polarized flux densities were generated by sampling from the polarization fraction distribution at 1.4 GHz by Hales et al. (2014). This distribution was found to be independent of flux density down to total intensity $\sim 10 \text{ mJy}$ and perhaps even 1 mJy . In the absence of better information, we have assumed that this distribution holds at all the frequencies. In the case of flat-spectrum sources we have exploited the high

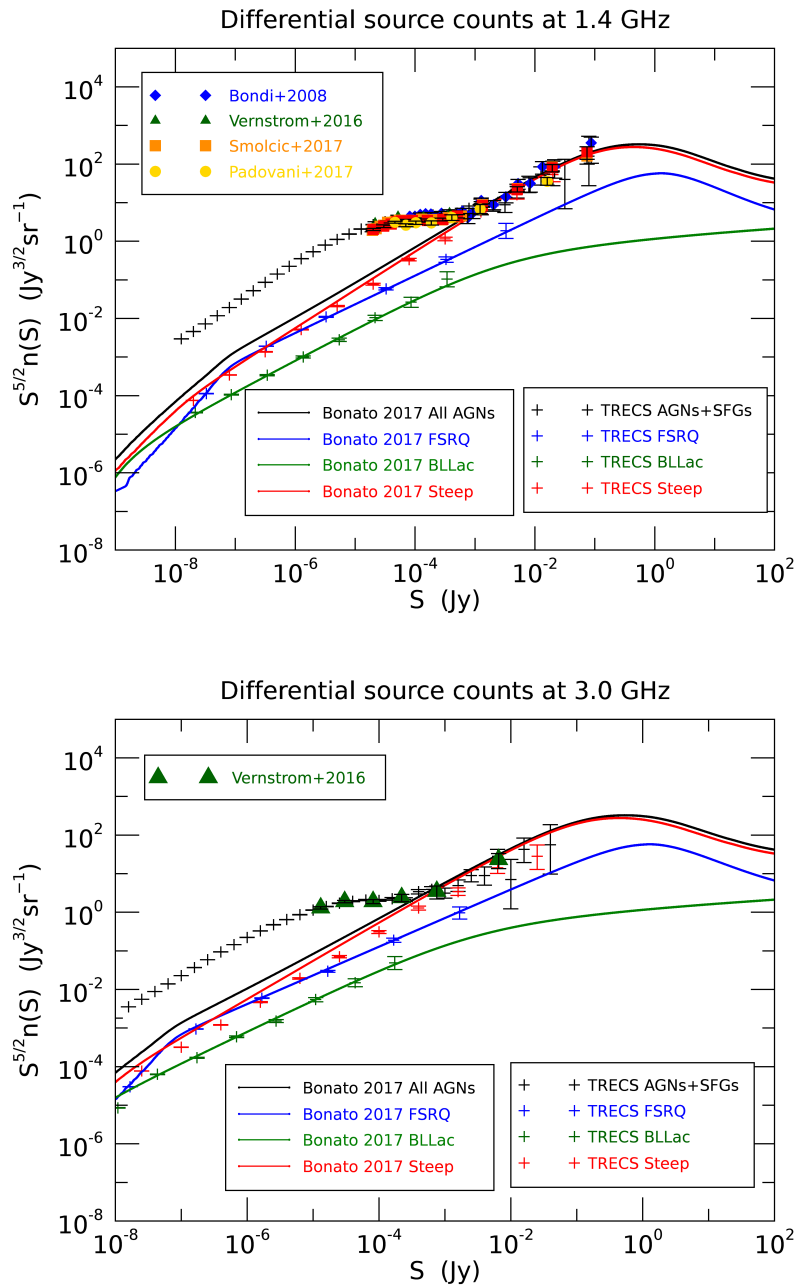


Figure 3.14: Comparison between source counts in total intensity at 1.4 (*upper panel*) and 3 GHz (*lower panel*) from the T-RECS generated catalogues on a 25 deg² patch (black pluses are from the sum of all the AGNs and star forming galaxies), red pluses for steep-spectrum AGNs, blue pluses for FSRQ and green pluses for BL Lacs. Solid curves refers to the Bonato 2017 model for all the AGNs (black solid line), the steep-spectrum objects (red solid line), the FSRQs (blue solid line) and the BL Lacs (green solid line). Any other symbol refers to source counts reported in literature, as indicated in the legend.

sensitivity polarization measurements in seven bands (centered at 2.1 , 5.5, 9, 18, 24, 33 and 38 GHz) of a complete sample of 104 compact extragalactic AT20G sources brighter than 200 mJy at 20 GHz, with $b < -65^\circ$ (described in the previous sections). Again, no indications of a flux-density dependence of the distribution of polarization fractions was found. Hence polarized flux densities at the first four frequencies were assigned sampling the observed distributions and interpolating at intermediate frequencies. The distribution at 1.4 GHz was computed using the polarization measurements by Condon et al. (1998) for a complete sample of 826 flat-spectrum sources brighter than 200 mJy at 20 GHz, drawn from the Australian Telescope Compact Array 20 GHz (AT20G) survey (Murphy et al. 2010). Below 1.4 GHz the polarization fraction of each source was kept constant to the 1.4 GHz value.

Coupling all these things with the model, we get a marginal match with the observationally determined counts in linear polarization (Grant et al. 2010; Stil et al. 2014; Hales et al. 2014, cf. Fig. 3.15) at 1.4 GHz (where the steep-spectrum objects dominate). Indeed the T-RECS simulation is currently under the last phase of testing before the release, hence we are still working to understand the origin of the discrepancy with Stil et al. (2014) (and Hales et al. (2014) as well) findings: as far as we understand, there seems to be a residual systematic factor of underestimation.

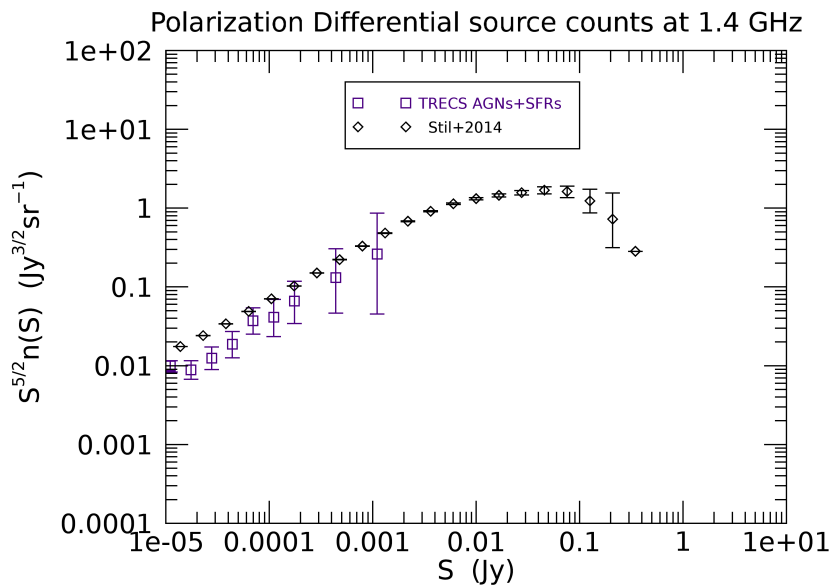


Figure 3.15: Preliminary comparison between source counts in polarization at 1.4 GHz from the T-RECS generated catalogues (on a 1 deg^2 patch): indigo squares are from the sum of all the AGNs and SF galaxies and black diamonds represent polarization source counts obtained from the NVSS survey by using a stacking technique.

Chapter 4

ALMA follow-up at 100 GHz of a complete sample of 32 radio sources

In this chapter we present the ALMA high sensitivity follow up of a complete sample of “faint PACO” sources at 97.5 GHz (Band 3), extending our spectral and polarimetric characterization to higher frequencies. We will compare our results with the very few information we can find in literature at these high frequencies, such as the PdBI observations of Trippe et al. (2012) of a $S_{90\text{GHz}} > 200\text{ mJy}$ complete sample of 86 sources, who found an average fractional polarization level of $\sim 2 - 7\%$, higher for BLLac ($\sim 7\%$) than for QSO ($\sim 5\%$) or Seyfert ($\sim 3\%$). The size scales relevant for the polarization emission measurements are found to be comparable to those of interest for total intensity flux density measurements. The ALMA Cycle 3 observations allow us to extend the PdBI findings to a fainter flux density limit, also allowing a better analysis of the population properties. We also compare our findings with Bonavera et al. (2017) which applies the stacking technique to the Planck all-sky maps in each channel (from 30 GHz to 353 GHz) around detected sources at 30 GHz, whose flux densities are collected in the Planck Catalogue of Compact Sources (PCCS2). By including the data available on our sources at lower frequencies we are able to (at least statistically) reconstruct the source polarization spectral behaviour across a wide frequency range (more than 3 decades).

4.1 Data analysis

We adopt a 3σ level for detections in polarization. The median sensitivity in polarization for our ALMA observations (by including the calibration error), is $\simeq 0.4\text{ mJy}$. We reach a detection rate of $\simeq 97\%$: only 1 object is non-detected, AT20GJ054641-641522. This is a quasar found to be largely non-detected in polarization also at our ATCA frequencies in both the 2014 and 2016 campaigns. In fact its flux density is fainter than 2 mJy (at 5σ in the 33 – 38 GHz band) in the 2016 campaign and even fainter than 0.7 mJy (at

5σ , again in the 33 – 38 GHz band) in 2014 observations. We exclude from the analysis the FRII source AT20GJ040848-750720, which was resolved by ALMA both in total intensity and polarization: we defer its discussion to the sec. 4.3, since comparing emissions which are clearly non co-spatial may hamper the analysis of derived quantities, e.g. the polarization fraction. In the following sub-sections we are going to extend the recipes presented in the papers Galluzzi et al. (2017) and Galluzzi et al. (2018) at ~ 100 GHz, hence we complement ALMA data with ATCA datasets of both September 2014 and March and April 2016, in order to characterize the spectro-polarimetric properties of this smaller sample from 2 GHz (epoch: March and April 2016), passing through 5.5 – 38 GHz (epoch: September 2014) up to 104.5 GHz (ALMA observations), and including GLEAM counterpart for all the sources.

4.1.1 Spectral behaviour

The ATCA and ALMA observations are not simultaneous. While ALMA observations were carried out at the end of August and at the end of September 2016, ATCA observations at 33 – 38 GHz were performed at the beginning of April 2016 for half of the present sample and at mid July 2016 for the other half. The whole sample of 32 objects was observed at 2.1 and 5.5 – 9 GHz in 2016 March-April, and only 13 objects have measurements repeated in July.

At frequencies higher than 20 GHz, variability frequently exceeds 10% even on time scales of few months. Therefore we have not attempted a joint fit of ALMA and ATCA data, also on account of the ~ 50 GHz frequency gap between the two data sets.

Figure 4.2 shows, for each source in our sample, a collection of total intensity and polarization measurements with, at the bottom, a plot of the linear polarization fractions and, below it, a plot of the position angles as a function of frequency.

The plotted data in total intensity include: the ALMA and ATCA 2016 measurements (filled red circles); the GLEAM flux densities (filled orange circles); the Sydney University Molonglo Sky Survey (SUMSS) flux density (filled yellow circle); the ATCA 2014 observations (orange squares); the PACO observations (2009-2010; blue stars).

The polarization data include: ATCA 2016 and ALMA observations (filled black circles; upper limits are shown as filled downwards-pointing black triangles); ATCA September 2014 observations (black squares).

In the linear polarization fraction panels, filled purple diamonds refer to ALMA and ATCA 2016 observations and purple squares refer to September 2014 ATCA observations. Upper limits are shown as downward purple triangles.

As for the polarization angle, the filled indigo diamonds refer to ATCA 2016 and ALMA observations and the indigo squares to the September 2014 ATCA observations.

The ALMA flux densities of most (26 out of 32) sources are somewhat in excess of expectations based on fits of the ATCA 2016 total intensity measurements. The median excess is of $\sim 40\%$, with a maximum of $\simeq 98\%$.

The polarization fraction however indicates that we are still dealing with synchrotron emission from the active nucleus. The unpolarized free-free and the weakly polarized dust emission associated to star formation in the host galaxies are expected to be much fainter. The excess is thus suggestive of a different component coming out at a few mm wavelengths.

For 3 sources the difference between expected and observed flux density is less than 10%, and may be accounted for by variability and/or measurement errors. Only 3 objects, namely AT20GJ050754-610442, AT20GJ051644-620706 and AT20GJ062307-643620, have ALMA flux densities fainter than expected. The deficits are of $\simeq 10\%$, 18% and 81% , respectively. However, even in the latter case there is no sign of a spectral break: the spectral index between 36.5 and 97.5 GHz is $\alpha_{36.5}^{97.5} \simeq -0.19$.

Figure 4.1 compares the spectral indices in total intensity and in polarization between 36.5 GHz (the central frequency of ATCA 2016 observations) and 97.5 GHz (the central frequency of ALMA observations). Total intensity spectral indices, $\alpha_{36.5}^{97.5}$, are, with few exceptions, in the range $-0.50 - 0.50$. In polarization there are a couple of sources with spectral indices, $\alpha_{p,36.5}^{97.5}$ as steep as -1.5 or even -2.0 .

There are also two sources with $\alpha_{p,36.5}^{97.5} \geq 1$ and 7 sources undetected in polarization at 35 or 38 GHz but detected at 97.5 GHz, i.e. with only a lower limit to $\alpha_{p,36.5}^{97.5}$. Only part of these lower limits may be understood in terms of the higher sensitivity of ALMA observations compared to the ATCA ones. In other cases they provide further support to indications of an additional synchrotron component showing up at frequencies of $\sim 200\text{--}300$ GHz in the source frame.

Figure 4.3 shows for all (unresolved or barely resolved) the sources ordered in RA the Stokes I (with superimposed polarization vector displaying the magnitude and direction of linear polarization), Q and U images.

4.1.2 Polarization fraction

The knot-like synchrotron emission at higher frequencies/energies are generally closer and closer to the base of the AGN jet. In those regions the ejection speed are typically closer to the speed of light and magnetic field should be more ordered to support the radiative process. As a consequence, an increase of the polarization fraction is, at least in principle, expected with frequency in these regimes. There is indeed another phenomenon which is poorly understood even in the non-relativistic regime: the turbulence. Its typical effect consists in an energy transport from higher spatial scales towards dissipation on smaller scales and, depending on the particular spectrum assumed, it may hamper ordering effects in magnetic field, lowering the polarization fraction. However, as stressed in the previous chapters, the lack of polarimetric data on large complete samples prevented any firm conclusion about the existence or not of such trend. Here we provide one of the first unbiased assessment about observed polarization fractions at ~ 100 GHz taking into account our complete sample of 32 objects. The median polarization fraction measured by ALMA for the full sample is $2.2 \pm 0.6\%$, close to the

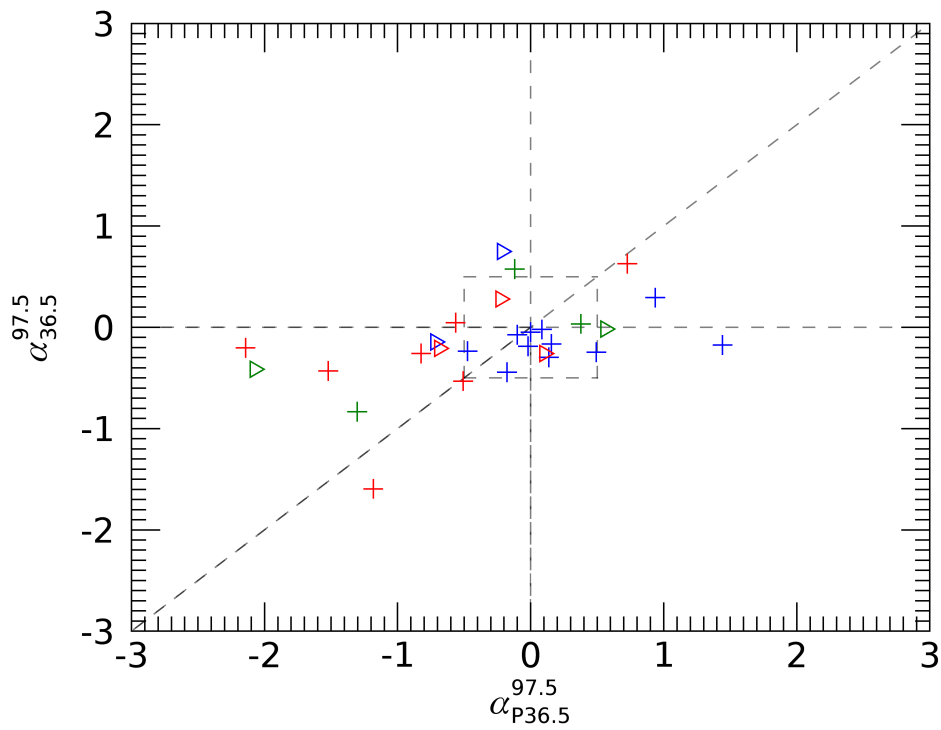


Figure 4.1: Colour-colour plot showing spectral indices in total intensity and polarization. Different colours refers to different sub-class in total intensity: red for steep, green for peaked and blue for flat-spectrum objects. Rightward triangles are for lower limits for spectral indices in polarization due to non-detections at ATCA frequencies.

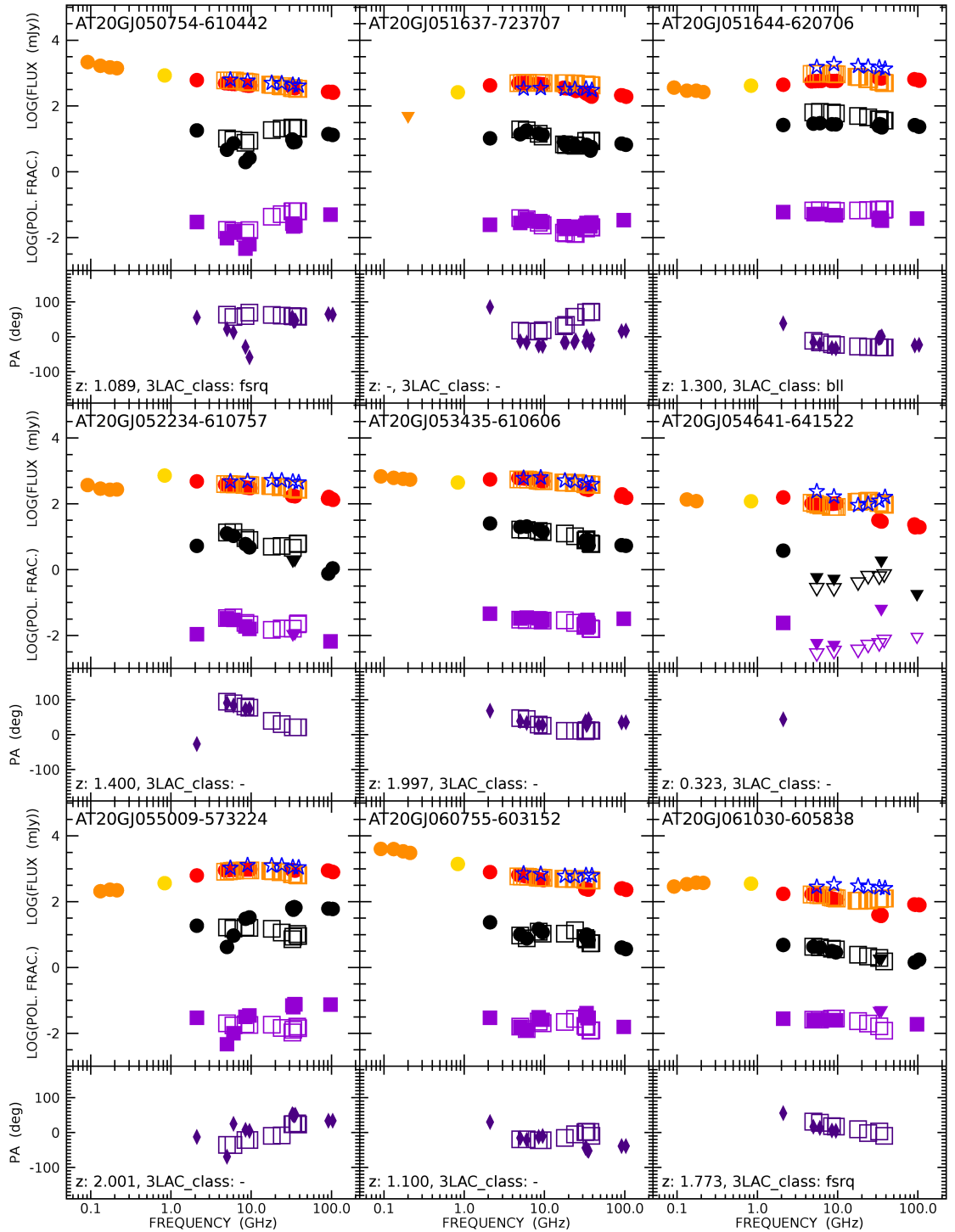


Figure 4.2: Spectra in total intensity and polarization, polarization fraction and polarization angle for the 32 objects of the faint PACO sample, observed in August and September 2016 with ALMA. The error bars are not displayed since they are smaller than symbols. **Total intensity:** filled red circles indicate ATCA 2016 and ALMA observations. The filled orange circles show MWA/GLEAM flux densities while the yellow one is for SUMMS. Orange squares are ATCA 2014 observations and blue stars are PACO observations (2009-2010). (*Continued...*)

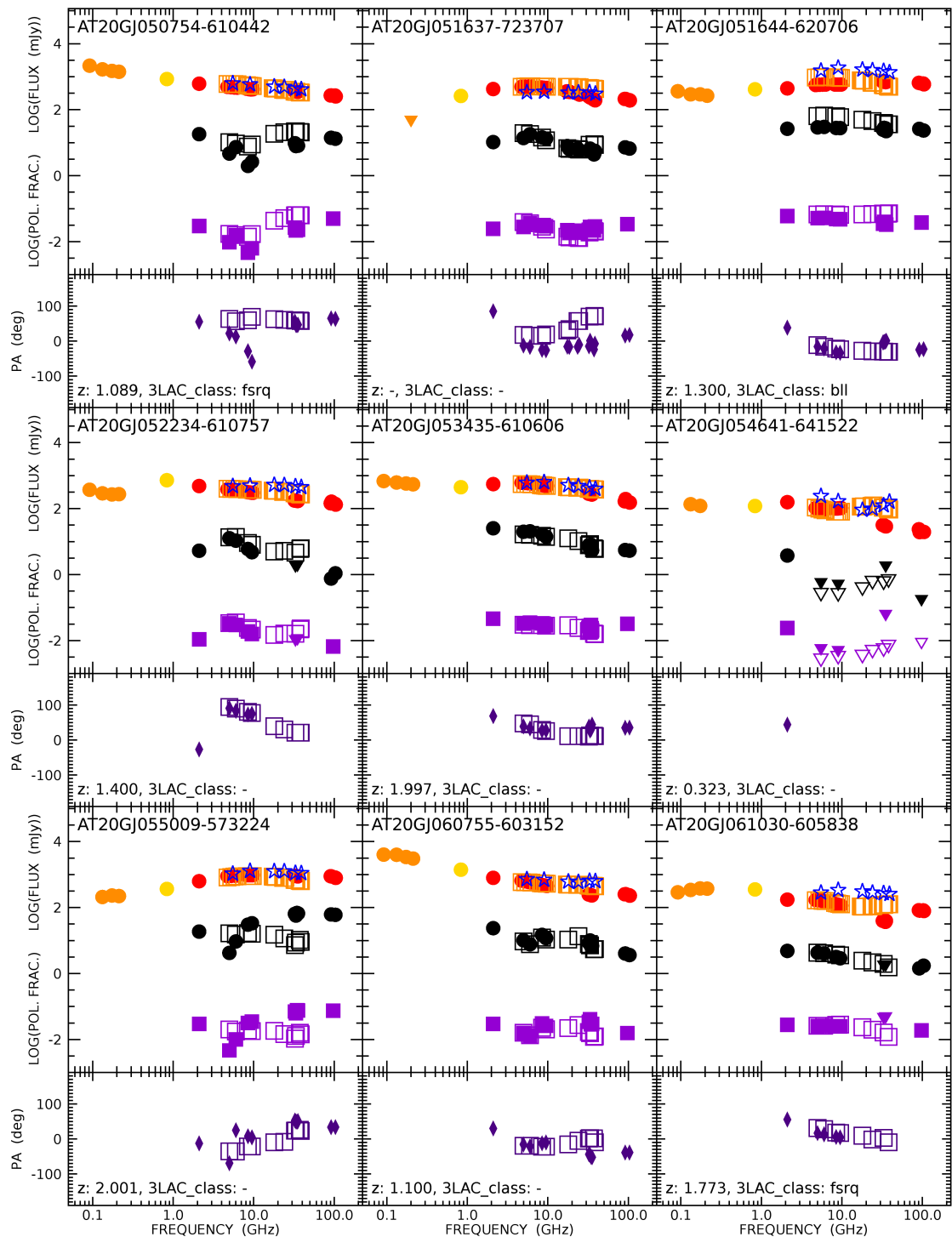


Figure 4.2: (Continued). **Polarization (flux density):** filled black circles refer to ATCA 2016 and ALMA observations. Upper limits are shown as black filled downwards triangles. Black squares represent previous ATCA observations (September 2014). (Continued...)

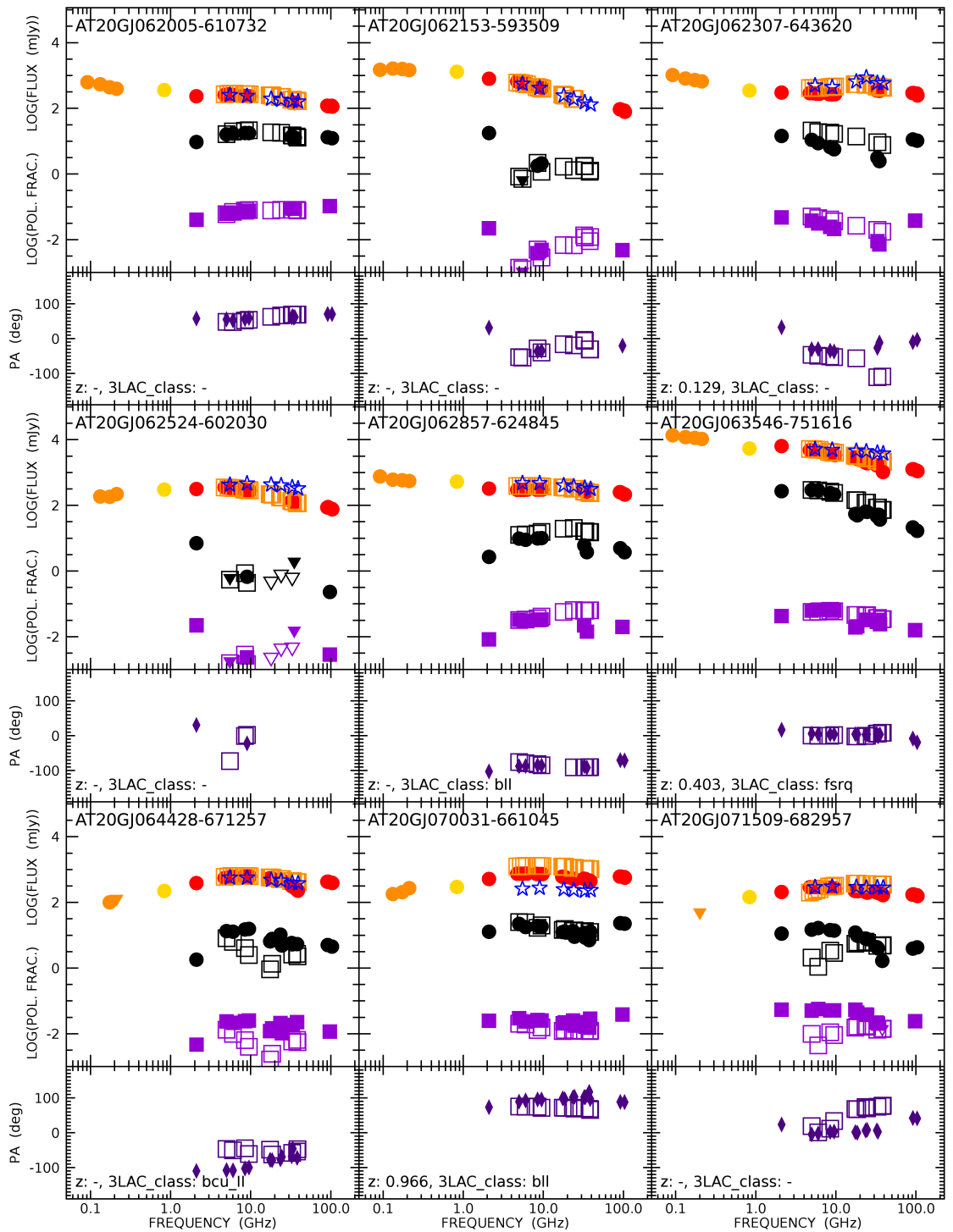


Figure 4.2: (*Continued*). **Linear polarization fractions:** filled purple diamonds with upper limits shown as downwards filled triangles for ALMA and ATCA observations; purple squares with upper limits shown as downward purple triangles for September 2014 ATCA observations. **Polarization angle:** filled indigo diamonds for ATCA 2016 and ALMA observations; indigo squares for previous September 2014 ATCA observations.

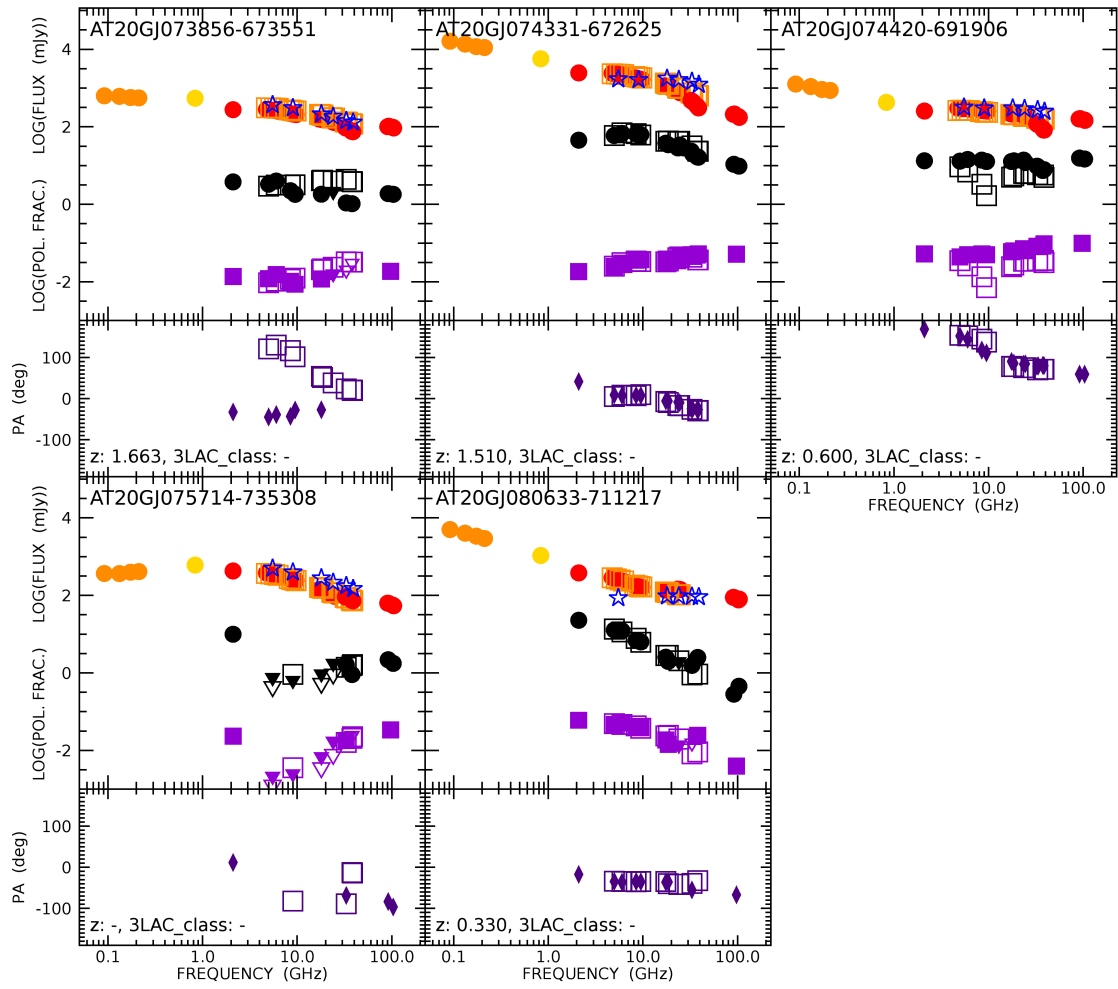


Figure 4.2: (Continued).

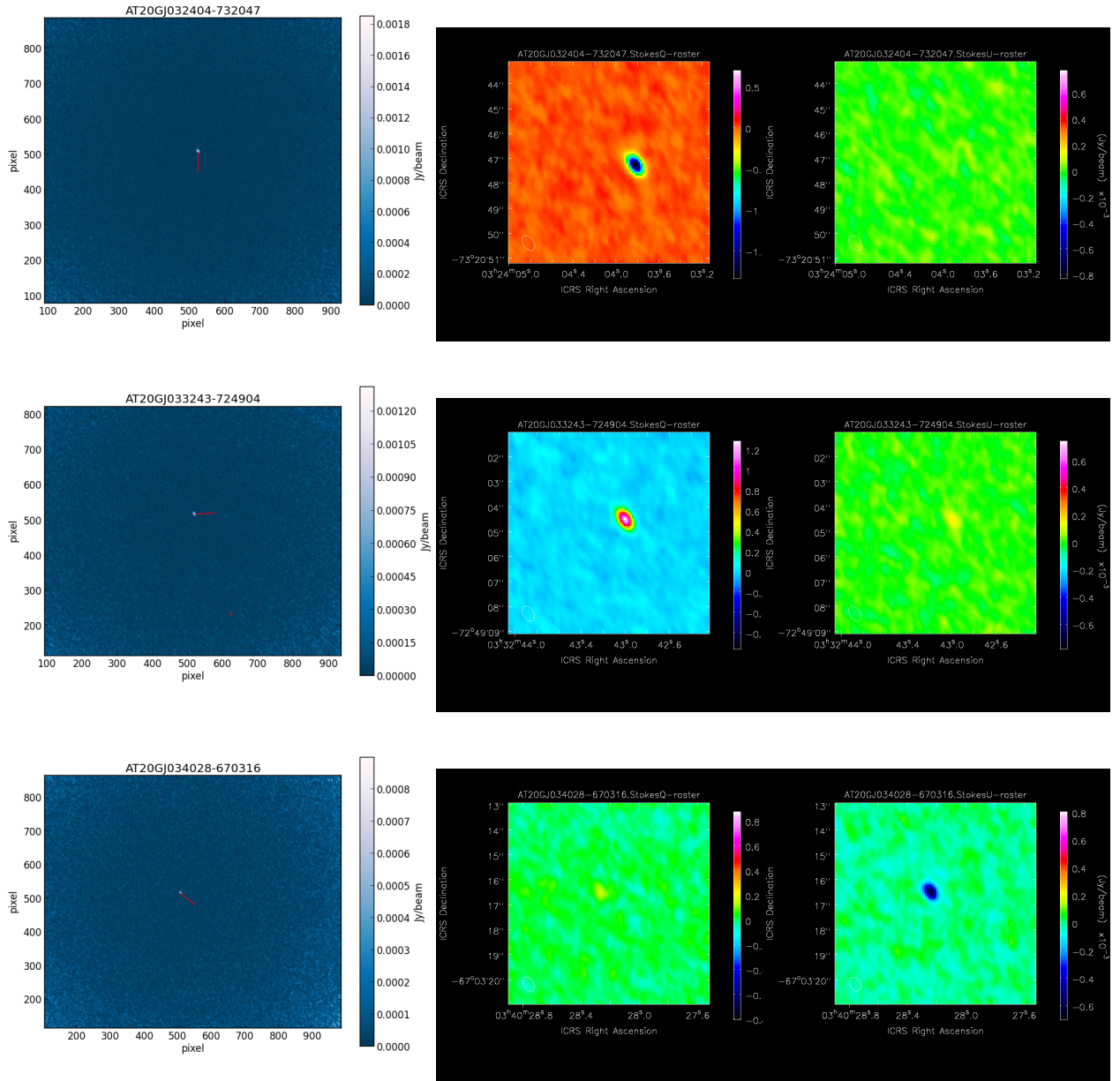


Figure 4.3: Images for Stokes I, Q and U for the 31 objects unresolved (or barely resolved) observed in September 2016 with ALMA (see the sec. 4.3 for images of the well resolved object AT20GJ040848-750720). When both Stokes are detected (the polarization angle can be determined), I maps also display the polarization vector (intensity being proportional to the linear polarized flux density) thanks to the software KAFE (the Keywords of Astronomical FITS-images Explorer, Burkutean & the Italian ALMA Regional Centre node 2018, submitted to Journal of Astronomical Telescopes, Instruments, and Systems).

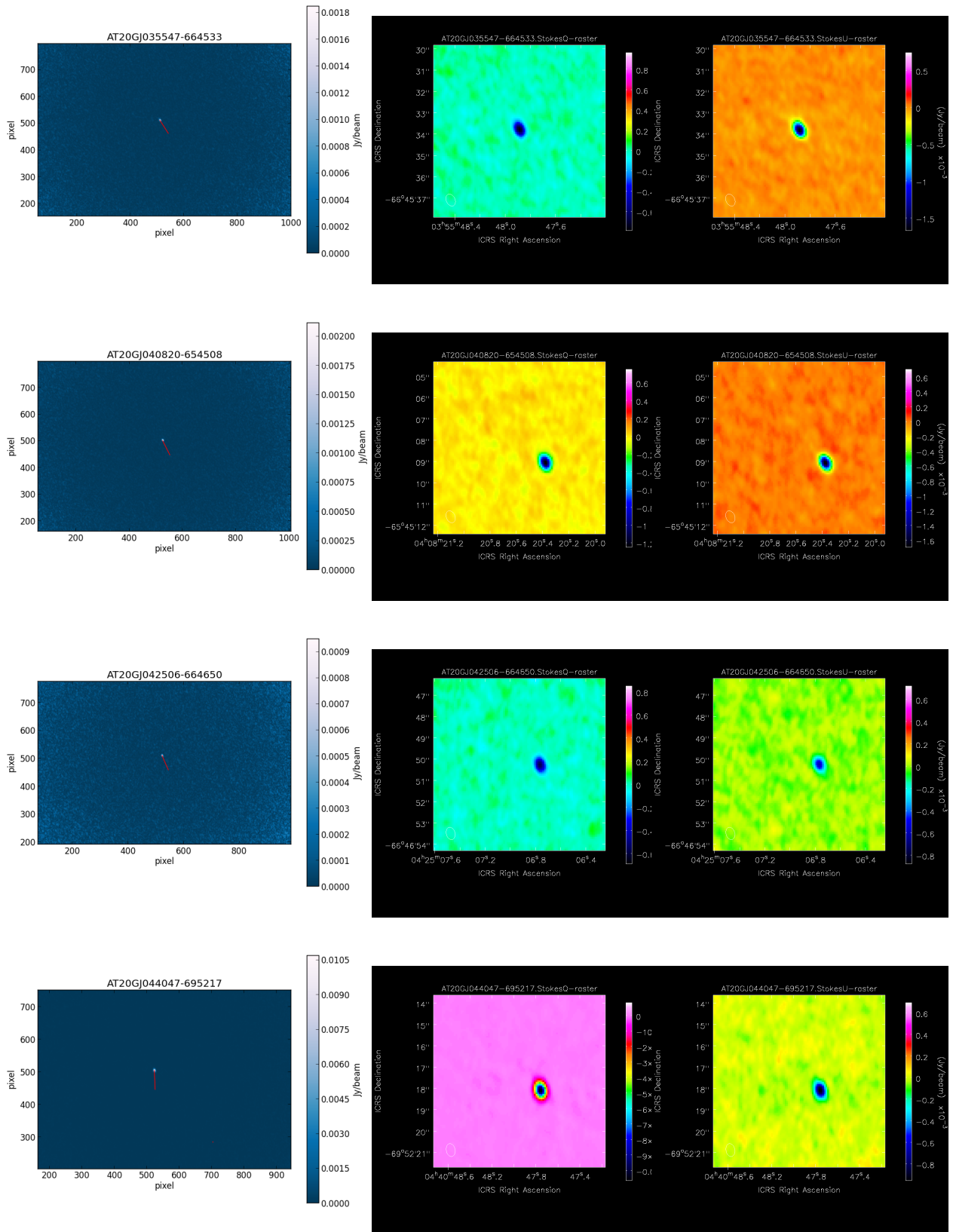


Figure 4.3: (Continued).

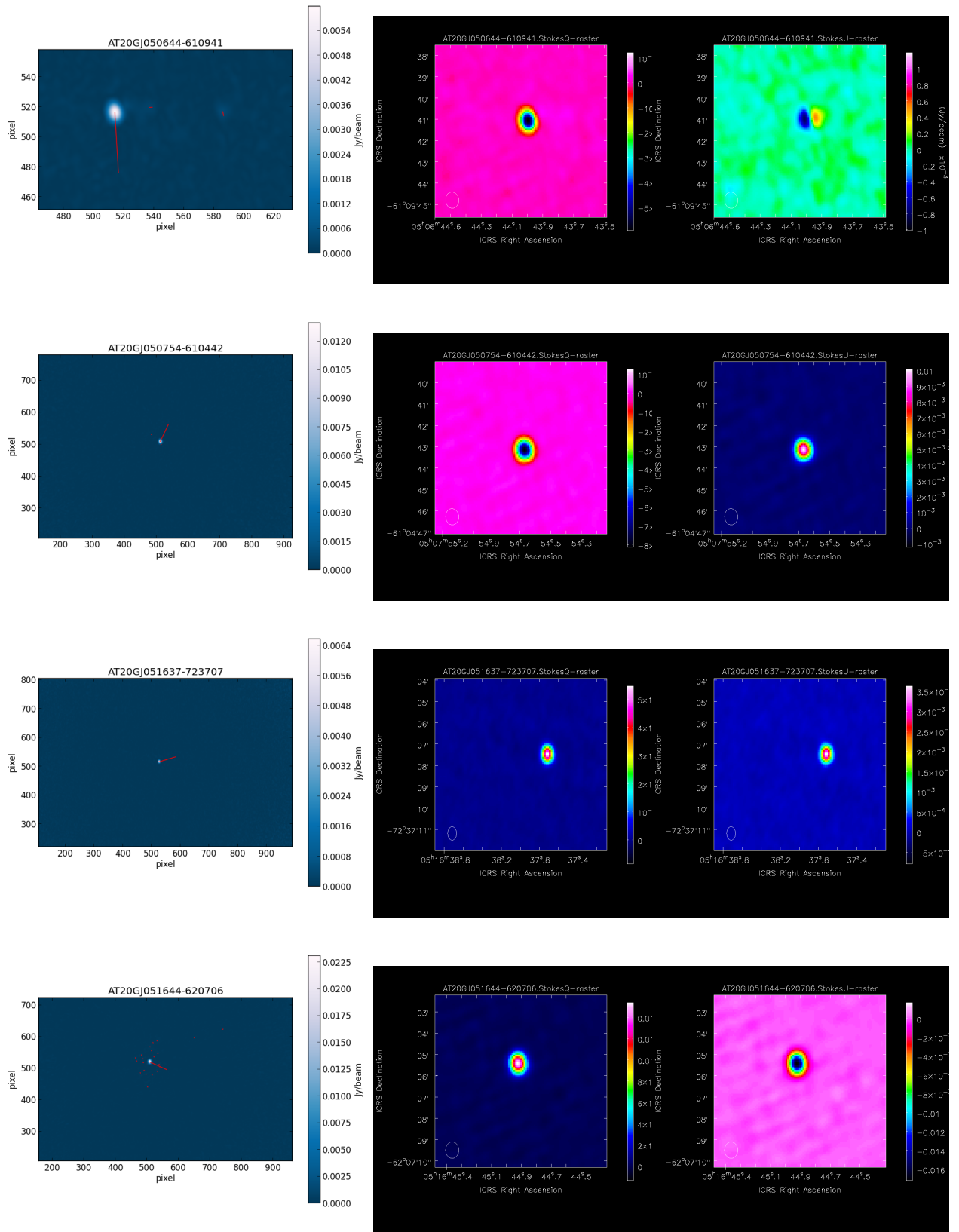


Figure 4.3: *Continued.*

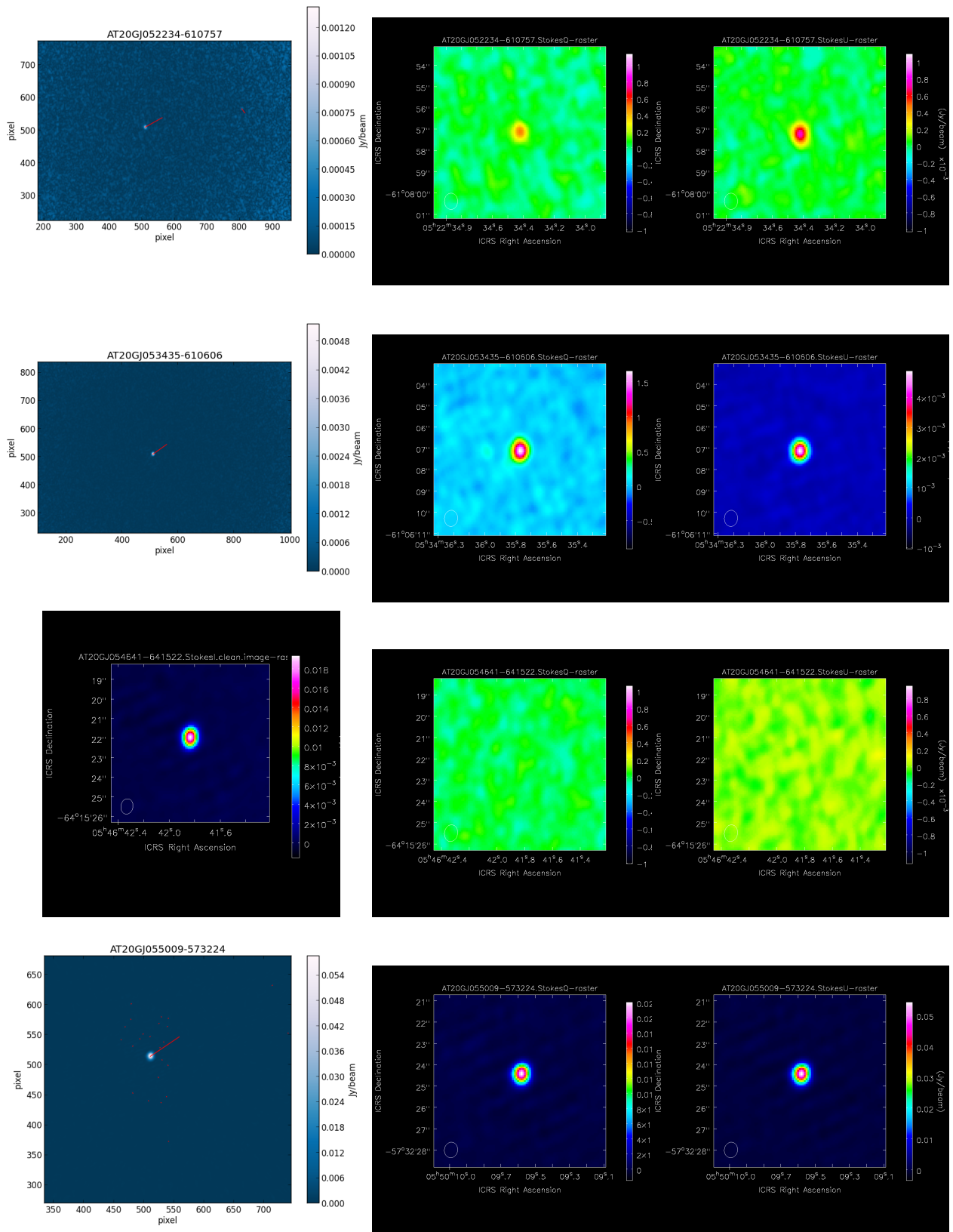


Figure 4.3: (Continued).

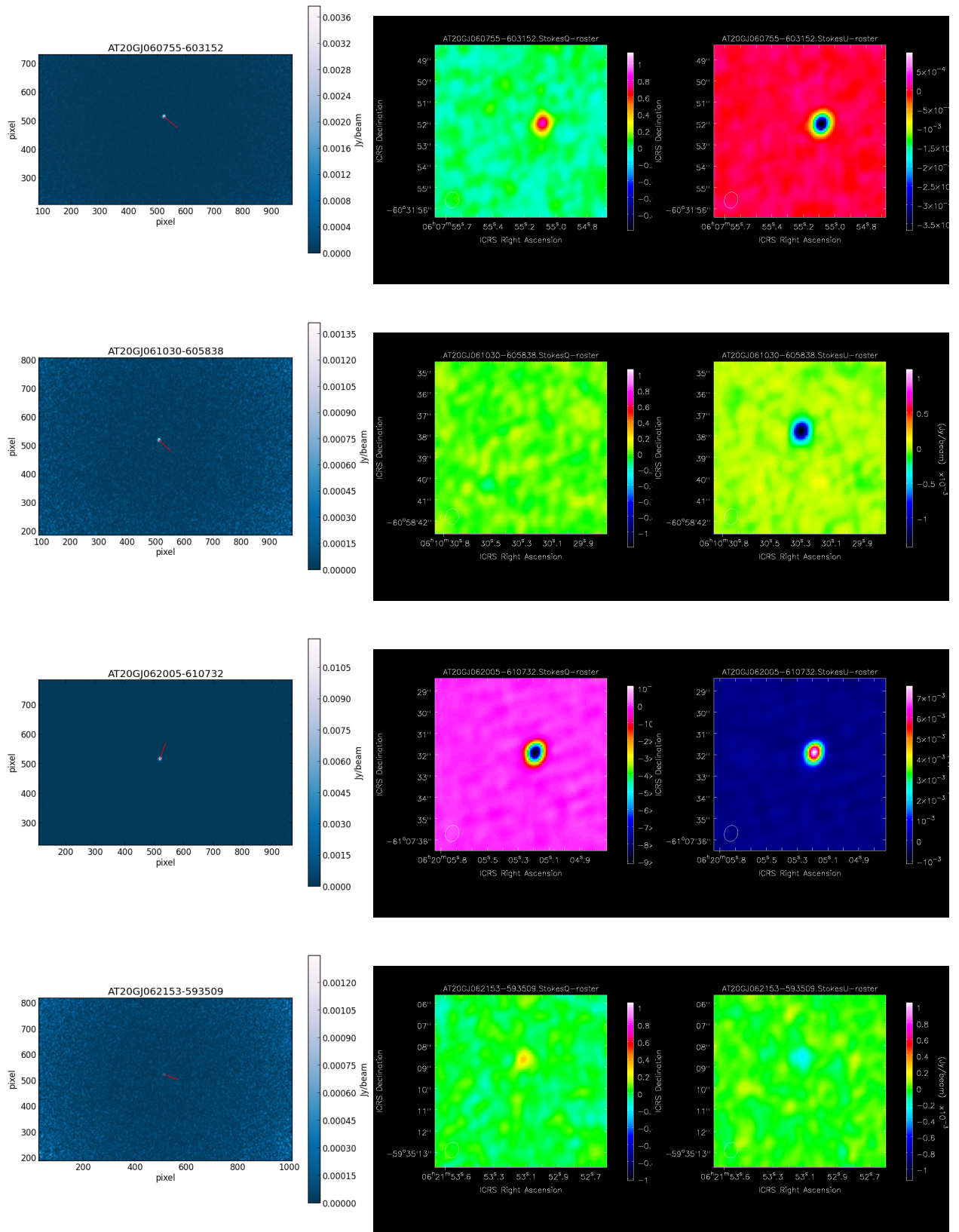


Figure 4.3: (Continued).

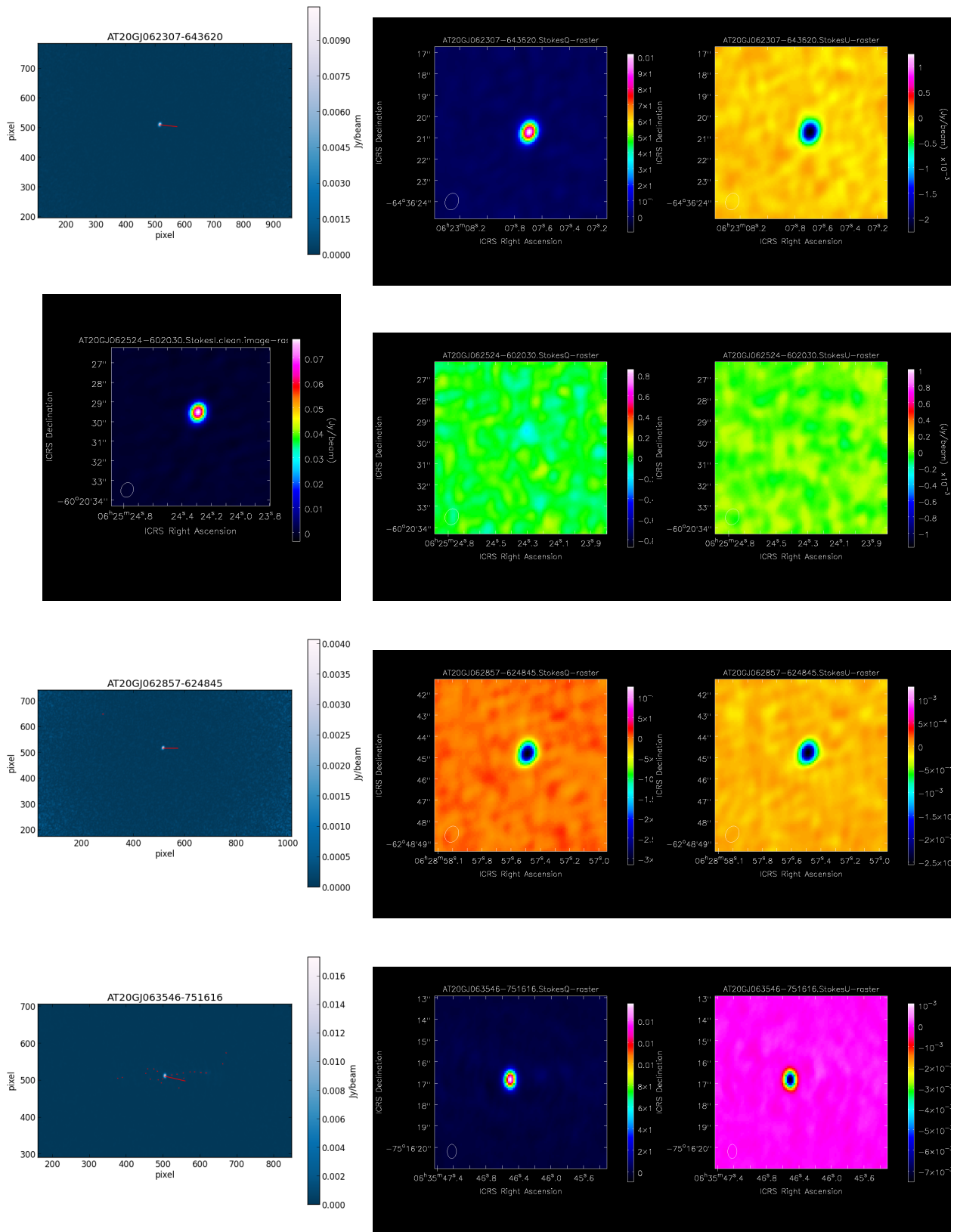


Figure 4.3: (Continued).

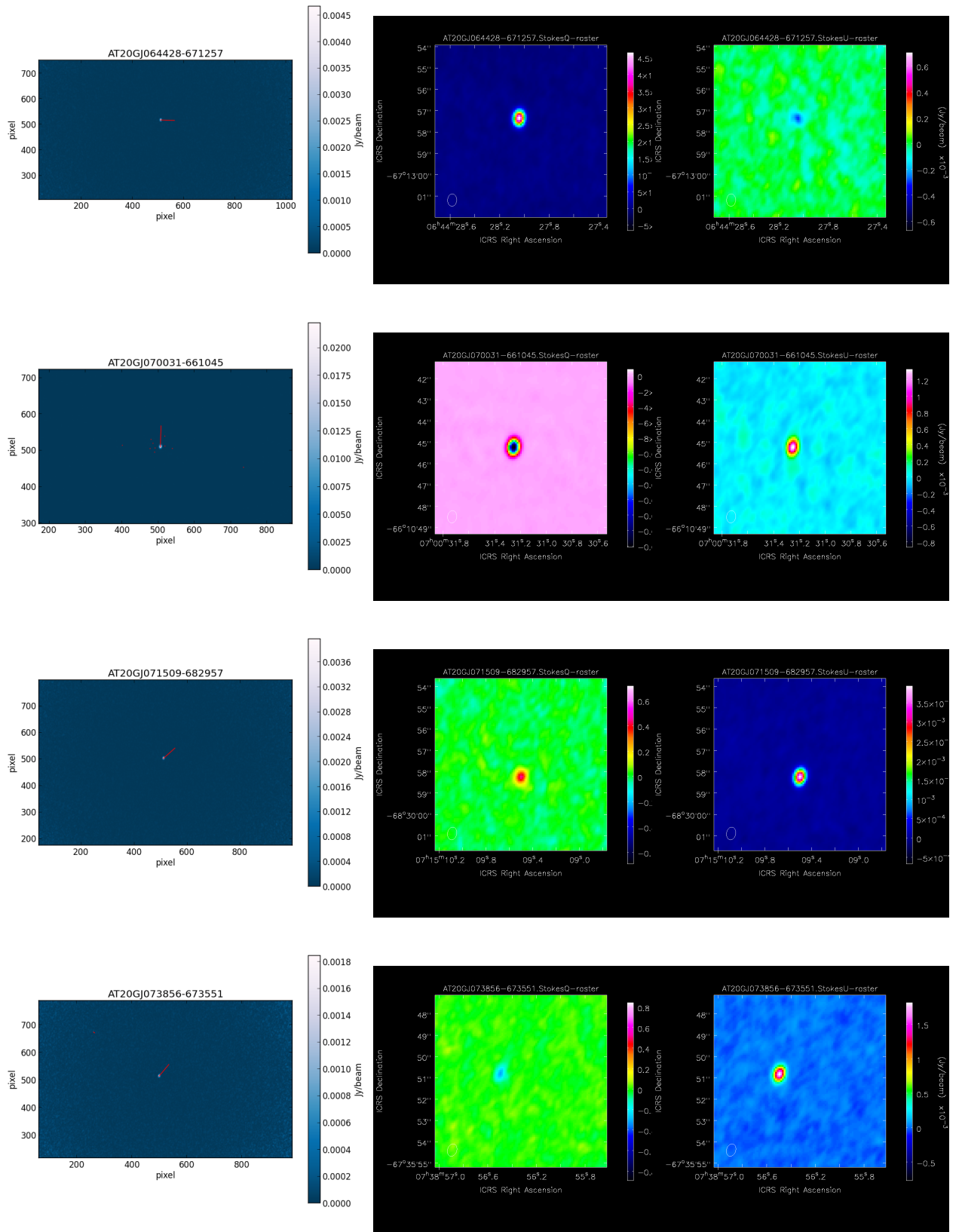


Figure 4.3: (Continued).

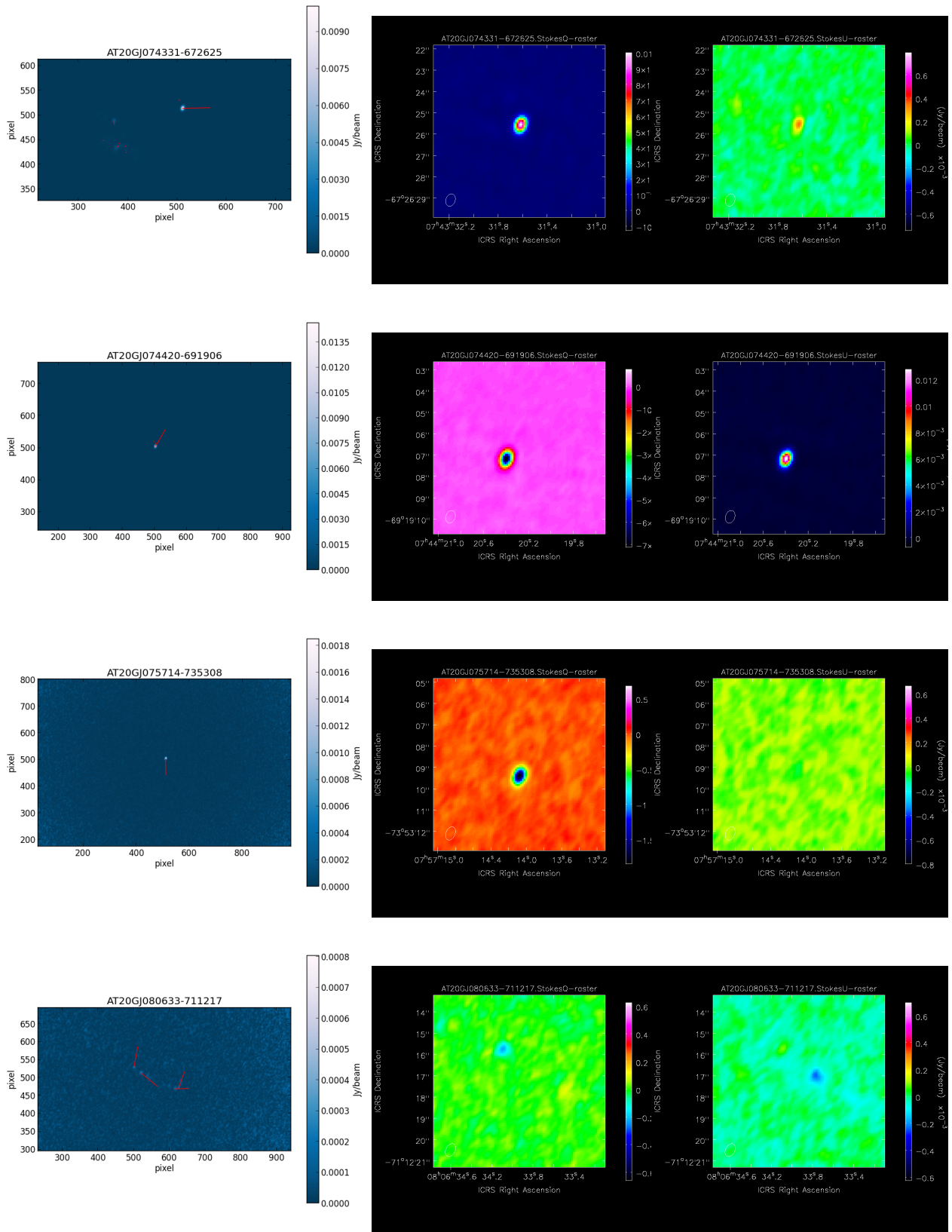


Figure 4.3: (Continued).

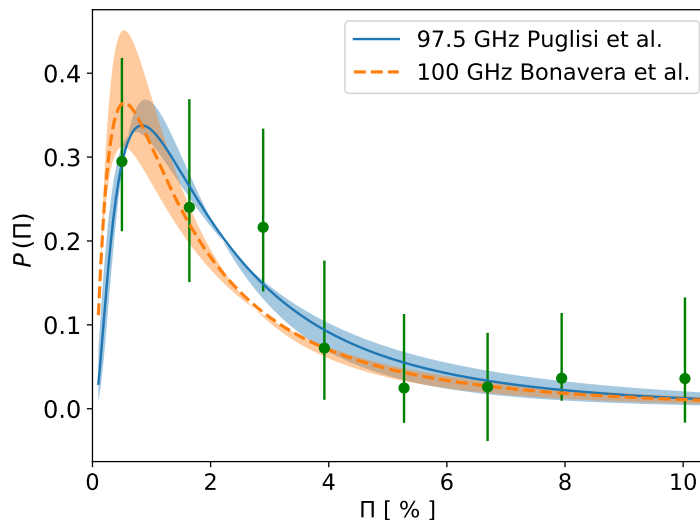


Figure 4.4: Distribution of the percentage polarization fraction at 97.5 GHz obtained with a bootstrap and re-sampling of the observed distribution of the polarization fractions (green points). The lognormal fit is shown by the blue solid line (the shaded area represents the 1σ uncertainty in the fitting curve). We also plot the distribution obtained by Bonavera et al. (2017) (the orange solid line with the relative 1σ shaded area).

median value at 38 GHz for the same sample (2.09%) based on measurements by Galluzzi et al. (2018). Our result is in good agreement with estimates obtained by stacking analyses of *Planck* maps at 100 GHz by Bonavera et al. (2017, 1.8 (+0.4, -0.3)%) and by Trombetti et al. (2017, $1.8 \pm 0.5\%$).

We also estimated the distribution of the percentage polarization fraction, Π , using a bootstrap and re-sampling approach. Each detection was associated with the mean value of a Gaussian with σ given by the error on the polarization fraction. When only an upper limit is available we used a uniform distribution between 0 and the 3σ upper limit. We then generated 1000 simulated data sets by resampling with repetitions the distributions of percentage polarization fractions of each source. The results of the simulation are reported in Fig. 4.4 and in Tab. 4.1. In Fig. 4.4 we also show the best fit lognormal function:

$$\mathcal{P}(\Pi) = \text{const} \frac{1}{\Pi \sigma \sqrt{2\pi}} \exp \left[-\frac{\ln^2(\Pi/\mu)}{2\sigma^2} \right], \quad (4.1.1)$$

with $\text{const} = 0.86$, $\mu = 2.05\%$ and $\sigma = 0.97$.

In chap. 3 (cf. Galluzzi et al. 2018) we briefly discussed the topic of spectral classification in this new era of a wider range in frequency coverage both in total intensity and polarization, arguing that purely spectral index based classifications are poor in investigating the physics of these objects. We thus proposed a novel method for inferring the minimal number of synchrotron components needed to explain the spectro-polarimetric behaviour of a given object. This more physically based criterion allowed us to find clear indications, e.g. in terms of polarization fraction and rotation measures behaviors between sub-populations which echo the argued spectral complexity.

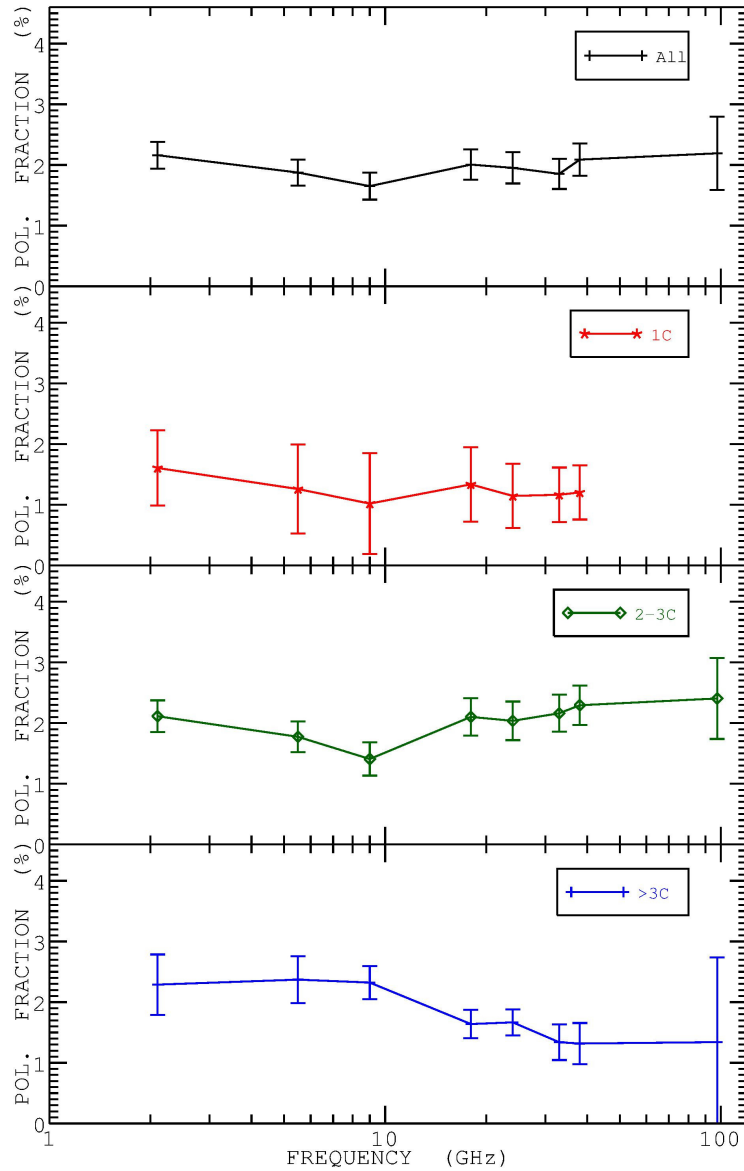


Figure 4.5: Frequency dependence of the median polarization fraction for sources with different spectral classification. At 2.1, 5.5, 9, 18, 24, 33 and 38 GHz we show the median polarization percentages, with their uncertainties, for the full sample by Galluzzi et al. (2018), comprising a total of 104 sources. To these estimates we have added the median polarization percentage at 97.5 GHz for the complete sub-sample of 32 objects observed with ALMA. We also subdivide the sources by the number of spectral components: 1 (1C), 2–3 (2–3C) and more ($> 3C$).

Table 4.1: Observed distribution of the percentage polarization fractions at 97.5 GHz for the full sample.

Π (per cent)	Probability	lower error	upper error
0.875	0.2212	0.0629	0.0841
2.625	0.1659	0.0542	0.0758
4.375	0.1106	0.0439	0.0661
6.125	<0.01843		
7.875	0.0369	0.0238	0.0486
9.625	0.0369	0.0238	0.0486

Here, we complement the analysis about the median polarization fraction with the frequency provided by Galluzzi et al. (2018) by investigating this aspect at higher frequencies (i.e. 100 GHz). We, again, apply the same classification in terms of synchrotron components in order to distinguish between sub-populations. However, we warn the reader that this classification is based on spectro-polarimetric data collected in the 2014 campaign of ATCA observations. We were not able to update this essentially neither because the lack of 18 – 24 GHz polarimetric observations for several objects in 2016 campaigns nor because ALMA observations are not strictly co-eval to 2016 ATCA ones (variability effect on a single source might bias the classification itself).

The results are presented in Fig. 4.5. The median polarization percentages at 2.1, 5.5, 9, 18, 24, 33 and 38 GHz refer to the full sample by Galluzzi et al. (2018), comprising a total of 104 sources. The median polarization percentage at 97.5 GHz is for the complete sub-sample of 32 objects observed with ALMA. The errors on median values are given by $1.253 \text{ rms} / \sqrt{N}$, where rms is the standard deviation around the mean and N is the number of objects (cf. Arkin & Colton 1970). The error bars at 97.5 GHz are larger since the size of the sample is smaller by a factor ~ 3 .

As illustrated by the figure, the data do not indicate any statistically significant trend with frequency for the full sample. According to the analyses by Bonavera et al. (2017) and Trombetti et al. (2017), the median polarization fraction remains essentially frequency independent over the full range of *Planck* polarization measurements (30–353 GHz). Moreover, negligible frequency dependency has been observed in Puglisi et al. (2017, ApJ in press), by combining data in a wide range of frequencies from (1.4 GHz to 217 GHz) of polarized sources detected in several catalogues.

As pointed out by Galluzzi et al. (2018), sources with 2–3 spectral components (2–3C) seem to show a minimum of the polarization fraction at ~ 10 GHz while for sources with more than 3 components ($> 3C$) a slight decrease above this frequency is indicated by the data. The ALMA measurements are consistent (although with large uncertainties) with frequency independent polarization fractions above some tens of GHz.

Trombetti et al. (2017) also found no evidence of a dependence of the median polarization fraction on the total flux density. As shown by Fig. 4.6

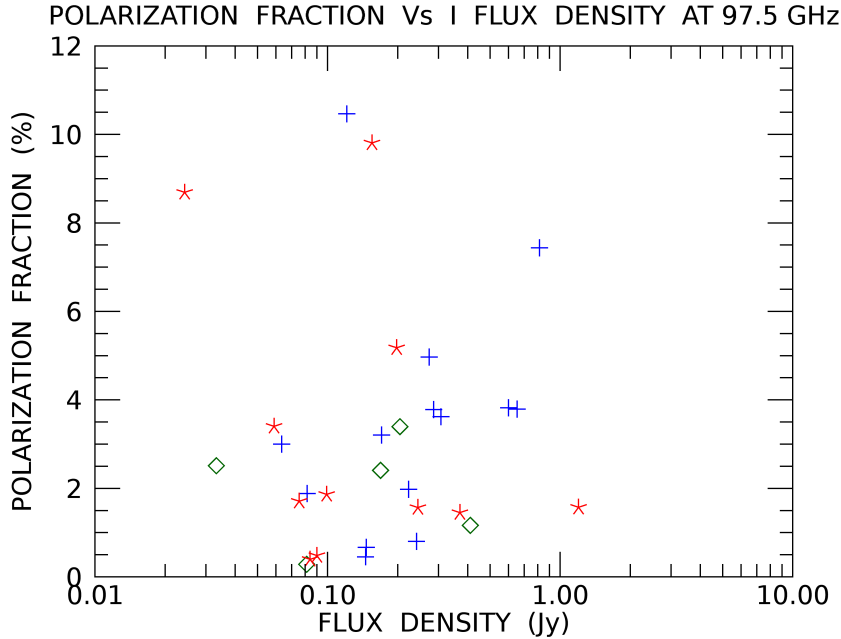


Figure 4.6: Polarization fraction against total flux density at 97.5 GHz for the complete sample of 32 objects observed with ALMA. Red stars, green plus signs and blue diamonds stand for steep-, peaked- and flat-spectrum objects respectively.

the ALMA data are consistent with this result: there is no sign of a correlation between the polarization fraction and the total flux density, neither for the full sample nor for steep-, peaked- and flat-spectrum objects (identified by red stars, green plus signs and blue diamonds, respectively) separately. However, the small size of the sample prevents any firm conclusion.

4.1.3 Rotation measures at ALMA frequencies

The sensitivity of our ALMA observations has allowed several detections in Stokes Q and U with signal to noise ratios of up to ~ 10 combining the four 2 GHz bands. For 22 objects out of 32 both Q and U were detected at a $\geq 6\sigma$ level, which in principle might allow us to have a 3σ detection in each band. Three well determined polarization angles are the minimum requirement to study the rotation measures (RMs) of our sources. We have also attempted to split each band into two 1 GHz sub-bands, bringing to 8 the maximum number of spectral measurements per source.

In the case of a foreground screen of magnetized plasma, the polarization angle varies as $\Delta\phi = RM\lambda^2$. The RMs were estimated using this relation. Following Galluzzi et al. (2018) we used the IDL “linfit” procedure, accepting only fits with a reduced $\chi^2 < 2$ and with a probability level > 0.1 . In Fig. 4.7 we show the 19 successful fits. As discussed in Galluzzi et al. (2018) the $1/\lambda^2$ contribution to the uncertainty make RM measurements extremely difficult at high frequencies. In our case only 8 objects have RMs not compatible with 0, assuming a 1 sigma level. In the Tab.4.2 we report the list of the

Table 4.2: List of the 8 objects with an observed RM in ALMA Band 3 (90 – 105 GHz) non-compatible with 0 at a 1σ level. We also report for each source the corresponding RMs found at lower frequencies (if any), the inferred number of synchrotron components and the redshift, whether available (provided by Galluzzi et al. 2018). All the values are in rad m^{-2} .

(AT20G) name	RM_{obs}			σ_{RM} 90 – 105 GHz	# Comp	z
	2 – 9	18 – 38	90 – 105			
J035547-664533	-12	-	52075	13673	>3	0.7
J044047-695217	-	1500	-4958	2734	2	-
J050754-610442	-	400	11593	10427	2	1.09
J051637-723707	-21	-3200	-12039	10037	2	-
J051644-620706	54	200	-11976	10482	3	1.3
J053435-610606	-	0	-14498	8696	>3	2.00
J063546-751616	16	-800	85187	7860	2	0.40
J075714-735308	-	-	98273	10877	2	-

observed RMs with the associated error provided by the fitting procedures. The median relative error for these cases is $\sim 58\%$ but we warn the reader that in three cases (i.e. AT20GJ050754-610442, AT20GJ051637-723707 and AT20GJ051644-620706, errors are as high as 85 – 90%). In the upper part of Tab. 4.3 we report the median values of the non-zero RMs derived from the above equation for these 8 objects. For the 5 objects with measured redshift we have computed the RMs at the source, correcting for the effect of redshift and for the relatively small contributions of our own Galaxy and of Earth’s ionosphere, as detailed by Galluzzi et al. (2018); the results are given in the lower part of the table. Also shown in the table are the results for the 2–3C and the $> 3\text{C}$ sources considered separately (there are no 1C objects in the sample).

Although the number of objects is too small to reach any firm conclusion, we note that the median RM at the source ($\simeq 130000 \text{ rad m}^{-2}$) is two orders of magnitude higher than that obtained for the 18 – 24 GHz frequency range and two orders of magnitude higher than that found for the 2 – 9 GHz range (cfr. Galluzzi et al. 2018, their Table 4).

Our results seems to be still consistent with the indication of an increase of the median RM with increasing number of spectral components, reported by Galluzzi et al. (2018). If confirmed, the extreme values derived from ALMA measurements would require very dense screens of magnetized plasma. Such screens may heavily depolarize the radiation emitted at the basis of the relativistic jet and, thus, offer an explanation for the lack of an observed increase of the polarization fraction with increasing frequency. In fact, the emission at higher and higher frequency is expected to come from regions closer and closer to the nucleus where the magnetic field should be more ordered and the polarization fraction correspondingly higher.

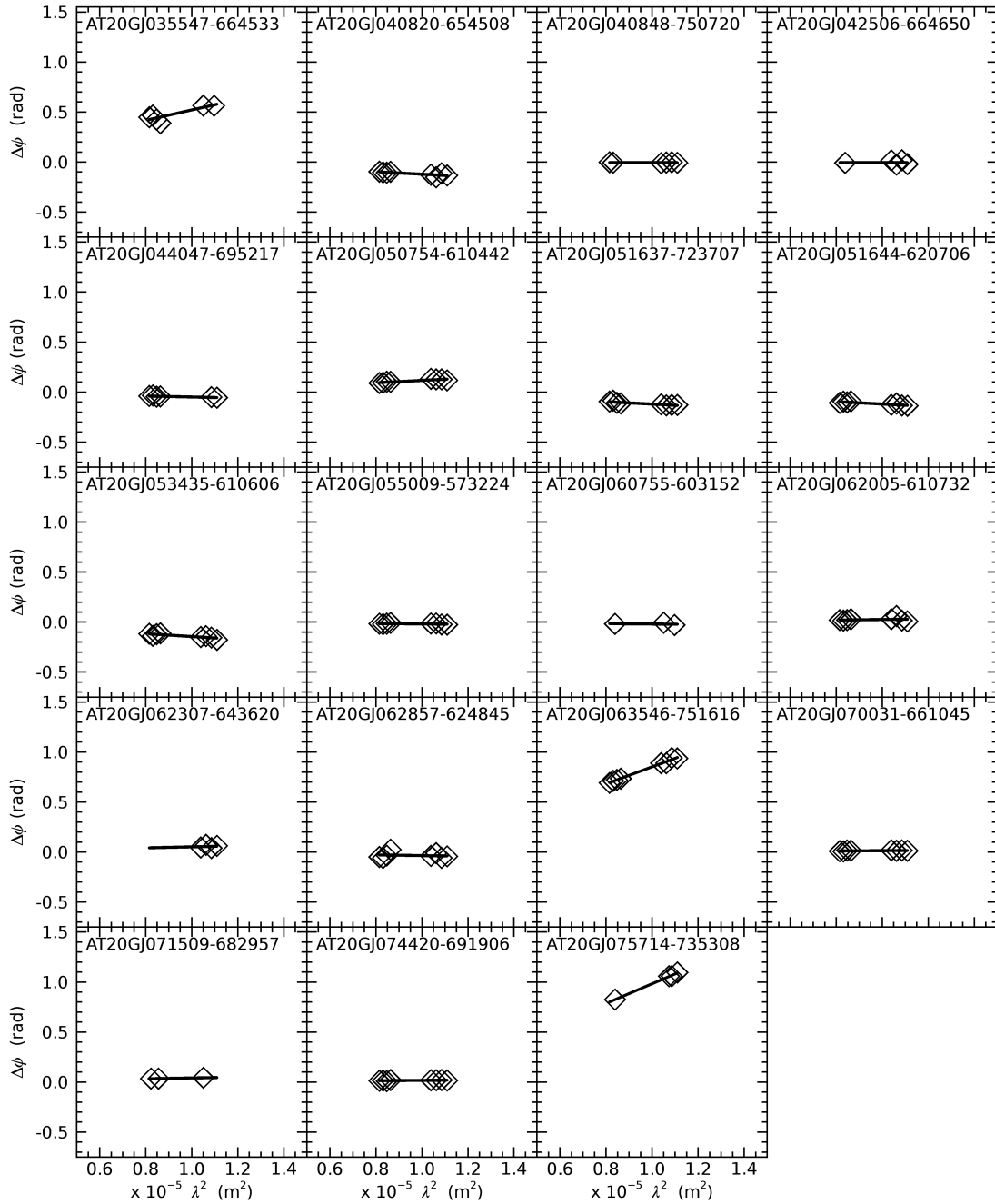


Figure 4.7: Successful RM fits for 19 objects of the complete sample observed with ALMA between 90 and 105 GHz.

Table 4.3: Median values of the RMs between 90 and 105 GHz. The upper part of the table refers to the observed RMs for the 19 sources with successful fits. The lower part gives the RMs at the source for the subset of sources for which redshift measurements are available. In parenthesis are the numbers of sources in each group. RMs are in rad m^{-2} .

All sample (8)	2-3C (6)	>3C (2)
1.3×10^4	1.2×10^4	3.3×10^4
All sample (5)	2-3C (3)	>3C (2)
1.3×10^5	6.3×10^4	1.4×10^5

4.2 Source Counts

We have exploited our ALMA polarization measurements to derive the differential source counts in polarization at 100 GHz, $n(P) \equiv dN/dP$. We started from the C2Ex model for total intensity source counts, $n(S)$, by Tucci et al. (2011) and used the approach of Tucci & Toffolatti (2012), like in sec. 3.5 for presenting our estimations at 20 GHz.

The Euclidean normalized differential source counts in polarized flux density derived from eq. (3.5.2) down to ≈ 1 mJy (approximately the 3σ detection limit of our ALMA observations) are shown Fig. 4.8 (triangles) and listed in Tab. 4.4. Given the relative smallness of the sample we have not distinguished among the sub-populations considered by the Tucci & Toffolatti (2012) model (FSRQs, BL Lacs and steep-spectrum radio sources, i.e. SSRs): the distribution of eq. (4.1.1) was applied to all sub-populations. The errorbar estimation of each data point takes into account the Poissonian contribution (cf. Gehrels 1986) and the lognormal parameters uncertainties which, in turn, are affected by the paucity of the sample. Hence, to evaluate this contribution, we use the semi-dispersion in the polarization number counts, resulting from the convolution with the maximum and minimum lognormal fitting curves, respectively. In Fig. 4.8 we also show, for comparison, the counts in total flux density at 100 GHz given by the De Zotti et al. (2005) model for each sub-population, as well as the total (the thick blue solid line). The C2Ex model is displayed as a thick grey solid line. The observed counts are from the South Pole Telescope (SPT; Mocanu et al. 2013) and from (Planck Collaboration et al. 2013). In polarization we also plot predictions for polarized source counts by Tucci & Toffolatti (2012) as a thin grey solid line and the convolution of De Zotti et al. (2005) with our distribution for the polarization fraction at 100 GHz as thin blue line (with other lines referring to the different sub-populations).

4.3 Peculiar objects

All the objects of the sample are selected to be point-like at 20 GHz but few of them are spatially resolved at higher frequency.

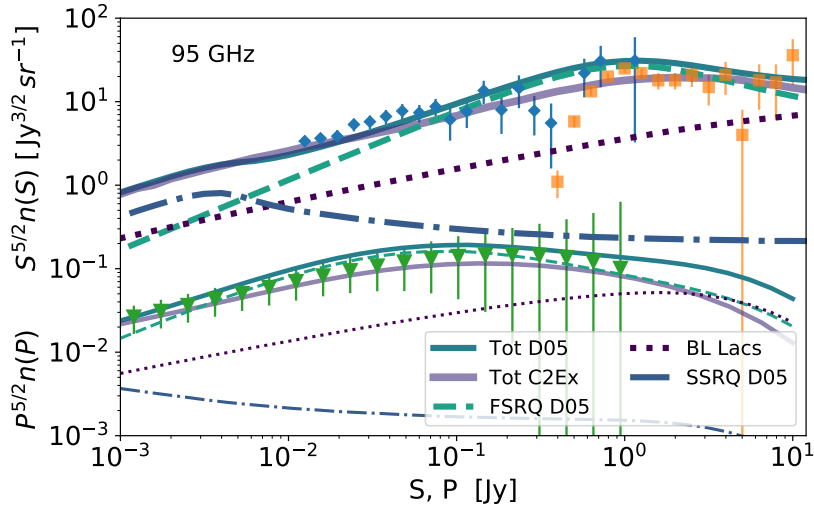


Figure 4.8: Euclidean normalized differential number counts at 100 GHz. The dotted, dashed, dot-dashed and blue solid lines represent the number counts for BL Lacs, FSRQs, SSRs and the total, respectively, as predicted by De Zotti et al. (2005) model in total intensity (upper lines) and in polarization (lower lines). The C2Ex model in total intensity and relative predictions in polarization presented by Tucci & Toffolatti (2012) are shown as grey solid lines (the thick one and the thin one, respectively). The observed total intensity source counts from SPT (diamonds; Mocanu et al. 2013) and from *Planck* (squares; Planck Collaboration et al. 2013) are also plotted. The differential number counts in polarized flux density computed via eq. (3.5.2) are shown by triangles.

AT20GJ040848-750720. This is an FR II at $z \simeq 0.69$. It is point-like at 20 GHz with ATCA (just an offset appears in polarization with respect to the total intensity centroid). Radio emission is dominated by two bright lobes: both lobes exhibits a high depolarization, slightly higher in the eastern one. The ALMA image (with 0.5 arcsec of resolution) shows this structure, also revealing a double substructure in the polarized intensity for the eastern lobe. The core instead is quite faint (it sits in the middle of the two hotspot bright features).

PKS0521-365. This object was the leakage calibrator of our ALMA campaign. It is a nearby ($z = 0.0554$) radio-loud object and bright FERMI source, exhibiting a variety of nuclear and extranuclear phenomena (Falomo et al. 2009). It is one of the most remarkable object in the southern sky: it is one of the three known BL Lac objects showing a kiloparsec-scale jet well resolved at all bands (Liuzzo et al. 2011). As showed in Fig. 4.10, a one-side radio jet extends in N-W side up to 7 arcsec, with the presence of many knots that are also detected from optical to X-rays (Falomo et al. 2009). An hotspot is also detected in all bands at 8 arcsec from the nucleus in the southeast direction. At low frequency, the arcsecond-scale radio structure is dominated by an extended lobe. The overall energy distribution of PKS0521-365 is consistent with a jet oriented at about 30° with respect to the line of sight. This is also in agreement with the absence of superluminal motion in the parsec-scale jet

Table 4.4: Euclidean normalized differential source counts at 100 GHz in polarized flux density given by eq. (3.5.2).

$\log [P(\text{Jy})]$	$S^{5/2}n(S)$ ($\text{Jy}^{3/2}\text{sr}^{-1}$)	lower error	upper error
-2.920	0.0263	0.0005	0.0005
-2.759	0.0308	0.0007	0.0007
-2.598	0.0362	0.0010	0.0010
-2.437	0.0427	0.0014	0.0014
-2.276	0.0504	0.0020	0.0020
-2.115	0.0594	0.0029	0.0029
-1.955	0.0699	0.0042	0.0042
-1.794	0.0817	0.0060	0.0060
-1.633	0.0944	0.0085	0.0085
-1.472	0.1075	0.0120	0.0120
-1.311	0.1201	0.0167	0.0167
-1.151	0.1313	0.0229	0.0229
-0.990	0.1401	0.0312	0.0391
-0.829	0.1456	0.0419	0.0560
-0.668	0.1472	0.0552	0.0806
-0.507	0.1442	0.0713	0.1179
-0.346	0.1359	0.0839	0.1714
-0.186	0.1214	0.0936	0.2604
-0.025	0.1007	0.1632	0.4538
0.136	<0.34383		
0.297	<0.59922		
0.458	<1.04429		
0.619	<1.81994		

(Falomo et al. 2009). In the millimeter bands, extended structures (hotspot and jet) of this object are detected up to 320 GHz, with similar structures from optical to X-rays (Liuzzo et al. 2015; Leon et al. 2016). An estimate of molecular gas content is also given together with an analysis of the SED of each source component (Liuzzo et al. 2015).

Pictor A. It is a classic double radio galaxy at redshift 0.035. It was identified as a D-type galaxy (Schilizzi & McAdam 1975; Schilizzi 1975) with strong X-ray emission (Marshall et al. 1978). As it is one of the brightest and most extended radio sources of the Southern hemisphere, it has been observed in many spectral bands both in total intensity and polarization at frequencies < 10 GHz. We indeed observed this object in mosaic mode during the July 2016 ATCA campaign (project C3085, PI: Massardi) at 33 – 35 GHz (see Fig. 4.11) by setting 50 pointing mosaic in the ATCA H75 configuration (with the 1-MHz per channel continuum CABB configuration) for at least 15 minutes/pointing, spread over several hour angles. Past observations demonstrated that this configuration should be sufficient to image the source at ~ 0.07 mJy/beam sensitivity with better than 15 arcsec resolution

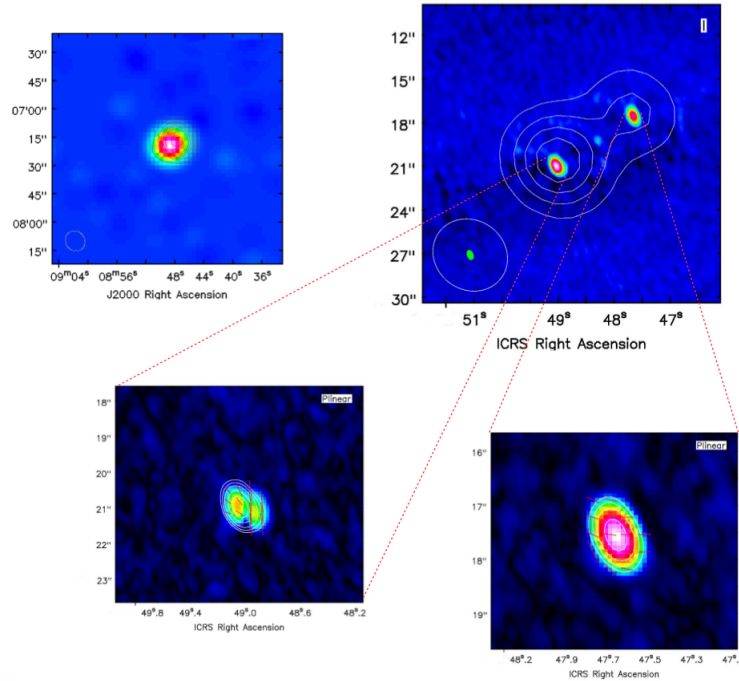


Figure 4.9: AT20GJ040848-750720 images. (*Upper-left panel*) ATCA image at 18 GHz (total intensity in rainbow and polarization in red contours); (*upper-right panel*) ALMA image at 97.5 GHz in total intensity (rainbow) with total intensity contours from the ATCA image at 38 GHz. ALMA polarization (rainbow) and total intensity (white contours) with superimposed magnetic field directions (in red) for the eastern lobe (lower-left panel) and the western lobe (lower-right panel), respectively.

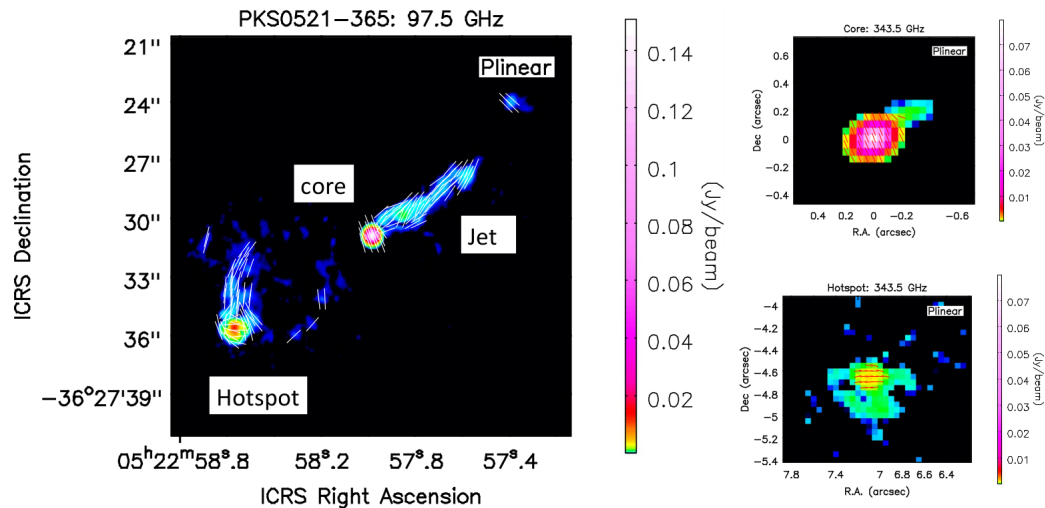


Figure 4.10: Linear polarization emission (colours) and position angles (vectors) in ALMA Band 3 and 7 of PKS0521-365.

imaging scales up to ~ 0.7 arcmin. We are going to plan a dedicated ALMA mapping of this object at 100 GHz. Both these campaigns will allow us to: perform the first mm-bands complete maps in total intensity and polarimetry for PicA; produce the model of use for cosmological experiments; investi-

gate the distribution of the spectral behaviour of the source, by comparing with the results of previous observations at lower frequencies; investigate the jet filamentary structure in the western lobe region. In planning such studies it is important to have an indication of how much the extended structure may hamper the characterization of the more compact features (such as the core or hotspots). About core properties, considering our recent experience with the leakage calibrator PKS0522-365 we can assess that when the core dominance is > 100 with respect to extended features (this is quite common when there is a Doppler boosting effect), then the compact region can be easily characterized and used, for example, to provide calibration for a cosmological project. At the same time, hotspot regions, like those we see in the FR II AT20GJ040848-750720 or, again, in PKS0522-365 seem to host more highly efficient particle reacceleration processes (Fermi-II or multi-shocks) which might also induce hadronic emissions. This physical processes usually make hotspots shine at higher frequencies, with higher brightnesses (and for a longer time) with respect less efficient radiative processes which regulate more diffuse components. Hence, also in this case, we argue it is possible to achieve a robust characterization against extended emissions.

Perley et al. (1997) presented a comprehensive investigation of PicA both in total intensity and polarization with the VLA at 6 bands between 400 and 2 cm. They describe the source to be $210/h$ kpc extent and composed by 2 round lobes of about $95/h$ kpc diameter each. A single hot spot is at the end of the western lobe and a double one is at the end of the eastern one. The western hotspot is located in the site of a prominent highly polarized (optical polarization degree $\sim 55\%$) optical knot attributed to pure synchrotron emission from radio to X-ray wavelengths, in a site of local particle acceleration (Röser et al. 1987). A deep optical study of the western hotspot by Thomson et al. (1995) confirms this conclusion. The study also notes strong polarization of the hotspot with a magnetic field oriented perpendicularly to the jet axis. A thorough X-ray study of Pictor A was done by Wilson et al. (2001), noting significant emission in the core, bright western hotspot, and along a jet from the core to the hotspot (see also Hardcastle 2015; Tingay et al. 2008). The roundness of the lobes indicates that the source is quietly expanding in a uniform medium, in which the source is confined. However, the strength of the hotspots suggests that it was recently reactivated. According to Perley et al. (1997), at cm wavelengths the polarization structure shows that the projected magnetic field lines are aligned with the isocontours of surface brightness. They also noted a small depolarization in the western lobe, but significantly higher in the eastern lobe, which is explained as the presence of a deeper foreground screen in front of the eastern lobe. The double nature of the eastern lobe requires a higher resolution to identify structure on the kpc scale (corresponding to roughly 1.45 arcsec at the source redshift). The inner component of the double hotspot is, in fact, more compact and shows a radial magnetic field, which is at odds with the expectation of alignment between field and brightness distribution. There is no observational evidence of the presence of an intervening magnetic cloud that could justify such a strong Faraday rotation, or enough material to explain this behaviour as due to internal de-

polarization. The investigation of this effect was limited by the resolution of these centimetric observations (10 arcsec). Higher frequency VLA observations are limited by the low elevation of the source. Burke-Spolaor et al. (2009) presented the ATCA 20 GHz observation of Pictor A among a sample of extended (more than 2.4 arcmin) and bright ($S_{AT\ 20G} > 0.5$ Jy) sources of the Southern hemisphere. They confirmed the strong polarized emission from the hotspot regions with magnetic field oriented perpendicularly to the jet axis, and faint polarized emission from the core region. More generally they found that all cores have either undetected or very low values of polarization that can be explained either by a complex scattering medium surrounding the inner regions of jet formation, or by a dense plasma, or by beam depolarization of close, compact regions of structure that we have not resolved due to low angular resolution. Burke-Spolaor et al. (2009) reached a 3σ measurement ($\sigma = 80$ mJy/beam) of the diffuse emission in the eastern lobe region, reaching a 16σ in the eastern hot spot with 43 arcsec resolution. They observed each of 13 mosaic regions for less than 3 min spread at various hour angles. The integrated flux density at 18 GHz is 6.32 ± 0.11 Jy and the polarization fraction is 7.9%. In the lobes of Pictor A, a notable edge-brightening effect in fractional polarization is visible probably due to the change in field geometry across the lobe (Perley et al. 1997). This interpretation can be supported by the absence of these effects in the geometry and strength of observed polarization in the linear jet regions in several extended sources characterized by linear jet geometry. Mapping of the lobe region at higher frequency might help disentangle the geometric effects from physical and spectral effects. The complex structure in polarization emission makes the source a perfect testbed for investigating the origin of the different behaviours in polarized emission down to arcsecond scale observations. Pilot mapping of the core and the western lobe regions of Pictor A were carried out in one run of the PACO project runs on July 2009 (at the beginning of the CABB era) in the H75 configuration with 2×2 GHz CABB bands centered at 18 – 24 and 33 – 39 GHz. The calibration scheme of that project does not allow a suitable accuracy for polarimetric observations of an extended target, as its main priority was for total intensity of relatively bright unresolved sources. Nevertheless, it gives important indications for a dedicated experiment. At 33 GHz we performed a 27 pointing mosaic. Each pointing lasted at least 5 min, reaching a 8 mJy/beam sensitivity (see 4.12).

Polarimetric data available for such resolved objects is very helpful to perform studies that, as stressed in the introduction, aims to address fundamental questions about AGN physics, such as the role of magnetic field in jetted/radio loud AGN, the plasma properties and particle acceleration mechanisms.

Nearly 10 – 20% of AGN are radio loud and the form of their spectra as a function of frequency implies that the radio emission is non-thermal (synchrotron) in origin, due to relativistic plasma moving in strong and ordered magnetic fields. Since the polarized signal in these objects is typically a few percentage of the total intensity, collecting information on magnetic field of Radio Loud AGN requires telescope with high sensitivity ($\ll 1$ mJy/beam) as ALMA. The results obtained for PKS0521-365 show that in only 10 mins

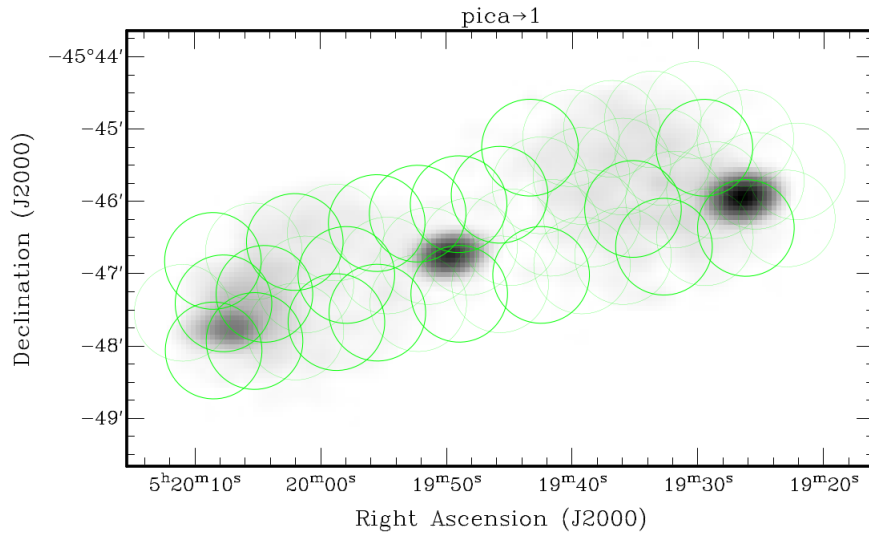


Figure 4.11: Mosaic pointing scheme for the ATCA observations at 33 – 35 GHz overlaid to the 18 GHz map of Pictor A obtained in total intensity by Burke-Spolaor et al. (2009).

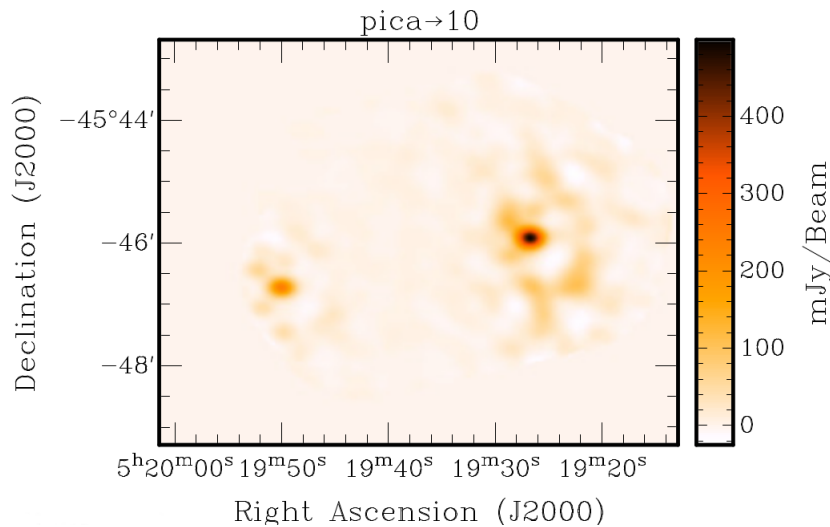


Figure 4.12: 33 GHz total intensity map of PictorA (preliminary results)

on source polarized emission is revealed even in the lobes with angular resolution < 0.5 arcsec, demonstrating that now with ALMA impressive results could be reached also for faint source components (< 0.1 mJy) and for large sample of sources.

The study of the rotation measure, defined as the change of polarization angle as a function of wavelength squared, is particularly important as this quantity is directly related to the plasma density and the strength of the magnetic field along the line of sight. ALMA can perform observations in spectropolarimetric mode. This offers a unique possibility to apply the Faraday Rotation (FR) Synthesis technique (Brentjens & de Bruyn 2005), allowing a 3D representation of the magnetic field at angular scale even of subarc. To do this,

it is however crucial to correct the observed polarized emission for any external/internal medium contribution. In the mm band, the observed FR could be dominated by either thermal, magnetized plasma external to the source or by the relativistic plasma responsible for the synchrotron emission from the jet. Procedures similar to those applied by O’Sullivan et al. (2012) could be used to discriminate the various scenarios.

The study of the magnetic field in bright compact regions at the terminations of powerful jets, i.e. hotspots, is also crucial. Those regions are believed to be shocks at which the jet material interacts with plasma already present in the lobes and the external one. With dedicated ALMA polarization observations, we will be also able to determine the unknown particle acceleration mechanism in the hotspot: Fermi-II acceleration or multiple shocks (e.g. Prieto et al. 2002).

4.4 Forecasts for forthcoming CMB ground-based experiment

To complement our results, we show how they have been applied by Puglisi et al. (2017) to generate forecasts for current and forthcoming cosmological surveys. The whole analysis presented here has been achieved with the python package Point Source ForeCast (PS4C) made publicly available¹. PS4C is a user friendly platform which allows to forecast the contribution of radio point sources both in total intensity and polarized flux-densities given the nominal specifics of a CMB experiment. In Tab.4.5 we summarize the specifics of the 5 CMB experiments with whom we forecast the ERS contribution with PS4C:

- the Q-U-I JOint TEnerife López-Caniego et al. (QUIJOTE 2014) CMB experiment designed to observe the polarized emissions from the CMB, our Galaxy and the extra-galactic sources at four frequencies in the range between 10 and 20 GHz and at FWHM resolution of $\sim 1^\circ$. Observations started observing in November 2012, covering $18,000 \text{ deg}^2$ of the Northern hemisphere, and achieved the sensitivity of $1800 \mu\text{K arcmin}$ in polarization;
- a generic CMB-S2 experiment observing at 95, 150 GHz within a patch including 2% of the sky at the resolution of 3.5 arcmin, at $25 \div 30 \mu\text{K arcmin}$ sensitivity;
- a CMB-Stage 3 ground based experiment as it has been defined in Abazajian et al. (2016). We adopt the so-called *strawman* configuration for the “measuring-r” survey, consisting of an array of small-aperture (SA, $\sim 1 \text{ m}$) telescopes and one large-aperture (LA, $\sim 5 \text{ m}$) telescope, observing at the accessible atmospheric windows in the sub-millimeter

¹<https://gitlab.com/giuse.puglisi/PS4C>

range (at about 30,40, 90, 150 GHz). The sensitivities at these frequencies are targeted to be about $1 \div 10 \mu\text{K arcmin}$.

- the Lite satellite for the studies of B-mode polarization and Inflation from cosmic Background Radiation Detection Matsumura et al. (Lite-BIRD 2016) is a satellite mission proposed to JAXA aimed at measuring the CMB polarized signal at degree angular scale. Its goal is to characterize the measurement of tensor to scalar ratio r with an uncertainty $\sigma(r) < 0.001$. In order to achieve such high accuracy, the target detector sensitivity is $2\mu\text{K arcmin}$ observing over a wide range of frequencies (from 40 to 320 GHz). The current effort aims to launch in 2025;
- the Cosmic ORigin Explorer (Delabrouille et al. 2017, CORE) is a next generation space-borne experiment and it has been proposed as a Medium-size ESA mission opportunity. It has been designed as the *Planck* satellite successor, though CORE is planned to have better angular resolution and sensitivity than *Planck*. We consider the *CORE150* configuration: i.e. a satellite involving a 1.5 m telescope, observing over a wide range of frequency channels (up to 800 GHz) with sensitivities ranging from ~ 10 to $5 \mu\text{K arcmin}$. Here we restrict our analysis to a selection of frequency channels, (see the last row of Tab. 4.5) to compare the expectations with the ones previously obtained by De Zotti et al. (2016).

Table 4.5: Nominal specifics of CMB experiments described in sec.4.4.

	Frequency [GHz]	Sensitivity [$\mu\text{K arcmin}$]	FWHM	f_{sky}
QUIJOTE	11,13,17,19	1800	1°	50%
CMB-S2	95, 150	25,30	$3.5'$	5%
CMB-S3 SA	30, 40, 95,150	8, 6, 1, 2	1°	20%
CMB-S3 LA	30, 40, 95,150	8, 6, 1, 2	$10', 7', 3', 2'$	20%
LiteBIRD	40, 50, 60, 68, 78	53, 32, 25, 19, 15	1°	100%
	89, 100,119, 140,166	12, 15.6, 12.6, 8.3, 8.7	1°	100%
CORE150	60, 100, 145	10.6, 7.1, 5.1	$14', 8', 6'$	100%

Although most of the future experiments frequency channels range up to 350 GHz, we forecast up to 150 GHz. The reason for this choice is mainly due to the fact that at higher frequencies the contribution coming from dusty galaxies and Cosmic Infrared Background cannot be neglected² (Negrello et al. 2013; De Zotti et al. 2016). Bonavera et al. (2017) estimated the polarized contribution of dusty galaxies by stacking about 4700 sources observed by *Planck* at 143, 217, 353 GHz HFI channels. They estimated the polarized

² We have already planned to include into the package the contribution from dusty galaxies and forecasts with PS4C will be presented in a future release that will be described in a future paper.

Table 4.6: Number of polarized ERS detected above the $P_{3\sigma}$ flux density detection limit in polarization, by current and forthcoming CMB ground based experiments. Counts are estimated both from the (model De Zotti et al. 2005, thereafter D05) and the C2Ex predictions (in brackets).

CMB -S2			CMB -S3			
ν [GHz]	$P_{3\sigma}$ [mJy]	$N_{3\sigma}$	SA	LA		
			$P_{3\sigma}$ [mJy]	$N_{3\sigma}$	$P_{3\sigma}$ [mJy]	$N_{3\sigma}$
30	15	236 (191)	1.5	2329 (2278)
40	15	215 (156)	1.5	1867 (1810)
95	100	3 (2)	10	355 (222)	1	2432 (2136)
150	100	3 (1)	15	146 (74)	1.5	1145 (867)

Table 4.7: Number of sources detected above the $\geq S_{lim}$ and $\geq P_{lim}$ flux densities limit by the QUIJOTE experiment, assuming the nominal and conservative values for sensitivity. Values are estimated using D05 and C2Ex models (ins brackets).

ν [GHz]	S_{lim} [Jy]	N_{src}	P_{lim} [Jy]	N_{src}
11	0.5	694 (673)	0.5	6 (4)
	1	347 (340)	1	2 (1)
13	0.5	445 (434)	0.5	2 (1)
	1	210 (205)	1	0 (0)
17	1	201 (197)	1	0 (0)
	2	86 (83)	2	0 (0)
19	1	128 (125)	1	0 (0)
	2	52 (51)	2	0 (0)

contribution of dusty galaxies to B-mode power spectra and found that at frequencies larger than 217 GHz these population of sources might remarkably contaminate the primordial B-modes.

We compute one realization of CMB power spectra by means of the CAMB package (Lewis et al. 2000) by assuming the *Planck* best fit cosmological parameters (Planck Collaboration et al. 2016) and a tensor to scalar ratio $r = 0.05$ (slightly below the current upper limits).

To assess the contribution of ERS to the power spectrum level, we assume their distribution in the sky to be Poissonian, since the contribution of clustering starts to be relevant for $S < 10$ mJy (González-Nuevo et al. 2005; Tofolatti et al. 2005). The power spectrum of temperature fluctuations coming from a Poissonian distribution of sources is expected to be a constant contribution at all multipoles. In particular, we consider as *masked* all sources whose flux-density is above 3σ the detection limit $S_{cut} = 3\sigma_{det}$ and we do not include them to estimate power spectrum

$$C_\ell^T = \left(\frac{dB}{dT}\right)^{-2} N \langle S^2 \rangle = \left(\frac{dB}{dT}\right)^{-2} \int_0^{S_{cut}} n(S) S^2 dS, \quad (4.4.1)$$

where $n(S)$ and N are respectively the differential and the integral number counts per steradian, and dB/dT is the conversion factor from brightness to

Table 4.8: Number of sources observed above $3\sigma_{det}$ limit in terms of polarized flux density $P_{3\sigma}$ by the LiteBIRD experiment. Bracketed values are estimated using the C2Ex model.

ν [GHz]	$P_{3\sigma}$ [mJy]	$N_{3\sigma}$
40	450	4 (3)
50	240	11 (8)
60	210	9 (6)
68	300	4 (3)
78	240	6 (4)
89	210	12 (8)
100	240	10 (7)
119	210	14 (10)
140	270	8 (4)
166	270	7 (4)

temperature, being

$$\left(\frac{dB}{dT}\right)^{-1} \approx 10^{-2} \frac{(e^x - 1)^2}{x^4 e^x} \frac{\mu\text{K}}{\text{Jy sr}^{-1}},$$

with $x = \nu/57$ GHz. Tucci et al. (2004b) found that it is possible to relate the ERS polarization power spectrum to the intensity one (4.4.1) as follows

$$\begin{aligned} C_\ell^Q &= \left(\frac{dB}{dT}\right)^{-2} N \langle Q^2 \rangle \\ &= \left(\frac{dB}{dT}\right)^{-2} N \langle S^2 \Pi^2 \cos^2 2\phi \rangle \\ &= \left(\frac{dB}{dT}\right)^{-2} N \langle S^2 \rangle \langle \Pi^2 \rangle \langle \cos^2 2\phi \rangle \\ &= \frac{1}{2} \left(\frac{dB}{dT}\right)^{-2} \langle \Pi^2 \rangle C_\ell^T, \end{aligned} \quad (4.4.2)$$

where the $1/2$ factor comes from the average value of $\cos^2 2\phi$, if the polarization angle ϕ is uniformly distributed and the value for $\langle \Pi^2 \rangle$ is derived at each frequency from the linear fit provided by Bonavera et al. (2017), i.e.

$$\begin{aligned} \langle \Pi^2 \rangle^{1/2}(\nu) &= (0.005 \pm 0.006 \text{GHz}^{-1}) \nu \\ &+ (4.170 \pm 0.22). \end{aligned} \quad (4.4.3)$$

Since we do expect point sources to equally contribute on average both to Q and U , and thus to the E - and B - modes, we can approximate $C_\ell^B \simeq C_\ell^E \simeq C_\ell^U \simeq C_\ell^Q$. In the following, power spectra are normalized by the usual normalization factor $\mathcal{D}_\ell = \ell(\ell + 1)C_\ell/2\pi$.

To forecast the number of sources that will be observed in intensity and polarized flux-density above a given detection limit, we integrate the differential number counts, $n(S)$ and $n(P)$ as:

$$N(> S) = \int_{S_{cut}}^{\infty} n(S) dS, \quad (4.4.4)$$

$$N(> P) = \int_{P_{cut}}^{\infty} n(P) dP. \quad (4.4.5)$$

Finally, to compare the level of contamination produced by the ERS with the Galactic foregrounds one, we rescale the Galactic foreground emission at a given f_{sky} , frequency ν and multipole order ℓ as in Planck Collaboration et al. (2015),

$$\mathcal{D}^{FG}(\ell, \nu, f_{sky}) = \frac{\text{Var}[\text{Sync}, f_{sky}]}{\text{Var}[\text{Sync}, f_{sky,0}]} q_s \left(\frac{\ell}{80} \right)^{\alpha_s} \frac{s_s(\nu)}{s_s(\nu_s)} + \frac{\text{Var}[\text{Dust}, f_{sky}]}{\text{Var}[\text{Dust}, f_{sky,0}]} q_d \left(\frac{\ell}{80} \right)^{\alpha_d} \frac{s_d(\nu)}{s_d(\nu_d)}. \quad (4.4.6)$$

with s, d referring respectively to synchrotron and dust. For all the parameters entering in eq. (4.4.6), we use the best fit values quoted in Planck Collaboration et al. (Table 11, 2015) estimated using the UPB77 mask (Planck Collaboration et al. 2016) that exclude the Galactic plane. The mask has been computed considering a common foreground mask after component separation analysis with 1° apodization scale. Therefore, we use eq. (4.4.6) to rescale this estimate to a patch with a smaller fraction of sky, f_{sky} , and we compute the variance of both synchrotron and thermal dust template maps within the considered patch and within the *Planck* region with $f_{sky,0} = 73\%$. The rescaled foreground power spectra are shown in Fig. 4.13 as dotted lines.

4.4.1 PS4C with current and forthcoming CMB ground based experiments

Fig. 4.13 shows our PS4C forecasts of foreground contamination to the recovery of the CMB B-mode for the different experiments in the different panels: we plot the expected spectrum in polarization of Galactic (dotted lines) and ERS (dashed lines) emissions at the different frequencies available for each experiment and the total CMB B-mode power spectrum (black solid line). The black dot-dashed lines show the primordial ($r = 0.05$) and lensed B-mode power spectra separately. The power spectra are computed in the region outside the UPB77 *Planck* mask (in order to exclude the Galactic plane and the ERS whose flux density is below the 3σ detection limit). The Galactic foreground turns out to be the most contaminating emission in the B-mode recovery. The different colors for the Galactic and ERS spectra are for different frequencies, going from purple to yellow as the frequency increases. It should be commented that there exists several *component separation* and *foreground cleaning* algorithms that can recover CMB intensity and polarization signals with great accuracy (Planck Collaboration et al. 2015). In addition, multi-frequency observations and joint analyses from different experiments (BICEP2/Keck and Planck Collaborations et al. 2015) can improve the foreground cleaning. So, even if in our work we are considering the most conservative cases, it should be stressed that such contamination could be lowered (at sub-percentage level, cf. Stompor et al. 2016; Errard et al. 2011) by applying such foreground removal algorithms.

In particular, Fig. 4.13 shows our forecasts for the QUIJOTE (top left) and CMB-S2 (top right) experiments. As for QUIJOTE, the Galactic emission is

much higher than the CMB one and higher than the contribution from undetected ERS, except at small angular scales where the ERS start to be dominant. Since the QUIJOTE experiment ranges from 10 to 20 GHz, we need to take into account the contribution from both FSRQs and SSRQs, with the resulting increase in the average fractional polarization and number counts. Tab. 4.7 summarizes the total number of sources in total intensity (third column) and polarization (fourth column) that QUIJOTE would detect (frequencies are given in the first column), assuming nominal and conservative sensitivity values (flux density limits in total intensity and polarization are listed in columns two and three respectively). We found 694, 445, 201 and 128 sources in total intensity at 11, 13, 17, 19 GHz respectively. In polarization only a few of them would be detected and just in the 11 and 13 GHz channels.

For the CMB-S2 experiment whose frequencies are greater than 90GHz, the Galactic emission (mostly thermal dust emission) is the most contaminating up to $\ell \sim 350$, while the ERS are important at small angular scales. Unlike the previous case, at these frequencies the CMB B-mode spectrum is comparable to the one of undetected ERS. In Fig. 4.14 the triangles show the C_ℓ^{BB} of undetected ERS estimated using eq.(4.4.2). The detection limits are given by the CMBS2 sensitivities. The C_ℓ^{BB} of the CMB B-mode are also plotted: the cyan dashed line is for the case $\ell \approx 80$ and $r = 0.05$ and the orange dashed line is for $\ell \approx 1000$. Fig. 4.14 shows what is the contamination due to undetected ERS and consequently the level of source detection required to detect primordial or lensing B-mode signal. In CMB-S2 the undetected ERS level of the power spectrum is comparable to the lensing B-mode one. In this case, given the experiment sensitivity and the size of the observed region, ~ 150 sources would be detected in total intensity and only few of them in polarization at a 3σ level.

Among the experiments studied in this work, the CMB-S3 is the one with the greatest sensitivity and best resolution. The results are shown in the central panels of Fig. 4.13 and in the left panel of Fig. 4.14 with circles and diamonds. As summarized in Tab. 4.6, the maximum number of polarized sources detected above a 3σ level and using the large aperture telescope is 2329 with flux density $P_{lim} \gtrsim 1$ mJy. When using a smaller aperture telescope, this number drops to a few hundreds with polarized flux densities $P_{lim} \gtrsim 10$ mJy. The contribution in polarization of undetected ERS is very small at high frequencies ($\nu \gtrsim 90$) and at low multipoles $\ell \lesssim 2000$. At lower frequencies, undetected ERS still can contaminate and they have to be taken into account to de-lens, lensing B-modes to get the primordial ones for $r \lesssim 0.05$.

4.4.2 PS4C with future space missions

The results for the LiteBIRD experiment are shown in the left bottom panel of Fig. 4.13 and the filled circles in the right panel of Fig. 4.14. On the whole, the most contaminating contribution is the Galactic one, except at small angular scales ($l \sim 400$) and high frequencies ($\nu > 70$ GHz) where the ERS contribution is comparable to the Galactic one. The ERS contribution, although generally lower than the Galactic one, is also important being higher

than the CMB B-mode level even at large scales ($l \gtrsim 7$) and $\nu < 70$ GHz (dashed purple and blue lines). Moreover, at $\nu > 80$ GHz and $l \gtrsim 70$ the ERS contribution is comparable to the B-mode power spectrum. The number of sources that would be detected in polarization above the 3σ level with this experiment are listed in Tab. 4.8 and they range from 4 at 10 and 68 GHz to 14 at 119 GHz. The first column is the frequency in GHz, the second is the polarized flux density limit in mJy and the third column is the number of sources that would be detected by LiteBIRD (values in the brackets are estimated from the C2Ex model).

Our findings for CORE are shown in the right bottom panel of Fig. 4.13 and in the right panel of Fig. 4.14 (filled circles). Galactic emission is the most contaminating for B-mode detection. The ERS are important only at 60 GHz, where their power spectrum is comparable to the one of the B-mode due to lensing. CORE would be able to detect up to 200 sources per steradian, implying a lower contamination for the CMB B-mode power spectrum with respect to LiteBIRD.

Table 4.9 compares the surface densities (i.e. number of sources per steradian, last two columns) at CORE frequencies (first column) of the polarized ERS above the $P_{4\sigma}$ flux density limit (second column) estimated by (De Zotti et al. 2016, thereafter DZ16) and PS4C (values in the brackets are for C2Ex estimate). In this comparison we use a 4σ flux density limit in order to be consistent with the estimates by De Zotti et al. (2016). Above 100 GHz, we find a discrepancy between D05 (model De Zotti et al. 2005) and DZ16 that could be due to two effects that become more important at higher frequencies: (i) the D05 predictions tend to over-estimate the polarized source number counts and (ii) at $\nu > 100$ the polarization fraction is expected to suffer a slight increase (from $\sim 4\%$ to $\sim 5\%$ from 100 to 150 GHz) as can be seen in eq. (4.4.3).

On one hand, at 100 GHz, we find that accounting solely for the observation in (ii), i.e. a 20% increase of Π to a value of 4.67%, the D05 forecasts predict source counts that are 20% larger than DZ16³. On the other hand, at 150 GHz, the surface density estimated with PS4C with D05 model is $\sim 65\%$ larger than the value referred by DZ16. By means of eq. (4.4.3), we expect a 25% fractional increase of Π to 4.92%. Thus, we argue that both (ii) and (i) effects have to be taken into account to compensate the observed discrepancy at 150 GHz.

Contrary to the D05 forecasts, the C2Ex model is in reasonable agreement with De Zotti et al. (2016), meaning that the C2Ex predictions are more robust than the D05 one at least at higher frequencies.

4.4.3 An alternative to stacking for characterizing extragalactic radio sources: the IDA method

In Trombetti et al. (2017) we revisited the estimates of the mean polarization fraction of extragalactic sources (radio-loud AGNs and dusty galaxies)

³ For this estimate, we assume that differential source counts are described by a power law with spectral index > 1

Table 4.9: Comparison of surface densities of polarized ERSs brighter than $P_{4\sigma}$ estimated by De Zotti et al. (2016, DZ16) and by PS4C. Values in brackets refer to C2Ex estimates.

ν [GHz]	$P_{4\sigma}$ [mJy]	$N_{4\sigma}$ [sr ⁻¹]	
		DZ16	PS4C
60	5.2	212	214 (198)
100	5.2	184	229 (164)
145	4.6	165	271 (142)

based on data from the *Planck* polarization maps at 30, 44, 70, 100, 143, 217 and 353 GHz of Bonavera et al. (2017) and Bonavera et al. (2017) by using the intensity distribution analysis (IDA; De Zotti et al. 1989; Barcons et al. 1995). Briefly, this method consists of measurements of signals in a map at the positions of a given source catalogue. The distribution of signals is compared with that for the “blank sky”, measured at random positions, away from sources (control fields). If some statistical test detect a significant difference, meaning that the source distribution is shifted towards higher values than that of control fields, a signal is detected. For this purpose a one-sided Kolmogorov-Smirnov (KS) statistics has been used.

This analysis overcomes the two most delicate aspects of the application of stacking techniques (e.g. Bonavera et al. 2017), i.e. the approximation of the average polarization fraction, $\langle \Pi \rangle = \langle P/S \rangle$, with the ratio of the mean polarized flux density to the mean total flux density, $\langle P \rangle / \langle S \rangle$, and the need of simulations to correct for the noise bias. The adopted approach considers the objects one by one. This allows to identify the flux density range that contributes significantly to the polarization signal. We find that the method allows us to detect, on *Planck* maps, mean polarized flux densities at few tens of mJy levels. For comparison, the detection limits in total intensity are at a few to several hundred mJy levels (cf. Table 13 of Planck Collaboration et al. 2016). Also, the subtraction of the median of the polarization signal of control fields removes the contributions of the noise and of the other polarized components (CMB and Galactic emissions), thus removing the “noise bias” without the need of simulations.

For radio sources the median polarization degree, averaged over frequencies, $\Pi_{\text{IDA,median}} \simeq 2.75\%$, in good agreement with Bonavera et al. (2017) as well as with the ground based measurements of a fainter sample at 33 and 38 GHz (Galluzzi et al. 2018) and of a bright sample at 86 GHz (Agudo et al. 2014). They do not find any significant dependence of Π on either flux density or frequency, in agreement with earlier analyses at frequencies of up to 43 GHz but not with the increase of Π from 86 to 229 GHz claimed by Agudo et al. (2014, 2017). At variance with Bonavera et al. (2017) they do not detect any polarization signal from dusty galaxies.

The contamination of CMB maps in polarization by extragalactic sources is dominated by radio loud AGNs up to $\simeq 100$ GHz. The amplitude of their power spectra depends on their detection limit in polarization, S_d . For the

values of S_d expected for the next generation CMB experiments, we confirm that at $\simeq 70$ GHz, i.e. in correspondence to the minimum Galactic emission, the point radio source contamination is well below primordial E-modes, as found by previous analyses. On the other hand, it is close to the level of lensing B-modes and of primordial B-modes for $r \simeq 0.01$. The contribution of dusty galaxies to the point source power spectra is still poorly constrained, but may be substantial, or even dominant at $\gtrsim 100$ GHz.

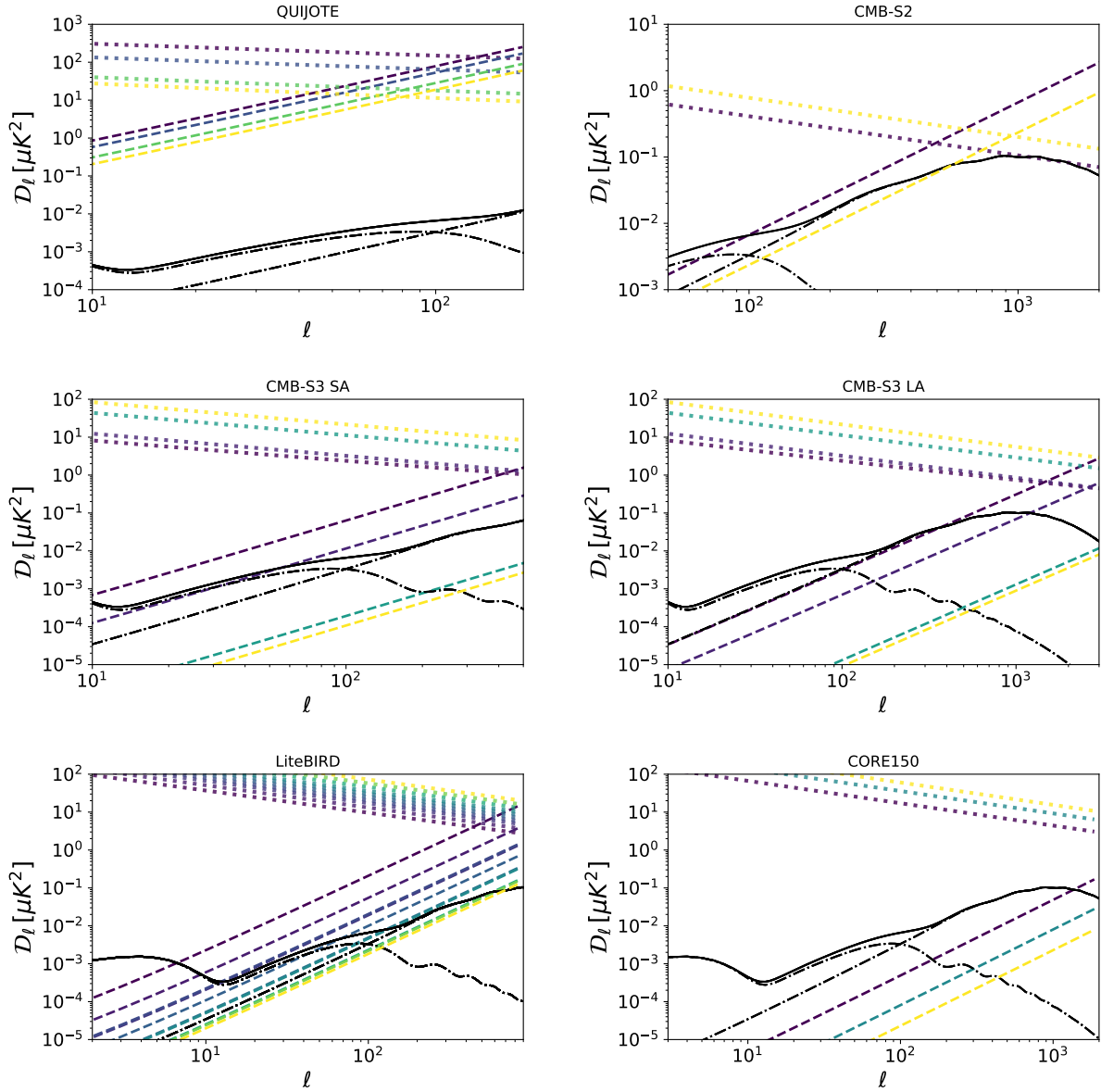


Figure 4.13: Forecasts of foreground contamination with PS4C. In all panels, the black dot-dashed lines show the primordial ($r = 0.05$) and lensed CMB B-mode power spectra and the black solid line is the the total CMB B-mode power spectrum. The dotted (dashed) lines are the power spectrum of the polarized Galactic emission (ERS emission) at the different frequencies available for each experiment, the color scale is such that the colors go from purple to yellow as the frequency increases. The power spectra depend are estimated using eq.(4.4.6) in the region outside the UPB77 *Planck* mask (in order to exclude the Galactic plane and ERS above the 3σ detection limit). The different panels corresponds to predictions for different experiments. From top to bottom and from left to right: QUIJOTE (11, 13, 17, 19 GHz), CMB-S2 (95 and 150 GHz), CMB-S3 observing with small and large aperture telescopes (30, 40, 95, 150 GHz), LiteBIRD (frequencies between 40–166 GHz) and CORE150 (60, 100, 145 GHz).

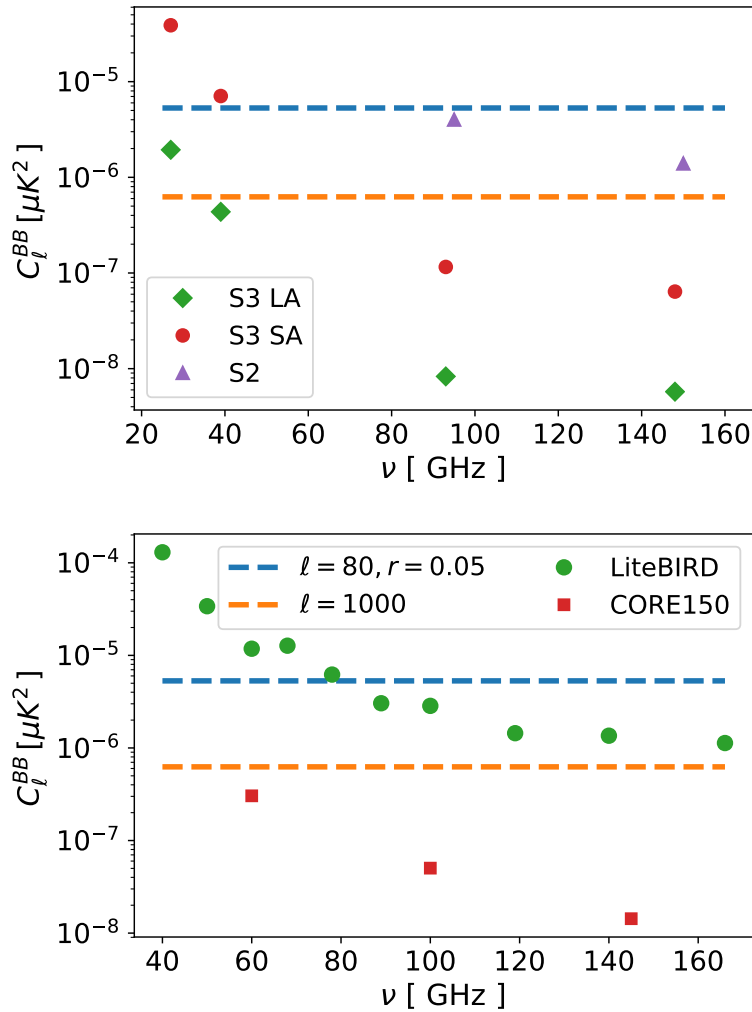


Figure 4.14: Power spectra in polarization of undetected ERS in current and future CMB experiments. Left panel: CMB-S2 (triangles) and CMB-S3 (circles for the small aperture telescope and diamonds for the large aperture telescope). Right panel: LiteBIRD (circles) and CORE150 (squares). The dotted lines are the B-mode power spectra at the acoustic scale ($\ell = 80$) and at the lensing B-modes peak scale ($\ell \approx 1000$).

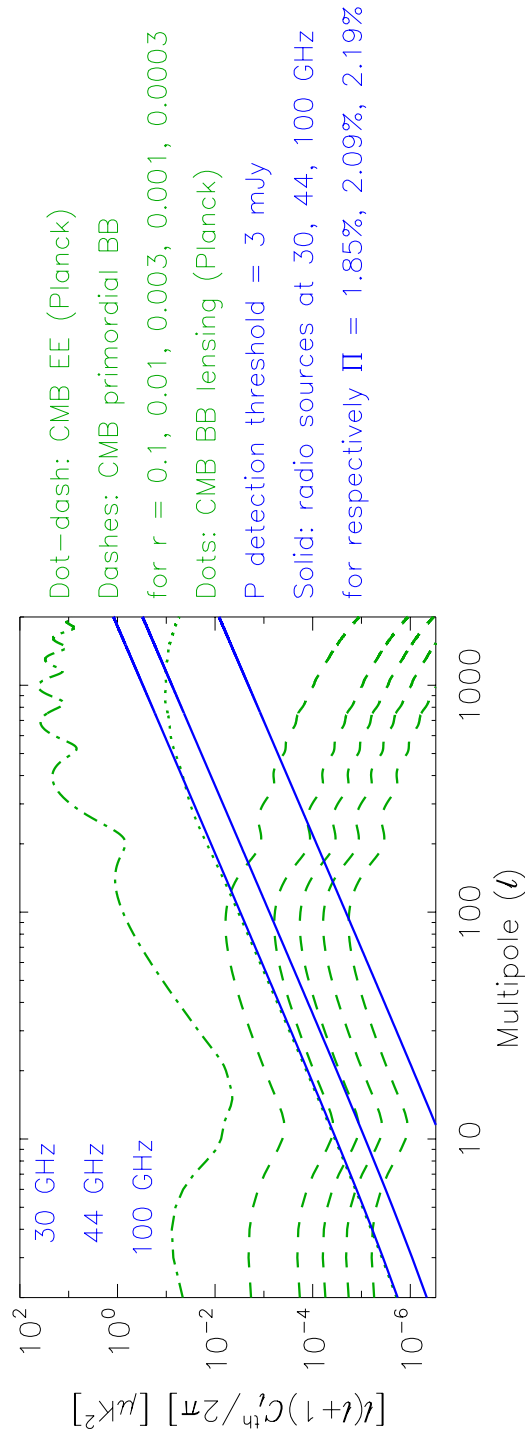


Figure 4.15: Polarization E/B-mode power spectra of radio sources with the CMB E-mode and B-mode for five values of the tensor to scalar ratio r (0.1, 0.01, 0.003, 0.001, 0.0003); see text for details. Since unresolved point sources contribute, on average, equally to E- and B-mode, their total power spectra have been divided by a factor of 2.

Conclusions

The high-frequency (> 20 GHz), bright flux density (> 200 mJy) radio population is dominated by blazars (BL Lacs and Flat Spectrum Radio Quasars), i.e. compact Doppler-boosted objects observed closely to the line of sight, whose emission at higher and higher frequency mostly arises from self-absorbed, knot-like synchrotron structures in the relativistic jet closer and closer to the active nucleus. Their polarization properties was so far poorly constrained at high frequency, since spectra become steeper and the polarization fraction is typically few percents ($\sim 2.5\%$ at 20 GHz) of the total intensity flux density. Thus, observations requires sub-mJy sensitivities and results in literature are easily affected by spectral, detection and variability-related biases. Most of the current estimates rely on extrapolations from low-frequency samples, which are affected by large uncertainties.

Extending the characterization of polarization properties of radio sources to high frequencies provides invaluable information about magnetic fields and plasma in the inner and unresolved regions of relativistic jets. Furthermore, extragalactic radio sources are an important contaminant to the microwave sky in total intensity and in polarization at scales smaller than 30 arcmin up to 100 GHz: an accurate determination of radio source emission is therefore crucial to extract the Cosmic Microwave Background (CMB) angular power spectrum and, in particular, to study the primordial B-mode polarization that might be extremely weak for low values of the tensor to scalar perturbations ratio ($r = T/S$) associated with the stochastic background of gravitational waves, one of the most ambitious goal of current and future CMB projects.

We have presented and discussed high sensitivity polarimetric observations in 7 bands, centered at 2.1, 5.5, 9, 18, 24, 33 and 38 GHz (made with the Australia Telescope Compact Array in two epochs in 2014 and 2016), of a complete sample of 104 extragalactic sources with $S_{20\text{GHz}} \geq 200$ mJy in the AT20G catalogue. The rms error in the polarized flux density is 0.6 mJy at $\nu \geq 5.5$ GHz and 1 mJy at 2.1 GHz, due to the heavy RFI contamination.

The selected sources constitute a complete ($b < -65^\circ$ and $S_{20\text{GHz}} > 200$ mJy) sub-sample of the Planck-ATCA Co-eval Observation (PACO) faint sample. The PACO project aimed to investigate the total intensity spectral behaviour and variability of Planck detected radio sources, exploiting simultaneous ground-based and Planck satellite observations. This project expands the investigation to polarimetry.

The observational determination of the continuum total intensity spectra has been extended by exploiting the GLEAM survey data at 20 frequencies

between 72 and 231 MHz (Hurley-Walker et al. 2017), available for 89 (\simeq 86%) of our sources. For these sources we have the unparalleled coverage of 2.7 decades in frequency.

The total intensity data from 5.5 to 38 GHz could be interpreted in terms of a single emission region (Galluzzi et al. 2017). A joint analysis of the more extended total intensity spectra (from 72 MHz to 38 GHz) and of the polarization spectra reveals a more complex astrophysics. About 93% of our sources show clear indications of at least two emission components, one (or sometimes more) dominating at the higher frequencies and self-absorbed at a few GHz, and another one, generally steeper, emerging at lower frequencies. The most straightforward interpretation of these results is in terms of recurrent activity, with the extension (and, correspondingly, the age) of emission components increasing with decreasing frequency, i.e. with younger components showing up at higher frequencies.

There is no evidence of trends of the linear polarization fraction with the frequency for the full sample and for the single component (“1C”) subset. However, sources with 2 or 3 components (“2-3C”) have a minimum of the polarization fraction at \simeq 9 GHz, consistent with the presence of different emission components at lower and higher frequencies. For multi-component (“>3C”) objects there is a hint of a *decrease* of the polarization fraction with increasing frequency, although the statistics is very poor.

Further indications of different origins for the low- and high-frequency emissions come from our analysis of rotation measures. The data suggest two regimes for the RM vs λ^2 relation, one at cm-wavelengths, with typical *intrinsic* RM of \sim 90 rad/m², and the other for mm-wavelengths with median intrinsic RM \sim 2300 rad/m² (but with large errors). The “>3C” seem to have very high RMs (\sim 4000 rad/m²). Again, the statistics is very poor but it is suggestive that, at mm wavelengths, the large RMs echo the low polarization fraction.

Our high sensitivity polarimetry has allowed a 5σ detection of the weak circular polarization for \sim 38% of data. The measured values of Stokes’ V , while much lower than the linear polarization amplitude, are much higher than expected for the intrinsic circular polarization of synchrotron emission corresponding to the typical magnetic field intensities in radio emitting regions. This is consistent with previous conclusions in the literature that circular polarization is predominantly produced by Faraday conversion of linear polarization.

Taking into account the PACO and the AT20G measurements, the observations of September 2014 and the March-April (and July 2016) campaigns we have at least four epochs of observations in total intensity and three epochs in polarization. Thus, the typical global time span of our dataset ranges from 1.5 yr up to 9 – 10 yr. Analysis of variability indices as function of frequency for different time lags seems to confirm the fact that radio emissions we observe are typically driven by a superposition of synchrotron components experiencing recurrent flaring activity triggered by a newly emitted magnetoionic component along the jet. The latter constitutes a major flaring component, generally traced by frequencies higher than 30 GHz (which corresponds to a

region close to the base of the jet). This “major” event is less frequent than the typical flaring activity due to the interacting recollimating regions along the jet (synchrotron knots) which alone would result in a lower level of variability due to the fact that the major disturbance travels reactivating the previous emitted regions in different epochs. Variability indices in polarization turn out to be systematically larger than those in total intensity (by a factor $\sim 1.5 - 2$), with a not clear frequency dependence if we consider the 9 – 10 yr period, but with a mild increasing trend displayed by 1.5 yr time lag data for all the sample. We also report a clear trend for steep objects only: for both peaked and flat objects we find similar high values, i.e. $\approx 22 - 25\%$, while for steep-spectrum objects there is an increasing trend in frequency again with typical values higher by a factor ~ 2 with respect to the total intensity counterparts. These findings are compatible with the structure we argue for the objects in the sample.

We have presented a new estimate of the counts in linear polarization at 18 GHz derived from the convolution of the distribution of polarization fractions for our sample with the model for total intensity source counts by De Zotti et al. (2005) that, thanks to the high sensitivity of our data, allows to reach deeper polarized flux density levels than obtained so far.

ATCA observations gave the possibility to contribute to the SKA-oriented simulation project T-RECS “Tiered Radio Extragalactic continuum simulation”) project (PI: Anna Bonaldi, SKA Headquarters) with polarimetric characterization of objects.

An ALMA project observed in cycle 3 extends the analysis up to 100 GHz for a (complete) sub-sample of 32 objects. We detect synchrotron signal in almost all the objects (at least at a 3σ level) with no sign of any break, nor thermal as well as dust emissions (up to ~ 300 GHz in redshift-corrected frequency). Median polarization fraction for all the sample is $\sim 2.1\%$ and seems to indicate that magnetic order (if any) is hampered by other phenomena in this regime: turbulence, unresolved substructures and exceptionally dense Faraday screens may play this role. Then, given that in 22 objects out of 32 we have both Q and U detected at least at a 6 sigma level, we take into account polarization position angles at these frequencies to study RMs in our sample. Remarkably, estimated values (median RM ≈ 13000 rad/m²) are at least two orders of magnitude higher than those obtained for the 18 – 24 GHz frequency range. The latter, in turn, are larger by 2 orders of magnitude than values observed for the 2 – 9 GHz range. Despite the small numbers of data available here for the analysis there is a clear confirmation that objects with an higher number of inferred components tend to show an higher degree of RM. In fact, median corrected values are ~ 63000 rad/m² and ~ 140000 rad/m² for 2-3C and >3C objects, respectively. The latter extreme values strongly suggest the presence of particularly dense screens of non-relativistic electrons. We argue that natural candidates can be found in clouds of the narrow line regions (for which the involved electron densities are expected to be in the $10^4 - 10^6$ cm⁻³ range): any synchrotron component very close to the base of jet and collimated by an intense magnetic field might be heavily depolarized in case part of the emitted radiation is intercepted by such dense screens.

In addition, ATCA and ALMA observations together provide useful information both for better evaluating the statistical and systematic accuracies of PPA obtained with ALMA and for exploring the possibility of using ALMA measurements of bright and strongly polarized radio sources, in order to help in calibrating the polarization in CMB experiments. In fact, such calibration accuracy is becoming the limiting factor of several CMB polarization measurements. To this purpose we computed the extragalactic radio source number counts in polarization at ~ 100 GHz by means of convolution of our found polarization fraction distribution with one of the most updated models for total intensity source counts (Tucci et al. 2011). This allowed us to forecast the contribution of unresolved extragalactic radio sources to the CMB polarization power spectra for forthcoming CMB experiments: though no correlation has been observed between the level of fractional polarization and the total intensity flux at larger fluxes at all the observed frequencies (from 2.1 up to 97.5 GHz), we stress that future observations in polarization are needed to further probe even at higher frequencies at deeper flux density levels. Indeed CMB experiments are going to observe an increasing number of polarized extragalactic radio sources because of their improving sensitivities. Hence, we assess that polarized extragalactic radio sources can contaminate the cosmological B-mode polarization if the tensor-to-scalar ratio is < 0.05 and they have to be robustly controlled to de-lens CMB B-modes at the arcminute angular scales. The contribution of undetected source has to be taken into account especially at smaller angular scales (i.e. $\ell > 1000$) at frequencies $\nu > 100$ GHz.

Our observations and analysis spread light on the radio source total intensity and polarimetric behaviour for the first time over a very large range in frequency and to high sensitivity for the bright radio source population. Our sample turned out to be mostly constituted by blazars, as expected on the basis of its selection criteria. Similar analysis of fainter larger samples or surveys at the frequencies we already investigated are the future approach to expand our findings to other radio source populations. On the other side, the indications coming from ALMA observations at 100 GHz, which allowed us to unveil the origin of the signal also observed by the PACO project, indicate another possible development for our study. In fact ALMA, with the unprecedented sensitivity performances, the frequency coverage up to 1 THz and the high polarimetric purity achievable, will allow to statistically probe (e.g. for the blazar class) frequency domains where synchrotron break occurs and other host galaxy radiative processes start to significantly contribute.

Appendix A

MIRIAD scripts for ATCA data reduction

A.1 September 2014 campaign

A.1.1 Script for data reduction at 5.5 GHz

```
#!/usr/bin sh
## It's called a shebang, and tells the parent shell which interpreter should be used to execute the script.

frequency="5500"
Bandpass_Flux_cal="0537-441"
Phase_Leakage_cal="j0529-7245"

rm -rf C2922@$frequency.uv
rm -rf C2922@$frequency.uvindex
rm -rf *.$frequency
rm -rf Plots@$frequency
mkdir -p Plots@$frequency/Diagnostics

atlod in="./RPFITS/2014-09-28_1721.C2922,./RPFITS/2014-09-28_2121.C2922" out="C2922@$frequency.uv"
options="opcorr, birdie, noauto, rflag, xycorr" ifsel=1

uvflag vis="C2922@$frequency.uv" select="shadow(22.5)" flagval=flag
uvflag vis="C2922@$frequency.uv" select="ant(6)" flagval=flag #The baselines with antenna CA06 are all flagged
uvindex vis="C2922@$frequency.uv" log="C2922@$frequency.uvindex"
uvsplit vis="C2922@$frequency.uv"

while read src; do
pgflag vis="$src.$frequency" stokes="i,q,u,v" flagpar="8,5,5,3,6,3" command="<b" device="/xs"
done < FPACO_53srclist_Ext559.txt #This file includes the list of targets and calibrators

mfcal vis=$Bandpass_Flux_cal.$frequency refant=2 interval=0.1

while read src; do
if [ $src != $Bandpass_Flux_cal ]; then
gpcopy vis=$Bandpass_Flux_cal.$frequency out=$src.$frequency
fi
done < FPACO_53srclist_Ext559.txt

while read src; do
pgflag vis="$src.$frequency" stokes="i,q,u,v" flagpar="8,5,5,3,6,3" command="<b" device="/xs"
pgflag vis="$src.$frequency" stokes="i,v,u,q" flagpar="8,2,2,3,6,3" command="<b" device="/xs"
pgflag vis="$src.$frequency" stokes="i,v,q,u" flagpar="8,2,2,3,6,3" command="<b" device="/xs"
done < FPACO_53srclist_Ext559.txt

while read src; do
uvflag vis="$src.$frequency" line="ch,15,1889" flagval=flag
```

```

uvflag vis="$src.$frequency" select="ant(1,2)(2,3)" line="ch,45,1065" flagval=flag
uvflag vis="$src.$frequency" select="ant(2,3)(4)" line="ch,45,1065" flagval=flag
uvflag vis="$src.$frequency" line="ch,20,1310" flagval=flag
done < FPACO_53src1ist_Ext559.txt

#Here below there are dedicated flagging instructions for targets still affected by RFI
#after the automatic pgflag runs.
uvflag vis="j0340-6703.5500" select="ant(1)(4),time(14Sep28:19:49:00,14Sep28:19:52:00)" flagval=flag
uvflag vis="j0355-6645.5500" select="ant(1)(4),time(14Sep28:19:51:00,14Sep28:19:54:00)" flagval=flag

#The model for the bandpass calibrator in total intensity (determined (via 1934-638) by using both IFs
#from observations of the day before) is specified in the keyword "flux".
mfcal vis=$Bandpass_Flux_cal.$frequency flux="3.5155,4.0,0.0796" refant=2 interval=0.1
gpcopy vis=$Bandpass_Flux_cal.$frequency out=$Phase_Leakage_cal.$frequency
gpcal vis=$Phase_Leakage_cal.$frequency refant=2 interval=0.1 nfbn=2 options="xyvary,qusolve"
gpcopy vis=$Phase_Leakage_cal.$frequency out=$Bandpass_Flux_cal.$frequency
gpcal vis=$Bandpass_Flux_cal.$frequency refant=2 interval=0.1 nfbn=2 options="xyvary,nopol"

#####Diagnostic_section#####
uvplt vis=$Phase_Leakage_cal.$frequency axis="time,parang" options=nobase
device="Plots@$frequency/Diagnostics/PhLcal_parang@$frequency"/png
varplt vis=$Phase_Leakage_cal.$frequency yaxis=chi
device="Plots@$frequency/Diagnostics/PhLcal_chi@$frequency"/png
uvflux vis=$Phase_Leakage_cal.$frequency stokes="i,q,u,v"
uvplt vis=$Bandpass_Flux_cal.$frequency stokes="i" axis="real,imag" options="equal,nobase"
device="Plots@$frequency/Diagnostics/scatter_plot_I_BFcal@$frequency"/png
uvplt vis=$Bandpass_Flux_cal.$frequency stokes="q,u,v" axis="real,imag" options="equal,nobase"
device="Plots@$frequency/Diagnostics/scatter_plot_QUV_BFcal@$frequency"/png
uvplt vis=$Phase_Leakage_cal.$frequency stokes="i" axis="real,imag" options="equal,nobase"
device="Plots@$frequency/Diagnostics/scatter_plot_I_PhLcal@$frequency"/png
uvplt vis=$Phase_Leakage_cal.$frequency stokes="q,u,v" axis="real,imag" options="equal,nobase"
device="Plots@$frequency/Diagnostics/scatter_plot_QUV_PhLcal@$frequency"/png
gpplt vis=$Phase_Leakage_cal.$frequency yaxis=phase options=xygains
device="Plots@$frequency/Diagnostics/phase_mod_xygains@$frequency"/png
gpplt vis=$Phase_Leakage_cal.$frequency yaxis=amp options=bandpass
device="Plots@$frequency/Diagnostics/bandpass_phase_cal@$frequency"/png
gpplt vis=$Phase_Leakage_cal.$frequency yaxis=phase options=gains
device="Plots@$frequency/Diagnostics/phase_gains@$frequency"/png
uvplt vis=$Bandpass_Flux_cal.$frequency options=nobase axis="time,el"
device="Plots@$frequency/Diagnostics/BF_elevation@$frequency"/png
uvplt vis=$Phase_Leakage_cal.$frequency options=nobase axis="time,el"
device="Plots@$frequency/Diagnostics/PhL_cal@$frequency"/png
#####

gpboot vis=$Phase_Leakage_cal.$frequency cal=$Bandpass_Flux_cal.$frequency select="time(14Sep28:19:00,14Sep28:19:10)"
mfboot vis="$Bandpass_Flux_cal.$frequency,$Phase_Leakage_cal.$frequency" select="source($Bandpass_Flux_cal)"
flux="3.5155,4.0,0.0796" device=/xs

#In this final block, calibration solutions are applied to targets.
while read src; do
  if [ $src != $Phase_Leakage_cal ] && [ $src != $Bandpass_Flux_cal ]; then
    gpcopy vis=$Phase_Leakage_cal.$frequency out=$src.$frequency
    fi
    uvspec vis=$src.$frequency options=nobase stokes="i" axis="ch,amp"
    device="Plots@$frequency/fluxesI_$src@$frequency"/png
    uvspec vis=$src.$frequency options=nobase stokes="q" axis="ch,amp"
    device="Plots@$frequency/fluxesQ_$src@$frequency"/png
    uvspec vis=$src.$frequency options=nobase stokes="u" axis="ch,amp"
    device="Plots@$frequency/fluxesU_$src@$frequency"/png
    uvspec vis=$src.$frequency options=nobase stokes="v" axis="ch,amp"
    device="Plots@$frequency/fluxesV_$src@$frequency"/png
    uvplt vis=$src.$frequency stokes=i options=nobase axis="uvdist,amp"
    device="Plots@$frequency/AmpVsUVdist_$src@$frequency"/png
    uvflux vis=$src.$frequency stokes="i,q,u,v"
  done < FPACO_53src1ist_Ext559.txt

```

A.1.2 Script for data reduction at 18 GHz

```

#!/usr/bin sh
## It's called a shebang, and tells the parent shell which interpreter should be used to execute the script.

#This first block of the script run two times (for each of the 2 IFs) serves to determine
#the model for the bandpass calibrator (via 1934-638).
frequency="18000"
Band_Lea_cal="0537-441"
Flux_cal="1934-638"
Phase_cal="j0529-7245"

rm -rf C2922@$frequency.uv
rm -rf C2922@$frequency.uvindex
rm -rf *.$frequency
rm -rf Plots@$frequency
mkdir -p Plots@$frequency/Diagnostics

atlod in="./RPFITS/2014-09-26_1346.C2922,./RPFITS/2014-09-26_1446.C2922,./RPFITS/2014-09-26_1847.C2922"
out="C2922@$frequency.uv" options="opcorr, birdie, noauto, rflag, xycorr" ifsel=1

uvflag vis="C2922@$frequency.uv" select="shadow(22.5)" flagval=flag
uvflag vis="C2922@$frequency.uv" select="ant(6)" flagval=flag #The baselines with antenna CA06 are all flagged
uvindex vis="C2922@$frequency.uv" log="C2922@$frequency.uvindex"
uvsplit vis="C2922@$frequency.uv"

while read src; do
pgflag vis="$src.$frequency" stokes="i,q,u,v" flagpar="8,5,5,3,6,3" command="<b" device="/xs"
done < FPACO_53srclist_Ext1838.txt #This file includes the list of targets and calibrators

mfcal vis=$Band_Lea_cal.$frequency refant=2 interval=0.1

while read src; do
if [ $src != $Band_Lea_cal._cal ]; then
gpcopy vis=$Band_Lea_cal.$frequency out=$src.$frequency
fi
done < FPACO_53srclist_Ext1838.txt

while read src; do
pgflag vis="$src.$frequency" stokes="i,q,u,v" flagpar="8,5,5,3,6,3" command="<b" device="/xs"
pgflag vis="$src.$frequency" stokes="i,v,u,q" flagpar="8,2,2,3,6,3" command="<b" device="/xs"
pgflag vis="$src.$frequency" stokes="i,v,q,u" flagpar="8,2,2,3,6,3" command="<b" device="/xs"
done < FPACO_53srclist_Ext1838.txt

while read src; do
uvflag vis="$src.$frequency" select="ant(2)(3,5)" line="ch,45,475" flagval=flag
uvflag vis="$src.$frequency" select="ant(2)(4)" line="ch,50,1150" flagval=flag
done < FPACO_53srclist_Ext1838.txt

mfcal vis=$Band_Lea_cal.$frequency refant=2 interval=0.1
gpcopy vis=$Band_Lea_cal.$frequency out=$Phase_cal.$frequency
gpcal vis=$Phase_cal.$frequency refant=2 interval=0.1 nfbn=2 options="xyvary,qusolve"
gpcal vis=$Band_Lea_cal.$frequency refant=2 interval=0.1 nfbn=2 options="xyvary,qusolve"
gpcopy vis=$Band_Lea_cal.$frequency out=$Phase_cal.$frequency options="nocal"
gpcopy vis=$Phase_cal.$frequency out=$Flux_cal.$frequency
gpcal vis=$Flux_cal.$frequency refant=2 interval=0.1 nfbn=2 options="xyvary,nopol"

#####Diagnostics_section#####
uvplt vis=$Flux_cal.$frequency stokes="i,q,u,v" axis="real,imag" options="equal,nobase,nofqav"
device="Plots@$frequency/Diagnostics/scatter_plot_flux_cal@$frequency"/png
uvplt vis=$Phase_cal.$frequency axis="time,parang" options=nobase
device="Plots@$frequency/Diagnostics/PhLcal_parang@$frequency"/png
varplt vis=$Phase_cal.$frequency yaxis=chi device="Plots@$frequency/Diagnostics/Phase_chi@$frequency"/png
uvflux vis=$Phase_cal.$frequency stokes="i,q,u,v"
uvplt vis=$Phase_cal.$frequency stokes="i" axis="real,imag" options="nobase"
device="Plots@$frequency/Diagnostics/scatter_plot_I_Phase_cal@$frequency"/png
uvplt vis=$Phase_cal.$frequency stokes="q,u,v" axis="real,imag" options="nobase"
device="Plots@$frequency/Diagnostics/scatter_plot_QUV_Phase_cal@$frequency"/png
gpplt vis=$Phase_cal.$frequency yaxis=phase options=xygains
device="Plots@$frequency/Diagnostics/phase_mod_xygains@$frequency"/png
gpplt vis=$Phase_cal.$frequency yaxis=amp options=bandpass

```

```

device="Plots@$frequency/Diagnostics/bandpass_phase_cal@$frequency"/png
gpplt vis=$Phase_cal.$frequency yaxis=phase options=gains
device="Plots@$frequency/Diagnostics/phase_cal_gains@$frequency"/png
uvplt vis=$Flux_cal.$frequency options=nobase axis="time,e1"
device="Plots@$frequency/Diagnostics/Fluxcal_elevation@$frequency"/png
uvplt vis=$Phase_cal.$frequency options=nobase axis="time,e1"
device="Plots@$frequency/Diagnostics/Phase_cal_elevation@$frequency"/png
uvplt vis=$Band_Lea_cal.$frequency options=nobase axis="time,e1"
device="Plots@$frequency/Diagnostics/Band_Lea_cal_elevation@$frequency"/png
#####
gpboot vis=$Band_Lea_cal.$frequency cal=$Flux_cal.$frequency select="time(14Sep26:14:45,14Sep26:15:15)"

#The bandpass calibrator model, once determined by using the above script block, is adopted in the following part
#to reduce the dataset
frequency="18000"
BFL_cal="0537-441"
Phase_cal="j0529-7245"

mfcal vis=$BFL_cal.$frequency flux="3.8079,18.0,-0.0660" refant=2 interval=0.1
gpcopy vis=$BFL_cal.$frequency out=$Phase_cal.$frequency
gpcal vis=$Phase_cal.$frequency refant=2 interval=0.1 nfbn=2 options="xyvary,qusolve"
gpcal vis=$BFL_cal.$frequency refant=2 interval=0.1 nfbn=2 options="xyvary,qusolve"
gpcopy vis=$BFL_cal.$frequency out=$Phase_cal.$frequency options="nocal"

gpboot vis=$Phase_cal.$frequency cal=$BFL_cal.$frequency select="time(14Sep26:15:00,14Sep26:15:15)"
mfboot vis="$Phase_cal.$frequency,$BFL_cal.$frequency" select="source($BFL_cal)" flux="3.8079,18.0,-0.0660" device=/xs

#In this final block, calibration solutions are applied to targets.
while read src; do
  if [ $src != $Phase_cal ] && [ $src != $BFL_cal ] && [ $src != $Flux_cal ]; then
    gpcopy vis=$Phase_cal.$frequency out=$src.$frequency
    fi
    uvspec vis=$src.$frequency options=nobase stokes="i" axis="ch,amp"
    device="Plots@$frequency/fluxesI_$src@$frequency"/png
    uvspec vis=$src.$frequency options=nobase stokes="q" axis="ch,amp"
    device="Plots@$frequency/fluxesQ_$src@$frequency"/png
    uvspec vis=$src.$frequency options=nobase stokes="u" axis="ch,amp"
    device="Plots@$frequency/fluxesU_$src@$frequency"/png
    uvspec vis=$src.$frequency options=nobase stokes="v" axis="ch,amp"
    device="Plots@$frequency/fluxesV_$src@$frequency"/png
    uvplt vis=$src.$frequency stokes=i options=nobase axis="uvdist,amp"
    device="Plots@$frequency/AmpVsUVdist_$src@$frequency"/png
    uvflux vis=$src.$frequency stokes="i,q,u,v"
  done < FPACO_53srcList_Ext1838.txt

```

A.2 March–April 2016 campaign

A.2.1 Script for data reduction at 2.1 GHz

```

#!/usr/bin sh
## It's called a shebang, and tells the parent shell which interpreter should be used to execute the script.

frequency="2100"
BanLea_cal="n0538-4405"
PhaFlu_cal="v0529-7245"

rm -rf C2922@$frequency.uv
rm -rf C2922@$frequency.uvindex
rm -rf *.$frequency
rm -rf Plots@$frequency
mkdir -p Plots@$frequency/Diagnostics

atlod in="../RPFITS/2016-03-29_0543.C2922,../RPFITS/2016-03-29_0622.C2922,../RPFITS/2016-03-29_0944.C2922"
out="C2922@$frequency.uv" options="birdie, noauto, rfi flag, xycorr, opcrr" ifsel=1

uvflag vis="C2922@$frequency.uv" select="shadow(22.5)" flagval=flag

```

```
uvflag vis="C2922@$frequency.uv" select="ant(6)" flagval=flag #The baselines with antenna CA06 are all flagged
#[... Other flagging instructions, mainly due to RFI flagging ...]
```

```
uvindex vis="C2922@$frequency.uv" log="C2922@$frequency.uvindex"
uvsplit vis="C2922@$frequency.uv"
```

```
mfcal vis=$BanLea_cal.$frequency refant=3 interval=0.1
gpcal vis=$BanLea_cal.$frequency refant=3 interval=0.1 nfbn=2 options="xyvary,qusolve"
gpcopy vis=$BanLea_cal.$frequency out=$PhaFlu_cal.$frequency
gpcal vis=$PhaFlu_cal.$frequency refant=3 interval=1.0 nfbn=2 flux="8.142E-01,1.000E-02,2.390E-03,-1.698E-03"
options="xyvary,nopol"
```

```
#####Diagnostic_block#####
uvplt vis=$PhaFlu_cal.$frequency stokes="i,q,u,v" axis="real,imag" options="nobase,nofqav"
device="Plots@$frequency/Diagnostics/scatter_plot_flux_cal@$frequency"/png
uvplt vis=$PhaFlu_cal.$frequency axis="time,parang" options=nobase
device="Plots@$frequency/Diagnostics/PhLcal_parang@$frequency"/png
varplt vis=$PhaFlu_cal.$frequency yaxis=chi device="Plots@$frequency/Diagnostics/Phase_chi@$frequency"/png
uvflux vis=$PhaFlu_cal.$frequency stokes="i,q,u,v"
uvplt vis=$PhaFlu_cal.$frequency stokes="i" axis="real,imag" options="nobase"
device="Plots@$frequency/Diagnostics/scatter_plot_I_Phase_cal@$frequency"/png
uvplt vis=$PhaFlu_cal.$frequency stokes="q,u,v" axis="real,imag" options="nobase"
device="Plots@$frequency/Diagnostics/scatter_plot_QUV_Phase_cal@$frequency"/png
gpplt vis=$PhaFlu_cal.$frequency yaxis=phase options=xygains
device="Plots@$frequency/Diagnostics/phase_mod_xygains@$frequency"/png
gpplt vis=$PhaFlu_cal.$frequency yaxis=amp options=bandpass
device="Plots@$frequency/Diagnostics/bandpass_phase_cal@$frequency"/png
gpplt vis=$PhaFlu_cal.$frequency yaxis=phase options=gains
device="Plots@$frequency/Diagnostics/phase_cal_gains@$frequency"/png
uvplt vis=$PhaFlu_cal.$frequency options=nobase axis="time,e1"
device="Plots@$frequency/Diagnostics/Fluxcal_elevation@$frequency"/png
#####
```

```
#In these final blocks, calibration solutions are applied to targets.
while read src; do
```

```
  if [ $src != $PhaFlu_cal ] && [ $src != $BanLea_cal ]; then
    gpcopy vis=$PhaFlu_cal.$frequency out=$src.$frequency
    fi
    uvspec vis=$src.$frequency options=nobase stokes="i" axis="ch,amp"
    device="Plots@$frequency/fluxesI_$src@$frequency"/png
    uvspec vis=$src.$frequency options=nobase stokes="q" axis="ch,amp"
    device="Plots@$frequency/fluxesQ_$src@$frequency"/png
    uvspec vis=$src.$frequency options=nobase stokes="u" axis="ch,amp"
    device="Plots@$frequency/fluxesU_$src@$frequency"/png
    uvspec vis=$src.$frequency options=nobase stokes="v" axis="ch,amp"
    device="Plots@$frequency/fluxesV_$src@$frequency"/png
    uvplt vis=$src.$frequency stokes=i options=nobase axis="uvdist,amp"
    device="Plots@$frequency/AmpVsUVdist_$src@$frequency"/png
    uvflux vis=$src.$frequency stokes="i,q,u,v"
```

```
done < Islot_2GHz_indexlist_g0529.log #This file contains the target lists for PKS0530-727.
```

```
gpboot vis=$BanLea_cal.$frequency cal=$PhaFlu_cal.$frequency select="time(16Mar29:09:40,16Mar29:09:50)"
```

```
while read src; do
```

```
  if [ $src != $PhaFlu_cal ] && [ $src != $BanLea_cal ]; then
    gpcopy vis=$BanLea_cal.$frequency out=$src.$frequency
    fi
    uvspec vis=$src.$frequency options=nobase stokes="i" axis="ch,amp"
    device="Plots@$frequency/fluxesI_$src@$frequency"/png
    uvspec vis=$src.$frequency options=nobase stokes="q" axis="ch,amp"
    device="Plots@$frequency/fluxesQ_$src@$frequency"/png
    uvspec vis=$src.$frequency options=nobase stokes="u" axis="ch,amp"
    device="Plots@$frequency/fluxesU_$src@$frequency"/png
    uvspec vis=$src.$frequency options=nobase stokes="v" axis="ch,amp"
    device="Plots@$frequency/fluxesV_$src@$frequency"/png
    uvplt vis=$src.$frequency stokes=i options=nobase axis="uvdist,amp"
    device="Plots@$frequency/AmpVsUVdist_$src@$frequency"/png
    uvflux vis=$src.$frequency stokes="i,q,u,v"
```

```
done < Islot_2GHz_indexlist_g0537.log #This file contains the target lists for PKS0537-441.
```

A.2.2 Script for data reduction refinement at 5.5 GHz (merging the I, II slot and the IGT)

```

#!/usr/bin sh
## It's called a shebang, and tells the parent shell which interpreter should be used to execute the script.

frequency="5500"
Flux_cal="1934-638"
PhaLea_cal="v0529-7245"
PhaLea_cal2="0537-441"

rm -rf *.$frequency
rm -rf Plots@$frequency
mkdir -p Plots@$frequency/Diagnostics

#"uvcat" instructions merge visibilities from different slots once the calibration solutions
#(separately determined in each slot) it found are applied.
#Whenever objects were observed in just one slot, it simply copy in the output folder the visibilities
#(again, after having applied calibration tables).
while read src; do
uvcat vis="./UVFITS_Islot_5e9GHz/$src.$frequency" out=$src.$frequency
done < onlyIslot_5e9GHz_indexlist.log

while read src; do
uvcat vis="./UVFITS_IIslot_5e9GHz/$src.$frequency" out=$src.$frequency
done < onlyIIslot_5e9GHz_indexlist.log

uvcat vis="./UVFITS_IGT_5e9GHz/$Flux_cal.$frequency" out=$Flux_cal.$frequency
uvcat vis="./UVFITS_Islot_5e9GHz/$PhaLea_cal2.$frequency,./UVFITS_IIslot_5e9GHz/$PhaLea_cal2.$frequency"
  out=$PhaLea_cal2.$frequency
uvcat vis="./UVFITS_Islot_5e9GHz/$PhaLea_cal.$frequency,./UVFITS_IGT_5e9GHz/$PhaLea_cal.$frequency,
  ./UVFITS_IIslot_5e9GHz/$PhaLea_cal.$frequency" out=$PhaLea_cal.$frequency
uvcat vis="./UVFITS_Islot_5e9GHz/0637-752.$frequency,./UVFITS_IGT_5e9GHz/0637-752.$frequency,
  ./UVFITS_IIslot_5e9GHz/0637-752.$frequency" out=0637-752.$frequency

gpcal vis=$PhaLea_cal.$frequency refant=3 interval=0.1 nfbn=2 options="xyvary,qusolve"
gpcopy vis=$PhaLea_cal.$frequency out=$Flux_cal.$frequency
gpcal vis=$Flux_cal.$frequency refant=3 interval=0.1 nfbn=2 options="xyvary,nopol"

#####Diagnostic_block#####
uvplt vis=$Flux_cal.$frequency stokes="i,q,u,v" axis="real,imag" options="nobase,nofqav"
  device="Plots@$frequency/Diagnostics/scatter_plot_flux_cal@$frequency"/png
uvplt vis=$PhaLea_cal.$frequency axis="time,parang" options=nobase
  device="Plots@$frequency/Diagnostics/PhLcal_parang@$frequency"/png
varplt vis=$PhaLea_cal.$frequency yaxis=chi device="Plots@$frequency/Diagnostics/Phase_chi@$frequency"/png
uvflux vis=$PhaLea_cal.$frequency stokes="i,q,u,v"
uvplt vis=$PhaLea_cal.$frequency stokes="i" axis="real,imag" options="nobase"
  device="Plots@$frequency/Diagnostics/scatter_plot_I_Phase_cal@$frequency"/png
uvplt vis=$PhaLea_cal.$frequency stokes="q,u,v" axis="real,imag" options="nobase"
  device="Plots@$frequency/Diagnostics/scatter_plot_QUV_Phase_cal@$frequency"/png
gpplt vis=$PhaLea_cal.$frequency yaxis=phase options=xygains
  device="Plots@$frequency/Diagnostics/phase_mod_xygains@$frequency"/png
gpplt vis=$PhaLea_cal.$frequency yaxis=amp options=bandpass
  device="Plots@$frequency/Diagnostics/bandpass_phase_cal@$frequency"/png
gpplt vis=$PhaLea_cal.$frequency yaxis=phase options=gains
  device="Plots@$frequency/Diagnostics/phase_cal_gains@$frequency"/png
uvplt vis=$Flux_cal.$frequency options=nobase axis="time,el"
  device="Plots@$frequency/Diagnostics/Flux_cal_elevation@$frequency"/png
uvplt vis=$PhaLea_cal.$frequency options=nobase axis="time,el"
  device="Plots@$frequency/Diagnostics/Phase_Lea_cal_elevation@$frequency"/png
uvplt vis=$PhaLea_cal2.$frequency options=nobase axis="time,el"
  device="Plots@$frequency/Diagnostics/Phase_Lea_cal2_elevation@$frequency"/png
#####

#In these final blocks, calibration solutions are applied to targets.
while read src; do
  if [ $src != $PhaLea_cal ] && [ $src != $PhaLea_cal2 ] && [ $src != $Flux_cal ]; then
gpcopy vis=$PhaLea_cal.$frequency out=$src.$frequency
fi
  uvspec vis=$src.$frequency options=nobase stokes="i" axis="ch,amp"

```

```

device="Plots@$frequency/fluxesI_$src@$frequency"/png
uvspec vis=$src.$frequency options=nobase stokes="q" axis="ch,amp"
device="Plots@$frequency/fluxesQ_$src@$frequency"/png
uvspec vis=$src.$frequency options=nobase stokes="u" axis="ch,amp"
device="Plots@$frequency/fluxesU_$src@$frequency"/png
uvspec vis=$src.$frequency options=nobase stokes="v" axis="ch,amp"
device="Plots@$frequency/fluxesV_$src@$frequency"/png
uvplt vis=$src.$frequency stokes=i options=nobase axis="uvdist,amp"
device="Plots@$frequency/AmpVsUVdist_$src@$frequency"/png
uvflux vis=$src.$frequency stokes="i,q,u,v"
done < IslotIGTIIslot_5e9GHz_indexlist_g0529.log #This file contains the target lists for PKS0530-727.

gpcopy vis=$PhaLea_cal.$frequency out=$PhaLea_cal2.$frequency
gpcal vis=$PhaLea_cal2.$frequency refant=3 interval=0.1 nbin=2 options="xyvary,nopol"
gpboot vis=$PhaLea_cal2.$frequency cal=$PhaLea_cal.$frequency select="time(16Mar29:09:35,16Mar29:09:40)"

while read src; do
  if [ $src != $PhaLea_cal ] && [ $src != $PhaLea_cal2 ] && [ $src != $Flux_cal ]; then
    gpcopy vis=$PhaLea_cal2.$frequency out=$src.$frequency
    fi
    uvspec vis=$src.$frequency options=nobase stokes="i" axis="ch,amp"
    device="Plots@$frequency/fluxesI_$src@$frequency"/png
    uvspec vis=$src.$frequency options=nobase stokes="q" axis="ch,amp"
    device="Plots@$frequency/fluxesQ_$src@$frequency"/png
    uvspec vis=$src.$frequency options=nobase stokes="u" axis="ch,amp"
    device="Plots@$frequency/fluxesU_$src@$frequency"/png
    uvspec vis=$src.$frequency options=nobase stokes="v" axis="ch,amp"
    device="Plots@$frequency/fluxesV_$src@$frequency"/png
    uvplt vis=$src.$frequency stokes=i options=nobase axis="uvdist,amp"
    device="Plots@$frequency/AmpVsUVdist_$src@$frequency"/png
    uvflux vis=$src.$frequency stokes="i,q,u,v"
  done < IslotIGTIIslot_5e9GHz_indexlist_g0537.log #This file contains the target lists for PKS0537-441.

```

A.2.3 Script for data reduction at 33 GHz

```

#!/usr/bin sh
## It's called a shebang, and tells the parent shell which interpreter should be used to execute the script.

frequency="33000"
Bandpass_cal="0537-441"
Flux_cal="1934-638"
PhaLea_cal="0537-441"
PhaLea_cal2="0637-752"
PhaLea_cal3="v0529-7245"

rm -rf *.$frequency
rm -rf Plots@$frequency
mkdir -p Plots@$frequency/Diagnostics

uvsplit vis="../UVFITS_Loaded_Flagged/C2922_IIIsIslotIIIGT_1833GHz.uv" select="frequency(31,35)"

uvflag vis=$Bandpass_cal.$frequency select="ant(1)(2),polarization(xy,yx)"
  line="ch,40,435" flagval=flag
uvflag vis=$Bandpass_cal.$frequency select="ant(2)(3,4,5),polarization(xy,yx)"
  line="ch,20,455" flagval=flag
uvflag vis=$Bandpass_cal.$frequency select="ant(2)(1,3,5),polarization(xy,yx)"
  line="ch,90,640" flagval=flag
uvflag vis=$Bandpass_cal.$frequency select="ant(2)(4),polarization(xy,yx)"
  line="ch,110,610" flagval=flag
uvflag vis=$Bandpass_cal.$frequency select="ant(2)(1,3,4,5),polarization(xy,yx)"
  line="ch,40,1185" flagval=flag
uvflag vis=$Bandpass_cal.$frequency select="ant(2)(1,3,4,5),polarization(xy,yx)"
  line="ch,40,1480" flagval=flag

while read src; do
pgflag vis=$src.$frequency stokes="i,q,u,v" flagpar="8,5,5,3,6,3" command="<b" device="/xs"
done < IIIIsIslotIIIGT_33e38GHz_indexlist.log #This file includes the list of targets and calibrators

mfcal vis=$Bandpass_cal.$frequency refant=3 interval=0.1

```

```

while read src; do
if [ $src != $Bandpass_cal ]; then
gpcopy vis=$Bandpass_cal.$frequency out=$src.$frequency
fi
done < IIIslotIIIGT_33e38GHz_indexlist.log

while read src; do
pgflag vis="$src.$frequency" stokes="i,q,u,v" flagpar="8,5,5,3,6,3" command="<b" device="/xs"
pgflag vis="$src.$frequency" stokes="i,v,u,q" flagpar="8,2,2,3,6,3" command="<b" device="/xs"
pgflag vis="$src.$frequency" stokes="i,v,q,u" flagpar="8,2,2,3,6,3" command="<b" device="/xs"
done < IIIslotIIIGT_33e38GHz_indexlist.log

frequency="33000"
BandLea_cal="0537-441"
PhaFlu_cal="v0529-7245"

mfcal vis=$BandLea_cal.$frequency refant=3 interval=0.1
gpcal vis=$BandLea_cal.$frequency refant=3 interval=0.1 nfbn=2 options="xyvary,qusolve"
gpcopy vis=$BandLea_cal.$frequency out=$PhaFlu_cal.$frequency options="nocal"
gpcal vis=$PhaFlu_cal.$frequency refant=3 interval=0.1 nfbn=2 flux="9.954E-01,-9.729E-03,-2.143E-02,2.280E-03"
options="xyvary,qusolve,nopol"

#####Diagnostic_block#####
uvplt vis=$PhaFlu_cal.$frequency stokes="i,q,u,v" axis="real,imag" options="nobase,nofqav"
device="Plots@$frequency/Diagnostics/scatter_plot_flux_cal@$frequency"/png
uvplt vis=$PhaFlu_cal.$frequency axis="time,parang" options=nobase
device="Plots@$frequency/Diagnostics/PhLcal_parang@$frequency"/png
varplt vis=$PhaFlu_cal.$frequency yaxis=chi device="Plots@$frequency/Diagnostics/Phase_chi@$frequency"/png
uvflux vis=$PhaFlu_cal.$frequency stokes="i,q,u,v"
uvplt vis=$PhaFlu_cal.$frequency stokes="i" axis="real,imag" options="nobase"
device="Plots@$frequency/Diagnostics/scatter_plot_I_Phase_cal@$frequency"/png
uvplt vis=$PhaFlu_cal.$frequency stokes="q,u,v" axis="real,imag" options="nobase"
device="Plots@$frequency/Diagnostics/scatter_plot_QUV_Phase_cal@$frequency"/png
gpplt vis=$PhaFlu_cal.$frequency yaxis=phase options=xygains
device="Plots@$frequency/Diagnostics/phase_mod_xygains@$frequency"/png
gpplt vis=$PhaFlu_cal.$frequency yaxis=amp options=bandpass
device="Plots@$frequency/Diagnostics/bandpass_phase_cal@$frequency"/png
gpplt vis=$PhaFlu_cal.$frequency yaxis=phase options=gains
device="Plots@$frequency/Diagnostics/phase_cal_gains@$frequency"/png
uvplt vis=$PhaFlu.$frequency options=nobase axis="time,el"
device="Plots@$frequency/Diagnostics/Fluxcal_elevation@$frequency"/png
uvplt vis=$PhaLea_cal2.$frequency options=nobase axis="time,el"
device="Plots@$frequency/Diagnostics/Phase_cal2_elevation@$frequency"/png
#####

#In these final blocks, calibration solutions are applied to targets.
while read src; do
if [ $src != $PhaFlu_cal ] && [ $src != $Bandpass_cal ] && [ $src != $Flux_cal ]; then
gpcopy vis=$PhaFlu_cal.$frequency out=$src.$frequency
fi
uvspec vis=$src.$frequency options=nobase stokes="i" axis="ch,amp"
device="Plots@$frequency/fluxesI_$src@$frequency"/png
uvspec vis=$src.$frequency options=nobase stokes="q" axis="ch,amp"
device="Plots@$frequency/fluxesQ_$src@$frequency"/png
uvspec vis=$src.$frequency options=nobase stokes="u" axis="ch,amp"
device="Plots@$frequency/fluxesU_$src@$frequency"/png
uvspec vis=$src.$frequency options=nobase stokes="v" axis="ch,amp"
device="Plots@$frequency/fluxesV_$src@$frequency"/png
uvplt vis=$src.$frequency stokes=i options=nobase axis="uvdist,amp"
device="Plots@$frequency/AmpVsUVdist_$src@$frequency"/png
uvflux vis=$src.$frequency stokes="i,q,u,v"
done < IIIslotIIIGT_33e38GHz_indexlist_g0529.log #This file contains the target lists for PKS0530-727.

gpboot vis=$BandLea_cal.$frequency cal=$PhaFlu_cal.$frequency select="time(16Mar31:10:15,16Mar31:10:45)"

while read src; do
if [ $src != $PhaFlu_cal ] && [ $src != $Bandpass_cal ] && [ $src != $Flux_cal ]; then
gpcopy vis=$BandLea_cal.$frequency out=$src.$frequency
fi
uvspec vis=$src.$frequency options=nobase stokes="i" axis="ch,amp"

```

```
device="Plots@$frequency/fluxesI_$src@$frequency"/png
uvspec vis=$src.$frequency options=nobase stokes="q" axis="ch,amp"
device="Plots@$frequency/fluxesQ_$src@$frequency"/png
uvspec vis=$src.$frequency options=nobase stokes="u" axis="ch,amp"
device="Plots@$frequency/fluxesU_$src@$frequency"/png
uvspec vis=$src.$frequency options=nobase stokes="v" axis="ch,amp"
device="Plots@$frequency/fluxesV_$src@$frequency"/png
uvplt vis=$src.$frequency stokes=i options=nobase axis="uvdist,amp"
device="Plots@$frequency/AmpVsUVdist_$src@$frequency"/png
uvflux vis=$src.$frequency stokes="i,q,u,v"
done < IIIslotIIIGT_33e38GHz_indexlist_g0537.log #This file contains the target lists for PKS0537-441.
```


Bibliography

- Abazajian K. N., Adshead P., Ahmed Z., Allen S. W., Alonso D., Arnold K. S., Baccigalupi C., Bartlett J. G., et al. 2016, ArXiv e-prints
- Ade P. A. R., Akiba Y., Anthony A. E., Arnold K., Atlas M., Barron D., Boettger D., Polarbear Collaboration 2014, Physical Review Letters, 113, 021301
- Agudo I., Thum C., Gómez J. L., Wiesemeyer H., 2014, A&A, 566, A59
- Agudo I., Thum C., Ramakrishnan V., Molina S. N., Casadio C., Gomez J. L., 2017, ArXiv e-prints
- Agudo I., Thum C., Wiesemeyer H., Krichbaum T. P., 2010, ApJS, 189, 1
- Aller M. F., Aller H. D., Hughes P. A., 1992, ApJ, 399, 16
- Aller M. F., Aller H. D., Hughes P. A., Latimer G. E., 1999, ApJ, 512, 601
- André P., Baccigalupi C., Banday A., Barbosa D., Barreiro B., Bartlett J., Bartolo N., Battistelli E., Battye R., Bendo G., Benoît A., et al. 2014, J. Cosmology Astropart. Phys., 2, 006
- Argüeso F., González-Nuevo J., Toffolatti L., 2003, ApJ, 598, 86
- Arkin H., Colton R., 1970, Statistical methods. College outline series, Barnes & Noble
- Barcons X., Franceschini A., de Zotti G., Danese L., Miyaji T., 1995, ApJ, 455, 480
- Battye R. A., Browne I. W. A., Peel M. W., Jackson N. J., Dickinson C., 2011, MNRAS, 413, 132
- Best P. N., Ker L. M., Simpson C., Rigby E. E., Sabater J., 2014, MNRAS, 445, 955
- BICEP2/Keck and Planck Collaborations Ade P. A. R., Aghanim N., Ahmed Z., Aikin R. W., Alexander K. D., Arnaud M., Aumont J., Baccigalupi C., Banday A. J., et al. 2015, Phys. Rev. Lett., 114, 101301
- Blandford R. D., Königl A., 1979, ApJ, 232, 34

- Blandford R. D., Payne D. G., 1982, MNRAS, 199, 883
- Blandford R. D., Znajek R. L., 1977, MNRAS, 179, 433
- Bonaldi A., Bonavera L., Massardi M., De Zotti G., 2013, MNRAS, 428, 1845
- Bonato M., Negrello M., Mancuso C., De Zotti G., Ciliegi P., Cai Z.-Y., Lapi A., Massardi M., Bonaldi A., Sajina A., Smolčić V., Schinnerer E., 2017, MNRAS, 469, 1912
- Bonavera L., González-Nuevo J., Argüeso F., Toffolatti L., 2017, MNRAS, 469, 2401
- Bonavera L., González-Nuevo J., De Marco B., Argüeso F., Toffolatti L., 2017, MNRAS, 472, 628
- Bonavera L., Massardi M., Bonaldi A., González-Nuevo J., De Zotti G., Ekers R. D., 2011, MNRAS, 416, 559
- Brentjens M. A., de Bruyn A. G., 2005, A&A, 441, 1217
- Bridle A. H., Hough D. H., Lonsdale C. J., Burns J. O., Laing R. A., 1994, AJ, 108, 766
- Burke-Spolaor S., Ekers R. D., Massardi M., Murphy T., Partridge B., Ricci R., Sadler E. M., 2009, MNRAS, 395, 504
- Burn B. J., 1966, MNRAS, 133, 67
- Callingham J. R., Gaensler B. M., Ekers R. D., Tingay S. J., Wayth R. B., Morgan J., Bernardi G., Bell M. E., Bhat R., et al. 2015, ApJ, 809, 168
- Carroll S. M., Field G. B., Jackiw R., 1989, in Bulletin of the American Astronomical Society Vol. 21 of BAAS, Astrophysical Limits on a Modified Electrodynamics. p. 1173
- Chen X., Rachen J. P., López-Caniego M., Dickinson C., Pearson T. J., Fuhrmann L., Krichbaum T. P., Partridge B., 2013, A&A, 553, A107
- Ciaramella A., Bongardo C., Aller H. D., Aller M. F., De Zotti G., Lähteenmaki A., Longo G., Milano L., Tagliaferri R., Teräsranta H., Tornikoski M., Urpo S., 2004, A&A, 419, 485
- Condon J. J., 1984, ApJ, 287, 461
- Condon J. J., Cotton W. D., Greisen E. W., Yin Q. F., Perley R. A., Taylor G. B., Broderick J. J., 1998, AJ, 115, 1693
- Danese L., de Zotti G., 1984, A&A, 131, L1

- De Zotti G., Danese L., Franceschini A., Persic M., Toffolatti L., 1989, in Hunt J., Battrick B., eds, Two Topics in X-Ray Astronomy, Volume 1: X Ray Binaries. Volume 2: AGN and the X Ray Background Vol. 296 of ESA Special Publication, Contributions of discrete sources to the X ray background
- De Zotti G., Gonzalez-Nuevo J., Lopez-Caniego M., Negrello M., Greenslade J., Hernandez-Monteagudo C., Delabrouille J., Cai Z.-Y., Bonato M., Achúcarro A., et al. 2016, ArXiv e-prints
- de Zotti G., Massardi M., Negrello M., Wall J., 2010, *A&ARv*, 18, 1
- De Zotti G., Ricci R., Mesa D., Silva L., Mazzotta P., Toffolatti L., González-Nuevo J., 2005, *A&A*, 431, 893
- Delabrouille J., de Bernardis P., Bouchet F. R., Achúcarro A., Ade P. A. R., Allison R., Arroja F., Artal E., Ashdown M., Baccigalupi C., for the CORE collaboration 2017, ArXiv e-prints
- di Serego Alighieri S., 2015, *International Journal of Modern Physics D*, 24, 1530016
- di Serego Alighieri S., Finelli F., Galaverni M., 2010, *ApJ*, 715, 33
- Eichendorf W., Reinhardt M., 1979, *Ap&SS*, 61, 153
- Errard J., Stivoli F., Stompor R., 2011, *Phys. Rev. D*, 84, 069907
- Falomo R., Pian E., Treves A., Giovannini G., Venturi T., Moretti A., Arcidiano C., Farinato J., Ragazzoni R., et al. 2009, *A&A*, 501, 907
- Fanaroff B. L., Riley J. M., 1974, *MNRAS*, 167, 31P
- Fanti C., Pozzi F., Dallacasa D., Fanti R., Gregorini L., Stanghellini C., Vigotti M., 2001, *A&A*, 369, 380
- Farnes J. S., Gaensler B. M., Carretti E., 2014, *ApJS*, 212, 15
- Galluzzi V., Massardi M., Bonaldi A., Casasola V., Gregorini L., Trombetti T., Burigana C., Bonato M., De Zotti G., Ricci R., Stevens J., Ekers R. D., et al. 2018, *MNRAS*, 475, 1306
- Galluzzi V., Massardi M., Bonaldi A., Casasola V., Gregorini L., Trombetti T., Burigana C., De Zotti G., Ricci R., Stevens J., Ekers R. D., Bonavera L., et al. 2017, *MNRAS*, 465, 4085
- Gaskell C. M., Goosmann R. W., Klimek E. S., 2008, *Mem. Soc. Astron. Italiana*, 79, 1090
- Gehrels N., 1986, *ApJ*, 303, 336
- Ghisellini G., Celotti A., 2001, *A&A*, 379, L1

- Ginzburg V. L., Syrovatskii S. I., 1969, *ARA&A*, 7, 375
- Gold B., Odegard N., Weiland J. L., Hill R. S., Kogut A., Bennett C. L., Hinshaw G., Chen X., Dunkley J., et al. 2011, *ApJS*, 192, 15
- González-Nuevo J., Toffolatti L., Argüeso F., 2005, *ApJ*, 621, 1
- Grant J. K., Taylor A. R., Stil J. M., Landecker T. L., Kothes R., Ransom R. R., Scott D., 2010, *ApJ*, 714, 1689
- Hafez Y. A., Davies R. D., Davis R. J., Dickinson C., Battistelli E. S., Blanco F., Cleary K., Franzen T., Genova-Santos R., et al. 2008, *MNRAS*, 388, 1775
- Hales C. A., Norris R. P., Gaensler B. M., Middelberg E., 2014, *MNRAS*, 440, 3113
- Hanson D., Hoover S., Crites A., Ade P. A. R., Aird K. A., Austermann J. E., Beall J. A., Bender A. N., Benson B. A., Bleem L. E., et al. 2013, *Physical Review Letters*, 111, 141301
- Hardcastle M., 2015, in Contopoulos I., Gabuzda D., Kylafis N., eds, *The Formation and Disruption of Black Hole Jets Vol. 414 of Astrophysics and Space Science Library, Kiloparsec-Scale AGN Jets*. p. 83
- Heckman T. M., Best P. N., 2014, *ARA&A*, 52, 589
- Huffenberger K. M., Araujo D., Bischoff C., Buder I., Chinone Y., Cleary K., Kusaka A., Monsalve R., Næss S. K., QUIET Collaboration 2015, *ApJ*, 806, 112
- Hurley-Walker N., Callingham J. R., Hancock P. J., Franzen T. M. O., Hindson L., Kapińska A. D., Morgan J., Offringa A. R., Wayth R. B., Wu C., Zheng Q., Murphy T., et al. 2017, *MNRAS*, 464, 1146
- Impey C. D., Neugebauer G., 1988, *AJ*, 95, 307
- Jackson N., Battye R. A., Browne I. W. A., Joshi S., Muxlow T. W. B., Wilkinson P. N., 2007, *MNRAS*, 376, 371
- Jackson N., Browne I. W. A., Battye R. A., Gabuzda D., Taylor A. C., 2010, *MNRAS*, 401, 1388
- Jiang L., Helly J. C., Cole S., Frenk C. S., 2014, *MNRAS*, 440, 2115
- Johnston-Hollitt M., Ekers R. D., 2004, *ArXiv Astrophysics e-prints*
- Kapahi V. K., 1981, *A&AS*, 43, 381
- Kaufman J. P., Keating B. G., Johnson B. R., 2016, *MNRAS*, 455, 1981
- Kellermann K. I., 1964, *ApJ*, 140, 969

- Kellermann K. I., Sramek R., Schmidt M., Shaffer D. B., Green R., 1989, *AJ*, 98, 1195
- Klein U., Mack K.-H., Gregorini L., Vigotti M., 2003, *A&A*, 406, 579
- Laing R. A., 1996, in Hardee P. E., Bridle A. H., Zensus J. A., eds, *Energy Transport in Radio Galaxies and Quasars Vol. 100 of Astronomical Society of the Pacific Conference Series, Brightness and Polarization Structure of Decelerating Relativistic Jets*. p. 241
- Leahy J. P., 1993, in Röser H.-J., Meisenheimer K., eds, *Jets in Extragalactic Radio Sources Vol. 421 of Lecture Notes in Physics*, Berlin Springer Verlag, DRAGNs. p. 1
- Leon S., Cortes P. C., Guerard M., Villard E., Hidayat T., Ocaña Flaquer B., Vila-Vilaro B., 2016, *A&A*, 586, A70
- Lewis A., Challinor A., Lasenby A., 2000, *Astrophys. J.*, 538, 473
- Lister M. L., Homan D. C., 2005, *AJ*, 130, 1389
- Lister M. L., Tingay S. J., Preston R. A., 2001, *ApJ*, 554, 964
- Liuzzo E., Falomo R., Treves A., 2011, *ArXiv e-prints*
- Liuzzo E., Nagai H., Giovannini G., Mignano A., 2015, in Iono D., Tatematsu K., Wootten A., Testi L., eds, *Revolution in Astronomy with ALMA: The Third Year Vol. 499 of Astronomical Society of the Pacific Conference Series, The Jet of the BL Lac Object PKS 0521-365 in the mm-Band: ALMA Observations*. p. 129
- López-Caniego M., Massardi M., González-Nuevo J., Lanz L., Herranz D., De Zotti G., Sanz J. L., Argüeso F., 2009, *ApJ*, 705, 868
- López-Caniego M., Rebolo R., Aguiar M., Génova-Santos R., Gómez-Reñasco F., Gutierrez C., Herreros J. M., Hoyland R. J., López-Caraballo C., Pelaez Santos A. E., et al. 2014, *ArXiv e-prints*
- Mahony E. K., Sadler E. M., Croom S. M., Ekers R. D., Bannister K. W., Chhetri R., Hancock P. J., Johnston H. M., Massardi M., Murphy T., 2011, *MNRAS*, 417, 2651
- Marscher A. P., Gear W. K., 1985, *ApJ*, 298, 114
- Marshall F. E., Mushotzky R. F., Boldt E. A., Holt S. S., Rothschild R. E., Serlemitsos P. J., 1978, *Nature*, 275, 624
- Massardi M., Bonaldi A., Bonavera L., De Zotti G., Lopez-Caniego M., Galluzzi V., 2016, *MNRAS*, 455, 3249
- Massardi M., Bonaldi A., Bonavera L., López-Caniego M., de Zotti G., Ekers R. D., 2011, *MNRAS*, 415, 1597

- Massardi M., Bonaldi A., Negrello M., Ricciardi S., Raccanelli A., de Zotti G., 2010, *MNRAS*, 404, 532
- Massardi M., Burke-Spolaor S. G., Murphy T., Ricci R., López-Caniego M., Negrello M., Chhetri R., De Zotti G., Ekers R. D., Partridge R. B., Sadler E. M., 2013, *MNRAS*, 436, 2915
- Massardi M., Ekers R. D., Murphy T., Mahony E., Hancock P. J., Chhetri R., De Zotti G., Sadler E. M., Burke-Spolaor S., Calabretta M., Edwards P. G., Ekers J. A., et al. 2011, *MNRAS*, 412, 318
- Massardi M., Ekers R. D., Murphy T., Ricci R., Sadler E. M., Burke S., de Zotti G., Edwards P. G., Hancock P. J., Jackson C. A., Kesteven M. J., Mahony E., Phillips C. J., Staveley-Smith L., Subrahmanyan R., Walker M. A., Wilson W. E., 2008, *MNRAS*, 384, 775
- Massardi M., Galluzzi V., Paladino R., Burigana C., 2016, *International Journal of Modern Physics D*, 25, 1640009
- Matsumura T., Akiba Y., Arnold K., Borrill J., Chendra R., Chinone Y., Cukierman A., de Haan T., Dobbs M., Dominjon A., Elleflot T., et al. 2016, *Journal of Low Temperature Physics*, 184, 824
- Mauch T., Murphy T., Buttery H. J., Curran J., Hunstead R. W., Piestrzynski B., Robertson J. G., Sadler E. M., 2003, *MNRAS*, 342, 1117
- McAlpine W., 2013, PhD thesis, George Mason University
- Mesa D., Baccigalupi C., De Zotti G., Gregorini L., Mack K.-H., Vigotti M., Klein U., 2002, *A&A*, 396, 463
- Mocanu L. M., Crawford T. M., Vieira J. D., Aird K. A., Aravena M., Austermann J. E., Benson B. A., Béthermin M., Bleem L. E., Bothwell M., et al. 2013, *ApJ*, 779, 61
- Murphy T., Sadler E. M., Ekers R. D., Massardi M., Hancock P. J., Mahony E., Ricci R., Burke-Spolaor S., Calabretta M., Chhetri R., de Zotti G., Edwards P. G., Ekers J. A., et al. 2010, *MNRAS*, 402, 2403
- Nartallo R., Gear W. K., Murray A. G., Robson E. I., Hough J. H., 1998, *MNRAS*, 297, 667
- Negrello M., Clemens M., Gonzalez-Nuevo J., De Zotti G., Bonavera L., Cosco G., Guarese G., Boaretto L., Serjeant S., Toffolatti L., et al. 2013, *MNRAS*, 429, 1309
- O’Dea C. P., 1998, *PASP*, 110, 493
- Offringa A. R., van de Gronde J. J., Roerdink J. B. T. M., 2012, *A&A*, 539
- Okudaira A., Tabara H., Kato T., Inoue M., 1993, *PASJ*, 45, 153

- Oppermann N., Junklewitz H., Greiner M., Enßlin T. A., Akahori T., Carretti E., Gaensler B. M., Goobar A., Harvey-Smith L., Johnston-Hollitt M., Pratley L., Schnitzeler D. H. F. M., Stil J. M., Vacca V., 2015, *A&A*, 575, A118
- Pacholczyk A. G., 1973, *MNRAS*, 163, 29P
- Padovani P., 2017, *Nature Astronomy*, 1, 0194
- Partridge B., López-Cañiego M., Perley R. A., Stevens J., Butler B. J., Rocha G., Walter B., Zacchei A., 2016, *ApJ*, 821, 61
- Pasetto A., Kraus A., Mack K.-H., Bruni G., Carrasco-González C., 2016, *A&A*, 586, A117
- Peacock J. A., Wall J. V., 1982, *MNRAS*, 198, 843
- Perley R. A., 1982, *AJ*, 87, 859
- Perley R. A., Roser H.-J., Meisenheimer K., 1997, *A&A*, 328, 12
- Peterson B. M., Horne K., 2004, *Astronomische Nachrichten*, 325, 248
- Planck Collaboration 2015, *Astronomy & Astrophysics*, 594, A26
- Planck Collaboration Aatrokoski J., Ade P. A. R., Aghanim N., Aller H. D., Aller M. F., Angelakis E., Arnaud M., Ashdown M., Aumont J., et al. 2011, *A&A*, 536, A15
- Planck Collaboration Adam R., Ade P. a. R., Aghanim N., Alves M. I. R., Arnaud M., Ashdown M., Aumont J., Baccigalupi C., Gregorio A., Gruppuso A., Gudmundsson J. E., Hansen F. K., Hanson D., 2015, *ArXiv e-prints*, 10, 1
- Planck Collaboration Adam R., Ade P. A. R., Aghanim N., Arnaud M., Ashdown M., Aumont J., Baccigalupi C., Banday A. J., Barreiro R. B., et al. 2016, *A&A*, 594, A9
- Planck Collaboration Ade P. A. R., Aghanim N., Argüeso F., Arnaud M., Ashdown M., Atrio-Barandela F., Aumont J., Baccigalupi C., Balbi A., Banday A. J., et al. 2013, *Astronomy & Astrophysics*, 550, A133
- Planck Collaboration Ade P. A. R., Aghanim N., Argüeso F., Arnaud M., Ashdown M., Aumont J., Baccigalupi C., Banday A. J., Barreiro R. B., et al. 2016, *A&A*, 594, A26
- Planck Collaboration Ade P. A. R., Aghanim N., Armitage-Caplan C., Arnaud M., Ashdown M., Atrio-Barandela F., Aumont J., Baccigalupi C., Banday A. J., et al. 2014, *A&A*, 571, A16
- Planck Collaboration Ade P. A. R., Aghanim N., Arnaud M., Ashdown M., Aumont J., Baccigalupi C., Banday A. J., Barreiro R. B., Bartlett J. G., et al. 2016, *A&A*, 594, A13

- Polko P., Meier D. L., Markoff S., 2010, *ApJ*, 723, 1343
- Prieto M. A., Brunetti G., Mack K.-H., 2002, *Science*, 298, 193
- Procopio P., Massardi M., Righini S., Zanichelli A., Ricciardi S., Libardi P., Burigana C., Cuttaia F., Mack K.-H., et al. 2011, *MNRAS*, 417, 1123
- Puglisi G., Galluzzi V., Bonavera L., Gonzalez-Nuevo J., Lapi A., Massardi M., Perrotta F., Baccigalupi C., Celotti A., Danese L., 2017, *ArXiv e-prints*
- Pushkarev A. B., Kovalev Y. Y., Lobanov A. P., 2008, *Mem. Soc. Astron. Italiana*, 79, 1170
- Rayner D. P., Norris R. P., Sault R. J., 2000, *MNRAS*, 319, 484
- Ricci R., Prandoni I., Gruppioni C., Sault R. J., de Zotti G., 2006, *A&A*, 445, 465
- Röser H. J., Perley R. A., Meisenheimer K., 1987, in Asseo E., Gresillon D., eds, *Magnetic Fields & Extragalactic Objects Optical and Radio Observations of Hot Spots and Lobes in Pictor A*. p. 361
- Rudnick L., Jones T. W., Aller H. D., Aller M. F., Hodge P. E., Owen F. N., Fiedler R. L., Puschell J. J., Bignell R. C., 1985, *ApJS*, 57, 693
- Ruszkowski M., Begelman M. C., 2002, *ApJ*, 573, 485
- Sadler E. M., Ricci R., Ekers R. D., Ekers J. A., Hancock P. J., Jackson C. A., Kesteven M. J., Murphy T., Phillips C., Reinfrank R. F., Staveley-Smith L., Subrahmanyam R., Walker M. A., Wilson W. E., de Zotti G., 2006, *MNRAS*, 371, 898
- Sajina A., Partridge B., Evans T., Stefl S., Vechik N., Myers S., Dicker S., Korngut P., 2011, *ApJ*, 732, 45
- Sault R. J., Teuben P. J., Wright M. C. H., 1995, in Shaw R. A., Payne H. E., Hayes J. J. E., eds, *Astronomical Data Analysis Software and Systems IV Vol. 77 of Astronomical Society of the Pacific Conference Series, A Retrospective View of MIRIAD*. p. 433
- Schilizzi R. T., 1975, *Mem. RAS*, 79, 75
- Schilizzi R. T., McAdam W. B., 1975, *Mem. RAS*, 79, 1
- Schmitt H. R., Antonucci R. R. J., Ulvestad J. S., Kinney A. L., Clarke C. J., Pringle J. E., 2001, *ApJ*, 555, 663
- Simard-Normandin M., Kronberg P. P., Button S., 1981, *ApJS*, 46, 239
- Simpson C., 2005, *Monthly Notices of the Royal Astronomical Society*, 360, 565
- Snellen I. A. G., 2008, *ArXiv e-prints*

- Stil J. M., Keller B. W., George S. J., Taylor A. R., 2014, *ApJ*, 787, 99
- Stompor R., Errard J., Poletti D., 2016, *Phys. Rev. D*, 94, 083526
- Subrahmanyan R., Ekers R. D., Saripalli L., Sadler E. M., 2010, *MNRAS*, 402, 2792
- Tabara H., Inoue M., 1980, *A&AS*, 39, 379
- Taylor A. R., Stil J. M., Grant J. K., Landecker T. L., Kothes R., Reid R. I., Gray A. D., Scott D., Martin P. G., Boothroyd A. I., Joncas G., Lockman F. J., English J., Sajina A., Bond J. R., 2007, *ApJ*, 666, 201
- Thomson R. C., Crane P., Mackay C. D., 1995, *ApJ*, 446, L93
- Tingay S. J., de Kool M., 2003, *AJ*, 126, 723
- Tingay S. J., Lenc E., Brunetti G., Bondi M., 2008, *AJ*, 136, 2473
- Toffolatti L., Negrello M., González-Nuevo J., de Zotti G., Silva L., Granato G. L., Argüeso F., 2005, *A&A*, 438, 475
- Trippe S., Neri R., Krips M., Castro-Carrizo A., Bremer M., Piétu V., Fontana A. L., 2010, *A&A*, 515, A40
- Trippe S., Neri R., Krips M., Castro-Carrizo A., Bremer M., Piétu V., Winters J. M., 2012, *A&A*, 540, A74
- Trombetti T., Burigana C., De Zotti G., Galluzzi V., Massardi M., 2017, *ArXiv e-prints*
- Tucci M., Martínez-González E., Toffolatti L., González-Nuevo J., De Zotti G., 2004a, *MNRAS*, 349, 1267
- Tucci M., Martínez-González E., Toffolatti L., González-Nuevo J., De Zotti G., 2004b, *MNRAS*, 349, 1267
- Tucci M., Toffolatti L., 2012, *Advances in Astronomy*, 2012, 624987
- Tucci M., Toffolatti L., de Zotti G., Martínez-González E., 2011, *A&A*, 533, A57
- Urry C. M., Padovani P., 1995, *PASP*, 107, 803
- Wardle J. F. C., Homan D. C., 2003, *Ap&SS*, 288, 143
- Wardle J. F. C., Kronberg P. P., 1974, *ApJ*, 194, 249
- Wilson A. S., Young A. J., Shopbell P. L., 2001, *ApJ*, 547, 740
- Wright E. L., Chen X., Odegard N., Bennett C. L., Hill R. S., Hinshaw G., Jarosik N., Komatsu E., Nolte M. R., Page L., Spergel D. N., et al. 2009, *ApJS*, 180, 283